CLD full simulation and the study of displaced vertices for the FCC-ee

Anita Sadowski

Université de Strasbourg

École doctorale
Physique, chimie-physique
ED 182
Université de Strasbourg

UNIVERSITÉ DE STRASBOURG

ÉCOLE DOCTORALE DE PHYSIQUE ET CHIMIE-PHYSIQUE

Institut Pluridisciplinaire Hubert Curien (IPHC), UMR 7178

THÈSE présentée par

Anita Sadowski

soutenue le: **30 septembre 2025**

pour obtenir le grade de: **Docteur de l'Université de Strasbourg**
Discipline/Spécialité: Physique des particules

CLD full simulation and the study of displaced vertices for the FCC-ee

THÈSE dirigée par:

Jeremy Andrea — Directeur de recherche CNRS, IPHC
Ziad El Bitar — Directeur de recherche CNRS, IPHC

RAPPORTEURS:

Emmanuel Perez — Chargé de recherche CERN
Jessica Lévêque — Directrice de recherche CNRS, LAPP

AUTRES MEMBRES DU JURY:

Juliette Alimena — Chargée de recherche DESY
Christian Finck — Directeur de recherche CNRS, IPHC
Brieuc François — Chargé de recherche CERN

Contents

Résumé

Chapitre 1 – Le Modèle Standard et les motivations pour la physique au-delà, avec l'apport du FCC-ee

Le **Modèle Standard (MS)** constitue aujourd'hui le cadre théorique central de la physique des particules. Il décrit avec une précision remarquable les constituants élémentaires de la matière et les interactions fondamentales qui les gouvernent, à l'exception de la gravité. Sa construction résulte de découvertes expérimentales et de progrès théoriques majeurs au XX$^{\text{e}}$ siècle : l'unification électrofaible par Glashow, Weinberg et Salam, la formulation de la chromodynamique quantique (QCD), et l'édification d'une théorie de jauge fondée sur le groupe

$$SU(3)_C \times SU(2)_L \times U(1)_Y.$$

Fondations du Modèle Standard

Le MS classe les particules élémentaires en deux catégories :

- les **fermions**, de spin demi-entier, qui constituent la matière (six quarks et six leptons répartis en trois générations) ;
- les **bosons de jauge**, de spin entier, qui assurent la médiation des interactions fondamentales : photon pour l'électromagnétisme, gluons pour la force forte, bosons $W^{\pm}$ et Z^0 pour l'interaction faible.

S'y ajoute le **boson de Higgs**, découvert en 2012 au LHC, qui fournit un mécanisme cohérent de brisure spontanée de la symétrie électrofaible et confère une masse aux bosons W, Z ainsi qu'aux fermions par les couplages de Yukawa.

Les interactions sont décrites par des théories de jauge locales : QED pour l'électromagnétisme ($U(1)$), la théorie électrofaible ($SU(2)_L \times U(1)_Y$), et la QCD ($SU(3)_C$). Le formalisme repose sur le **lagrangien du MS**, qui regroupe les secteurs de jauge, des fermions, du Higgs et de Yukawa. Ce cadre mathématique fournit des prédictions d'une précision exceptionnelle, vérifiées par une multitude de mesures expérimentales (anomalie magnétique de l'électron, diffusion inélastique profonde, mesures électrofaibles de précision au LEP).

Succès et limites du Modèle Standard

Le MS est l'une des théories les plus abouties de l'histoire des sciences. Ses prédictions ont été confirmées par :

- la découverte des bosons W et Z dans les années 1980,
- la mise en évidence des gluons et du quark top,
- la précision des mesures électrofaibles au LEP,

- et enfin la découverte du boson de Higgs au LHC.

Pour autant, plusieurs phénomènes échappent à son cadre, liste non exhaustive :

- les **masses des neutrinos**, révélées par les oscillations de saveur, absentes du formalisme initial ;
- la **matière noire** et l'**énergie noire**, qui constituent près de 95% du contenu de l'Univers ;
- l'**asymétrie matière–antimatière**, trop faible pour s'expliquer par la seule violation de CP du MS ;
- l'absence d'une **description quantique de la gravité**.

Ces limites motivent le développement de théories **au-delà du Modèle Standard (BSM)** : supersymétrie, grandes unifications, dimensions supplémentaires, ou encore neutrinos stériles et leptogenèse.

Recherches expérimentales actuelles

L'exploration BSM s'appuie sur des approches complémentaires :

- **Les collisionneurs hadroniques**, avec le LHC et ses expériences généralistes ATLAS et CMS, qui cherchent directement de nouvelles particules (supersymétriques, candidats matière noire) tout en mesurant avec précision les propriétés du boson de Higgs et des observables électrofaibles. C'est aussi le cas de LHCb (dans la physique de la saveur).
- **La physique des neutrinos**, qui bénéficie de programmes dédiés (T2K, NOvA, JUNO, DUNE, Hyper-Kamiokande) afin de mesurer la hiérarchie de masse, la violation de CP et la nature de Majorana des neutrinos.
- **L'astroparticule et la cosmologie**, qui explorent la matière noire par détection directe (XENONnT, LZ, PandaX), l'étude des rayons cosmiques et neutrinos d'ultra-haute énergie (IceCube, KM3NeT), les observations cosmologiques (Planck, relevés de grande structure) et plus récemment les ondes gravitationnelles (LIGO, Virgo).

Ces approches n'ont pas encore révélé de signal direct de nouvelle physique, mais elles ont fortement contraint les modèles théoriques et guident les futures recherches.

Futurs collisionneurs et FCC-ee

Afin de dépasser les limitations actuelles, plusieurs projets de futur collisionneurs sont en développement : ILC (Japon), CLIC (CERN), CEPC (Chine). Parmi eux, le **Future Circular Collider (FCC)** au CERN occupe une place centrale. Conçu dans un tunnel de 100 km, il déploiera une stratégie par étapes :

- une première phase électron–positon (**FCC-ee**),
- suivie à plus long terme d'un collisionneur proton–proton (**FCC-hh**).

Le **FCC-ee** vise des mesures de précision inégalées grâce à sa luminosité exceptionnelle. Plusieurs régimes d'énergie sont prévus :

- **au pôle** Z (~ 91 GeV), avec la production de 10^{12} bosons Z permettant une "usine à Z" ;
- **au seuil** WW (~ 160 GeV), pour la masse et les couplages des bosons W ;

- **au seuil** ZH (240–250 GeV), pour déterminer les propriétés du boson de Higgs à la précision du pourcent ;
- **au seuil** $t\bar{t}$ ($\sim$ 365 GeV), pour la masse et les couplages du quark top.

Avec cet éventail, FCC-ee se situe à la frontière de la précision :

- en testant le MS avec une exactitude inédite, susceptible de révéler de faibles écarts trahissant une nouvelle physique lourde ;
- en offrant une sensibilité unique à des signatures **exotiques** comme les particules à vie longue, stériles ou faiblement couplées.

FCC-ee apparaît ainsi comme un instrument sans équivalent, à la fois **métrologie de haute précision** et **chasse aux nouvelles physiques**.

Chapitre 2 – Théorie et méthodes du suivi de particules (trajectographie)

Le suivi des particules chargées, ou **tracking**, constitue une étape centrale de la reconstruction des événements en physique des hautes énergies. Il permet de mesurer les trajectoires des particules, d'en déduire leur impulsion et leur charge, et de localiser les points d'interaction ou de désintégration. La qualité du suivi conditionne directement la précision des analyses ultérieures, qu'il s'agisse de la reconstruction des jets, du vertexing, ou de la recherche de nouvelles particules.

Contexte théorique et historique

Depuis les premières chambres à bulles et détecteurs à fils, le suivi des particules a toujours joué un rôle fondamental en physique expérimentale. Avec l'avènement des détecteurs tout-silicium, comme au LHC ou au futur FCC-ee, le tracking atteint une précision micrométrique, permettant non seulement de mesurer les impulsions mais aussi de reconstruire des vertices secondaires à courte distance du point d'interaction.

Le principe repose sur l'effet de la **force de Lorentz** : une particule chargée se déplaçant dans un champ magnétique homogène suit une trajectoire hélicoïdale. La courbure est inversement proportionnelle à l'impulsion transverse, de sorte que la mesure précise de la trajectoire permet d'inférer l'impulsion et la charge électrique de la particule. Le tracking est ainsi au cœur de la chaîne de reconstruction, fournissant les informations nécessaires à l'identification des particules.

Effets limitants et contraintes expérimentales

La précision du suivi dépend de plusieurs facteurs : la résolution spatiale des détecteurs, l'uniformité du champ magnétique et le budget de matière. Un facteur limitant majeur est la **diffusion multiple**, qui correspond à des déviations angulaires successives lors de la traversée de la matière. L'angle typique de diffusion est donné par la formule de Highland :

$$\theta_0 \simeq \frac{13.6\,\mathrm{MeV}}{\beta p}\, z \sqrt{\frac{x}{X_0}} \left[1 + 0.038 \ln\left(\frac{x}{X_0}\right)\right],$$

où p est l'impulsion, β la vitesse relative, z la charge, x l'épaisseur et X_0 la longueur de radiation. Cet effet devient particulièrement pénalisant pour les particules de basse impulsion et impose de limiter le matériel passif (supports, refroidissement, câbles) dans la conception des détecteurs.

Dans le cas des collisions e^+e^-, les conditions expérimentales sont plus propres que dans un collisionneur hadronique, grâce à l'absence de pile-up et de jets sous-jacents. Néanmoins, des arrière-plans demeurent : paires incohérentes, conversions de photons, interactions hadroniques secondaires. Les algorithmes doivent donc être robustes pour maintenir une efficacité élevée et limiter la reconstruction de **fausses trajectoires**.

Modèle de trajectoire et paramètres de piste

Dans un champ magnétique homogène, la trajectoire est décrite par une hélice. Elle peut être paramétrée à l'aide de cinq paramètres indépendants :

- la **courbure** $\Omega = q/p_T$, liée à l'impulsion transverse ;
- l'angle azimutal ϕ_0 au point de plus proche approche ;
- le **paramètre d'impact transverse** d_0, distance minimale au faisceau dans le plan transverse ;
- le **paramètre d'impact longitudinal** z_0, décalage par rapport au plan transverse au point d'impact ;

- la pente $\tan\lambda = p_z/p_T$, reliée à l'angle polaire.

Ces paramètres permettent de reconstruire le vecteur impulsion complet. Leur précision conditionne la physique accessible : d_0 est critique pour la reconstruction de vertices déplacés (décroissance de hadrons lourds, particules à vie longue), tandis que Ω est directement liée à la résolution en impulsion. La covariance entre ces paramètres est également essentielle pour les analyses de précision (mesures de masse, fits cinématiques).

Méthodes de reconstruction

La reconstruction se décompose en deux étapes : la recherche de motifs (*track finding*) et l'ajustement (*track fitting*).

Conformal tracking. La transformation conforme $(x, y) \mapsto (u, v)$ avec

$$u = \frac{x}{x^2 + y^2}, \quad v = \frac{y}{x^2 + y^2},$$

convertit les cercles passant par l'origine en droites. Ainsi, les trajectoires hélicoïdales dans le plan transverse deviennent des droites, ce qui simplifie grandement la reconnaissance. Les hits sont regroupés par un **automate cellulaire**, qui associe des segments locaux en structures cohérentes. Chaque cellule représente un lien possible entre deux hits, et l'évolution de l'automate construit progressivement les candidats-traces. Cette approche est efficace en présence d'un bruit de fond modéré et permet de traiter des topologies complexes comme les kinks ou les conversions de photons.

Filtrage de Kalman. Une fois des candidats identifiés, leurs paramètres sont ajustés par un **filtre de Kalman** (KF). Cet algorithme récursif procède en deux étapes :

1. **Prédiction** : extrapolation de l'état vers le prochain plan de détection en utilisant les équations du mouvement dans un champ magnétique ;
2. **Mise à jour** : correction à partir du hit mesuré, pondérée par l'incertitude de mesure et les processus stochastiques (diffusion multiple, perte d'énergie).

Le KF fournit à chaque étape une estimation locale du vecteur d'état et de sa matrice de covariance. Un *smoothing* final combine les informations de tous les hits pour raffiner l'estimation globale. Cet algorithme est particulièrement adapté aux détecteurs complexes et constitue la méthode standard dans les expériences modernes.

Application au CLD. Le détecteur **CLD**, proposé pour le FCC-ee, adopte une chaîne complète :

1. transformation locale-globale des hits simulés,
2. transformation conforme et construction de candidats par automate,
3. fit par Kalman et lissage,
4. suppression des doublons et sélection des traces de meilleure qualité.

Cette stratégie garantit une efficacité élevée et un faible taux de fausses traces, tout en restant flexible face aux arrière-plans.

Vertexing et reconstruction de jets

Le **vertexing** consiste à reconstruire les points d'interaction primaire et secondaire. Des algorithmes basés sur la minimisation du χ^2, le filtrage de Kalman ou encore des méthodes adaptatives permettent d'atteindre une précision micrométrique. La reconstruction des vertices secondaires est essentielle pour l'identification des hadrons lourds (b, c) et pour la recherche de particules à vie longue comme les neutrinos lourds.

La **reconstruction de jets** au FCC-ee repose sur l'approche **Particle Flow Algorithm (PFA)**. Celle-ci combine les mesures des traces (pour les particules chargées) avec celles des calorimètres. Le suivi joue donc un rôle crucial : plus de 60 % de l'énergie visible d'un événement provient de particules chargées. Une excellente efficacité de tracking est indispensable pour obtenir une résolution énergétique optimale des jets.

Synthèse

Le suivi des particules constitue un élément central de la reconstruction d'événements en physique des hautes énergies. Les méthodes modernes, associant transformation conforme, automates cellulaires et filtrage de Kalman, permettent d'atteindre des performances remarquables dans des détecteurs tout-silicium comme le CLD. Couplés au vertexing et à la reconstruction de jets, ces outils forment la base indispensable pour réaliser le programme ambitieux du FCC-ee, à la fois en termes de **mesures de précision du Modèle Standard** et de **recherche de nouvelles physiques**.

Chapitre 3 – Capteurs MAPS et digitalisation du signal : tests faisceaux du CE-65

Introduction et motivations

Les détecteurs de vertex et de trajectographie des futurs collisionneurs électron–positon doivent répondre à des contraintes particulièrement sévères : une **résolution spatiale micrométrique**, une **faible masse** afin de limiter la diffusion multiple, et une **consommation électrique minimale** afin de réduire les besoins en refroidissement et en câblage. Le FCC-ee, avec ses objectifs de physique de précision, pousse ces exigences à leur maximum : une résolution d'impact transverse de l'ordre de $2-3$ μm est nécessaire pour les mesures de saveur lourde et la recherche de particules à vie longue.

Pour atteindre ces objectifs, les **Monolithic Active Pixel Sensors (MAPS)** apparaissent comme prometteurs. Leur architecture monolithique, intégrant la diode de détection et l'électronique de lecture sur le même substrat, permet d'obtenir un compromis unique entre finesse de pitch, consommation et faible matériel passif. Après le succès de l'ITS2 d'ALICE au LHC, la communauté explore désormais des générations avancées de MAPS adaptées aux futurs collisionneurs : ITS3, CE-65, etc.

Principes et exigences des MAPS

Les MAPS doivent satisfaire simultanément plusieurs critères :

- **Efficacité proche de 100 %**, même à seuils élevés, pour garantir une détection fiable ;
- **Résolution spatiale de** 2–3 μ**m**, requise pour atteindre les performances de vertexing au FCC-ee ;
- **Tolérance aux radiations**, typiquement jusqu'à 10^{14} n_{eq}/cm^2 et quelques centaines de kGy ;
- **Faible densité de puissance**, cible ~ 20 mW/cm^2 pour limiter les besoins en refroidissement.

Deux grandes philosophies de conception existent :

1. **Électrode de collecte large**, qui assure un champ électrique uniforme et une collection rapide de la charge, mais augmente la capacité et donc le bruit et la consommation.
2. **Électrode de collecte petite**, qui réduit la capacité et le bruit, autorise des pixels plus fins, mais demande des optimisations du procédé (épilayer haute résistivité, implants profonds) pour maintenir l'efficacité et la robustesse sous irradiation.

Le capteur de référence ALPIDE

Le capteur **ALPIDE**, utilisé pour le télescope de référence lors des tests, illustre la maturité atteinte par les MAPS. Développé pour l'ITS2 d'ALICE, il associe :

- un pitch de 28×28 μm^2,
- une résolution spatiale ~ 5 μm,
- une consommation < 40 mW/cm^2,
- une intégration complète des fonctions d'amplification et de discrimination dans le pixel.

Il fournit une trajectographie précise, avec une pointing resolution de l'ordre de 2 μm, indispensable pour mesurer la performance des prototypes CE-65.

Le capteur CE-65 et ses variantes

Les prototypes **CE-65**, développés dans le procédé CMOS 65 nm de TPSCo, explorent plusieurs dimensions de conception :

- des pitchs de 15 et 22.5 μm, permettant de comparer finesse spatiale et puissance dissipée ;
- des structures de diodes standards et modifiées, testant différentes dynamiques de collecte ;
- une variante *Modified With Gap (MWG)*, introduisant un champ latéral renforcé pour accélérer la collecte et réduire le partage de charge.

Le design **standard** favorise un partage de charge significatif entre pixels voisins, ce qui permet une interpolation fine mais rend la résolution sensible au réglage du seuil. Le design **MWG** concentre la charge dans le pixel central (plus de 80 % du signal), assurant une efficacité très élevée même à seuils élevés, au prix d'une résolution légèrement dégradée.

Setup expérimental et reconstruction

La campagne de tests s'est déroulée en avril 2024 sur la ligne H6 du SPS, avec un faisceau de hadrons de 120 GeV/c.

- Le **DUT** (Device Under Test) était placé au centre d'un télescope de six plans ALPIDE.
- Les trajectoires étaient reconstruites avec l'algorithme *General Broken Lines* (GBL) dans Corryvreckan, incluant l'effet de diffusion multiple.
- La précision du télescope (~ 2.1 μm) permet une extraction fiable de la résolution intrinsèque du DUT à partir des résidus.

L'efficacité de détection est définie comme la fraction de traces ayant un cluster associé dans une fenêtre de 75 μm. Les clusters sont reconstruits sur des matrices 3×3 autour du pixel graine, avec un seuil exprimé en multiples du bruit RMS.

Résultats : efficacité et résolution

Les résultats montrent que :

- le design standard atteint une résolution < 2 μm à bas seuil, mais voit son efficacité chuter pour des seuils > 150 e^- ;
- le design MWG maintient une efficacité > 99 % même à des seuils élevés (jusqu'à 180 e^-), mais avec une résolution plus constante autour de 2.5–5 μm ;
- le partage de charge, bénéfique pour la résolution, doit être équilibré avec la robustesse vis-à-vis des seuils et du bruit.

Digitalisation du signal

Un enjeu majeur pour les détecteurs de grande surface est la réduction des données et de la puissance. La lecture analogique intégrale est prohibitive ; la digitalisation locale est donc incontournable. Deux schémas ont été étudiés :

Digitalisation 1 bit. Chaque pixel fournit une information binaire (hit/non hit). Avantage : simplicité et très faible consommation. Inconvénient : perte d'information sur le partage de charge, ce qui dégrade la résolution. Les résultats montrent une perte de 60–70 % pour les capteurs standard, mais seulement quelques pourcents pour les capteurs MWG.

Digitalisation 2 bits. Quatre niveaux de codage permettent de conserver une partie de l'information topologique. Après optimisation des seuils (guidée par les distributions de charge), la perte de résolution est limitée à 20–25 % par rapport à l'analogique. Ceci permet d'envisager des **résolutions proches du cas analogique ($\sim 3\ \mu$m)** tout en réduisant considérablement puissance et volume de données. En pratique, cela signifie qu'une résolution de l'ordre de 5 μm peut être obtenue avec des pixels de pitch plus large, ce qui réduit la densité et donc la consommation.

Perspectives et conclusion

Ces résultats confirment que :

- les MAPS en technologie 65 nm sont capables de répondre aux objectifs du FCC-ee,
- une digitalisation 2 bits constitue un compromis très favorable entre performance et consommation,
- le choix de l'architecture (standard vs MWG) doit être guidé par l'équilibre entre résolution, robustesse et contraintes système.

À l'avenir, plusieurs développements sont nécessaires :

- validation des performances sous irradiation,
- optimisation automatique des seuils par algorithmes adaptatifs ou apprentissage machine,
- extension vers une digitalisation temporelle (time-over-threshold, 4D tracking),
- intégration dans un système de lecture complet avec gestion thermique et mécanique.

Les travaux sur le CE-65 démontrent donc la faisabilité de détecteurs MAPS adaptés aux contraintes du FCC-ee. Ils constituent une **preuve de concept** que la digitalisation multi-bits permet de conserver une résolution quasi-analogue tout en permettant possiblement une réduction de la consommation de puissance, ouvrant ainsi la voie à des détecteurs de vertex de nouvelle génération.

Chapitre 4 – Performances de suivi du détecteur CLD au FCC-ee

Introduction

Le projet **Future Circular Collider (FCC)** constitue l'une des initiatives les plus ambitieuses en physique des particules, visant à prolonger l'héritage du LHC au-delà de 2040. Sa première phase, le **FCC-ee**, correspond à un collisionneur électron–positon de 91 km, conçu pour réaliser des mesures de précision sans précédent des particules du Modèle Standard (boson de Higgs, bosons électrofaibles, quark top), et pour sonder indirectement la nouvelle physique.

La réussite de ce programme repose sur la performance des détecteurs placés aux points d'interaction. Parmi les concepts étudiés, le **CLIC-Like Detector (CLD)** constitue la référence adoptée dans cette thèse. Dérivé du détecteur CLICdet initialement conçu pour un collisionneur linéaire, le CLD a été adapté aux conditions spécifiques d'une machine circulaire comme FCC-ee : hautes luminosités, faisceau continu, environnement de bruit de fond différent.

L'objectif de ce chapitre est de présenter les performances attendues du **système de suivi du détecteur CLD**, en s'appuyant sur des études en simulation complète et sur le développement d'un outil dédié, **k4DetPerformance**, réalisé dans le cadre de ces travaux de doctorat.

Concepts de détecteurs au FCC-ee

Quatre concepts de détecteurs ont été proposés pour FCC-ee, chacun optimisé selon des philosophies différentes :

- **CLD** : tout-silicium, avec calorimétrie très granulaire inspirée de CLICdet, adapté au Particle Flow.
- **IDEA** : tracker à fil léger combiné à un calorimètre dual-readout, misant sur la simplicité et une consommation réduite.
- **ALLEGRO** : concept plus compact avec segmentation fine, visant à maximiser la reconstruction par flux de particules.
- **ILD adapté** : version modifiée du détecteur ILD de l'ILC, intégrant une chambre à projection temporelle (TPC) pour le PID et le suivi.

Le reste de ce chapitre se concentre sur le CLD, qui représente la base des études menées dans cette thèse.

Description du détecteur CLD

Le détecteur CLD combine plusieurs sous-détecteurs complémentaires :

- **Vertex detector** : constitué de trois double-couches cylindriques et de trois doubles-disques avant/arrière, basé sur des capteurs MAPS à pixels de 25×25 μm^2, visant une résolution ponctuelle de 3 μm.
- **Tracker silicium** : tout-silicium, avec trois couches internes et trois couches externes, complétées par sept disques internes et quatre disques externes, pour une couverture complète jusqu'à un rayon de 2.1 m.
- **Calorimétrie** : un ECAL silicium–tungstène très granulaire (cellules 5×5 mm^2, 40 couches), et un HCAL à tuiles scintillantes (44 couches), optimisés pour le **Particle Flow Algorithm (PFA)** et une résolution jet de 3–4%.
- **Système magnétique** : solénoïde supraconducteur de 2 T, avec retour de flux en fer segmenté et chambres à muons intégrées.

La conception cherche un compromis entre **résolution en moment transverse** (nécessitant un grand bras de levier et un champ magnétique fort) et **précision en paramètre d'impact** (exigeant un vertex proche et peu de matière).

Développement du framework k4DetPerformance

Dans le cadre de cette thèse, le framework **k4DetPerformance** a été développé pour évaluer systématiquement les performances du suivi au FCC-ee. Intégré à l'écosystème **Key4HEP**, il permet :

- la lecture des données simulées au format EDM4hep,
- le calcul d'indicateurs standard : efficacité de reconstruction, taux de faux et doublons, résolution en moment, en angle et en paramètres d'impact,
- des études comparatives entre géométries et configurations magnétiques.

Ce développement a nécessité de surmonter des problèmes logiciels (reconstruction initialement non fonctionnelle, incohérences géométriques) et constitue désormais un outil partagé dans la communauté FCC.

Performances avec la géométrie de référence

Les études en simulation complète (basées sur Geant4 et la reconstruction Key4HEP) montrent que :

- la résolution en paramètre d'impact transverse d_0 atteint 5 μm pour des traces centrales de 10 GeV,
- la résolution en moment transverse est de l'ordre de 2×10^{-5} GeV^{-1}, comparable à CLICdet malgré un champ magnétique plus faible (2 T contre 4 T), grâce au grand rayon du tracker,
- l'efficacité de reconstruction est supérieure à 99 % sur une large gamme de p_T et d'angles polaires, hors zones extrêmes.

Ces performances respectent les objectifs du FCC-ee pour les mesures de précision.

Études de géométries alternatives

Plusieurs variantes ont été étudiées :

- **Beam pipe plus réaliste** : réduction du rayon à 10 mm avec couches de refroidissement, améliorant de 20% la résolution en d_0 à 10 GeV mais augmentant l'occupation due aux paires incohérentes.
- **Résolution du vertex** : une dégradation de 3 $\rightarrow$ 5–7 μm entraîne une perte nette en précision des paramètres d'impact, surtout à haute impulsion.
- **Réduction du volume du tracker pour PID** : introduire un RICH compact réduit le bras de levier, dégradant la résolution en p_T de 15–20%.
- **Champ magnétique plus fort (3 T)** : compense partiellement cette perte, en améliorant la résolution en impulsion, au prix de la nécessité d'un champ plus élevé.

Ces études illustrent les compromis inévitables entre précision en impulsion, vertexing, intégration de sous-systèmes supplémentaires et contraintes de machine.

Conclusion et perspectives

Le détecteur CLD, dans sa configuration de référence, est capable d'atteindre les performances de suivi nécessaires au programme du FCC-ee. L'outil **k4DetPerformance**, développé dans cette thèse, fournit un cadre robuste pour explorer systématiquement les effets de modifications géométriques ou de paramètres expérimentaux.

Les résultats montrent que :

- le suivi au CLD atteint les objectifs de précision du FCC-ee pour la physique des saveurs et du Higgs,
- des marges d'optimisation existent, notamment sur la géométrie du beam pipe et la digitalisation du vertex,
- l'intégration de sous-détecteurs supplémentaires (PID, timing) doit se faire en tenant compte de l'équilibre entre performances globales et contraintes d'ingénierie.

Ces études démontrent la **robustesse du concept CLD**, tout en soulignant l'importance de poursuivre l'optimisation, notamment avec des modèles de digitisation plus réalistes et des évaluations de bruit de fond détaillées. Le cadre méthodologique mis en place constitue une base solide pour les futures études de performance et pour guider les choix de design vers le détecteur final du FCC-ee.

Chapitre 5 – Leptons Lourds Neutres et étude de sensibilité au FCC-ee

Motivations théoriques

Les **Leptons Lourds Neutres (HNLs)** constituent l'un des scénarios les plus simples et motivés de physique au-delà du Modèle Standard. Introduits dans le cadre du mécanisme de seesaw de type I, ils expliquent naturellement la petitesse des masses des neutrinos observées en oscillations. Selon leur nature (Dirac ou Majorana), ils peuvent également violer le nombre leptonique et contribuer à l'asymétrie baryonique de l'Univers via la leptogenèse. Enfin, dans des extensions telles que le νMSM, l'un des HNLs peut même jouer le rôle de **candidat à la matière noire**.

Sur le plan phénoménologique, les HNLs sont des états singlets du groupe de jauge du SM, couplant uniquement par mélange avec les neutrinos actifs. Ces couplages très faibles impliquent des largeurs de désintégration petites et donc des durées de vie macroscopiques : les HNLs sont des **particules à longue durée de vie (LLP)**. Leur signature typique en collisionneurs est la présence de **vertices déplacés**, parfois situés à plusieurs dizaines de centimètres du point d'interaction.

Production et signatures aux collisionneurs

Au FCC-ee, la production principale d'HNLs provient de la désintégration du boson Z :

$$e^+e^- \to Z \to N\nu,$$

avec une portée en masse limitée à $m_N < m_Z$. À plus haute énergie ($\sqrt{s}$ = 240–365 GeV), la production par échange de bosons W et Z hors-masse permet d'accéder à des masses supérieures.

Les HNLs se désintègrent en canaux leptoniques et hadroniques, par exemple :

$$N \to e^{\pm}W^{\mp}, \quad N \to \nu Z, \quad N \to \nu h.$$

Pour $m_N < m_W$, seules les désintégrations à trois corps sont ouvertes, entraînant de longues durées de vie. Ces signatures se traduisent expérimentalement par :

- des **électrons ou muons issus de sommets secondaires**, décalés par rapport au point de collision,
- des jets hadroniques émergeant loin du point d'interaction,
- un excès d'**energie transverse manquante** associé aux neutrinos.

La distinction entre HNLs de type Dirac et Majorana repose sur la recherche d'événements **dileptons de même signe**, caractéristiques des violations de nombre leptonique.

Simulation et reconstruction

Une étape importante de cette thèse a été la **reproduction de l'analyse HNL en simulation complète**, au-delà des études phénoménologiques initiales basées sur `Delphes`.

Simulation rapide (fast sim). Delphes fournit un outil efficace pour générer rapidement de grands échantillons en paramétrisant la résolution des détecteurs. Il permet de scanner l'espace des paramètres et d'optimiser des coupes, mais ne simule pas les effets fin de detection.

Simulation complète (full sim). À l'inverse, Geant4 et la chaîne de reconstruction `Key4HEP` offrent une description des interactions dans le détecteur CLD et du processus complet de reconstruction. Cette approche est plus coûteuse en temps de calcul, mais indispensable pour évaluer le plus précisément possible :

- la **performance du tracking** pour des trajectoires très décalées,
- l'efficacité de reconstruction de vertices déplacés.

Un problème spécifique détecté lors de ces travaux a concerné le réglage des paramètres de l'algorithme de tracking conforme (*MaxCellAngle*). Après réoptimisation, la reconstruction de vertices déplacés a pu être rétablie jusqu'à 600 mm, en accord avec les études de référence.

Analyse des performances

L'analyse s'est concentrée sur la recherche de désintégrations HNLs de type :

$$N \to e^+e^-\nu,$$

sélectionnées par la présence de deux électrons et de manquant transverse.

Les principales étapes de l'étude sont :

- **Comparaison fast/full sim** : les variables cinématiques (masse invariante des électrons, énergie manquante) sont stables. Les différences d'efficacité de reconstruction de vertex entre fast et full sim restent à comprendre.
- **Fonds principaux** : $Z \to \tau^+\tau^-$, $Z \to b\bar{b}$ et $Z \to e^+e^-$, générant des électrons associés à de l'énergie manquante.

Sensibilité attendue

Les projections en simulation complète montrent que :

- la sensibilité reste **proche de celle estimée en fast sim**, mais avec une description plus réaliste des effets de détecteurs,
- le FCC-ee au pôle Z pourra explorer des mélanges $|V_{eN}|^2$ de l'ordre de 10^{-11}–10^{-9} pour des masses m_N comprises entre 10 et 80 GeV,
- les résultats soulignent l'importance d'une **optimisation logicielle** du tracking et d'une **prise en compte systématique des incertitudes**, encore manquante à ce stade.

Conclusion et perspectives

Ce travail démontre que les HNLs constituent une cible naturelle et prometteuse pour le FCC-ee. La simulation complète valide les résultats phénoménologiques obtenus en fast sim, tout en reproduisant de manière plus réaliste les effets de détecteurs.

À terme, plusieurs développements sont nécessaires :

- l'intégration de la **digitalisation réaliste des capteurs** (MAPS),
- une évaluation quantitative des **incertitudes systématiques**,
- l'extension à d'autres canaux (muons déplacés, jets hadroniques),
- la confrontation aux contraintes cosmologiques et astrophysiques.

Ainsi, l'étude des HNLs au FCC-ee illustre l'interaction directe entre **performance du détecteur** et **potentiel de découverte**. Elle ouvre la voie à des recherches complémentaires sur d'autres signatures de particules à longue durée de vie, consolidant le rôle unique du FCC-ee comme machine de précision et de découverte.

Introduction

The Future Circular Collider in its electron–positron phase (FCC-ee) is designed to be the next flagship facility of high-energy physics. With its extremely high luminosity and multiple energy stages, FCC-ee will provide measurements of unprecedented precision within the Standard Model (SM), from Higgs couplings to electroweak observables. At the same time, its clean experimental environment and vast statistics will open a window to new physics beyond the Standard Model, offering sensitivity to rare processes and unconventional signatures such as long-lived particles.

The Standard Model itself has been remarkably successful in describing the fundamental constituents of matter and their interactions, culminating in the discovery of the Higgs boson in 2012. Yet, it leaves key questions unanswered: the origin of neutrino masses, the matter–antimatter asymmetry of the Universe, and the nature of dark matter. These open issues drive the development of both new theoretical frameworks and new experimental approaches.

A central ingredient in this programme is the ability to reconstruct the properties of particles produced in high-energy collisions. Tracking theory and methods, based on well-established tools such as conformal mapping and Kalman filter–based fits, play a key role in determining momenta, charges, and decay vertices of charged particles. Precise tracking is especially crucial for identifying displaced vertices, which are a distinctive signature of long-lived BSM particles.

Reaching the required performance calls for advanced detector technologies. In particular, Monolithic Active Pixel Sensors (MAPS) have emerged as a promising solution for future collider tracking systems thanks to their fine spatial granularity and low material budget. This thesis presents studies of a new generation of MAPS prototypes, the CE-65 sensors, tested in beam campaigns at CERN, with a focus on digitisation strategies and their impact on resolution.

Building on these developments, the performance of the CLIC-Like Detector (CLD), one of the reference detector concepts for FCC-ee, has been carefully assessed. Dedicated simulation studies of tracking efficiency, momentum resolution, and vertexing demonstrate the capabilities and limitations of the CLD design, and inform optimisation of its geometry and operating conditions.

Finally, the thesis turns to a motivated new-physics scenario: Heavy Neutral Leptons (HNLs). These hypothetical fermions arise naturally in seesaw models that explain neutrino masses and may also play a role in generating the baryon asymmetry. Depending on their parameters, HNLs can be long-lived, producing signatures such as displaced vertices that FCC-ee is uniquely positioned to probe. Using full detector simulation, the sensitivity of FCC-ee to HNLs has been investigated, highlighting the interplay between detector performance and discovery potential.

In summary, this thesis combines theoretical motivation, detector technology development, performance studies, and physics analysis. Together, these elements demonstrate how advances in tracking and sensor technology directly enable searches for new particles, with Heavy Neutral Leptons serving as a benchmark case at the precision frontier of the FCC-ee.

Chapter 1

Standard model

Contents

1.1 Foundations of the Standard Model

The Standard Model (SM) of particle physics is the theoretical framework that describes the fundamental constituents of matter and the forces that govern their interactions, with the exception of gravity. It is rooted in the cumulative progress of experimental discoveries and theoretical advancements made throughout the 20^{th} century.

The earliest steps toward understanding matter began with the identification of the electron by Thomson in 1897 [1], followed by Rutherford's nuclear model in 1911 [2], and Chadwick's discovery of the neutron in 1932 [3], which established the classical picture of the atom. However, the post-1930s discovery of a multitude of new particles, beyond just protons, neutrons, and electrons, challenged this simplistic view, necessitating the development of a more comprehensive theory of fundamental interactions.

The formal structure of the Standard Model was constructed during the 1970s, notably with the unification of the electromagnetic and weak forces into the electroweak theory by Glashow [4], Weinberg [5], and Salam [6], and the development of Quantum Chromodynamics (QCD) to describe the strong interaction. These theoretical milestones were experimentally validated over the subsequent decades, with key discoveries including the W and Z bosons, gluons, the top quark, and ultimately the Higgs boson.

The SM combines quantum field theory with gauge symmetry to provide a coherent and predictive framework for particle physics up to the electroweak scale. It has been remarkably successful, with its predictions confirmed across a wide range of phenomena. This success culminated in the observation of the Higgs boson [7] in 2012 by the ATLAS [8] and CMS [9] experiments at the Large Hadron Collider (LHC) [10], confirming the mechanism of electroweak symmetry breaking.

Despite these achievements, the SM is widely regarded as incomplete. It does not account for several key observations, such as the existence of dark matter, the origin of the matter-antimatter asymmetry in the universe, and the finite masses of neutrinos implied by oscillation experiments. These open questions motivate the development of new theoretical frameworks, collectively known as Beyond the Standard Model (BSM) physics.

1.1.1 Fundamental Particles

The Standard Model classifies all known elementary particles into two broad categories: **fermions** and **bosons** [11].

Fermions are the building blocks of matter and possess half-integer spin ($\frac{1}{2}$). They are subdivided into:

- **Quarks**: up (u), down (d), charm (c), strange (s), top (t), and bottom (b);
- **Leptons**: electron (e), muon (μ), tau (τ), and their associated neutrinos (ν_e, ν_μ, ν_τ).

These fermions are organized into three **generations**, each containing a pair of quarks and a pair of leptons. The first generation forms the stable matter that constitutes ordinary atoms, while the second and third generations are heavier and unstable, decaying into first-generation particles.

Gauge bosons are integer-spin particles that mediate the fundamental interactions between fermions:

- The **photon** (γ), which mediates the electromagnetic force;
- The $\mathbf{W}^{\pm}$ and $\mathbf{Z}^0$ bosons, responsible for the weak interaction;
- The **gluons** (g), eight in number, which mediate the strong interaction.

In addition to these force carriers, the Standard Model includes the **Higgs boson** (H), a scalar particle associated with the mechanism of electroweak symmetry breaking. It provides mass to the W and Z bosons as well as to fermions through Yukawa couplings [7, 12].

A schematic summary of the 12 fundamental fermions and 5 bosons of the Standard Model, along with their interaction links, is illustrated in Figure 1.1.

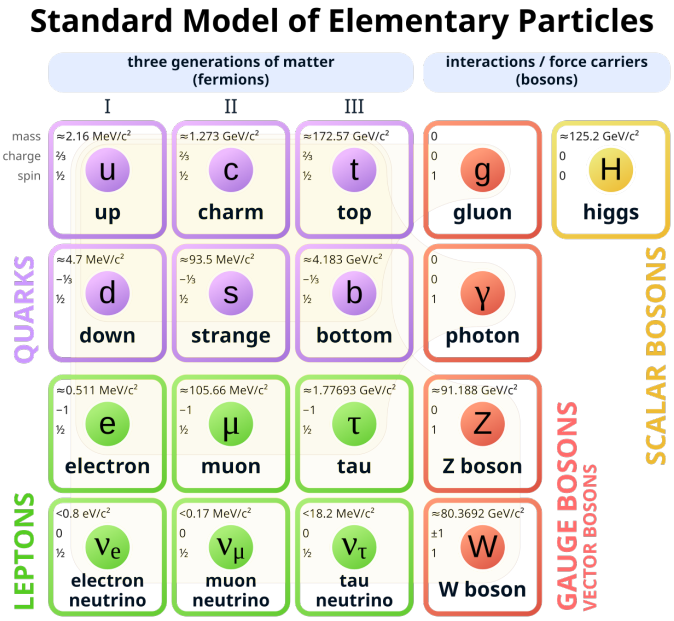

Figure 1.1: Standard Model of elementary particles: the 12 fundamental fermions and 5 fundamental bosons. Brown loops indicate which bosons (red) couple to which fermions (purple and green) [13].

Each of these particles is characterized by specific quantum numbers, such as electric charge, weak isospin, colour charge (for quarks and gluons), and mass.

The interactions among these particles are governed by the symmetries of the Standard Model, encoded in the gauge group:

$$SU(3)_C \times SU(2)_L \times U(1)_Y$$

where:

- $SU(3)_C$ corresponds to the colour symmetry of the strong interaction;
- $SU(2)_L$ is associated with the weak isospin;
- $U(1)_Y$ corresponds to the weak hypercharge.

Together, these particles and symmetries form the rich and predictive structure of the Standard Model, whose accuracy has been repeatedly confirmed by experimental results [14].

1.1.2 Fundamental Interactions

The Standard Model encompasses three of the four known fundamental forces of nature: the electromagnetic, weak, and strong interactions. Each of these interactions is described by a quantum gauge theory based on a local symmetry group [15]. The gravitational interaction is not included in the Standard Model, as it currently lacks a consistent quantum field theory description.

Moreover, gravity is extremely weak compared to the other interactions at the energy scales probed by particle colliders, and its effects can be neglected in high-energy physics experiments.

The SM encompasses three fundamental forces:

- **Electromagnetic interaction**: Described by Quantum Electrodynamics (QED), a U(1) gauge theory mediated by photons [16, 17].
- **Weak interaction**: An $SU(2)_L$ gauge symmetry mediated by $W^{\pm}$ and Z^0 bosons, responsible for processes like beta decay and neutrino interactions [4, 5, 6].
- **Strong interaction**: Governed by Quantum Chromodynamics (QCD), an $SU(3)_C$ gauge theory, mediating interactions via gluons that confine quarks within hadrons [18, 19].

1.1.2.1 Electromagnetic Interaction

The electromagnetic force is described by Quantum Electrodynamics (QED), a U(1) gauge theory. Its mediator is the massless photon (γ), which couples to electric charge. QED was the first quantum field theory to achieve remarkable agreement with experiment, particularly in phenomena such as the anomalous magnetic moment of the electron and the Lamb shift [20, 21]. The gauge invariance under the U(1) group implies the conservation of electric charge.

1.1.2.2 Weak Interaction

The weak interaction is responsible for processes like beta decay and neutrino scattering. It is governed by an SU(2) gauge symmetry and mediated by the massive $W^{\pm}$ and Z^0 bosons [4, 5, 6]. The weak interaction is governed by an SU(2) gauge symmetry and mediated by the massive $W^{\pm}$ and Z^0 bosons [4, 5, 6], which acquire mass through the spontaneous breaking of the unified electroweak symmetry $SU(2)_L \times U(1)_Y$ via the Higgs mechanism [7, 12]. The weak interaction is unique in that it violates parity (P) and charge-parity (CP) symmetries [22, 23], and only couples to left-handed fermions and right-handed antifermions.

The unification of the electromagnetic and weak forces into the electroweak theory is a cornerstone of the Standard Model. This unification is described by a combined $SU(2)_L \times U(1)_Y$ symmetry, which breaks down to $U(1)_{EM}$ after symmetry breaking [24].

1.1.2.3 Strong Interaction

The strong interaction binds quarks into hadrons (such as protons and neutrons) and is described by Quantum Chromodynamics (QCD), a non-Abelian $SU(3)_C$ gauge theory [18, 19]. The interaction is mediated by eight massless gluons, which themselves carry colour charge, leading to self-interaction, a feature absent in QED. Two important properties of QCD are:

- **Asymptotic freedom**: At high energies (short distances), quarks behave almost as free particles [18, 19].
- **Confinement**: At low energies, quarks and gluons are confined into colour-neutral hadrons, and cannot be observed in isolation [25, 26].

Despite being well tested experimentally (e.g., in deep inelastic scattering and hadron colliders), confinement remains a non-perturbative phenomenon and one of the theoretical challenges of QCD [26].

1.1.3 The Standard Model Lagrangian

The Lagrangian of the Standard Model is the mathematical expression that encapsulates the dynamics and interactions of all known fundamental particles, respecting the gauge symmetry:

$$SU(3)_C \times SU(2)_L \times U(1)_Y$$

[15, 27].

It is composed of several parts:

$$\mathcal{L}_{\text{SM}} = \mathcal{L}_{\text{gauge}} + \mathcal{L}_{\text{fermion}} + \mathcal{L}_{\text{Higgs}} + \mathcal{L}_{\text{Yukawa}}$$

[28].

Gauge Sector

This part describes the dynamics of the gauge fields associated with the strong, weak, and electromagnetic forces:

$$\mathcal{L}_{\text{gauge}} = -\frac{1}{4} G^a_{\mu\nu} G^{a\mu\nu} - \frac{1}{4} W^i_{\mu\nu} W^{i\mu\nu} - \frac{1}{4} B_{\mu\nu} B^{\mu\nu}$$

where:

- $G^a_{\mu\nu}$ is the gluon field strength tensor (SU(3)_C),
- $W^i_{\mu\nu}$ is the SU(2)_L field strength tensor,
- $B_{\mu\nu}$ is the U(1)_Y field strength tensor.

[18, 19].

Fermion Sector

This part governs the kinetic terms and gauge interactions of the quarks and leptons:

$$\mathcal{L}_{\text{fermion}} = \sum_{\text{generations}} \bar{\psi}_f i\gamma^\mu D_\mu \psi_f$$

The covariant derivative D_μ introduces interactions with the gauge bosons. Fermions are arranged in left-handed SU(2) doublets and right-handed singlets, reflecting the chiral nature of weak interactions [28].

Higgs Sector

The Higgs sector introduces a complex scalar SU(2)_L doublet Φ:

$$\mathcal{L}_{\text{Higgs}} = (D_\mu \Phi)^\dagger (D^\mu \Phi) - V(\Phi)$$

with the Higgs potential:

$$V(\Phi) = \mu^2 \Phi^\dagger \Phi + \lambda (\Phi^\dagger \Phi)^2$$

For $\mu^2 < 0$, the potential has a non-zero vacuum expectation value (VEV), leading to spontaneous symmetry breaking [7, 12].

Yukawa Sector

This sector generates fermion masses via interactions with the Higgs field:

$$\mathcal{L}_{\text{Yukawa}} = -y_f \bar{\psi}_L \Phi \psi_R + \text{h.c.}$$

where y_f are the Yukawa couplings, and ψ_L, ψ_R are the left- and right-handed fermion fields. After electroweak symmetry breaking (EWSB), these terms give masses to the fermions proportional to y_f [15, 28].

1.1.4 The Electroweak Theory

The Electroweak Theory unifies the electromagnetic and weak interactions into a single theoretical framework, based on the gauge symmetry:

$$SU(2)_L \times U(1)_Y$$

[4, 5, 6].

This unification was developed by Glashow, Weinberg, and Salam, earning them the Nobel Prize in 1979. It forms a crucial part of the Standard Model and is experimentally validated by the discovery of the W and Z bosons [29, 30] and the electroweak precision measurements at LEP and SLC [31].

Gauge Fields and Fermions

The theory introduces four gauge fields [11]:

- W_μ^1, W_μ^2, W_μ^3 from the $SU(2)_L$ group,
- B_μ from the $U(1)_Y$ group.

Fermions are arranged in doublets and singlets based on their chirality and weak isospin:

$$\text{Leptons:} \quad L = \begin{pmatrix} \nu_e \\ e \end{pmatrix}_L, \quad e_R \qquad \text{Quarks:} \quad Q = \begin{pmatrix} u \\ d \end{pmatrix}_L, \quad u_R, d_R$$

[28].

Left-handed fields transform as doublets under $SU(2)_L$, while right-handed fields are singlets. The hypercharge Y is related to the electric charge Q and weak isospin T_3 through the Gell-Mann–Nishijima relation:

$$Q = T_3 + \frac{Y}{2}$$

[32].

Covariant Derivative and Interactions

The covariant derivative acting on fermions is:

$$D_\mu = \partial_\mu - ig\frac{\sigma^i}{2}W_\mu^i - ig'\frac{Y}{2}B_\mu$$

where g and g' are the $SU(2)_L$ and $U(1)_Y$ coupling constants, respectively, and σ^i are the Pauli matrices [15].

From the gauge fields, we define the physical bosons:

$$W_\mu^\pm = \frac{1}{\sqrt{2}}(W_\mu^1 \mp iW_\mu^2)$$
$$Z_\mu = \cos\theta_W W_\mu^3 - \sin\theta_W B_\mu$$
$$A_\mu = \sin\theta_W W_\mu^3 + \cos\theta_W B_\mu$$

Here, A_μ corresponds to the photon, Z_μ to the neutral weak boson, and $W^\pm$ to the charged weak bosons. The angle θ_W is the Weinberg angle (or weak mixing angle), defined as:

$$\tan\theta_W = \frac{g'}{g}$$

[5].

Neutral and Charged Currents

The electroweak interaction features two types of currents:

- **Charged current** (CC): mediated by $W^\pm$, involves flavor-changing transitions (e.g., β decay: $n \to p + e^- + \bar{\nu}_e$) [22].
- **Neutral current** (NC): mediated by Z^0, involves no change in electric charge (e.g., $\nu_\mu + e^- \to \nu_\mu + e^-$) [33].

Flavour-changing neutral current (FCNC) processes, which would involve changes in quark flavour without a change in electric charge, are strongly suppressed in the Standard Model due to the Glashow–Iliopoulos–Maiani (GIM) mechanism [34].

The electromagnetic interaction emerges as a residual unbroken U(1) symmetry after the electroweak symmetry is spontaneously broken via the Higgs mechanism [7, 12].

1.1.5 Electroweak Symmetry Breaking and the Higgs Mechanism

The Higgs mechanism provides the dynamical origin of mass for both gauge bosons and fermions within the Standard Model, while preserving gauge invariance [7, 12, 35]. It is responsible for the spontaneous breaking of the electroweak symmetry:

$$SU(2)_L \times U(1)_Y \to U(1)_{\text{EM}}$$

leaving the electromagnetic interaction unbroken.

The mechanism is implemented via the introduction of a complex scalar field Φ, which transforms as an $SU(2)_L$ doublet with hypercharge $Y = 1$:

$$\Phi = \begin{pmatrix} \phi^+ \\ \phi^0 \end{pmatrix}$$

The scalar potential for the Higgs field is defined as:

$$V(\Phi) = \mu^2 \Phi^\dagger \Phi + \lambda(\Phi^\dagger \Phi)^2$$

where $\lambda > 0$ ensures stability, and $\mu^2 < 0$ triggers spontaneous symmetry breaking [15, 27]. The potential exhibits a "Mexican hat" shape, with a continuum of minima characterized by:

$$|\langle\Phi\rangle| = \frac{v}{\sqrt{2}} = \sqrt{-\frac{\mu^2}{\lambda}}$$

Selecting a specific vacuum expectation value (VEV) to preserve $U(1)_{\text{EM}}$:

$$\langle \Phi \rangle = \frac{1}{\sqrt{2}} \begin{pmatrix} 0 \\ v \end{pmatrix}$$

breaks the $SU(2)_L \times U(1)_Y$ symmetry and endows the electroweak gauge bosons with mass:

$$M_W = \frac{1}{2} g v, \qquad M_Z = \frac{1}{2} \sqrt{g^2 + g'^2}\, v$$

while the photon remains massless, as expected for the electromagnetic interaction. The weak mixing angle θ_W is defined via:

$$\sin \theta_W = \frac{g'}{\sqrt{g^2 + g'^2}}$$

[5].

The Higgs field initially contains four real degrees of freedom. Three of these are absorbed ("eaten") by the $W^{\pm}$ and Z bosons, providing them with longitudinal polarization states [15]. The remaining degree of freedom manifests as a physical scalar particle: the Higgs boson H, with a mass:

$$M_H = \sqrt{2\lambda} v$$

The discovery of the Higgs boson at a mass of approximately 125 GeV by the ATLAS and CMS collaborations at the LHC in 2012 [8, 9] confirmed the existence of the Higgs mechanism in nature.

Beyond giving mass to the gauge bosons, the Higgs field couples to fermions through Yukawa interactions:

$$\mathcal{L}_{\text{Yukawa}} = -y_f \bar{\psi}_L \Phi \psi_R + \text{h.c.}$$

where y_f is the Yukawa coupling for a given fermion f. After symmetry breaking, this interaction generates fermion masses proportional to their coupling to the Higgs field:

$$m_f = \frac{y_f v}{\sqrt{2}}$$

[11].

In summary, the Higgs mechanism explains:

- The mass of the W and Z bosons while keeping the photon massless,
- The mass spectrum of fermions via Yukawa couplings,
- The preservation of the $U(1)_{\text{EM}}$ gauge symmetry, ensuring the electromagnetic interaction remains long-range and unbroken.

1.2 Achievements and Beyond the Standard Model

The Standard Model (SM) stands as one of the most successful frameworks in the history of physics [24, 11]. Its predictive power has been confirmed by a wide array of precision measurements, notably at collider experiments such as LEP [31], the Tevatron [36], and the LHC [8, 9]. The accurate predictions of electroweak observables, the running of the strong coupling constant in QCD, and the precise agreement between theory and experiments in flavour physics have solidified the SM's status as the cornerstone of particle physics [14].

One of the SM's crowning achievements was the prediction and eventual discovery of the Higgs boson [7, 12]. This discovery completed the particle spectrum predicted by the model and directly confirmed the mechanism of electroweak symmetry breaking via the Higgs field. The study of

the Higgs boson's properties remains a primary avenue to test the SM's robustness and explore potential deviations hinting at new physics.

Yet, despite these successes, the SM is widely regarded as incomplete. Several empirical observations remain unexplained within its framework:

- **Neutrino Masses:** Neutrinos are massless in the SM, but neutrino oscillation experiments have established that they possess small but non-zero masses [37, 38], implying the need for an extension of the model.
- **Dark Matter and Dark Energy:** Astrophysical and cosmological data indicate that around 95% of the Universe is composed of dark matter and dark energy [39], entities that the SM does not account for.
- **Matter-Antimatter Asymmetry:** The observed dominance of matter over antimatter in the Universe cannot be fully explained by the CP violation contained within the SM [40].
- **Gravity:** The SM lacks a description of gravity, and attempts to reconcile quantum field theory with general relativity remain an open challenge, motivating research in quantum gravity [41].

These limitations have spurred the development of **Beyond the Standard Model (BSM)** theories, which seek to address the SM's shortcomings and provide a more complete understanding of fundamental physics. Key BSM frameworks include:

- **Supersymmetry (SUSY):** Proposes a symmetry between bosons and fermions, predicting a superpartner for each SM particle [42]. SUSY offers a potential solution to the *hierarchy problem*, the question of why the Higgs boson mass remains stable and much lighter than the Planck scale despite large quantum corrections. It also provides viable dark matter candidates.
- **Grand Unified Theories (GUTs):** Aim to unify the strong, weak, and electromagnetic forces within a single gauge group [43].
- **Extra Dimensions:** Theories such as those proposed by Arkani-Hamed, Dimopoulos, and Dvali (ADD) [44], or the Randall–Sundrum models [45], introduce additional spatial dimensions as a possible solution to the *hierarchy problem*, that is, why gravity appears so much weaker than the other fundamental forces. In these models, gravity can propagate into the extra dimensions, effectively diluting its strength in our 4D spacetime.
- **Heavy Neutral Leptons (HNLs):** Extensions involving right-handed or sterile neutrinos offer a natural explanation for the smallness of neutrino masses through *seesaw mechanisms* [46, 47]. Depending on their mass and lifetime, HNLs can also act as viable *dark matter candidates* (if they are light and long-lived), or contribute to *baryogenesis via leptogenesis*, a process in which CP, violating decays of HNLs in the early universe create an asymmetry in the lepton sector that is partially converted into a baryon asymmetry [48].

These theoretical proposals guide the ongoing experimental searches at colliders with the dual aim of discovering new particles or uncovering subtle deviations from SM predictions. The interplay between theoretical innovation and experimental exploration continues to be essential in the quest to uncover the physics beyond the Standard Model.

1.3 Experimental Searches for BSM Physics

The search for physics beyond the Standard Model (BSM) is an active and diverse field, combining efforts across high-energy colliders, neutrino experiments, and astroparticle physics. These complementary approaches explore different energy scales, phenomena, and signatures where new physics might manifest [11].

1.3.1 Collider Experiments

Collider experiments remain the most direct way to probe BSM physics by attempting to produce new particles in high-energy collisions. The **Large Hadron Collider (LHC)** at CERN is currently the highest energy collider in operation, colliding protons at center-of-mass energies up to 14 TeV [49]. The LHC's general-purpose detectors, **ATLAS** [50] and **CMS** [51], have conducted extensive searches for supersymmetric particles [52], dark matter candidates [53], among other exotic states.

While no direct evidence for new particles has yet emerged, these searches have placed stringent limits on various BSM scenarios [52, 53]. Additionally, precision measurements of the Higgs boson's properties [54, 55], electroweak observables, and rare decay processes provide indirect sensitivity to BSM effects, complementing direct searches.

The LHC continues to operate with increasing luminosity, enhancing its potential to uncover rare processes or subtle deviations from Standard Model predictions [56].

1.3.2 Neutrino Experiments

Neutrino physics offers a unique window into BSM phenomena, particularly due to the discovery of neutrino oscillations [37, 38], which imply that neutrinos have mass, something the Standard Model does not accommodate. A variety of dedicated experiments are aimed at exploring neutrino properties in greater depth:

- **T2K** [57] and **NOvA** [58] focus on measuring neutrino oscillation parameters and searching for CP violation in the lepton sector.
- **JUNO** [59] is a reactor neutrino experiment in China designed to determine the neutrino mass ordering with high precision.
- **DUNE** [60], currently under construction in the United States, aims to measure CP violation in the lepton sector, determine the mass hierarchy, and detect supernova neutrinos.
- **Hyper-Kamiokande** [61], the successor to Super-Kamiokande and T2K, will provide enhanced sensitivity to neutrino oscillations and nucleon decay.
- **KATRIN** [62] seeks to measure the absolute mass scale of neutrinos via beta decay experiments.
- Searches for **neutrinoless double beta decay** (e.g., **GERDA** [63], **CUORE** [64]) aim to determine whether neutrinos are Majorana particles, which would have profound implications for the origin of neutrino mass and leptogenesis.

The detection of sterile neutrinos, if they exist, is another major objective of ongoing and planned experiments [65].

1.3.3 Astroparticle Physics and Cosmology

Astroparticle physics and cosmology provide complementary probes of BSM physics, exploiting observations of the universe at large scales and extreme energies:

- **Dark Matter Searches:** Direct detection experiments like **XENONnT** [66], **LUX-ZEPLIN (LZ)** [67], and **PandaX** [68] seek to observe interactions between dark matter particles and atomic nuclei.
- **High-Energy Cosmic Rays and Neutrinos:** Observatories such as **IceCube** [69], **ANTARES** [70], **KM3NeT** [71], and the **Pierre Auger Observatory** [72] investigate ultra-high energy cosmic rays and neutrinos, providing insights into astrophysical phenomena and potential new physics.
- **Cosmological Observations:** Precision measurements of the cosmic microwave background, such as by **Planck** [39], and large-scale structure surveys constrain cosmological parameters sensitive to BSM physics.
- **Gravitational Waves:** The detection of gravitational waves by **LIGO** and **Virgo** [73] opens a new observational window, potentially probing early universe phenomena linked to BSM physics [74].

While current experiments have yet to conclusively reveal BSM physics, the constraints they provide help refine theoretical models and guide future experimental efforts. The increasing precision and energy reach of ongoing searches, especially with the HL-LHC [56], ensure that the exploration will continue into the next decade.

1.4 Future Colliders and Prospects for New Physics

As illustrated in the previous section, despite the successes of the Standard Model, several key questions in fundamental physics remain unanswered. These open issues, such as the origin of neutrino masses, the nature of dark matter, and the matter-antimatter asymmetry, provide strong motivation to pursue the next generation of particle colliders. Such facilities aim both to perform high-precision measurements, capable of revealing subtle deviations from SM predictions, and to explore new energy frontiers where direct evidence of new physics may emerge.

One of the primary motivations is the need for both high-precision measurements and the exploration of higher energy frontiers. Precision studies of the Higgs boson, the electroweak sector, and the top quark could reveal subtle deviations from SM predictions that hint at new physics scales [75, 76]. Simultaneously, higher energy collisions might directly produce new particles beyond the current reach of the LHC [77].

Several future collider projects have been proposed, each offering distinct advantages and scientific opportunities. The **International Linear Collider (ILC)** is a proposed linear electron-positron collider in Japan, designed to operate initially at 250 GeV as a Higgs factory, with possible upgrades to higher energies [78]. The **Compact Linear Collider (CLIC)** at CERN proposes a staged linear collider reaching up to 3 TeV, enabling both precision studies and direct searches for new particles [79]. In China, the **Circular Electron-Positron Collider (CEPC)** aims to provide high-luminosity collisions at energies 240 GeV, primarily focused on Higgs physics [76].

Among these proposals, the **Future Circular Collider (FCC)** at CERN proposes a versatile, staged collider program within a 100 km tunnel, combining electron-positron, proton-proton, and electron-proton collision capabilities [80]. In this thesis, particular attention is given to the FCC because it constitutes the main framework of the ongoing research project presented here.

The primary scientific objectives of these future colliders include performing precision measurements of the Higgs boson couplings, mass, and self-coupling, scrutinizing electroweak parameters with unprecedented accuracy, and probing rare processes that are sensitive to BSM contributions [75, 77]. They also aim to explore flavour physics anomalies, test lepton flavour universality, and search for new particles that could account for dark matter, neutrino masses, or explain the matter-antimatter asymmetry [11].

1.4.1 The Future Circular Collider (FCC)

The **Future Circular Collider (FCC)** is CERN's ambitious proposal for a next-generation research infrastructure, **planned** to succeed the LHC [81]. Conceived as a comprehensive and multipurpose facility, the FCC is envisioned to be constructed in a new 100-kilometer underground tunnel around the Geneva region. The FCC integrated program is structured in three main phases, each targeting distinct physics goals and energy regimes [80].

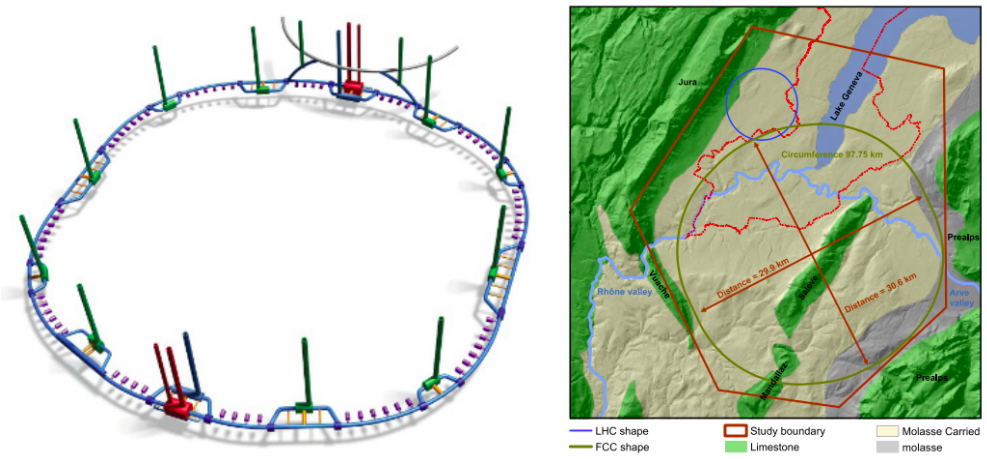

Figure 1.2: **Left:** illustrative 3D schematic (not to scale) of the planned underground infrastructure for the FCC. **Right:** geographical overview of the study area, highlighting key topographical and geological features, with the existing LHC tunnel shown in blue and the proposed FCC tunnel layout in brown [82].

The first phase, **FCC-ee**, is a high-luminosity electron-positron collider optimized for precision studies at various energy points, including the Z boson pole, the WW threshold, the Higgs production peak, and the top quark pair production threshold [75]. Following FCC-ee, the program envisions a transition to **FCC-hh**, a hadron collider operating at center-of-mass energies of 100 TeV, providing an unprecedented energy frontier for direct searches of new physics [81]. An intermediate phase, **FCC-eh**, would allows for electron-proton collisions, enabling unique probes of QCD dynamics and electroweak processes [83].

The FCC program is designed to rigorously test the Standard Model's predictions while searching for signs of new physics. Precision measurements of the Higgs boson, top quark properties, and electroweak observables are central to this strategy [80]. Furthermore, FCC aims to explore connections with cosmology and astroparticle physics, such as shedding light on the nature of dark matter, mechanisms of baryogenesis, or the role of the Higgs field in the early universe [75, 77].

1.4.2 FCC-ee: Precision Frontier

The **FCC-ee** constitutes the first stage of the FCC program, focused on high-precision studies using electron-positron collisions [80, 75]. As a circular collider, FCC-ee offers several operational modes, each targeting specific energy regimes:

- **Z-pole run**: Operating at the Z boson mass energy (91 GeV), enabling the production of up to 10^{12} Z bosons for ultra-precise electroweak measurements [82].
- **WW threshold**: Around 160 GeV, optimized for precision studies of W boson properties and interactions [82].

- **Higgs factory**: At 240-250 GeV, focusing on Higgsstrahlung processes to measure the Higgs couplings and branching ratios with percent-level accuracy [75, 82].
- **Top threshold**: Near 350-365 GeV, designed to determine the top quark mass and couplings with high precision [80].

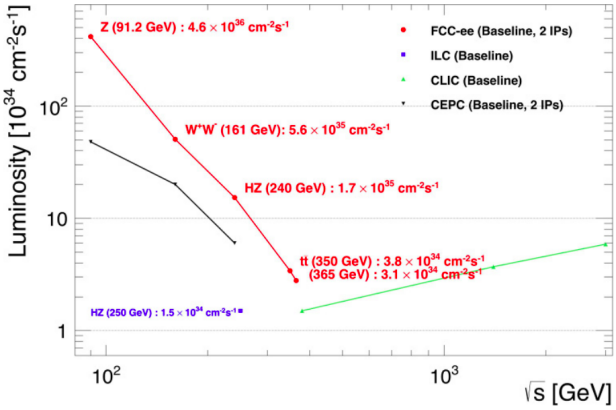

Figure 1.3: Projected baseline luminosities (summed over all interaction points) as a function of centre-of-mass energy $\sqrt{s}$ for the four major proposed e^+e^- collider projects. The comparison includes ILC (blue squares), CLIC (green upward triangles), CEPC (black downward triangles), and FCC-ee (red circles), each shown with a 10% safety margin [82].

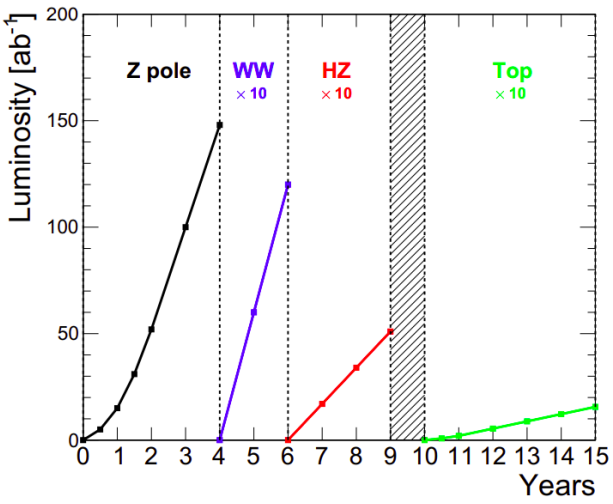

Figure 1.4: Planned operational timeline for FCC-ee based on the five-year conceptual design study. The plot shows the cumulative integrated luminosity delivered over time at key energy stages: Z pole (black), WW threshold (blue), Higgs factory (red), and top-pair threshold (green). The hatched region denotes the scheduled shutdown period required to prepare the collider for high-energy operation [82].

FCC-ee is projected to achieve extremely high luminosities, surpassing the capabilities of previous e^+e^- colliders [81]. Advanced detector technologies will ensure excellent vertex resolution, momentum measurement, and flavour tagging, crucial for studying rare decays and subtle effects [80].

The precision attainable at FCC-ee will allow stringent tests of the Standard Model, refining the determination of the electroweak mixing angle, W and Z boson masses, and the Higgs boson's

couplings [75]. Additionally, it provides sensitivity to **indirect effects of heavy new physics**, which could manifest as deviations in precision observables even if new particles are too heavy to be directly produced [75, 84].

Furthermore, FCC-ee will explore potential **flavour anomalies** observed in current experiments, investigate lepton flavour violation, and provide constraints on scenarios involving sterile neutrinos, dark sectors, and other BSM frameworks [75, 84]. In combination, these capabilities establish FCC-ee as the precision frontier, laying the groundwork for subsequent energy frontier explorations with FCC-hh.

Chapter 2

Tracking

Contents

Tracking is a central component of event reconstruction, essential for determining particle momenta and locating interaction vertices. By accurately measuring the trajectories of charged particles, the tracking system provides critical information for a wide range of physics analyses, from identifying particle types to probing fundamental interactions. High-precision and efficient tracking enables the reconstruction of particle trajectories and the determination of properties such as momentum and electric charge.

The following sections introduce the theoretical and experimental foundations of track reconstruction in high-energy physics. Section 2.1 outlines the track model and key reconstruction parameters. Section 2.2 presents the Conformal Tracking and Kalman filter methods, with a focus on their implementation in the CLD detector. Finally, Section 2.3 explores vertexing and jet reconstruction techniques, highlighting their connection to tracking and their role in the overall event reconstruction process.

2.1 Theoretical and experimental context

This section presents the theoretical and experimental foundations of charged particle tracking in high-energy physics. It begins with a general overview of tracking principles and their relevance, followed by a discussion tailored to electron-positron collisions. The final parts describe the track model and parameters used in reconstruction algorithms.

2.1.1 Particle Tracking in High-Energy Physics

Charged particles produced in collisions induce electronic signals in position-sensitive detectors as they pass through the tracking system. These signals, or hits, are processed by reconstruction algorithms to form tracks (Section 2.2), which are continuous representations of particle trajectories. The precision of the track parameters extracted from these trajectories depends not only on the spatial resolution of the detectors and the performance of the reconstruction algorithms, but also on the material budget and the strength and uniformity of the magnetic field.

Tracking is one of the first steps in the event reconstruction chain and lays the foundation for all subsequent analyses. It enables momentum and charge determination, particle identification, and vertex reconstruction.

- Principles of Particle Tracking: Particle tracking is based on the behaviour of charged particles in a magnetic field. When traversing such a field, these particles are submitted to the Lorentz force, which causes them to follow curved trajectories. The radius of curvature depends on the particle's momentum projected in the transverse plane of the magnetic field direction, charge, and the strength of the magnetic field. Tracking detectors are placed at various positions along the path of the particles and record the points where the particles intersect them. By reconstructing the full trajectory and analysing its curvature, one can infer the particle's momentum with high precision.

- Challenges in High-Energy Particle Tracking: High-energy physics experiments pose unique challenges for tracking:

  - High Collision Rates: Particle accelerators produce a large number of collisions per second, requiring fast and efficient tracking systems to keep up with the data rate.

  - Radiation Environment: The detectors used in tracking must operate in a harsh radiation environment near the collision point, necessitating robust and radiation-resistant materials and technologies.

2.1.1.1 Multiple scattering

When a charged particle traverses material, such as the layers of a tracking detector, it undergoes numerous small-angle deflections due to Coulomb interactions with the atomic nuclei. This phenomenon is known as **multiple Coulomb scattering**, or simply **multiple scattering**[85, 86]. Although each individual scattering event is small, the cumulative effect can significantly alter the particle's trajectory, especially at low momenta.

In high-energy physics tracking systems, multiple scattering imposes a fundamental limitation on the spatial resolution and momentum measurement of charged particles. The angular deviation θ_0 due to multiple scattering can be approximated by the Highland formula[86]:

$$\theta_0 \approx \frac{13.6 \text{ MeV}}{\beta p} z \sqrt{\frac{x}{X_0}} \left[1 + 0.038 \ln \left(\frac{x}{X_0} \right) \right] \tag{2.1}$$

With β the particle's velocity relative to the speed of light, p the momentum, z the particle charge, x the thickness of the material traversed, and X_0 the radiation length of the material, which characterizes how quickly high-energy electrons lose energy via bremsstrahlung.

This expression highlights that the effect is more pronounced for low-momentum particles and increases with material budget. Therefore, minimising the amount of passive material in the tracker, such as support structures, cables, and cooling systems, is crucial to reduce the impact of multiple scattering on track reconstruction.

To ensure precise tracking, especially for low-momentum particles, the detector must be as light as possible. Minimizing the material budget reduces multiple scattering effects and is a key design consideration.

2.1.2 Tracking at e^+e^- collision

The experimental scenario of future high-energy particle physics experiments at a electron-positron collider can be summarised as follows:

- Multiple scattering is expected when crossing materials, such as detector frames, support and cooling structures.
- Secondary interactions can produce significant activity in the detector, and recognising and correctly reconstructing these effects is essential for accurate event interpretation. Common examples include high-energy electrons produced by charged particles traversing the detector, hadronic interactions of pions and other hadrons with detector material, as well as electromagnetic processes such as photon conversions and bremsstrahlung from electrons. These secondary products must be properly identified and incorporated into the overall event reconstruction.

Track reconstruction in high-energy physics is usually divided into *track finding* and *track fitting*. In track finding, the pattern recognition problem is solved as the signals generated by charged particles in tracker detectors are grouped into track candidates. In track fitting, the best estimation of the track parameters is derived by error minimisation. For both track finding and track fitting a large variety of methods have been developed in the past decades. A detailed overview of the history and an introduction into the subject can be found in [87].

From a physics perspective, several aspects of event reconstruction rely heavily on the quality of track fitting. Accurate track parameters are essential for a wide range of analyses, including (but not limited to):

- Precise determination of invariant masses, with well-estimated uncertainties. This is crucial not only for discovering new resonances but also for detecting subtle deviations in known mass peaks that could signal new physics.

- Reconstruction of secondary vertices to measure lifetimes of short-lived particles such as heavy-flavour hadrons.
- Efficient identification of kinks in tracks, which is important for recognizing decays involving invisible particles like neutrinos.
- Reliable charge and momentum measurements, which are fundamental for particle identification and for separating signal from background in many physics channels.

Achieving optimal track fitting performance requires detailed knowledge of detector response and magnetic field behaviour, along with careful treatment of multiple scattering, energy loss, and a robust track model that accurately describes particle trajectories.

2.1.2.1 Expected background

In high-energy e^+e^- collisions, various background processes can mask or mimic the signals of interest. Understanding and estimating these background contributions is critical for the design of tracking detectors, especially the vertex detector, and for the development of reconstruction algorithms. Backgrounds typically arise from both physical processes occurring within the detector and instrumental effects that may introduce fake signals.

Types of Background

- **Beam-induced backgrounds:**
  These are primarily due to the interaction of the incoming beams, including phenomena such as beamstrahlung, where photons are emitted from the electron or positron beams during collisions. These photons can convert into e^+e^- pairs or produce electromagnetic showers when interacting with the detector material. Beam-beam interactions such as incoherent pair production and hadronic events from $\gamma\gamma$ collisions contribute significantly to the background environment. For example, at FCCee Z-pole operation, simulations predict several tens of incoherent pairs per bunch crossing, leading to hit densities of $\mathcal{O}(0.1\text{–}1)$ hits/mm^2 per layer per event in the innermost vertex layers[82].
- **Fake tracks:**
  Fake tracks refer to reconstructed trajectories that do not correspond to any real particle. While electronic noise is generally negligible in modern silicon detectors, fake tracks often arise from the mis-association of real hits, especially in dense environments or when detector occupancy increases. Studies at CLIC and FCCee show that with optimised pattern recognition, the fake track rate can be kept below 1–2% [88], but may rise in events with high background occupancy or poorly constrained track seeds.
- **Pile-up:**
  In high-luminosity e^+e^- collisions, overlapping signals from different events can still affect reconstruction. Unlike hadron colliders, FCCee does not suffer from multiple interactions per bunch crossing. However, **out-of-time pile-up** can occur, particularly in the calorimeters and to a lesser extent in the silicon tracking layers. For example, bunch spacing at FCCee is of the order of 20 ns at the Z pole, and detector components with integration times longer than this can record energy deposits from adjacent bunch crossings. While manageable, this effect requires careful timing design and filtering in the reconstruction.

Track Selection and Background Suppression

Effective background rejection strategies are crucial for achieving high precision in particle tracking and identification. Several methods are commonly employed to mitigate the effects of backgrounds:

- **Track quality cuts:** Various track-quality cuts are applied to improve the signal-to-background ratio. These cuts often focus on parameters like the track fit χ^2, track isolation, or the impact parameter with respect to the primary vertex.
- **Particle identification (PID):** Particle identification relies on multiple detector technologies and methods. These include measuring the energy loss per unit length (dE/dx) in tracking detectors, time-of-flight (ToF) measurements, and the use of dedicated subdetectors such as electromagnetic and hadronic calorimeters, muon chambers, and Ring Imaging Cherenkov (RICH) detectors. RICH detectors are particularly effective for identifying charged hadrons over a wide momentum range by measuring the Cherenkov angle of emitted light. Combining information from these systems enables efficient discrimination between different particle species and improves the rejection of background particles.
- **Monte Carlo simulation:** Detailed simulations of the background processes provide a benchmark for understanding and estimating the background in the detector environment. These simulations help to model various background sources and develop strategies for their rejection in the analysis.

In high-luminosity environments, understanding the expected background levels and developing robust background rejection techniques is crucial to achieve the desired precision in tracking measurements.

2.1.3 Track model

To extract these properties, the trajectory must be described mathematically in terms of a finite set of parameters. The set of solutions to the particle's equation of motion in the magnetic field defines the *track model*[87].

The equation of motion of a charged particle in a magnetic field is described by the Lorentz force [89]:

$$\vec{\mathrm{F}} = \frac{d}{dt}\left(m\frac{d\vec{x}(s)}{dt}\right) = q\vec{v} \wedge \vec{B}(\vec{x}(s)) \tag{2.2}$$

where $\vec{F}$ is the Lorentz force, q and $\vec{v}$ are the particle's charge and velocity, respectively, and $\vec{B}(\vec{x}(s))$ is the static magnetic field at the particle's position. The trajectory of the particle is denoted by $\vec{x}(s)$, a position vector parametrised by the path length s, which is the distance travelled along the trajectory from a chosen starting point. Using $s(t)$ as the arc length travelled up to time t, and the absolute value of the velocity $v = ds/dt$, the following identities hold:

$$\frac{d\vec{x}(s)}{dt} = \frac{d\vec{x}(s)}{ds}\frac{ds}{dt} = \frac{d\vec{x}(s)}{ds}v \tag{2.3}$$

$$\frac{d^2\vec{x}(s)}{dt^2} = \frac{d^2\vec{x}(s)}{ds^2}v^2 \tag{2.4}$$

Equation 2.2 can be rewritten as

$$\frac{d^2\vec{x}(s)}{ds^2} = \frac{q}{mv}\frac{d\vec{x}(s)}{ds} \wedge \vec{B}(\vec{x}(s)) \tag{2.5}$$

If the particle mass is known, solving Equation 2.5 requires six integration constants: three to specify the initial position and three for the initial momentum (or direction of motion). These constants fully define the trajectory of the particle in the magnetic field. By introducing an identity and defining a specific coordinate surface as the *reference surface*, the number of independent parameters needed to describe a track can be reduced to five. These typically include two parameters for the impact position on the reference surface, two for the track direction at that point, and one for the particle momentum.

In the special case of a homogeneous magnetic field, $\vec{B}$ can be taken parallel to the z-axis and written as $\vec{B} = B\,\vec{e}_z$, where $\vec{e}_z = (0,\, 0,\, 1)^T$, such as the one provided by a solenoid. Under this condition, the equations of motion simplify to:

$$\left(\frac{dx}{ds}\right)^2 + \left(\frac{dy}{ds}\right)^2 + \left(\frac{dz}{ds}\right)^2 = 1 \tag{2.6}$$

$$\frac{d^2x}{ds^2} = \frac{q}{mv}\frac{dy}{ds}B \tag{2.7}$$

$$\frac{d^2y}{ds^2} = -\frac{q}{mv}\frac{dx}{ds}B \tag{2.8}$$

$$\frac{d^2z}{ds^2} = 0 \tag{2.9}$$

Under the assumption of a uniform magnetic field oriented along the z-axis, a charged particle follows a helical path. This path results from the Lorentz force, which causes the particle to curve in the transverse plane while drifting along the z-direction. The helical trajectory can be described parametrically in terms of the arc length s, using initial values for position and momentum.

The set of equations below express the particle's coordinates along the helix, based on geometrical and kinematic parameters such as the curvature radius R_H, dip angle λ, and azimuthal angle Φ_0.

$$x(s) = x_0 + R\left(\cos\left(\Phi_0 + \frac{hs}{R}\cos\lambda\right) - \cos\Phi_0\right) \tag{2.10}$$

$$y(s) = y_0 + R\left(\sin\left(\Phi_0 + \frac{hs}{R}\cos\lambda\right) - \sin\Phi_0\right) \tag{2.11}$$

$$z(s) = z_0 + s\sin\lambda \tag{2.12}$$

A schematic view of the relevant parameters is shown in Figure 2.1.

In practice, real detector magnetic fields are not perfectly uniform. Accurately predicting a charged particle's path in such inhomogeneous conditions requires detailed knowledge of the field map, along with a numerical integration method to solve the equations of motion. A commonly used technique is the fourth-order Runge-Kutta method [87], which iteratively estimates the particle's next position and momentum based on local field values.

2.1.4 Track parameters

The basis for the parametrisation of tracks is the LDC coordinate system as defined in [91]. It is Cartesian and right-handed with its origin located at the nominal point of interaction. Further insights into track parameters within LCIO can be found in [92].

- **Z-axis** aligns with the mean beam direction
- **Y-axis** points upwards, perpendicular to the Earth's surface
- **X-axis** completes the right-handed system, lying in the plane of the Earth's surface

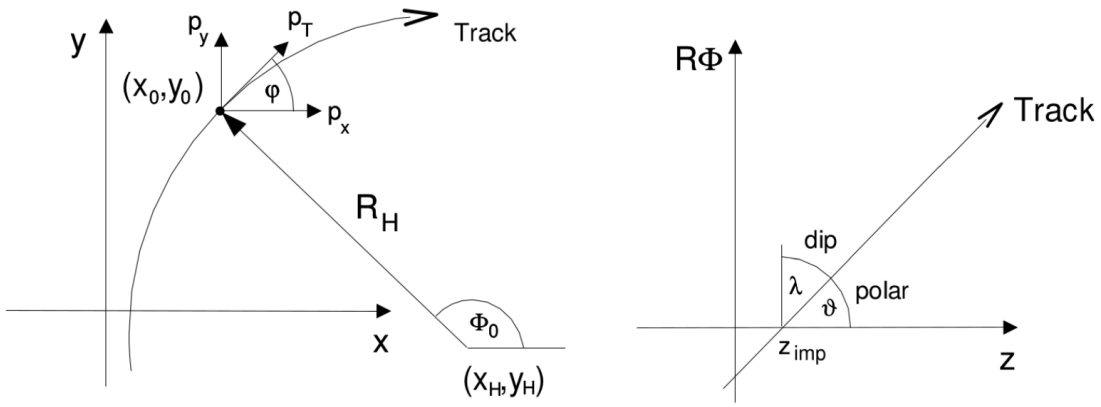

(a) (b)

Figure 2.1: Helix parameters in the x - y (a) and RΦ - z (b) plane for a constant magnetic field parallel to the z-axis. Figure taken from [90]

Let's define $\hat{\mathbf{p}}_{e^-}$ ($\hat{\mathbf{p}}_{e^+}$) as the direction of the three-momentum of incoming electrons (positrons). The z-axis aligns with the mean beam direction, which is the line bisecting the smaller angle between $\hat{\mathbf{p}}_{e^-}$ and $\hat{\mathbf{p}}_{e^+}$. In general the z axis is parallel to $\hat{\mathbf{p}}_{e^-}$ **-** $\hat{\mathbf{p}}_{e^+}$. In the case of colliding beams aligned along the same axis, the z-axis is taken parallel to $\hat{\mathbf{p}}_{e^-}$, the electron beam direction. The y-axis points vertically upward. This coordinate system is henceforth referred to as the reference system. An arbitrary vector $\boldsymbol{v} = (v_x,\ v_y,\ v_z)$ in the reference system can also be represented in spherical coordinates $|\boldsymbol{v}|$, θ, and ϕ with the transformation:

$$\boldsymbol{v} = \begin{pmatrix} |\boldsymbol{v}| & \sin\theta\cos\phi \\ |\boldsymbol{v}| & \sin\theta\sin\phi \\ |\boldsymbol{v}| & \cos\theta \end{pmatrix} \quad \begin{matrix} with & \theta \in [0,\pi] \\ & \phi\ in] -\pi,\pi] \end{matrix} \tag{2.13}$$

where θ is the polar and ϕ the azimuthal angle.

2.1.4.1 Parametrisation of a track

When a charged particle interacts with a constant magnetic field, it follows a helicoidal path, assuming negligible energy loss and multiple scattering effects. The magnetic field is assumed to be uniform and aligned with the z-axis of the coordinate system. Consequently, the trajectory of a charged particle is a segment of a circle when projected onto the xy plane and the z displacement is a linear function of the length s of the arc that is described in the xy plane. This results in a straight line in the sz plane. The parametrisation of the movement of a charged particle is defined by a reference point, $\mathbf{P}^{\mathrm{r}} = (P_x^r,\ P_y^r,\ P_z^r)$, and five *track parameters* (Ω, ϕ_0, d_0, z_0 and $\tan\lambda$). In general the reference point can be any point in space. For convenience, the reference point is generally chosen to be $\mathbf{P}^{\mathrm{r}} = (0,\ 0,\ 0)$. The five track parameters refer to a specific point $\mathbf{P}^0 = (P_x^0,\ P_y^0,\ P_z^0)$ along the helix. In this text $\mathbf{P}^0$ is the point of closest approach (pca) to the reference point in the xy plane (see Figure 2.2).

- xy Plane (transverse plane)

In the transverse (x–y) plane, a charged particle's path is typically described using a reference point (often the origin) and three key parameters: the curvature (Ω, the azimuthal angle ϕ_0 at the

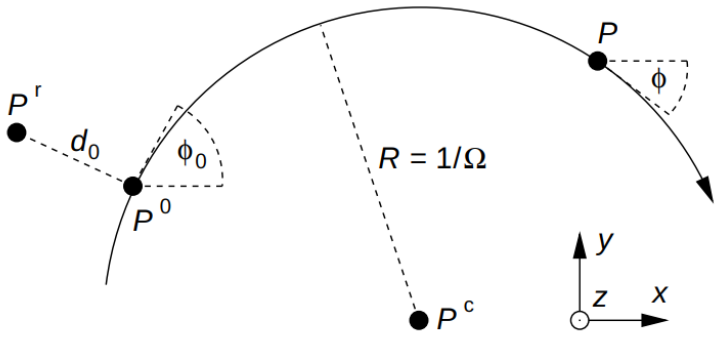

Figure 2.2: Schematic of a charged particle's helical projection in the transverse plane. The figure illustrates the curvature radius, point of closest approach, and reference point relevant for defining transverse track parameters. Figure taken from [92]

point of closest approach (pca), and the transverse impact parameter d_0. The curvature, defined as $\Omega = 1/R$, determines the bending of the trajectory in the magnetic field and reflects the particle's charge sign. The angle ϕ_0 specifies the track's direction at the pca, while d_0 is the signed distance between the pca and the reference point, orthogonal to the particle's momentum vector.

These quantities define the track geometry in the transverse plane. Figure 2.2 provides a schematic view of these parameters.

$$\mathbf{d} = \mathbf{P}^0 - \mathbf{P}^{\mathrm{r}} \tag{2.14}$$

and

$$\boldsymbol{n}_{pca} = \begin{pmatrix} -\sin\phi \\ \cos\phi \end{pmatrix} \tag{2.15}$$

$$d_0 = \boldsymbol{n}_{pca} \cdot \mathbf{d} = -(P_x^r - P_x^0)\sin\phi_0 + (P_y^r - P_y^0)\cos\phi_0 \tag{2.16}$$

Given that $|\boldsymbol{n}_{pca}| = 1$, $|d_0|$ represents the distance between $\mathbf{P}^{\mathrm{r}}$ and $\mathbf{P}^0$ in the xy plane. The convention for sign is established as follows: looking from the reference point to the pca, then $d_0 > 0$ if the particle travels downstream with respect to P^r, and $d_0 < 0$ if the particle travels upstream with respect to P^r. This results in $\mathrm{sgn}(\Omega) = \mathrm{sgn}(d_0)$ if $\mathbf{P}^{\mathrm{r}}$ is inside and inversely in $\mathrm{sgn}(\Omega) =$ -$\mathrm{sgn}(d_0)$ if $\mathbf{P}^{\mathrm{r}}$ is outside the arc.

The centre point $\mathbf{P}^c = (P_x^c,\ P_y^c)$ of the circle in the xy plane is usually different from the reference point $\mathbf{P}^{\mathrm{r}}$. If ϕ is defined as the azimuthal angle of the momentum vector at a given point $\mathbf{P} = (P_x,\ P_y,\ P_z)$ on the track, the coordinates of $\mathbf{P}^c$ can be calculated as:

$$P_x^c = P_x^r + (\frac{1}{\Omega} + d_0) \cdot \sin\phi_0 \tag{2.17}$$

$$P_y^c = P_y^r - (\frac{1}{\Omega} + d_0) \cdot \cos\phi_0 \tag{2.18}$$

In this case $\mathbf{P}$ turns into $\mathbf{P}^0$, which can be expressed using d_0 and ϕ_0.

- sz Plane

In the longitudinal (s–z) plane, the helical trajectory of a charged particle reduces to a straight line. This linear motion can be described using two additional parameters: the slope $\tan\lambda$ and the longitudinal impact parameter z_0. The slope $\tan\lambda$ represents the angle of inclination of the track

with respect to the transverse plane and is directly related to the polar angle θ of the momentum vector. Meanwhile, z_0 gives the z-coordinate of the point of closest approach relative to the chosen reference point. see Figure 2.3.

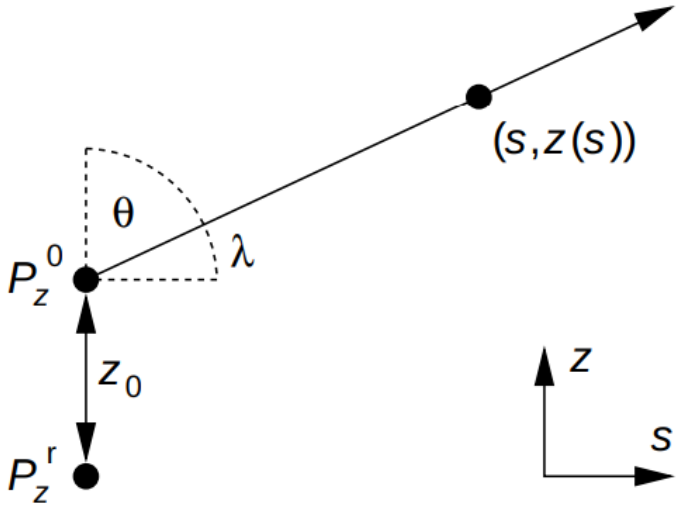

Figure 2.3: The projection of a helix in the sz plane is a straight line. The variable s at a point $\mathbf{P}$ is the arc length in the xy plane from $\mathbf{P}^0$ to $\mathbf{P}$. This also implies that $s = 0$, if $z = z^0$. Figure taken from [92]

The longitudinal trajectory can be expressed as a linear function of the arc length s, starting from the pca:

$$z(s) = z_0 + s \cdot \tan\lambda \tag{2.19}$$

2.1.4.2 Remarks on Track Reconstruction

In the initial stages of track reconstruction, the direction in which a particle travels along its trajectory is often not yet determined. A common assumption is that tracks originate from the interaction point and propagate outward, which sets the sign of the curvature Ω. However, for certain cases such as backscattered or curling particles, this assumption may not hold.

As a result, the same helical trajectory can be described using two different but mathematically equivalent parameter sets, depending on the assumed direction of motion. This ambiguity affects the signs of Ω, d_0, and $\tan\lambda$, but not the overall geometry of the track.

$$\begin{aligned} \phi_0^{'} &= (\phi_0 + \pi \bmod 2\pi) \\ \Omega^{'} &= -\Omega \\ d_0^{'} &= -d_0 \\ \tan\lambda^{'} &= -\tan\lambda = -\cot\theta \qquad \text{with} \quad \lambda^{'} = -\lambda, \theta^{'} = \pi - \theta \\ z_0^{'} &= z_0 \end{aligned} \tag{2.20}$$

This highlights that the sign of Ω does not directly encode the handedness of the helix.

Track parameters are typically defined with respect to the detector origin, but for analysis purposes, it is often preferable to reparametrize them relative to the true production vertex (primary or secondary), adjusting ϕ_0, d_0, and z_0 accordingly. Additionally, the reference point can be chosen freely along the track, for instance at subdetector boundaries.

2.1.4.3 Physics Track Variables

The geometrical parameters that describe a particle's helical trajectory, Ω, ϕ_0, d_0, z_0, and $\tan\lambda$, provide the basis for calculating physical observables such as the momentum and electric charge. In a solenoidal field aligned with the z-axis, the curvature Ω is directly related to the particle's transverse momentum:

$$p_T = a \cdot \left| \frac{B_z}{\Omega} \right| \tag{2.21}$$

where a is a constant that ensures unit consistency (typically 3×10^{-4} if p_T is in GeV/c, B_z in Tesla, and Ω in mm^{-1}).

The longitudinal momentum is reconstructed using the track's dip angle:

$$p = \frac{p_T}{\cos\lambda} \tag{2.22}$$

From this, the full momentum vector (p_x, p_y, p_z) can be derived using the azimuthal angle ϕ_0 and the polar angle θ. The sign of the electric charge is inferred from the product $B_z \cdot \Omega$, with the convention:

$$q = \mathrm{sign}(B_z/\Omega) \tag{2.23}$$

The parametrisation involves a reference point and five key track parameters: curvature (Ω), azimuthal angle (ϕ_0), impact parameter (d_0), z-position at the closest approach (z_0), and the slope ($\tan\lambda$) in the sz plane. These parameters enable a comprehensive description of the movement of a particle, assuming a helical trajectory due to a constant magnetic field aligned with the z-axis. The resolutions on those parameters give important information on the track and event reconstruction:

- Curvature (Ω) Resolution: Affects the precision in measuring the momentum of charged particles. Poor resolution can lead to significant errors in momentum measurement, especially for high-energy particles, as the curvature becomes less pronounced. Good resolution is essential for accurate determination of particle momenta and, by extension, the reconstruction of decay chains and mass calculations.

- Azimuthal Angle (ϕ_0) Resolution: Impacts the accuracy of the particle trajectory direction at the closest approach. Poor resolution can lead to errors in determining the particle's flight direction, affecting vertex reconstruction and the ability to accurately trace the particle's origin or decay products.

- Impact Parameter (d_0) Resolution: Critical for identifying particles that have a significant lifetime and hence travel a measurable distance before decaying. Good resolution in the impact parameter is key to identifying displaced vertices, which is essential for studies involving heavy flavour quarks (b and c quarks) and tau leptons, and searching for new physics phenomena involving long-lived particles.

- Z-position (z_0) Resolution: Influences the ability to accurately determine the particle's position along the beam axis at the point of closest approach. High resolution is necessary for precise vertex reconstruction, especially in events with complex topologies or when distinguishing between primary and secondary vertices.

- Slope ($\tan\lambda$) Resolution: Affects the measurement of the angle of the track with respect to the beam axis, which is crucial for determining the particle's momentum component along the beam direction. Accurate resolution is vital for particle identification techniques based on energy loss and for reconstructing the kinematics of events.

Improvements in resolution for each of these parameters directly contribute to better particle identification, more accurate momentum measurements, improved vertex reconstruction, and enhanced overall detector performance. Conversely, poor resolution can lead to increased backgrounds, reduced signal sensitivity.

2.2 Conformal Tracking

The conformal tracking algorithm can be divided into two main blocks: the conformal mapping method and the cellular automaton-based track finding. In this regard, [88] provides crucial insights into the development and application of conformal tracking methods to the domain of all-silicon trackers at future electron–positron colliders.

Conformal tracking is a technique designed to simplify pattern recognition by using a mathematical transformation that maps curved particle trajectories into straight lines in a transformed space. This approach reduces the complexity of track finding and improves robustness against dense environments or non-prompt tracks.

2.2.1 Conformal mapping

Conformal mapping is a mathematical technique that transforms curved trajectories in the (x, y) plan in the global Euclidean space into straight lines in a new coordinate system the conformal space, denoted (u, v) [93]. This transformation is based on the concept that circles intersecting the origin of the (x, y) coordinate system can be transformed into straight lines in a different coordinate system (u, v). In the context of tracking, this method simplifies the pattern recognition task by converting circular arcs, such as those traced by charged particles in a magnetic field, into linear patterns that are easier to detect.

The circle equation in global coordinates (x, y):

$$(x - a)^2 + (y - b)^2 = r^2 \tag{2.24}$$

where a and b are the coordinates of the center of the circle, and r is the radius. The circle equation is equivalent to a straight line in the (u, v) plane:

$$v = -\frac{a}{b}u + \frac{1}{2b} \tag{2.25}$$

if the circle is passing through the origin such that r is fixed to $r^2 = a^2 + b^2$ and if the following transformations are applied:

$$u = \frac{x}{x^2 + y^2}, \quad v = \frac{y}{x^2 + y^2}. \tag{2.26}$$

Conformal mapping transforms the curved trajectories of charged particles in a magnetic field into straight lines in the (u,v) plane, simplifying track finding to a linear pattern recognition problem. A key feature of this transformation is that hit ordering is inverted: hits near the interaction point are mapped outward, while outer hits appear closer to the origin.

Early implementations of conformal tracking searched for aligned hits in conformal space by identifying peaks in the angular hit distribution [93]. However, this method does not fully account for deviations from ideal circular motion, which can arise from multiple scattering or from displaced (non-prompt) particles not originating at the detector center.

This is illustrated in Figure 2.4, where hits belonging to three muon tracks simulated in the CLIC tracker detector [88], are shown in both global and conformal space. One track is produced by a prompt high-momentum muon passing through the origin of the (x, y) plane and unperturbed

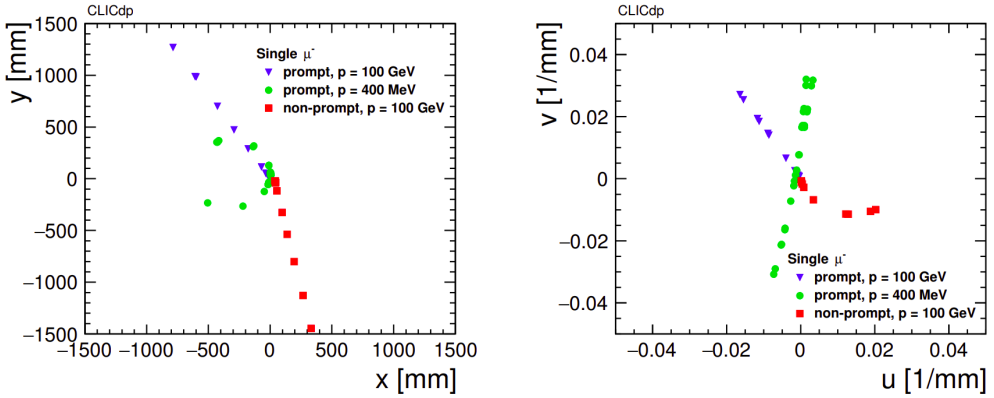

Figure 2.4: Examples of tracks in the $(x,\ y)$ global coordinate system (left) and in the $(u,\ v)$ conformal coordinate system (right). Hits produced by three track types are shown: prompt (blue), prompt with low momentum (green) and non-prompt (red). Figure taken from [88]

in its path, the second one corresponds to a prompt low-momentum muon undergoing multiple scattering, and the last one is a track produced by a non-prompt muon. In the latter two cases, the deviation of the trajectories from straight lines is clearly visible. To take these deviations systematically into account, pattern recognition in conformal space is performed via a cellular automaton (CA).

2.2.2 Cellular tracks reconstruction

The CA-based algorithm [94] used for track finding in conformal tracking consists of the creation and extension of cells, which are defined as segments connecting two hits. It is used to reconstruct cellular tracks and consists of two main algorithms: the building and the extension of cellular track candidates. These two algorithms can be used in a recursive way as the final track finding strategy, as shown in Section 2.2.4.2.

2.2.2.1 Building of cellular track candidates

To initiate the CA process effectively, since the CA can potentially create a vast number of cells, the first step is to create a small number of *seed* cells, which provide the basic set of track candidates to be further extended. This is done by limiting the seeding procedure only to a subset of hits, known as *seeding collection*, which can be customised based on specific requirements. Details regarding the different step for building cellular track candidates are describe below.

Seed cell creation

Firstly, hits in the seeding collection are sorted by decreasing conformal radius, such that the innermost hits in the detector (i.e., those furthest in conformal space) are considered first. A *seed hit* is defined as a single hit that serves as a starting point for building track candidates. From each seed hit, a search for neighbouring hits is performed based on the conformal polar angle, defined as $\Theta = \arctan(u/v) + \pi$. Only hits with a polar angle within the window $[\Theta_{\text{seed}} - \Delta\Theta_{\text{neighbours}}, \Theta_{\text{seed}} + \Delta\Theta_{\text{neighbours}}]$ are considered, where $\Delta\Theta_{\text{neighbours}}$ is a fixed parameter.
Once neighbouring hits are identified, combinations of three hits (referred to as *cells*) are formed. These cells serve as building blocks for constructing larger track segments through cellular automaton techniques.

The creation of seed cells is crucial for the effectiveness of the CA performance. Both the search window amplitude $\Delta\Theta_{\text{neighbours}}$ and the maximum cell length l_{max} will have a direct effect on the efficiency of the track finding, while the number of cells produced will influence the processing time. Therefore, these parameters are adjusted based on the reconstruction step and detector specifications.

Seed cell extrapolation

Once the seed cells are built, the algorithm attempts to extend them by following the direction of each segment and searching for compatible hits further outward. This is done using a second k-d tree, with hits selected based on their conformal radius, within a predefined window around the projected endpoint. This radius-based search avoids assuming a strict angular direction and is more robust against deviations in track curvature.
To ensure geometrical consistency, any new cell that forms an angle exceeding α_{max} with its seed cell is discarded. Accepted extensions are further propagated using the same approach, gradually building longer chains of hits.
Each cell stores its endpoints and a weight, which counts the number of direct connections to other cells. As more cells are linked, the weight increases, serving as a heuristic to prioritize segments likely to form valid tracks. Starting from the highest-weight seeds, connected cells are grouped into candidate tracks and fit with a linear regression in conformal space.

Cellular track candidates

Each cell, formed by connecting a pair of hits, stores its endpoints and a weight. This weight increases whenever the cell is successfully linked to a neighbouring cell, serving as a proxy for how well the segment integrates into a longer trajectory. Cells with higher weights are prioritized during the construction of candidate tracks, as they are more likely to represent real particle paths.
Track candidates are built by recursively linking compatible cells, starting from those with the highest weight. To ensure geometric consistency, links are only accepted if the angular deviation between cells remains below a predefined threshold. A minimum number of hits, denoted $N_{\text{hits}}^{\text{min}}$, is required for a sequence to be retained as a valid candidate. Each candidate is initially fit with a linear regression in the (u, v) conformal plane, allowing estimation of the track direction and curvature.
Since the conformal mapping projects the 3D trajectory into two dimensions, some spatial information is inevitably lost. To recover it, a second linear fit is performed in the (s, z) plane, where s denotes the arc length along the track in the transverse plane. Because the z-coordinate varies linearly with s for a helical trajectory, this allows a reconstruction of the longitudinal behaviour of the track.
From these fits, two normalized χ^2 values are computed:

$$\chi^2_{(u,v)}, \quad \chi^2_{(z,s)} \tag{2.27}$$

Tracks are retained only if both χ^2 values fall below a threshold χ^2_{max}. To improve robustness against spurious hits, each hit is temporarily removed from the candidate track, and the fits are repeated. If the removal leads to a substantial improvement in fit quality, the hit is considered inconsistent and excluded. This procedure is typically effective at removing isolated outlier hits, but it is applied conservatively to avoid discarding genuine hits. In well-reconstructed tracks, only a small number of hits, if any, are usually removed.
This filtering does not remove clones, tracks that share multiple hits. For candidates originating from the same seed, clone rejection is applied based on a combined metric:

$$\chi^2_{\text{tot}} = \chi^2_{(u,v)} + \chi^2_{(z,s)} \tag{2.28}$$

In case of duplicated hits, the longest track is kept. If candidates are of equal length, preference is given to the one with the lowest χ^2_{tot}.

2.2.2.2 Extension of cellular track candidates

Following the cellular track building phase, an extension algorithm is applied to refine and grow each candidate. This step requires the full hit collection and operates by classifying tracks based on an initial transverse momentum estimate, derived from the linear fit performed in conformal space (u, v). Two separate strategies are followed, depending on whether the estimated p_T exceeds a configurable threshold $p_{T,\text{cut}}$, which can be tuned according to the reconstruction stage or detector configuration.

Candidates with $p_T > p_{T,\text{cut}}$ are processed first. Since such tracks typically correspond to higher-momentum particles, they are more likely to follow regular trajectories and produce well-aligned hits. As a result, they are easier to extend reliably, and processing them first helps avoid ambiguities. The endpoints of these tracks are used as seeds to search for additional hits in the adjacent detector layer. Neighbouring hits are selected based on their angular proximity in conformal space, and a new segment is appended if it yields the lowest normalized χ^2_{tot} value. This procedure continues iteratively, extending the track layer by layer until the final tracking layer is reached.

The algorithm does not impose strict assumptions on the number or spacing of layers, which ensures compatibility with a wide range of detector geometries. Additionally, if no suitable hit is found in a given layer, the extension continues with the next layer, preserving the continuity of the reconstruction and maintaining high efficiency.

Once the higher-p_T tracks are reconstructed, their associated hits are marked as used. The remaining hits are then used to reconstruct tracks with lower p_T, such as looping or curling tracks. These particles often exhibit significant deviations from linearity in conformal space due to effects like multiple scattering, as illustrated in Figure 2.4. For this reason, the extension in this regime does not rely on nearest-neighbour searches. Instead, all unused hits (excluding those on the opposite z-side relative to the seed hit) are considered as extension candidates. The same cellular automaton principles are used, but the regression model is adapted to include a quadratic term, which improves the description of curved segments [93].

2.2.3 Track fitting with the Kalman filter

The Kalman Filter (KF), originally developed for estimating the unobservable states of dynamic systems, is widely used in track fitting and reconstruction[95, 96]. It provides a recursive least-squares fit through alternating *prediction* and *filtering* (update) steps. In this context, "recursive" means that the track parameters are updated step by step as new measurements are received, without needing to refit the entire trajectory from scratch. In tracking, the KF accounts for detector measurements, magnetic field effects, and material interactions such as multiple scattering and energy loss.

In the prediction step, the current state vector is extrapolated to the next detector surface, incorporating uncertainties from multiple scattering and other effects. In the filtering step, the predicted state is updated based on the closest measurement, typically using a χ^2-based criterion. Since the decision to associate hits is local, it may not account for global track ambiguities; however, this is usually not problematic in low-occupancy environments.

The KF is naturally suited for tracking since particle trajectories can be modelled as dynamic systems:

- The track state at surface k is represented by a 5-component vector $\vec{x}_k$. In this formalism, the track state vector $\vec{x}_k$ typically contains five parameters describing the particle's trajectory

at a given detector surface: transverse position, direction angles, and inverse momentum. Its evolution is governed by deterministic transport functions plus stochastic noise due to scattering. Its evolution between layers is given by:

$$\vec{x}_k = \vec{f}_{k-1}(\vec{x}_{k-1}) + \vec{w}_{k-1} \tag{2.29}$$

Here, $\vec{x}k$ represents the five parameters of a helical track: e.g. position, direction, and curvature. The transport function $\vec{f}k-1$ extrapolates the track from one detector layer to the next and $\vec{w}_{k-1}$ represents the process noise (e.g., multiple scattering).

- The measurement at surface k, $\vec{m}_k$, is related to the state vector by:

$$\vec{m}_k = \vec{h}_k(\vec{x}_k) + \vec{\epsilon}_k \tag{2.30}$$

where $\vec{h}_k$ is the measurement function and $\vec{\epsilon}_k$ is the measurement noise.

If $\vec{f}$ and $\vec{h}$ are linear, Eqs. (2.29) and (2.30) become:

$$\vec{x}_k = \mathbf{F}_{k-1}\vec{x}_{k-1} + \vec{w}_{k-1}, \qquad \vec{m}_k = \mathbf{H}_k\vec{x}_k + \vec{\epsilon}_k \tag{2.31}$$

For non-linear systems, first-order Taylor expansions are used, and the Jacobians are:

$$\mathbf{F}_{k-1} = \left.\frac{\partial \vec{f}}{\partial \vec{x}}\right|_{\vec{x}_{k-1}}, \qquad \mathbf{H}_k = \left.\frac{\partial \vec{h}}{\partial \vec{x}}\right|_{\vec{x}_k} \tag{2.32}$$

Prediction: Using previous information up to step $k-1$, the predicted state and its covariance are:

$$\hat{\vec{x}}_{k,\text{pred}} = \vec{f}_{k-1}(\hat{\vec{x}}_{k-1}), \qquad C_{k,\text{pred}} = \mathbf{F}_{k-1}C_{k-1}\mathbf{F}_{k-1}^{\top} + Q_{k-1} \tag{2.33}$$

where Q_{k-1} is the process noise covariance, which accounts for uncertainty introduced by material interactions such as multiple scattering and energy loss. $C_{k,\text{pred}}$ is the covariance matrix associated with the predicted state $\hat{\vec{x}}_{k,\text{pred}}$.

Filtering (update): The predicted state is updated using measurement $\vec{m}_k$:

$$\hat{\vec{x}}_{k,\text{upd}} = \hat{\vec{x}}_{k,\text{pred}} + K_k(\vec{m}_k - \vec{h}_k(\hat{\vec{x}}_{k,\text{pred}})) \tag{2.34}$$

$$C_{k,\text{upd}} = (I - K_k\mathbf{H}_k)C_{k,\text{pred}} \tag{2.35}$$

with the Kalman gain matrix:

$$K_k = C_{k,\text{pred}}\mathbf{H}_k^{\top}(\mathbf{H}_kC_{k,\text{pred}}\mathbf{H}_k^{\top} + V_k)^{-1} \tag{2.36}$$

The update adjusts the predicted state using the new measurement $\vec{m}_k$. The Kalman gain matrix K_k controls how much weight is given to the new measurement compared to the prediction. V_k represents the covariance matrix of the detector measurement noise, while I is the identity matrix.

Smoothing: After reaching the final measurement, the KF allows a backward pass (smoothing), which refines the state estimates at previous steps using all available measurements. This can also be done iteratively during the filtering process by combining forward and backward estimates.

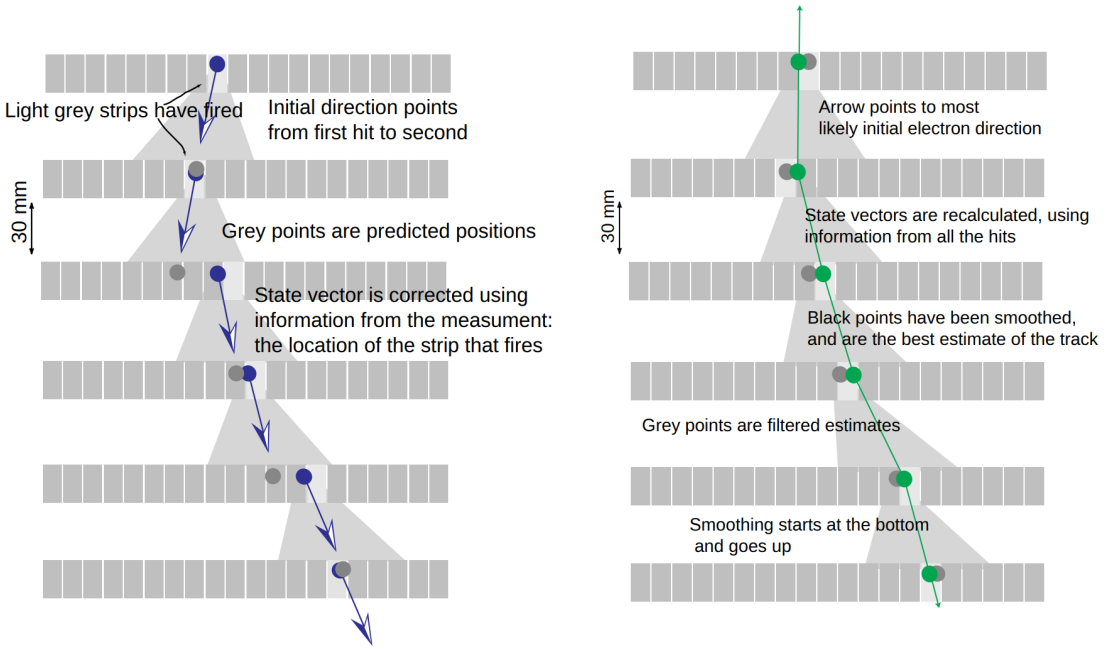

Figure 2.5: **Left:** Kalman filter used in track finding. **Right:** Kalman filter used in track fitting/smoothing[97].

Advantages: The KF offers several benefits:

- Its recursive nature allows it to be used both for track fitting and for pattern recognition during track finding.
- It is computationally efficient, requiring only small matrix operations at each layer.
- It can model complex detector effects such as inhomogeneous magnetic fields and multiple scattering.
- Linear approximations are only required between adjacent layers, improving flexibility in geometry.

A valid initial estimate (the *seed*) is required to start the filter. This seed is usually built in regions with high granularity or low occupancy, such as the innermost tracking layers.

2.2.4 Track reconstruction at CLD

The CLIC-Like Detector (CLD) [98], originally developed for the CLIC project [99], is a detector concept currently under study for the FCCee experiment. The CLD detector comprises a full silicon tracking system, including vertex detectors.

The effectiveness and robustness of the conformal tracking algorithm is presented using as an example the track reconstruction in the CLD tracker [98], where conformal tracking is adopted as the track finding technique.

Track reconstruction refers to the process of using a sequence of algorithms to estimate the momentum and position parameters of a charged particle crossing the detector. The inputs to the sequence are the reconstructed hits described in Section 2.2.4.1, while the final outputs are tracks which contain the hits they are made of and the information of the estimated track parameters Section 2.1.4. The number of parameters that describe a track can be reduced to five [100]: two parameters for the impact point positions, two describing the direction of the track at the impact point and one for the particle momentum.

The process of track reconstruction can be summarised as a sequence of four main algorithms:

- local-to-global hit coordinate transformation,
- pattern recognition or track finding,
- track fitting,
- track selection.

The reconstruction process begins with a local-to-global coordinate transformation, converting the sensor-level hit positions into the global detector frame. In a second step, the conformal mapping algorithm is applied to project global hit positions into the (u,v) space, where circular trajectories become straight lines (see Section 2.2.1). In a second step, hits are grouped into track candidates. Many different track finding techniques exist, which have been used in past and present high-energy physics experiments [101]. The strategy adopted for CLD (and CLIC detector [88]) is based on the conformal tracking presented in Section 2.2. The third step allows trajectories to be associated with the previously found track candidates. The results of this algorithm are for every track candidate the estimated parameters of a helix, their covariance or error matrix and a χ^2 statistic. The fitting technique applied for the CLD is based on a KF [102], which performs the track fitting by accounting for effects such as multiple scattering and detector resolution. The core reconstruction process begins with a conformal transformation of global hit positions, followed by track candidate formation using a cellular automaton in conformal space, and is completed by a KF fit to refine the track parameters. An additional, optional algorithm may be applied at the end of the chain to address specific issues, such as the suppression of spurious tracks or the removal of duplicate (clone) tracks. The full track reconstruction process is schematised in Figure 2.6.

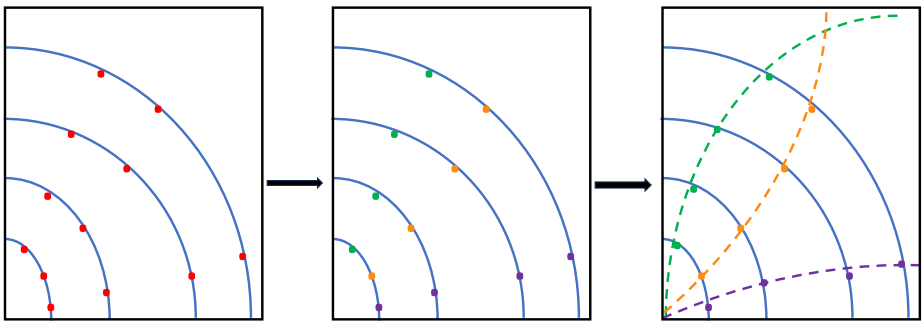

Figure 2.6: Step-by-step tracking process: **Hit measurement** Initial detection and recording of particle interactions, **Track finding** Determining which reconstructed hits belong to the same particle trajectory, **Track fitting** Optimising parameter estimates to reconstruct the particle's path accurately.

2.2.4.1 Hit treatment in simulation

In the simulation framework, the first step of the track reconstruction chain consists of converting *simulated hits*, generated when charged particles cross the sensitive layers of the detector, into *reconstructed hits*. These reconstructed hit positions and their uncertainties are defined in a local orthogonal coordinate system on the surface of each sensor. To simulate detector resolution effects, the local positions of all simulated hits are **smeared** using Gaussian distributions with a width corresponding to the assumed **single point resolution** of each subdetector. The position uncertainties are then set equal to these single point resolutions.

This smearing procedure is applied to all simulated hits from Monte Carlo particles, whether originating from physics events or background processes. Additional simulated quantities, such as energy deposition or time of arrival (assuming zero detector dead time), are also transferred to the reconstructed hit objects. The resulting collection of reconstructed hits serves as the input for the subsequent pattern recognition step.

2.2.4.2 Track finding

Conformal tracking, as described in Section 2.2, is used as pattern recognition algorithm for track reconstruction in CLD. Firstly, the conformal mapping is used to translate the hit positions from global space (x, y) into the conformal space (u, v). Then, the two CA algorithms of *building* (Section 2.2.2.1) and *extension* (Section 2.2.2.2) are run recursively on different hit collections and with an adapted sets of parameters to reconstruct cellular tracks. A schematic overview of the full pattern recognition chain is summarised in Table 2.1, including the values of the parameters used in the CA-based track finding, optimised for $t\bar{t}$ events at 3 TeV, for CLIC detector [88]. For all steps, the window size of the nearest neighbour search in polar angle $\Delta\Theta_{\text{neighbours}}$ is fixed at 0.05 rad. The search window size for nearest neighbours in radius $\Delta R_{\text{neighbours}}$ is set to 75% of the l_{max} of the current step.

- **Step 0** consists of the building of cellular track candidates using the hits in the vertex barrel as the seeding collection.
- **Step 1** performs the extension of cellular track candidates, found in step 0, limited to the set of hits in the vertex endcap.
- **Step 2** performs cellular track candidates building to recover remaining hits in the combined vertex barrel and endcap detectors, with tighter cuts at first to reconstruct higher-p_T tracks
- **Step 3** performs cellular track candidates building with looser cuts to reconstruct low-p_T tracks
- **Step 4** extends all the candidates obtained via steps 0 to 3 using hits in the tracker barrel and endcap detectors [1]

Once steps 0 to 4 are completed, the unused hits in the entire tracking system can be used to reconstruct the remaining tracks, which could be generated by **displaced particles** as defined in Section 2.2.1. As shown in Figure 2.4, their trajectories are not mapped into straight lines in conformal space. For this reason, the CA is executed with a special configuration for **step 5**:

- seed cells are formed at smaller conformal radius, i.e. in the outermost part of the tracker, and extended outwards in (u, v) space,
- the minimum number of hits required to form a track is increased with respect to the previous steps,
- looser cuts in the CA parameters are set,
- a quadratic term is included in the regression formula used to fit the cellular track candidates in conformal space, as was the case for the extension of low-p_T tracks.

[1] The layer ordering of the tracker subdetectors, used in the track extension, is the following: inner tracker barrel (layers ordered by increasing radius), inner tracker endcap (layers ordered by increasing z position), outer tracker barrel (layers ordered by increasing radius), outer tracker endcap (layer ordered by increasing z position).

Step	Algorithm	Hit collection	Parameters				
			$\alpha_{\max}$ [rad]	$l_{\max}$ [mm^{-1}]	$N_{\min}^{\text{hits}}$ -	$\chi^2_{\max}$ -	$p_{T,\text{cut}}$ [GeV]
0	Building	Vertex Barrel	0.005	0.02	4	100	-
1	Extension	Vertex Endcap	0.005	0.02	4	100	10
2	Building	Vertex	0.025	0.02	4	100	-
3	Building	Vertex	0.05	0.02	4	2000	-
4	Extension	Tracker	0.05	0.02	4	2000	1
5 (default)	Building	Vertex & Tracker	0.05	0.015	5	1000	-
5 (isolated)	Building	Vertex & Tracker	0.1	0.015	5	1000	-

Table 2.1: Overview of the configuration for the different steps of the pattern recognition chain. The last column shows some of the parameters of relevance for the CA as used for CLD: the maximum angle between cells $\alpha_{\max}$, the maximum cell length $l_{\max}$, the minimum number of hits on track $N_{\min}^{\text{hits}}$, the maximum $\chi^2_{\max}$for valid track candidates, and $p_{T,\text{cut}}$ used to discriminate between the two variations of the algorithm of track extension.

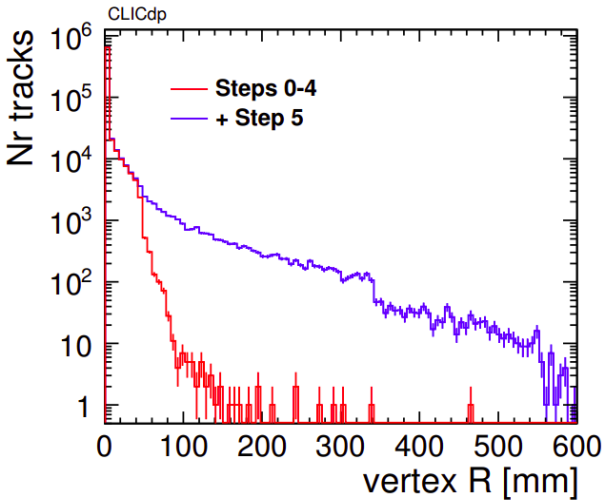

Figure 2.7: Cumulative distribution of the total number of tracks reconstructed by the conformal tracking algorithm in CLIC detector as a function of particle production vertex radius for step 0–4 (red) and including step 5 (blue). The particles were produced in $e^+e^- \to t\bar{t}$ events at 3 TeV centre-of-mass energy. Figure taken from [88]

The effect of this last step in the overall track reconstruction is clearly visible in Figure ?? where the cumulative distribution of the total number of tracks reconstructed using different steps in $e^+e^- \to t\bar{t}$ events at 3 TeV centre-of-mass energy is shown as a function of particle production vertex radius at CLIC detector. Given its special configuration, step 5 is the most computationally demanding part of the full pattern recognition chain. Two configurations are summarised in Table 2.1. In the "isolated" configuration, looser angular and radial cuts are applied to improve the reconstruction of displaced or low-momentum tracks. However, since this final step only processes a small number of remaining hits, or isolated particles in low-occupancy events, the number of hit combinations remains limited, and the computing time is not significantly affected.

In Figure 2.8 all cellular track candidates reconstructed by the full pattern recognition chain are shown for two example events: a single $b\bar{b}$ event at 500 GeV centre-of-mass energy and a single

$t\bar{t}$ event at 3 TeV at CLIC detector.

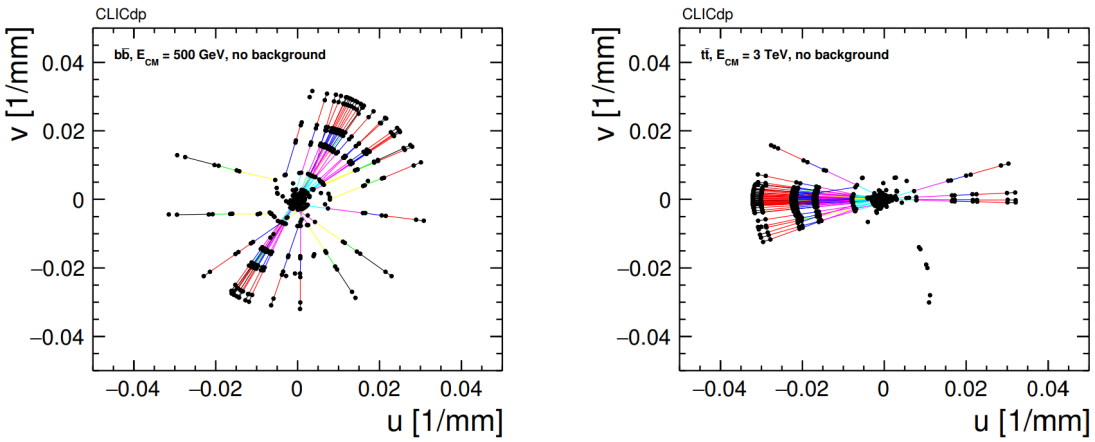

Figure 2.8: Cellular track candidates reconstructed by the conformal tracking algorithm in CLIC detector in the case of a single $b\bar{b}$ event at 500 GeV centre-of-mass energy (left) and a single $t\bar{t}$ event at 3 TeV (right). Figure taken from [88]

2.2.4.3 Track fitting

For each cellular track candidate reconstructed during the pattern recognition stage, the track fit is run with the aim of obtaining a precise estimation of the track parameters. It consists of a Kalman filter and smoother in the global (x, y, z) coordinate space [102]. Also described in Section 2.2.3.

As a first step, a simple helix is fitted to three hits of the track (typically first, middle and last hit) to obtain a first estimation of the trajectory parameters. This step is called *pre-fit*.

The parameters obtained from the pre-fit are used to initialise the Kalman filter, while the values of the corresponding covariance matrix are set several order of magnitudes larger than the expected ones to perform an unbiased fit. The KF and smoother is then run as implemented in the KalTest package described in [103]. It proceeds through the full list of hits on the track from the innermost to the outermost layer of the CLD tracking system, updating the track trajectory state, which contains the estimation of track parameters and their uncertainties, sequentially with each hit. In the smoother step, a second filter is initialised with the result of the first one and is run from the outermost layer to the innermost. In case the fit fails, the KF and smoother is attempted a second time using the hits collected in the tracks in reverse order.

Some of the hits on the cellular track candidates may be rejected during the track fitting step, based on requirements on the χ^2_{tot} set in the track fit itself. As a result, some tracks can have fewer hits than the minimum requirement imposed during the pattern recognition stage.

2.2.4.4 Track selection

The track finding procedure can yield a significant fraction of undesirable tracks, such as tracks that contain many spurious hits or share a number of hits with other tracks. Therefore, a track selection is applied as the final stage with the goal of reducing the number of these tracks while keeping high tracking efficiency.

To avoid track candidates sharing more than two hits, a global clone removal step is performed after the Kalman filter and smoother procedure, using the final track fit quality. In this case, the χ^2 used to select the best candidate is the one obtained from the full Kalman fit. This complements the local clone filtering performed earlier during the cellular candidate building.

As mentioned in Section 2.2.4.3, introducing a lower threshold on the total number of hits belonging to a track is an effective way to reduce the number of bad-quality tracks. The optimal minimum number of hits has been found to be equal to the minimum imposed on the first building step, i.e. 4. However, this is not entirely the case for the reconstruction of single isolated particles, for which rejecting three-hit tracks can result in efficiency loss with limited improvement on the track quality. Therefore, the requirement of number of hits larger than three is applied to the tracks as an offline requirement according to the event topology.

2.3 Vertexing

2.3.1 Vertex

In high-energy physics, a vertex refers to a point in space where particle interactions occur. This can either be a **primary vertex**, where the initial collision between particles takes place, or **secondary vertices**, which result from the decay of unstable particles produced in the collision. Vertex reconstruction is crucial for understanding the topology of an event, identifying particle origins, and inferring properties like the lifetime of particles.

Vertexing is inherently connected to tracking, as the precise determination of a vertex relies on the accurate reconstruction of charged particle trajectories. Tracks are extrapolated back to their points of closest approach, and from the convergence of these tracks, vertices are identified. A high-resolution vertex detector, combined with a performant tracking algorithm, enables the reconstruction of vertices with micrometer precision. This capability is particularly important in e^+e^- colliders, where the clean environment allows for the detailed study of secondary vertices from heavy-flavour hadron decays. Thus, vertexing plays a key role in flavour tagging, and in probing new physics signatures involving displaced decays.

Vertex reconstruction is the process of determining the spatial position of particle interaction points using the reconstructed trajectories of charged particles. It is a multi-step procedure that typically begins once individual tracks have been identified by the tracking algorithm. The core idea is to identify clusters of tracks whose extrapolated paths intersect or come very close together, indicating a common origin point.

Vertex reconstruction often start with a **vertex finding** phase, where candidate vertices are proposed based on proximity and compatibility of tracks. This is followed by **vertex fitting**, which refines the vertex position, often based on χ^2 minimisation [104], to account for the uncertainties in the track parameters.

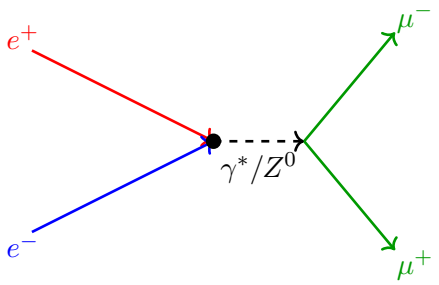

Figure 2.9: Primary Vertex(PV), also called Interaction Point (IP).

2.3.1.1 Vertex Fitting Techniques

Once the set of reconstructed tracks is available, vertex reconstruction proceeds in two stages: vertex finding and vertex fitting. In the vertex finding step, groups of tracks likely to originate from a common point are identified. This is typically done by looking for pairs or clusters of tracks that come close to each other in space, based on their extrapolated trajectories and impact parameters. Once candidate track groups are formed, vertex fitting is applied to precisely estimate the vertex position and its associated uncertainties. The goal of vertex fitting is to find the most probable point of intersection of the involved tracks, taking into account measurement errors and the full track covariance matrices.

The most widely used vertex fitting techniques are summarized below:

Kalman Filter Vertex Fitting

The Kalman filter, as explained in Section 2.2.3, is a recursive estimator particularly suited to systems with uncertainty and sequential data. In vertex fitting, it can be used to iteratively update the vertex position as each track is added, using both the position and the momentum information along with their uncertainties. Kalman-based vertexing offers a natural way to handle correlations between track parameters and can be extended to include constraints, such as fixed beam spot positions or known invariant masses of decaying particles.

Adaptive Vertex Fitting

In cases where a group of tracks may contain outliers, tracks that do not originate from the vertex of interest, adaptive vertex fitting provides a robust solution. Instead of treating all tracks equally, this algorithm assigns a weight to each track based on its compatibility with the vertex. The vertex is then iteratively refitted, updating the weights until convergence is achieved. This method improves the stability of the fit, especially in environments with high track multiplicities or in the presence of background.

Least Squares (χ^2) Minimisation

One of the simplest approaches is to use χ^2 minimisation, where the vertex position is adjusted to minimise the sum of the squared distances (weighted by their uncertainties) between the extrapolated tracks and the candidate vertex. This method is effective for small numbers of tracks with well-understood uncertainties but is less robust than adaptive methods in complex environments.

These vertex fitting techniques are implemented in particle physics software frameworks, and their performance is crucial for downstream tasks such as flavour tagging, lifetime measurement, and displaced vertex detection. At future e^+e^- colliders based on the CLD detector concept, the precision of vertex fitting will directly impact the sensitivity to Higgs decays, heavy-flavour processes, and new physics scenarios involving long-lived particles.

2.3.2 Jet

Before addressing jet reconstruction itself, it is essential to introduce the particle flow approach, which serves as the basis for reconstructing individual particles in high-granularity detectors such as the CLD. The Particle Flow Algorithm (PFA) [105, 106] aims to reconstruct all stable and pseudo-stable particles in an event by optimally combining the information from the different subdetectors:

charged particles are measured with high precision in the tracking system, photons are identified and measured in the electromagnetic calorimeter, and neutral hadrons are reconstructed using the hadronic calorimeter.

By assigning each reconstructed particle to the subdetector the PFA significantly improves the overall energy resolution compared to calorimeter-only reconstruction. The output of the PFA is a list of reconstructed particle candidates, known as Particle Flow Objects (PFOs), which serve as input to the jet clustering algorithms.

In high-energy collisions such as those occurring at e^+e^- colliders, the production of quarks and gluons is common. However, due to colour confinement, these partons cannot be observed directly. Instead, they hadronise into collimated streams of colour-neutral particles known as jets, as illustrated in Figure 2.10. Jets serve as experimental proxies for the original partons and are fundamental objects in particle physics analyses.

The reconstruction and identification of jets involve clustering the observed final-state particles, primarily tracks from charged particles and calorimeter deposits from neutrals, into distinct jet candidates. The most common jet clustering algorithms (such as the Durham or anti-k_t algorithms) use the kinematic properties of particles to group them based on angular and momentum criteria.

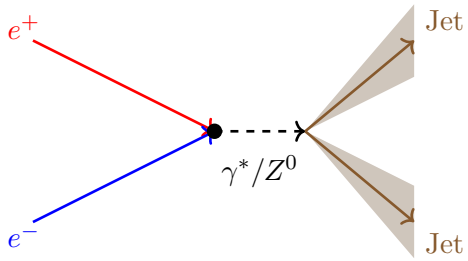

Figure 2.10: Primary Vertex with 2 jets.

Role of Tracking in Jet Reconstruction

Tracking plays a crucial role in jet reconstruction, particularly in improving the jet energy and angular resolution. On average, a typical jet at FCC-ee contains between 5 and 15 reconstructed charged tracks, though this number can increase for high-energy or gluon-initiated jets. Charged particles, which typically carry a significant fraction of a jet's energy, are reconstructed with high precision by the tracking system. This precise momentum information from tracks complements the coarser energy measurements from calorimeters, especially at low energies where calorimeters are less reliable.

Moreover, the ability to distinguish charged particles from neutral particles using tracking information is vital in jet reconstruction techniques like Particle Flow Algorithms (PFA). PFA aims to reconstruct each final-state particle individually by combining the strengths of tracking and calorimetry, resulting in high jet energy resolution.

Vertexing in Jet

While jet reconstruction relies on the list of reconstructed particles provided by the Particle Flow Algorithm (PFA), it is not part of the PFA itself. Once jets are formed from these particle flow objects (PFOs), vertexing plays a crucial role in enhancing jet analysis by enabling the identification of secondary vertices inside jets. These secondary vertices are characteristic signatures of the decays of long-lived particles, such as b- and c-hadrons.

This leads to the important concept of flavour tagging, where jets originating from bottom or charm quarks are identified based on the presence of displaced vertices, large impact parameters, or other long-lived decay topologies. For instance, b-tagging relies heavily on precise vertex reconstruction to distinguish b-jets from light-flavour jets. The b-hadrons typically have lifetimes of about 1.5 ps, corresponding to flight distances of a few millimetres before decaying. Similarly, c-tagging aims to identify charm jets, which is more challenging due to the shorter lifetimes of c-hadrons (around 1 ps) leading to decay lengths of the order of 100–500 μm.

The presence of a well-resolved secondary vertex within a jet significantly boosts confidence in assigning it a heavy-flavour origin. In this way, vertexing not only improves jet classification but also enables access to observables such as vertex mass, decay length, and lifetime, which are critical for precision measurements of the Higgs boson and top quark.

Tracking, vertexing, and jet reconstruction form the core of event reconstruction in high-energy physics experiments. Together, they transform raw detector hits into meaningful physical objects, that reflect particle interactions. At future e^+e^- colliders such as those employing the CLD detector concept, the clean environment and advanced detector technologies enable unprecedented precision in reconstructing these objects. High-resolution tracking systems provide the foundation for accurate momentum measurement and particle identification, while sophisticated vertexing techniques allow the reconstruction of primary and secondary interaction points with micrometer precision. Jet reconstruction, supported by particle flow algorithms and flavour tagging, relies on precise tracking and vertexing to accurately reconstruct jets, which are the observable signatures of quarks and gluons. This allows for detailed studies of jet properties and improves sensitivity to the underlying parton-level dynamics. The synergy among these components is essential not only for precision Standard Model measurements but also for enhancing sensitivity to new physics processes, such as those involving displaced vertices or long-lived particles. This integrated approach ensures that the full potential of the detector is realised in pursuit of the next discoveries in particle physics. A schematic illustration is shown in Figure 2.11.

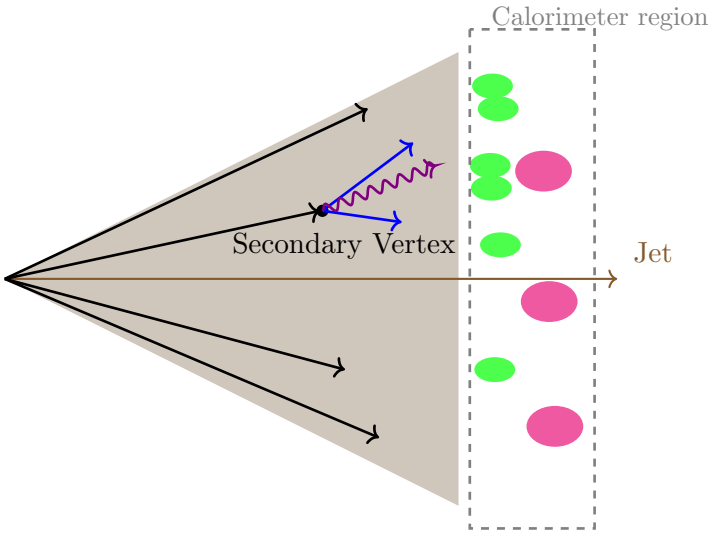

Figure 2.11: Schematic view of a hadronic jet, showing charged and neutral particles originating from a secondary vertex, along with their corresponding calorimetric energy deposits. Green clusters represent electromagnetic calorimeter deposits (e.g., from leptons or photons), while pink clusters represent hadronic calorimeter deposits.

Chapter 3

Signal Digitisation: Beam Tests and MAPS Sensors

Contents

3.1 Introduction

This chapter presents the work conducted on signal digitisation within the context of beam tests carried out at the CERN SPS in April 2024 [107]. These tests were part of a broader effort to evaluate the performance of advanced Monolithic Active Pixel Sensors (MAPS) for use in future high-precision tracking systems, such as those foreseen in particle physics experiments at colliders like the FCCee.

The primary objective of the beam test campaign was to characterise a new generation of MAPS prototypes developed in 65 nm CMOS technology, referred to as CE-65. A range of CE-65 sensor configurations were studied under controlled beam conditions using a reference tracking system composed of six ALPIDE sensors arranged as a telescope. The ALPIDE-based telescope provided precise particle trajectory measurements, enabling detailed spatial resolution studies of the devices under test (DUTs).

The focus of the work presented in this chapter is on the digitisation of the analogue charge signals collected by the CE-65 sensors. In particular, we investigate how reducing the signal to 1-bit or 2-bit digital encoding impacts the spatial resolution of reconstructed hits. This study is essential to evaluate potential data reduction strategies while preserving tracking performance. Such strategies are not only important for reducing data volume but also for limiting power dissipation, which is a critical constraint for large-scale MAPS-based detectors operating close to the interaction point.

3.2 Summary of Monolithic Active Pixel Sensors Technology

Monolithic Active Pixel Sensors (MAPS) are a silicon-based detector technology that integrates both the sensing layer and readout electronics on a single silicon substrate. Originally developed for visible light [108], MAPS have been successfully adapted for high-energy physics (HEP) applications[109, 110] thanks to their low material budget and potential for high spatial granularity. Their compact design is particularly advantageous for tracking detectors where minimising multiple scattering is essential.

Their monolithic architecture removes the need for complex bump bonding between sensor and readout chip, potentially simplifying integration in large-scale tracking systems[111, 112, 113].

3.2.1 Key Features and Requirements

MAPS designed for HEP experiments must fulfill specific requirements distinct from conventional imaging applications:

- **Single Particle Detection:** Capable of detecting individual particles with sparse occupancy, typically below 1% of the pixels per readout frame.
- **High Spatial Resolution:** Achieve position resolutions of a few micrometers, with a target of about ~ 3 μm as required for FCCee vertex detectors.
- **Radiation Tolerance:** Withstand non-ionizing energy loss (NIEL) fluences up to 10^{14} n_{eq}/cm^2 and total ionizing doses (TID) of a few hundred kGy, consistent with FCCee inner tracking requirements.
- **Low Power Consumption:** Minimize power density to reduce the material budget associated with cooling and cabling, especially near interaction points. For the innermost layers of the FCCee vertex detector, the target is approximately 20 mW/cm^2.

- **Fast Time Resolution:** Support timing capabilities adapted to the application. For 4D tracking at FCCee, resolutions of a few 100 ns are sufficient, whereas for particle identification via time-of-flight, resolutions down to a few tens of picoseconds are required.

Designing a MAPS sensor for high-energy physics therefore requires carefully balancing these competing constraints. For example, improving spatial resolution by reducing pixel size typically increases power consumption and readout complexity. Similarly, enhancing radiation tolerance may necessitate circuit modifications that impact signal-to-noise performance. The optimisation process must consider the detector's overall physics goals and integration constraints.

3.2.2 Technological Developments

To meet the demanding requirements outlined above, research and development is underway to optimise MAPS sensor design for future collider experiments. In the context of future colliders, which foresee extremely low material budgets and radiation environments, monolithic sensors fabricated in the TPSCo 65 nm CMOS imaging process represent a promising technology under evaluation, as exemplified by the CE-65 prototype chip.

The CE-65 programme explores monolithic sensors fabricated in a commercial 65 nm CMOS imaging process (TPSCo). This technology offers high integration density and potential improvements in timing, radiation tolerance, and spatial resolution. Within this framework, several sensor designs have been developed and tested under beam, exploring various architectural choices to evaluate their impact on performance.

Key areas of innovation include:

- **Process Innovations:** Techniques such as deep n-well implants, high-resistivity epitaxial layers, and custom modifications to the CMOS process enhance charge collection via drift and improve radiation hardness.

- **Pixel Architecture:** In CMOS MAPS technologies, designs can incorporate either large or small collection electrodes, optimising trade-offs between input capacitance, signal-to-noise ratio, and tolerance to radiation damage. Both approaches are actively explored in parallel, although typically not within the same CMOS process technology.

Two main sensor architectures have been developed to improve the radiation tolerance and overall performance of MAPS: the *large collection electrode* design and the *small collection electrode* design, as illustrated in Figure 3.1.

In the large electrode design (Figure 3.1a), the charge collection node covers most of the pixel area and embeds the readout electronics. This geometry ensures a strong and uniform electric field, which improves charge collection speed and radiation hardness, especially in high-fluence environments. However, it also increases the input capacitance, leading to higher noise and power consumption.

In contrast, the small electrode design (Figure 3.1b) minimises the collection node size and surrounds it with wells that isolate the in-pixel electronics. This reduces capacitance, improves signal-to-noise ratio, and enables finer pixel pitches. To achieve sufficient radiation tolerance, this design relies on advanced CMOS process modifications, such as high-resistivity epitaxial layers and deep well implants, to ensure full depletion and efficient drift-based charge collection.

These two approaches reflect different optimisation strategies and are being explored in parallel to evaluate the best trade-offs between resolution, power, and radiation hardness.

3.2.3 The ALPIDE Sensor

In the beam test campaign described in this chapter, particle tracks were reconstructed using a dedicated telescope based on ALPIDE sensors. Originally developed for the ALICE Inner

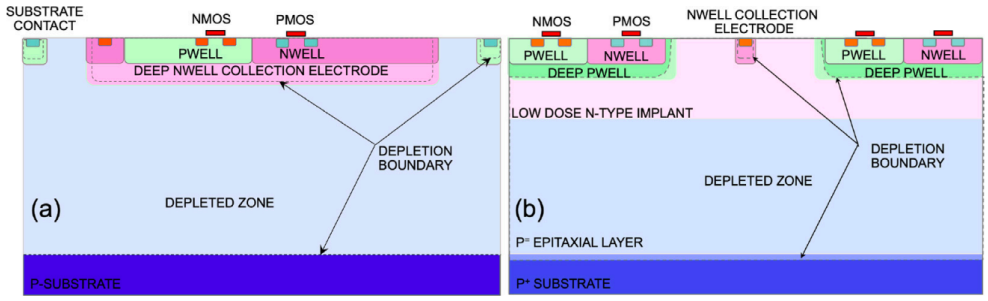

Figure 3.1: Schematic representation of two MAPS sensor designs for improved radiation tolerance: (a) a large collection electrode embedding the readout circuitry, providing a uniform electric field; (b) a small collection electrode surrounded by wells, with the readout circuitry isolated and supported by process optimisations for full depletion and accelerated charge collection. Adapted from [110].

Tracking System (ITS2)[114] upgrade at the LHC, the ALPIDE sensor provides excellent spatial resolution and low material budget, making it well-suited for use as a reference detector in test beam experiments.

The ALPIDE sensor[115, 116] is a Monolithic Active Pixel Sensor (MAPS) fabricated using the TowerJazz 180 nm CMOS imaging process. This technology includes features such as a high-resistivity epitaxial layer and a deep p-well implant, which allow the integration of full CMOS circuitry within each pixel while maintaining high charge collection efficiency. The sensor achieves a typical spatial resolution of about 5 μm with a pixel pitch of $29 \times 27\,\mu\text{m}^2$, and supports in-pixel amplification, discrimination, and zero suppression.

Its proven performance in high-energy physics environments, along with its fast and low-noise readout, makes ALPIDE a good choice for tracking telescopes in test beam setups aimed at characterising new sensor technologies.

3.2.3.1 Key Characteristics

The main features of the ALPIDE sensor include:

- **Pixel Matrix:** 512 $\times$ 1024 pixels with a size of 28 μm $\times$ 28 μm per pixel.
- **Power Consumption:** Less than 40 mW/cm^2 at hit rates of a few MHz/cm^2, enabling a lightweight detector design with minimal cooling requirements.
- **Spatial Resolution:** Approximately 5 μm.
- **Time Resolution:** The front-end peaking time is below 2 μs, but the overall time resolution of ALPIDE is limited to about 5 μs by its rolling-shutter readout architecture.
- **Radiation Hardness:** Tolerant to radiation levels up to 10^{13} 1 MeV n_{eq}/cm^2.

3.2.3.2 Sensor Architecture and Operation

The deep p-well implant allows PMOS transistors to be implemented inside the pixel without interfering with charge collection, as illustrated in Figure 3.2. This enables the use of full CMOS logic within each pixel, supporting a highly integrated and efficient readout architecture, in which each pixel includes a built-in discriminator to determine whether it has been hit.

Unlike traditional rolling-shutter architectures, where each row of pixels is read sequentially and at fixed time intervals, ALPIDE implements a data-driven, zero-suppressed readout scheme. In

this approach, only pixels registering a hit participate in the readout process, significantly reducing the power consumption and data volume. Internally, the system operates synchronously with a global clock, but the readout flow is driven by the presence of hits, improving timing granularity and scalability for high-occupancy environments.

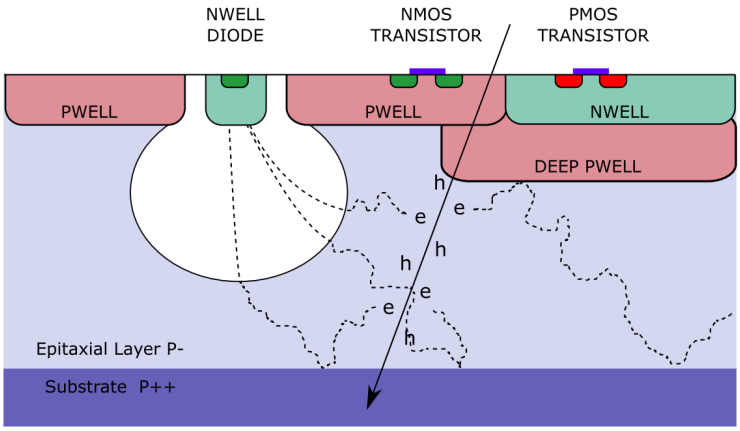

Figure 3.2: Schematic representation of the well-structure and charge collection in the ALPIDE sensor. The deep P-well shields the PMOS transistors from the epitaxial layer, ensuring efficient charge collection. The figure shows the internal well structure of a single ALPIDE pixel. The central N-well acts as the charge collection electrode, where signal electrons are attracted after being generated in the epitaxial layer. Surrounding this, the deep P-well allows PMOS transistors to be placed inside a large N-well for in-pixel processing. Without this shielding, signal electrons could be lost to the PMOS regions instead of being collected, reducing the efficiency. The use of both N-well and deep P-well structures is what enables full CMOS circuitry within the pixel while preserving excellent charge collection, a key innovation of the ALPIDE design. Adapted from [115].

3.2.4 Test Beam Setup at CERN SPS

To evaluate the performance of prototype MAPS sensors produced in the 65 nm CMOS technology (CE-65), a dedicated beam test was conducted in April 2024 at the CERN-SPS H6 beam line. In particular, the goal was to characterise the spatial resolution and charge collection properties of several CE-65 sensor configurations under different signal digitisation schemes (analogue, 1-bit, and 2-bit), in order to assess their suitability for future high-granularity trackers such as those foreseen at the FCCee.

The Device Under Test (DUT) was a CE-65 prototype chip mounted on a printed circuit board (PCB) and read out using custom DAQ hardware. The DUT was placed at the centre of a reference tracking system composed of six ALPIDE sensors arranged in a telescope configuration.

Data were collected using a 120 GeV/c positive hadron beam. The experimental setup also included trigger scintillators and remotely controlled motion stages to allow precise alignment and scanning of the sensor area.

The setup configuration is illustrated in Figure 3.3: two CE-65 prototype sensors were inserted between the ALPIDE planes. The leftmost CE-65 chip acted as the Device Under Test (DUT), while the second served as a trigger, mounted on a movable stage. The system was housed in a light-tight box and the DUT was maintained at a stable temperature of 15°C via a water-cooled jig.

Data analysis was performed using the `Corryvreckan` tracking software [118], employing the General Broken Lines (GBL) track model [119] to reconstruct high-precision particle trajectories

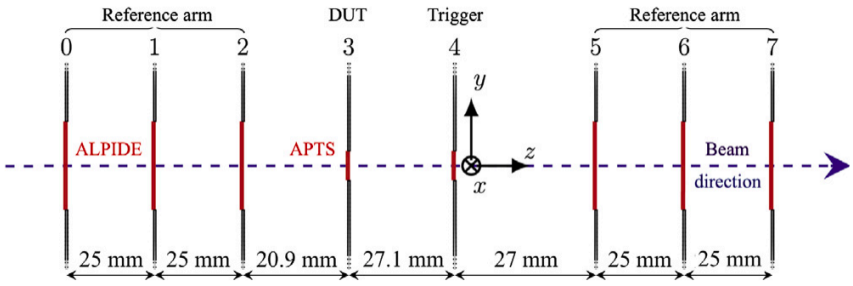

Figure 3.3: Schematic of the test beam telescope setup at the SPS. ALPIDE planes serve as reference, with two APTS sensors positioned in the middle. Adapted from [117].

from hits in the ALPIDE telescope planes.

Tracks were reconstructed from clusters found on all six ALPIDE planes and selected based on quality criteria, requiring single-track events with $\chi^2/\text{ndof} < 5$ and hits on all reference planes. The telescope provided a pointing resolution of $\sigma_{\text{track}} = 2.1\,\mu\text{m}$ at the DUT position [120].

The reconstructed tracks were extrapolated to the DUT plane. For each track, the position at the DUT was compared to clusters reconstructed on the DUT. If a cluster was found within a $75\,\mu\text{m}$ radius of the track intercept, it was associated to the track. This association was used to:

- Measure the **detection efficiency**, defined as the fraction of selected tracks with an associated cluster on the DUT.
- Evaluate the **spatial resolution**, by computing the *residual*, defined as the distance between the extrapolated track position and the associated cluster centroid on the DUT.

To suppress edge effects, only clusters whose seed pixel was located within the four central rows and columns of the DUT matrix were considered. Spatial resolution was studied using both purely digital hit patterns (binary information) and analogue charge information from the cluster. A noise threshold of 3 times the RMS noise was applied to define active pixels in digital cluster reconstruction.

3.2.4.1 Performance in Test Beams

Adapted from [115].

The ALPIDE sensor was selected as the reference plane for the beam telescope due to its proven high performance in test beam campaigns. Its excellent detection characteristics ensure precise reconstruction of particle trajectories, which is essential for evaluating the spatial resolution of the Device Under Test (DUT). In particular, the telescope track resolution at the DUT location ($\sigma_{\text{track}} \sim 2.1\,\mu\text{m}$) must be significantly better than the expected single-point resolution of the DUT to enable unbiased residual measurements.

Extensive test beam studies with ALPIDE prototypes, notably the pALPIDE-1, have demonstrated:

- **Detection Efficiency:** Greater than 99%.
- **Fake Hit Rate:** Less than 10^{-5} per pixel per event.
- **Sustained Performance Post-Irradiation:** Minimal degradation after neutron fluences up to 10^{13} $\text{n}_{\text{eq}}/\text{cm}^2$.

These results validate ALPIDE as the baseline sensor for the ALICE ITS2 and justify its use as a high-precision tracking reference in test beam studies of novel MAPS technologies.

3.2.5 The CE-65 Sensor in the 65 nm TPSCo CMOS Imaging Process

The CE-65 family of monolithic CMOS pixel sensors was developed to investigate the potential of the 65 nm TowerJazz Panasonic Semiconductor Company (TPSCo) CMOS imaging process for charged particle tracking in high-energy physics [121, 122]. Several prototypes were produced with different pixel pitches, primarily 15 μm and 22.5 μm, and varying sensing node layouts and in-pixel electronics architectures. Each sensor matrix consists of 64×32 pixels and is designed to explore key trade-offs between spatial resolution, charge sharing, power consumption, and radiation tolerance.

Design and Architecture

Two pixel diode designs were explored:

- **Basic diode:** standard small collection well with a simple geometry.
- **Optimized diode:** engineered to create a lateral electric field that enhances charge collection speed and minimizes charge sharing.

The pixel matrix was subdivided into submatrices featuring three readout architectures:

1. **AC-AMP:** AC-coupled preamplifier with flexible biasing,
2. **DC-AMP:** DC-coupled preamplifier with high gain,
3. **DC-SF:** traditional 3T source follower.

3.2.5.1 Cluster Formation and Signal Digitisation

To evaluate the spatial resolution of the CE-65 prototypes and their suitability for future tracking detectors, it is essential to understand how pixel signals are clustered and digitised. The digitisation process impacts both the precision of hit reconstruction and the efficiency of the sensor under realistic readout constraints.

The digitisation chain begins with the identification of clusters formed by pixel groups activated by a charged particle. A cluster typically consists of a central *seed* pixel with the highest charge, surrounded by neighbouring pixels that also register signal due to charge sharing. The size and shape of the cluster depend on sensor-specific parameters, such as pixel pitch, collection node geometry, and the local electric field configuration.

Once identified, the analogue charge collected in each pixel is converted to a digital representation through a quantisation process, the characteristics of which (e.g. 1-bit, 2-bit) can significantly influence the achievable spatial resolution.

To reduce readout time and power consumption, large-area pixel detectors cannot rely on fully analogue signal transmission. While analogue readout enables fine-grained charge measurements and optimal spatial resolution via interpolation, it is inherently slower and more power-intensive, making it impractical for high-rate environments such as FCCee. Digitisation provides a compact, fast, and low-power alternative, though it must be carefully designed to preserve resolution and efficiency.

Figure 3.4 shows the charge collected in the seed pixel versus the total cluster charge for two CE-65 sensor variants, the *basic* and the *optimized* diode structures, as measured with mono-energetic X-rays from a ^{55}Fe source (5.9 keV, ~90% of events), rather than with minimum ionising particles. It is important to note that the same amount of signal is generated in both variants; the difference lies in how the charge is distributed within the cluster. In the basic diode design, significant charge sharing occurs between neighbouring pixels, resulting in wider clusters. This behaviour is beneficial for spatial resolution when using centre-of-gravity interpolation, but it also

increases the risk of charge loss or split clusters during digitisation if thresholds are not properly tuned.

In contrast, the optimized diode design concentrates the signal in the seed pixel ($> 85\%$ of total cluster charge), reducing cluster size and simplifying hit reconstruction. This favours applications where precise timing and low-power readout are critical, albeit at the cost of spatial interpolation.

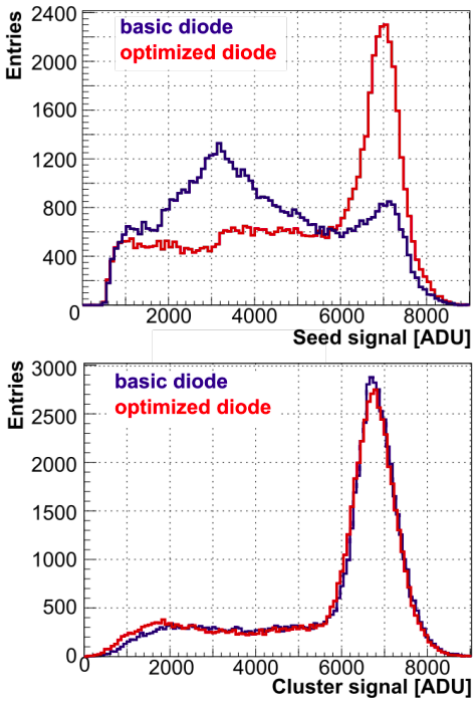

Figure 3.4: Charge collected for the basic (blue) and optimized (red) diode designs. The optimized geometry results in stronger charge localization. Adapted from [121].

To further illustrate the spatial distribution of collected charge, Figure 3.5 presents heatmaps of the average signal recorded in 3×3 clusters centered on the seed pixel. A *heatmap* is a two-dimensional colour-coded representation where each pixel indicates the average charge collected at that relative position within the cluster. This visualisation highlights the typical shape and spread of the deposited signal and spatial resolution.

The basic diode design shows a broad charge spread across neighbouring pixels, suggesting more extensive charge sharing. In contrast, the optimized diode confines the signal to a tighter core, resulting in more compact clusters. This behaviour directly influences cluster size, noise sensitivity, and the appropriate strategy for digitisation threshold optimisation.

These results validate the CE-65 design as a strong candidate for future high-resolution, low-power pixel detectors, and demonstrate the flexibility of the 65 nm TPSCo process for integrating complex front-end electronics with excellent sensing capabilities.

3.2.6 Sensor Design and Digitisation Performance

The CE-65v2 chip was produced in several process variants to study the impact of sensor layout on charge collection and digitisation. Figure 3.6 compares two key designs: the **Standard process** and the **Modified with Gap (MWG)** process. In the MWG variant, a physical gap is introduced in the deep p-well to enhance the lateral electric field, improving charge collection speed and reducing charge sharing.

These structural differences translate into clear performance differences in test beam results:

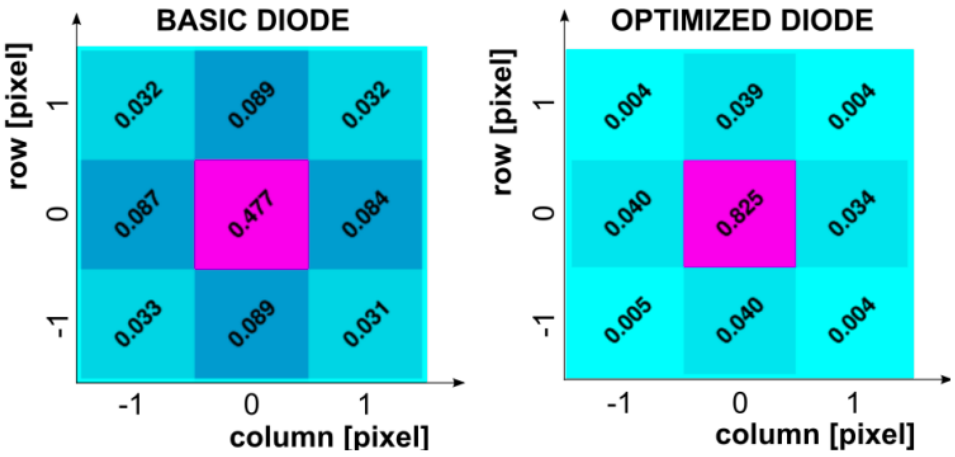

Figure 3.5: Mean signal per pixel in 3×3 clusters centered on the seed pixel for the basic (left) and optimized (right) diode designs. The basic diode shows stronger charge sharing, while the optimized geometry results in a tightly localized signal. Adapted from [121].

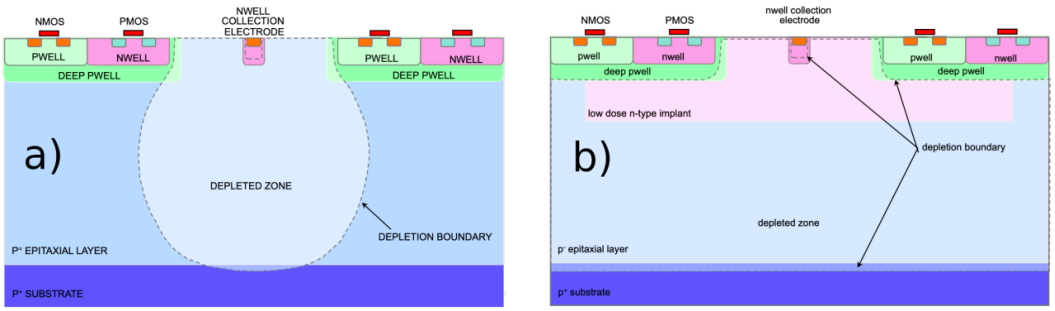

Figure 3.6: Cross-sectional views of CE-65v2 pixels in the Standard process (left) and Modified with Gap (right). The MWG design enhances lateral electric fields by introducing a gap in the deep p-well. Adapted from [107].

Efficiency: Across both 15 μm and 22.5 μm pixel pitches, the MWG (Modified With Gap) design maintains over 99% hit efficiency up to seed thresholds of around 180 e^-, while the Standard design shows a drop in efficiency beyond 130–150 e^- depending on the pitch. This difference is attributed to improved charge collection in the MWG architecture, which benefits from a significantly larger depletion region compared to the standard diode configuration. As a result, the MWG design offers more stable efficiency across a wider range of threshold values, reducing sensitivity to threshold optimisation and radiation-induced shifts in front-end performance.

Spatial Resolution: At low thresholds (e.g. 70 e^-), the Standard 15 μm sensor achieves micron spatial resolution (1.5 μm) due to extensive charge sharing and interpolation. However, this performance degrades rapidly with increasing threshold, exceeding 3–4 μm beyond 120 e^-. The MWG design, with its reduced charge sharing, shows more stable resolution (2.5–5 μm) across a broader range of thresholds, a favourable trade-off for high-rate or radiation-tolerant applications.

These results highlight the fundamental trade-off between spatial resolution and threshold tolerance, which must be considered when digitising analogue signals in MAPS sensors.

3.3 Track Reconstruction with the ALPIDE-Based Telescope

Track reconstruction was carried out using a standard clustering and fitting procedure implemented in the `Corryvreckan` framework. First, activated pixels on each ALPIDE plane were grouped into clusters based on spatial adjacency. The hit position within each cluster was then estimated using a centre-of-gravity method.

Since the test beam operated without a magnetic field, the trajectories of charged particles were assumed to be straight lines. Reconstructed hits across the six telescope planes were used to fit these trajectories via a χ^2 minimisation procedure, based on a linear track model. The resulting track parameters included the intercept and slope in both x and y projections, representing the equation of the straight-line path followed by each particle.

The quality of the reconstructed tracks was assessed by computing the residuals, defined as the distance between the predicted track position on a given plane and the measured hit position on that plane. These residuals are crucial for evaluating the intrinsic spatial resolution of the Device Under Test (DUT), especially when comparing the performance of different signal digitisation schemes.

3.3.1 Residuals and Spatial Resolution

To assess the spatial resolution of the Device Under Test (DUT), the residuals between the measured hit positions and the predicted track positions are analysed. The variance of the residual distribution can be expressed as:

$$\sigma^2_{\text{res}} = \sigma^2_{\text{tel}} + \sigma^2_{\text{DUT}} + \sigma^2_{\text{m.s.}} \tag{3.1}$$

- σ^2_{tel} is the track prediction uncertainty at the DUT surface plane, determined by the intrinsic resolution and geometry of the telescope planes.
- σ^2_{DUT} is the intrinsic single-point resolution of the DUT — the quantity to be extracted.
- $\sigma^2_{\text{m.s.}}$ represents the contribution of multiple Coulomb scattering, arising from material between the telescope planes and the DUT. This term also affects the extrapolation accuracy and is sometimes absorbed into the effective telescope resolution when not estimated separately.

When multiple scattering is negligible (e.g. at high beam energy or with minimal upstream material), the DUT resolution can be estimated by subtracting the telescope contribution in quadrature:

$$\sigma_{\text{DUT}} = \sqrt{\sigma^2_{\text{res}} - \sigma^2_{\text{tel}}}$$

Estimation of σ_{tel} from Telescope Geometry

The telescope resolution at the DUT position, σ_{tel}, depends on the spatial resolution of the individual telescope planes and their geometry. For a telescope composed of N planes with intrinsic resolution σ_{plane}, and assuming straight-line tracking, an approximate expression is:

$$\sigma_{\text{tel}} \approx \sigma_{\text{plane}} \cdot \sqrt{\frac{1}{N} + \left(\frac{d}{L}\right)^2}$$

where:

- d is the distance between the DUT and the nearest telescope plane,
- L is the total distance between the first and last telescope planes.

This expression assumes equal-weighted contributions from all planes and symmetric placement around the DUT. For precise evaluation, track fitting with inhomogeneous plane resolutions or Kalman filtering can be used.

A more complete treatment of residual analysis and spatial resolution extraction can be found in [100].

Signal Digitisation in CMOS Pixels

The digitisation process relies on front-end circuits embedded directly within the CMOS pixel matrix. After charge collection, the analogue signal is amplified and processed locally on the chip. In the CE-65 prototypes, this signal is not digitised on-chip but read out in analogue form and subsequently digitised with 12- or 14-bit resolution by the external DAQ board, which interfaces the sensor to the data acquisition system. The CE-65 sensors tested here integrate custom architectures in 65 nm CMOS, designed to support fine spatial resolution with reduced data rates.

Digitised outputs are used for cluster formation and hit reconstruction. Depending on the digitisation scheme, 1-bit, 2-bit, or *pseudo-analogue* (e.g. using an 8-bit ADC), different methods are applied to compute the cluster centre, which in turn affects the achievable tracking resolution.

3.3.2 Test Beam Characterisation of the CE-65v2 Sensor in the TPSCo 65 nm Process

As part of the ALICE ITS3 upgrade R&D, the CE-65v2 chip was developed to study the charge collection and spatial resolution performance of MAPS fabricated in the TowerJazz Panasonic Semiconductor Co. (TPSCo) 65 nm CMOS imaging process [107]. The chip matrix consists of 1152 pixels arranged in 48 columns and 24 rows, read out using a rolling shutter architecture.

In a rolling shutter scheme, pixels are not read out simultaneously; instead, rows (or groups of rows) are activated sequentially. This reduces power consumption and readout complexity but introduces a time skew between the top and bottom of the matrix, which may affect time resolution in fast environments.

The in-pixel electronics feature an AC-coupled amplifier with a reset node, allowing reverse biasing of the sensing diode up to 10 V. This enables full depletion of the epitaxial layer, enhancing charge collection by drift and improving radiation tolerance.

The CE-65v2 matrix includes 15 sensor variants designed to explore the impact of layout and fabrication process on charge collection and spatial resolution. These variants differ in:

- **Process:**
  - *Standard*, the baseline diode design.
  - *Modified*, introduces additional implants to improve depletion and lateral electric field uniformity.
  - *Modified with Gap (MWG)*, further improves charge collection by introducing a physical gap between implants, enabling deeper and more uniform depletion.
- **Pixel pitch:** 15, 18, and 22.5 μm.
- **Geometry:** square and staggered (hexagonal) pixel layouts.

The beam test focused on four configurations: sensors with 15 μm and 22.5 μm pitch using either the Standard or the Modified with Gap (MWG) process.

Laboratory Pre-Calibration with ^{55}Fe Source

Prior to beam testing, the CE-65v2 chips were calibrated in the laboratory using a ^{55}Fe radioactive source. This allowed the evaluation of gain and energy resolution across the matrix. Gaussian fits of the Kα emission line (5.9 keV) were used to determine the conversion gain. Pixel-wise spectra exhibited energy resolutions as good as 4.8% (FWHM/mean), while the matrix-averaged spectrum showed a resolution around 11.5%. Gain uniformity was stable at the level of $\mathcal{O}(5\%)$ across all sensor variants.

These calibration measurements provided essential charge-to-voltage conversion factors used for cluster charge analysis during the test beam [107].

Test Beam Setup and Analysis

Test beam measurements were carried out at the CERN SPS (H6 beamline) with a telescope consisting of six ALPIDE planes [115]. Track reconstruction was performed using Corryvreckan [118] with a resolution of 2.1 μm. CE-65v2 hit clusters were formed in 3×3 windows around seed pixels, with electron thresholds varied to study efficiency and resolution dependence.

Efficiency:

- **Standard process:** $> 99\%$ efficiency up to $\sim 130\, e^-$ (15 μm) and $\sim 150\, e^-$ (22.5 μm).
- **Modified with Gap:** $> 99\%$ efficiency maintained up to $\sim 180\, e^-$ for both pitches.

Spatial Resolution:

- **Standard process:** Micron resolution achieved at low thresholds (1.5 μm @ 70 e^- for 15 μm), degrading to 3–4 μm at higher thresholds.
- **Modified with Gap:** Slightly worse resolution (>2–5 μm), but more stable across thresholds.

Charge Sharing: Charge sharing analysis showed:

- **Standard process:** Extensive charge sharing, central pixel carries $\sim 45\%$ of total cluster charge.
- **Modified with Gap:** Sharper charge localization, central pixel holds $> 85\%$ of total charge.

Conclusion

The CE-65v2 study demonstrates that:

- The Standard process provides excellent spatial resolution ($< 2\,\mu$m), satisfying FCCee vertex detector goals, but suffers from narrow optimal threshold range and charge trapping sensitivity.
- The Modified with Gap process supports wider operational thresholds, faster collection, and reduced charge sharing, better suited for radiation environments despite a resolution penalty.

These findings validate both processes and pixel configurations for next-generation high-resolution, radiation-tolerant MAPS and are directly relevant for the digitisation studies presented in this chapter.

3.4 Signal Digitisation Strategy for Future MAPS-Based Detectors

Modern particle detectors increasingly rely on Monolithic Active Pixel Sensors (MAPS) for high-precision tracking with minimal material budget and power consumption. While analogue MAPS can provide detailed information about charge collection and cluster structure, large-scale detector systems, such as those foreseen at future colliders like FCCee, require fast, robust, and compact data formats. Digitisation, the process of converting analogue pixel responses into discrete digital codes, is therefore essential to enable on-chip processing, data compression, and integration with trigger and readout systems.

This chapter focuses on the digitisation strategy and its impact on spatial resolution, based on the test beam evaluation of CE-65v2 prototypes. In particular, it presents the work I conducted on the optimisation and performance benchmarking of 1-bit and 2-bit digitisation schemes, comparing them to pseudo-analogue readout as a reference. It should be noted that the 1-bit and 2-bit digitisation were not implemented on-chip in the prototypes, but instead reproduced offline in the analysis from the analogue data recorded during the beam test.

3.4.1 Digitisation and Cluster Formation

The goal of digitisation is to convert the continuous signal from each pixel into a discrete representation (e.g., number of bits or integer code) that retains the relevant physical information (position, charge spread) while suppressing noise. This process is tightly coupled with cluster formation, grouping neighbouring pixel responses into a single reconstructed hit.

3.4.2 Implementation and Illustration

To study the impact of signal digitisation on spatial resolution, I implemented a post-processing model that emulates different digitisation schemes using the pseudo-analogue data collected during the beam test (see Section 3.3.2). The goal is to simulate how various levels of charge quantisation, such as 1-bit or 2-bit encoding, affect cluster reconstruction and, consequently, the track-hit resolution of the DUT.

The digitisation strategy involves the following steps:

1. For each event, extract the 3×3 pixel cluster centred on the seed pixel.
2. Convert the analogue charge in each pixel into a digitised code by applying predefined threshold values. This emulates 1-bit or 2-bit quantisation schemes.
3. Recalculate the cluster barycentre using the digitised pixel values instead of the original analogue charges.
4. Associate the reconstructed cluster position to the nearest extrapolated telescope track and compute the residual distribution to extract the spatial resolution.

In earlier iterations of the procedure, pixel charges were normalised to the total cluster charge before quantisation, in an attempt to isolate relative charge patterns. However, this step was ultimately not retained in the final resolution studies, as it distorted absolute signal amplitudes that are critical for threshold optimisation.

This methodology enables a direct comparison between pseudo-analogue and low-bit digitisation schemes, under realistic signal and noise conditions.

Figure 3.7 illustrates this process. On the left, the original cluster is shown with its analogue response. The central matrix displays the corresponding normalised values, i.e. the charge fraction in each pixel. The right side shows the result after applying a digitisation scheme with three

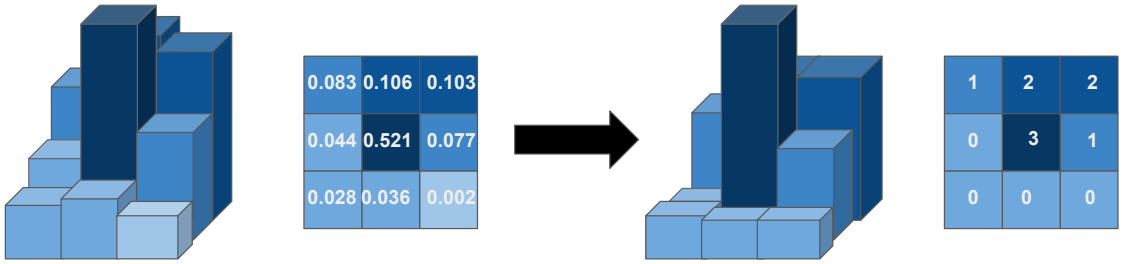

Figure 3.7: Illustration of the digitisation process applied to a 3×3 pixel cluster. **Left:** initial cluster with analogue pixel values. **Right:** result of discretised signal after applying 2-bit digitisation (4-level quantisation).

discrete levels: 0 (no signal), 1–2 (low-to-medium signal), and 3 (maximum signal, typically the seed pixel).

This 2-bit digitisation balances compact encoding with preservation of cluster topology. It captures key features such as the seed pixel intensity and nearby charge sharing, while reducing memory usage and allowing faster digital processing.

3.4.3 Threshold Optimisation

A critical aspect of signal digitisation is the choice of the threshold values used to assign discrete digital codes to analogue signals. In a multi-level scheme (such as the 2-bit digitisation shown in Figure 3.7), this involves defining transition points between quantisation levels, for example, determining which normalised charge values are mapped to digitised codes 0, 1, 2, or 3.

These threshold values cannot be chosen arbitrarily; they must be optimised for each sensor configuration and readout process. The optimal thresholds depend on several factors:

- the pixel pitch (e.g. $15\,\mu$m vs. $22.5\,\mu$m),
- the diode structure (e.g. Standard vs. Modified with Gap),
- the amount of charge sharing within a cluster,
- and the signal-to-noise characteristics of the front-end electronics.

As demonstrated in the test beam results (Section 3.3.2), different CE-65v2 configurations exhibit distinct cluster shapes and charge distributions. A threshold setting that captures the full signal in one configuration might under-represent or over-saturate another. Without proper tuning, the digitisation could lead to degraded spatial resolution, reduced hit efficiency, or distortions in the reconstructed cluster shape including artificial broadening or tightening depending on the threshold configuration.

Therefore, an essential part of the digitisation strategy is to calibrate the thresholds using either beam test data or high-statistics simulations. This ensures that the discrete representation remains faithful to the original analogue information, while maximising performance in terms of efficiency, resolution, and robustness.

3.4.4 One-Bit Digitisation and Resolution Trade-Offs

A particularly constrained digitisation scheme is the 1-bit case, in which each pixel stores only a binary state: hit (1) or no hit (0). This approach applies a single global threshold to all pixels and

significantly simplifies on-chip logic and memory requirements. However, the coarseness of this representation can limit spatial resolution, especially when charge sharing is significant.

To study the impact of 1-bit digitisation, the hit position resolution was evaluated as a function of the threshold value for three CE-65v2 sensor configurations:

- **PCB 18:** Standard process, pitch 22.5 μm, square geometry.
- **PCB 19:** Modified with Gap, pitch 15 μm, square geometry.
- **PCB 10:** Modified with Gap, pitch 22.5 μm, square geometry.

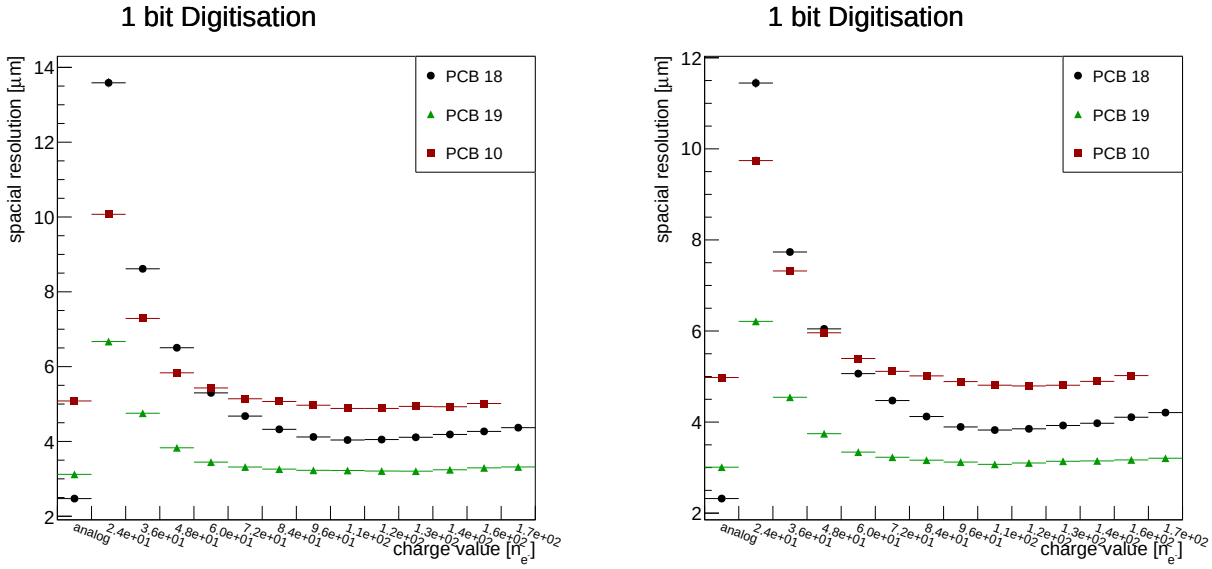

(a) Hit resolution in the X position.

(b) Hit resolution in the Y position.

Figure 3.8: Hit resolution in the X and Y position.

Figure 3.8 shows the hit position resolution in the X and Y directions as a function of the digitisation threshold (expressed in charge units) for each of the three sensors. Each curve exhibits a characteristic shape:

- At very low thresholds, the resolution is degraded due to noise and cluster broadening.
- With increasing threshold, the resolution improves and reaches a plateau: the optimal threshold range.
- Beyond this region, resolution slowly worsens again due to signal truncation.

Resolution Degradation (1-bit vs Analogue). The relative degradation observed in the optimal 1-bit threshold region (plateau) is as follows:

- **PCB 18 (Standard, 22.5 μm):**
  - $\sim$65% degradation in X,
  - $\sim$68% degradation in Y.
- **PCB 19 (Gap, 15 μm):**
  - $\sim$6% degradation in X,

  - ∼5% degradation in Y.

- **PCB 10 (Gap, 22.5 μm):**
  - ∼2% degradation in X,
  - ∼2% degradation in Y.

These results highlight that sensors with more compact charge collection (MWG design) are far less sensitive to digitisation granularity. In contrast, sensors relying on charge sharing to achieve fine resolution suffer significant resolution loss when analogue information is discarded. This underscores the importance of matching the digitisation strategy to the intrinsic characteristics of the sensor design.

3.4.5 Two-Bit Digitisation: Charge-Driven Threshold Optimisation

Two-bit digitisation offers a balanced trade-off between information retention and hardware simplicity. With four discrete codes (0 to 3), it allows a richer encoding of charge distribution across the cluster compared to the binary scheme, while still limiting memory and processing needs. However, this flexibility comes at the cost of increased complexity: **three thresholds** must now be optimised instead of just one.

The threshold configuration must reflect the internal structure of the signal within each cluster. In particular, it must distinguish:

- the intense seed pixel from weaker peripheral signals,
- significant neighbours from noise,
- and overlapping cases where charge sharing blurs the separation between levels.

This optimisation is sensor-dependent, as the amount and pattern of charge sharing vary with diode geometry and pixel pitch. To guide this process, I produced and analysed three diagnostic plots for each of the three CE-65v2 sensor configurations (PCB 18, 19, 10), based on test beam data.

The first visualisation (Figure 3.9) presents the correlation between seed charge and the total charge in its neighbours. Each panel corresponds to a different PCB. These 2D maps reveal how often specific charge combinations occur, and help identify natural boundaries in the charge space that can guide the placement of digitisation thresholds.

Figure 3.10 shows the distribution of seed pixel charge (in ADC units) for all three PCBs on a single plot. This highlights typical signal amplitudes in the most active pixel of a cluster, and informs the setting of the highest threshold level. For example, PCB 18 shows a tighter peak at higher counts, consistent with more confined charge collection, while PCB 19 exhibits a broader distribution with lower seed charge, indicating more charge sharing.

Finally, Figure 3.11 compares the charge recorded in the first, second, and third most active neighbours for each sensor. Each row corresponds to one sensor (PCB 18, 19, 10). These distributions help to distinguish meaningful peripheral signal (e.g., cluster tails) from noise, guiding the choice of intermediate thresholds in the 2-bit encoding.

To define the three threshold levels required for 2-bit digitisation, I adopted a data-driven approach based on the cluster charge distributions:

- The upper threshold was chosen near the peak of the seed charge distribution.
- The intermediate thresholds were guided by the charge distributions of the first, second, and third most active neighbour pixels, shown in Figure 3.11. These help distinguish meaningful signal in the cluster periphery from noise.

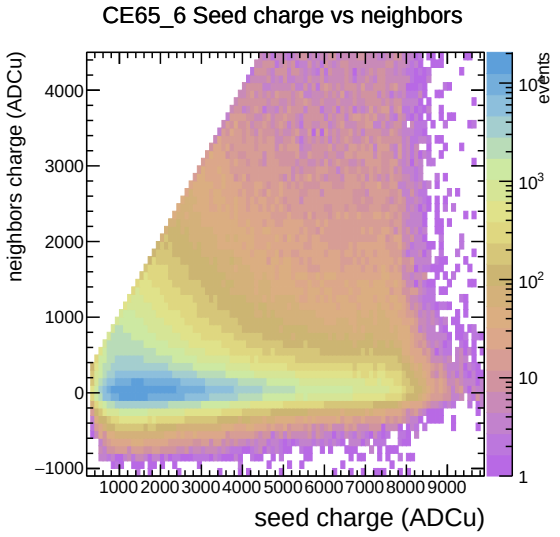

(a) PCB 18 (Standard, 22.5 μm)

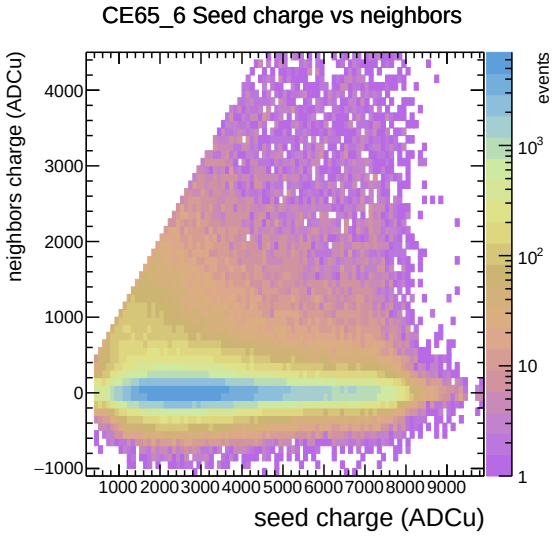

(b) PCB 19 (Gap, 15 μm)

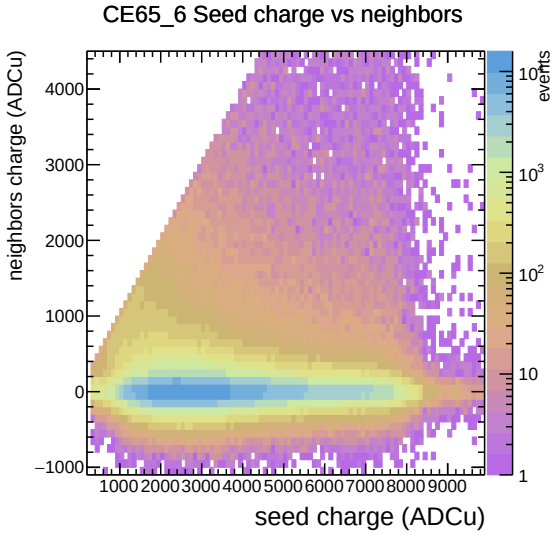

(c) PCB 10 (Gap, 22.5 μm)

Figure 3.9: Correlation between seed charge and total neighbour charge for each sensor. These 2D density maps are used to guide threshold placement in 2-bit digitisation. Strong diagonal structures indicate typical charge-sharing behaviour.

- Several strategies were explored, including fixed fraction cuts, quantile-based splits, and scans minimising the reconstructed resolution.

The final thresholds were selected to provide good separation between noise and signal while preserving relative charge information. Although not strictly optimised, they represent a practical and reasonably tuned configuration. Similar procedures were followed for PCB 19 and PCB 10, with adjustments to reflect their distinct signal shapes.

Figure 3.12 presents the results for two sensor configurations, using threshold settings guided by the observed cluster charge distributions (see Section 3.4.5). While not necessarily fully optimised, these threshold values represent a realistic and reasonably tuned scenario, allowing a meaningful comparison between analogue and low-bit digitised readout.

- **PCB 18:** Standard diode, pitch 22.5 μm.

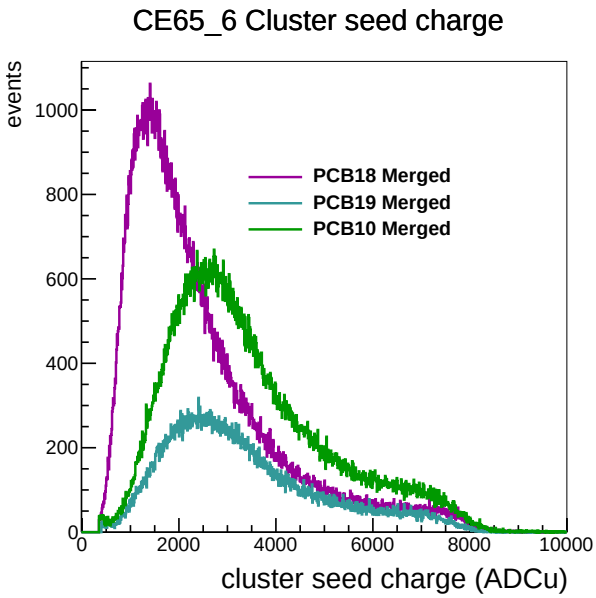

Figure 3.10: Distribution of seed pixel charge (in ADC units) for the three CE-65v2 sensors. This helps determine the upper threshold of the 2-bit digitisation window and evaluate dynamic range.

- **PCB 19:** Modified with Gap, pitch 15 μm.

The observed degradation in resolution remains small:

- **PCB 18:** The resolution degradation with 2-bit digitisation is approximately **26%** compared to the analogue case.
- **PCB 19:** The resolution degradation with 2-bit digitisation is approximately **20%** compared to the analogue case.

These results demonstrate that with appropriately tuned thresholds, 2-bit digitisation can retain a large fraction of the spatial resolution offered by full analogue readout, while enabling much more compact and faster data processing. In particular, sensors with reduced charge sharing (e.g. MWG designs like PCB 19) are especially well-suited to such low-bit encoding schemes.

Together, these figures enable a physics-driven calibration of the 2-bit digitisation thresholds, tailored to the actual cluster topologies observed in beam test data. Unlike the 1-bit case, 2-bit encoding captures the internal shape and asymmetry of the cluster, which can be exploited in high-precision reconstruction.

This trade-off highlights the importance of choosing a digitisation strategy that matches the sensor's native charge collection behaviour. While 1-bit schemes may be suitable for fast or radiation-hardened environments, multi-bit digitisation remains essential for applications requiring high spatial resolution.

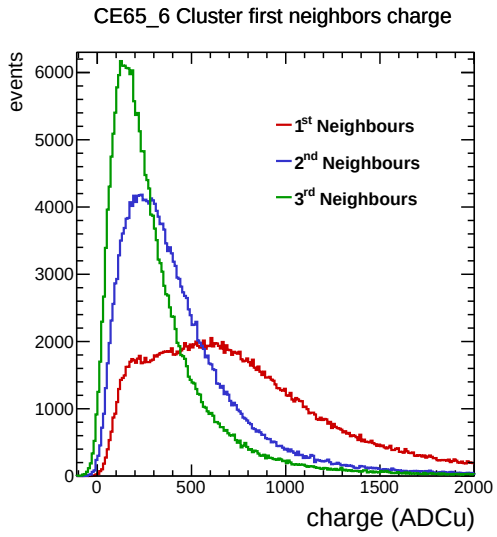

(a) PCB 18 (Standard, 22.5 μm)

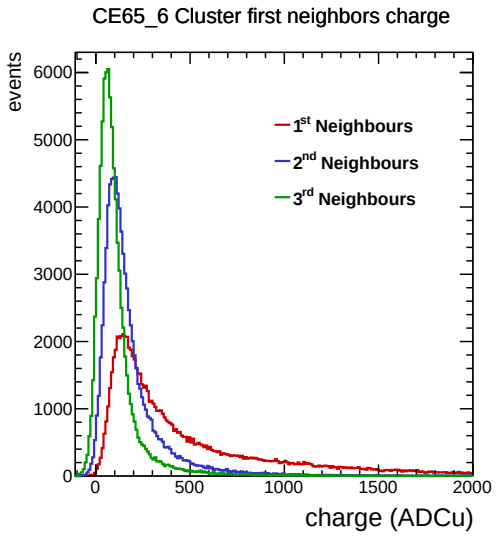

(b) PCB 19 (Gap, 15 μm)

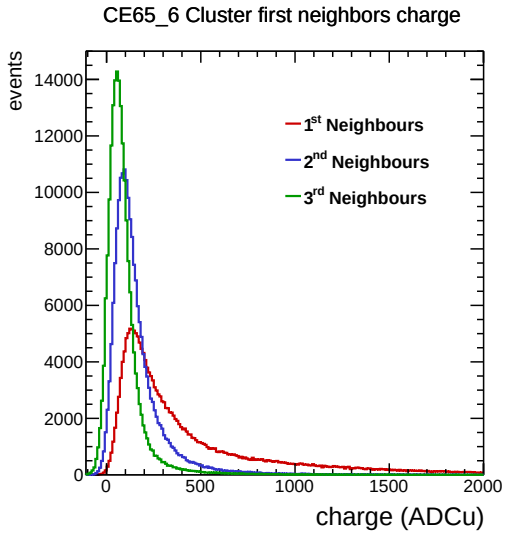

(c) PCB 10 (Gap, 22.5 μm)

Figure 3.11: Charge distributions of the first, second, and third most active neighbours in the cluster. Used to determine the lower and intermediate thresholds in the 2-bit encoding.

3.5 Outlook

The work presented in this chapter demonstrates the feasibility and challenges of implementing low-bit signal digitisation in monolithic CMOS pixel sensors for future high-energy physics experiments. By emulating 1-bit and 2-bit encoding schemes on test beam data from the CE-65v2 prototypes, I evaluated their impact on spatial resolution, cluster formation, and robustness across different sensor configurations.

The results show that, with proper threshold tuning, 1-bit digitisation can preserve spatial resolution within 10–15% of the pseudo-analogue baseline for sensors with significant charge sharing. In practice, this corresponds to resolutions still close to or below the ~ 3 μm target required for the FCCee vertex detector, demonstrating that such a reduced encoding scheme can remain compatible with physics performance goals. For 2-bit schemes, careful optimisation of multiple thresholds allows further improvement. The approach developed here provides a reusable framework to guide

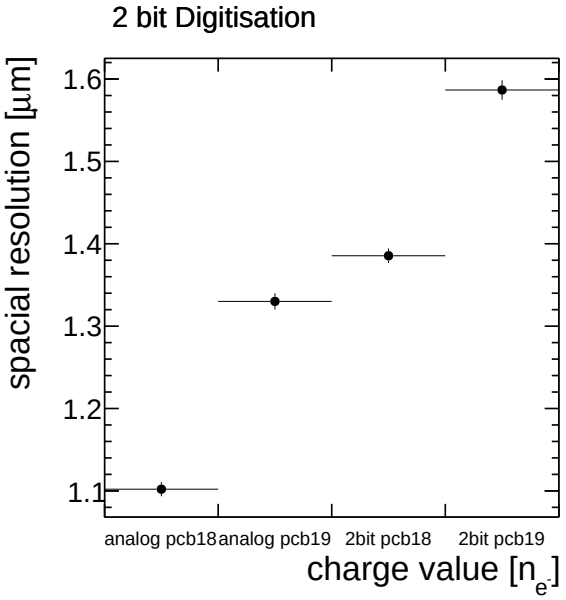

Figure 3.12: Comparison of hit position resolution between analogue and 2-bit digitisation for PCB 18 and PCB 19. The 2-bit strategy yields only a modest degradation in resolution while offering a substantial reduction in data volume.

digitisation architecture choices in future sensor design iterations.

Looking ahead, these findings support the integration of digitisation logic at the pixel or column level in future MAPS chips intended for tracking detectors at future colliders such as FCCee. Beyond collider applications, advances in low-bit digitisation are also of strong interest for medical and societal domains. In medical imaging, such compact and low-power readout schemes could enable faster and higher-resolution diagnostics while reducing system complexity. Similarly, in radiotherapy, optimised MAPS digitisation may improve real-time beam monitoring and dose verification, contributing to more precise and safer treatments.

- Automate threshold optimisation using machine learning or resolution-driven scans.
- Extend the digitisation model to include timing information and time-over-threshold encoding.
- Validate digitisation schemes in irradiated sensors and higher particle rate environments.

This work contributes to bridging the gap between sensor design, readout electronics, and system-level performance in the next generation of tracking detectors, while also opening perspectives for broader technological transfer to medical and societal applications.

Chapter 4

Performance Tracking of the CLD Detector

Contents

Introduction

The discovery of the Higgs boson [7, 9, 8] at the Large Hadron Collider (LHC) [10] marked a significant milestone in particle physics. It not only validated the existence of the Higgs field [7] but also opened up new avenues for exploring the fundamental building blocks of the universe. As we continue to probe the mysteries of the Standard Model and seek evidence of physics beyond it, future particle colliders are of paramount importance. While the FCC project includes both an electron-positron phase (FCCee) and a subsequent hadron-hadron phase (FCChh), ihis thesis focuses exclusively on FCCee, which is designed to provide unprecedented precision in the measurement of Higgs boson properties, electroweak observables, and rare processes, along with enhanced sensitivity to indirect signs of new physics [82].

Among the proposed detector concepts for FCCee [82], the CLIC-Like Detector (CLD) [98] was the first developed and is the one considered in this thesis. The successful operation of the CLD detector is crucial for the success of the entire FCCee project [82], as it enables us to explore a wide range of physics processes, including the study of electroweak interactions, the properties of the Higgs boson and top quark physics.

The CLD detector [98] comprises a full silicon tracking system, including vertex detectors. This tracking system plays a central role in the precise measurement of particle trajectories and momenta. It provides essential information for a wide range of physics analyses, from the identification of particle types to the determination of particle properties and the study of the fundamental interactions.

The accurate and efficient tracking of charged particles is a fundamental aspect of particle physics experiments, enabling the reconstruction of particle trajectories and the determination of important properties such as momentum and charge. Tracking is an indispensable tool for a wide range of physics analyses, from the discovery of new particles to precision measurements of known particles and their interactions.

The Future Circular Collider electron-positron (FCCee) [82] is one of the most ambitious projects in high-energy physics, aiming to provide unprecedented precision in the study of the electroweak sector. As part of the FCCee program, the four detectors planned at the interaction points will be essential for measuring collision events and the resulting particles. To fulfil this mission, their tracking systems must achieve outstanding performance in terms of precision, efficiency, and robustness.

This chapter presents the study I conducted on the tracking performance of the CLD [98] detector. Such an investigation is vital to ensure that the detector operates at its optimum efficiency and delivers high-quality data. Through this work, I aim to assess the capabilities and limitations of the tracking system, identify potential areas for improvement, and contribute to the ongoing optimisation of the CLD for future experiments at FCCee [82]. The primary objectives of this study are to evaluate the detector's resolution, energy and momentum measurement capabilities, particle identification performance, and its ability to accurately reconstruct the vertices of particle interactions.

In the following sections, we will delve into the methodology, data analysis techniques, and results of the performance tracking study. This study not only contributes to the successful operation of the FCCee [82] experiment but also advances our understanding of the capabilities and limitations of state-of-the-art particle detectors. By improving our grasp of detector performance, we pave the way for groundbreaking discoveries and a deeper comprehension of the fundamental principles.

4.1 The Future Circular Collider project

The Future Circular Collider (FCC)[1] is an ambitious international project led by CERN to define the next major facility for high-energy particle physics. Envisioned to be hosted in a new 91 km tunnel near Geneva, the FCC will succeed the Large Hadron Collider (LHC) [10] and extend the reach of particle physics both in precision and energy.
The FCCee [82] is the first phase of the FCC program and consists of a high-luminosity electron-positron collider designed for precision measurements of the Standard Model. It will operate at several center-of-mass energies, corresponding to key physics thresholds: the Z pole (∼91 GeV), the WW production threshold (∼160 GeV), the ZH production threshold (∼240–250 GeV), and the top-quark pair production threshold (∼365 GeV). These operation modes will enable extremely accurate studies of the Z boson, W boson, Higgs boson, and top quark, providing sensitivity to indirect effects from new physics at higher scales.

Following FCCee [82], the same infrastructure is planned to host a proton-proton collider (FCChh) [123] capable of reaching collision energies up to 100 TeV, opening a new frontier in the direct search for new particles and interactions.

4.2 FCCee detectors concept

The FCCee [82] is designed to be a next-generation high-precision particle physics experiment, requiring state-of-the-art detector technologies to fully exploit its potential. Various detector concepts have been proposed and studied, each optimized for the unique operational conditions of FCCee, including high luminosity, multi-stage energy operation, and the need for precise tracking, calorimetry, and particle identification. The detector concepts explored for FCCee include both adaptations of existing designs from previous collider projects [124, 125] and entirely new approaches tailored to the circular collider environment. This section provides an overview of four major detector concepts considered. Each of these detector concepts offers unique advantages and trade-offs, balancing precision, efficiency, and technological feasibility to meet the demands of FCCee physics. The following subsections detail their designs and key features.

In high-energy particle physics experiments, detectors are complex instruments designed to identify and measure the properties of particles produced in collisions. These detectors are typically composed of several subdetectors, each optimized to perform a specific task in the detection and reconstruction process. The subdetectors are arranged in a cylindrical geometry around the interaction point, where particles are produced.

Vertex Detector (VTX): The innermost component, placed closest to the interaction point, is the vertex detector. It consists of finely segmented silicon sensors that provide precise measurements of the trajectories of charged particles near the collision point. One of its main role is also to identify primary and secondary vertices, which is crucial for flavour tagging and the study of short-lived particles. The barrel region is complemented by forward endcaps to ensure full angular coverage.

Tracking System (Tracker): Surrounding the vertex detector, the tracking system continues to record the positions of charged particles as they move outward. Using the curvature of particle trajectories in a magnetic field, the tracker enables the precise determination of particle momenta.

Electromagnetic Calorimeter (ECAL): The ECAL is designed to measure the energy of electrons and photons by absorbing them and recording the resulting electromagnetic showers. It typically consists of alternating layers of absorber material (such as tungsten) and active sensors (such as silicon).

Hadronic Calorimeter (HCAL): Located outside the ECAL, the HCAL measures the energy of hadrons (such as pions and protons) through hadronic shower development. Like the ECAL, it

[1] fcc.web.cern.ch

usually uses a sampling structure, usually based on steel absorbers and scintillator tiles.

Magnet: A solenoidal magnet provides a strong and uniform magnetic field that bends the trajectory of charged particles. The curvatures of these trajectories is used to determine the particle momenta with high precision in the tracking detectors.

Muon System: The outermost subdetector is dedicated to identifying muons, which penetrate through the calorimeters and magnet yoke due to their minimal interactions with matter. Muon chambers detect these particles and help in their identification and momentum measurement.

Each subdetector provides unique and complementary information, and together they allow the full reconstruction of the final state of a collision. In addition to energy and momentum measurements, specific subdetectors contribute to particle identification. For example, the tracking system can provide particle identification through the measurement of energy loss per unit length ($\mathrm{d}E/\mathrm{d}x$). Timing information from dedicated detectors can help distinguish particles based on their velocity, while systems like Ring Imaging Cherenkov (RICH) detectors enable separation of particles such as pions, kaons, and protons across a wide momentum range.

4.2.1 CLIC-Like Detector (CLD)

The CLIC detector [99] was originally developed for a proposed high-energy linear electron-positron collider [125]. It emphasizes precision tracking and calorimetry to address the challenges of high luminosity and beam-induced backgrounds in a linear collider environment. Its design features a silicon-based tracking system, highly granular electromagnetic and hadronic calorimeters (using silicon–tungsten and steel–scintillator technologies, respectively), and a dedicated muon system, all embedded in a strong solenoidal magnetic field (4 T) to ensure excellent momentum resolution and particle identification. Schematic layout represented in Figure 4.1.

The CLD [98] is an adaptation of this concept tailored for the FCCee [82], a circular electron-positron collider. While it retains the core components and design philosophy of the CLIC detector, the CLD is optimised to accommodate the specific conditions of a circular machine. These include higher event rates and continuous operation, which require modifications to the geometry, timing capabilities, and radiation tolerance. The tracking system has been redesigned to ensure stable performance over extended periods, and the calorimeter and muon systems have been adapted to the FCCee beam structure and background environment. In particular, the interaction region has been modified to match the geometry of the beam pipe and the machine-detector interface (MDI), which significantly impacts the layout of the vertex detector. Specifically, the beam pipe radius for CLD is 15 mm, compared to 29.4 mm for the CLIC detector concept [98]. This reduced radius allows the vertex detector to be positioned closer to the interaction point, enhancing the impact parameter resolution. A schematic layout is shown in Figure 4.2.

At the FCCee, particularly at the Z pole, operating with a 4 T solenoidal field as in the CLIC detector is not feasible. Because of the crossing angle at the interaction point, particles near the IP would experience a non-zero Lorentz force, which would increase the beam emittance and thus reduce the luminosity. A compensating solenoid is foreseen between the LumiCal and the final focusing quadrupole to mitigate this effect, but the compensation is limited by available space and field uniformity constraints. As a result, the solenoidal field is limited to about 2 T at the Z pole (increasing it to 3 T would already lead to significant luminosity loss). To maintain good momentum resolution despite the reduced magnetic field, the tracking volume has been enlarged. Consequently, the hadronic calorimeter (HCAL) volume was reduced, to avoid increasing the radius of the surrounding solenoid, which is not necessary in any case, since FCCee will not reach the multi-TeV energies foreseen for CLIC.

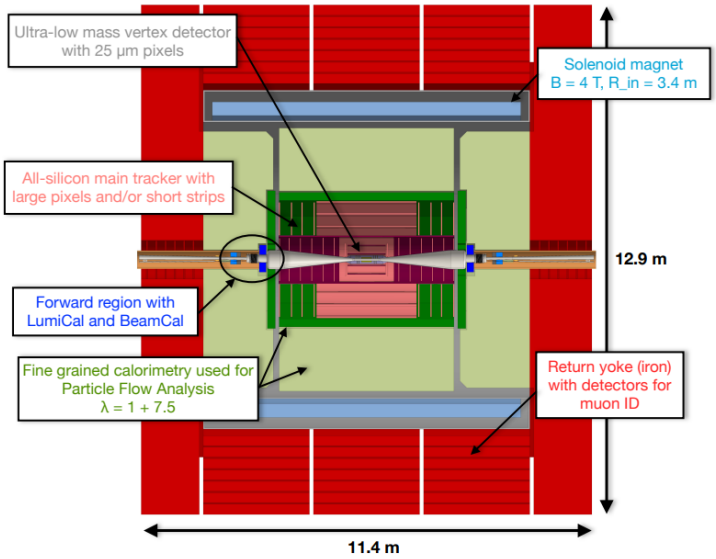

Figure 4.1: Schematic layout of the CLIC detector[99]

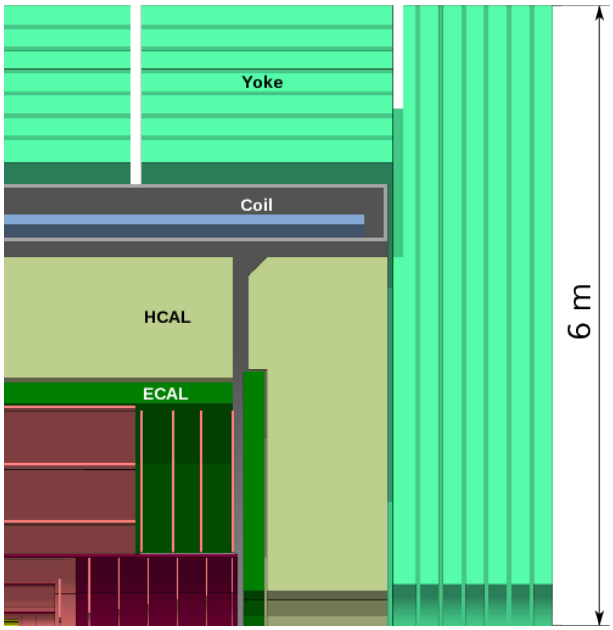

Figure 4.2: Schematic layout of the CLD detector[98]

4.2.2 IDEA

The IDEA (Innovative Detector for Electron-positron Accelerators) detector [126] concept is designed for the FCCee project [82]. It consists of several key components: A high-resolution silicon pixel vertex detector enables precise vertex reconstruction, complemented by a large-volume, ultra-light short-drift wire chamber. An additional layer of silicon micro-strip detectors is included at the outer radius to provide a precise final measurement point, thereby improving the determination of the track curvature and enhancing the transverse momentum resolution. Surrounding these tracking systems is a thin, low-mass superconducting solenoid coil that generates the magnetic field (2T) for charged particle bending. For calorimetry, IDEA features a pre-shower detector and a dual-readout calorimeter, which improves energy resolution by distinguishing between electromagnetic

and hadronic components. Finally, muon chambers are integrated within the magnet return yoke to facilitate efficient muon identification. Schematic layout represented in Figure 4.3.

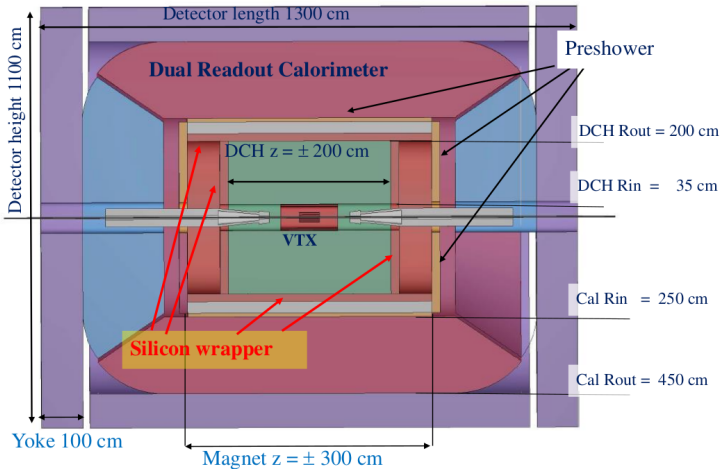

Figure 4.3: Schematic layout of the IDEA detector[126]

4.2.3 ALLEGRO

The ALLEGRO (A Lepton-Lepton collider Experiment with Granular Read-Out) detector concept [127] has been proposed for the FCCee project [82]. It features a lightweight tracking system, combined with advanced calorimetry and a 2 T superconducting solenoid. The design emphasizes particle flow reconstruction through fine detector segmentation and remains adaptable, with ongoing research and development (R&D) refining its structure and electronics. Schematic layout represented in Figure 4.4.

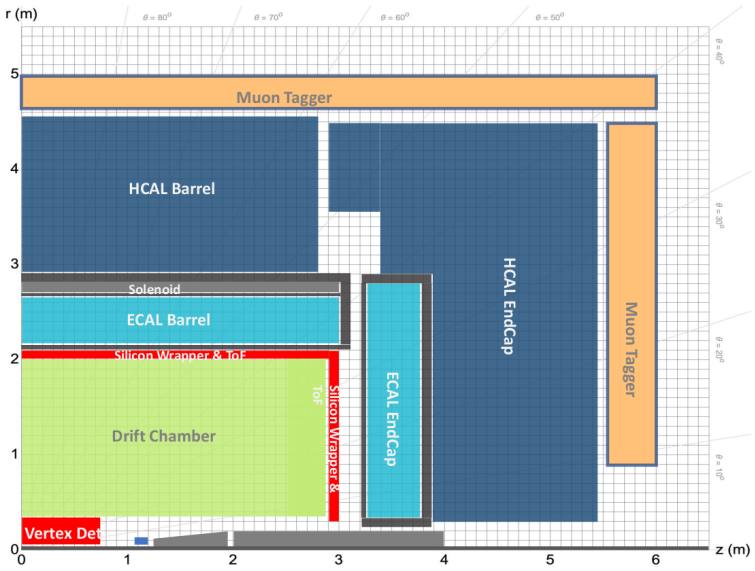

Figure 4.4: Schematic layout of the ALLEGRO detector [127]

4.2.4 ILD for FCCee

The International Large Detector (ILD) [128], originally designed for the International Linear Collider (ILC) [124], is being adapted for FCCee [82]. A key component, the Time Projection

Chamber (TPC), provides high-precision tracking and particle identification (PID) with minimal material. The modified ILD integrates a hybrid tracking system, combining a TPC with silicon-based inner and outer trackers. Compared to ILC, FCCee presents different background conditions, requiring optimisations in the machine-detector interface (MDI) and detector layout. Two main configurations are under study: one with a larger TPC, and another with a smaller TPC and an all-silicon inner tracker, aiming to improve tracking robustness in FCCee's forward-boosted environment. Isometric view of the CLD detector shown in Figure 4.5.

While several detector concepts have been proposed for FCCee, the remainder of this chapter concentrates on the CLD detector, the reference design adopted in this thesis. Each of its subdetectors is discussed in greater detail in the following sections.

4.3 CLD Vertex Detector

The CLD vertex detector, derived from the CLICdet design [99], consists of a cylindrical barrel section enclosed by forward discs. Its layout is based on double-layer structures. The detector uses 25×25 μm^2 pixels with a silicon sensor thickness of 50 μm, targeting a single-point resolution of 3 μm through charge sharing. It is worth noting that achieving such a resolution with a pixel pitch of 25×25 μm^2 and binary readout is challenging, as highlighted in recent studies (e.g., CE-65 [129]). Reaching this performance may require either a significant reduction in pixel pitch or the implementation of charge measurement to exploit charge sharing more effectively. The barrel region includes three double layers, while the forward region is instrumented with three pairs of double discs on each side of the barrel. An overview of the vertex detector layout is shown in Figure 4.7.

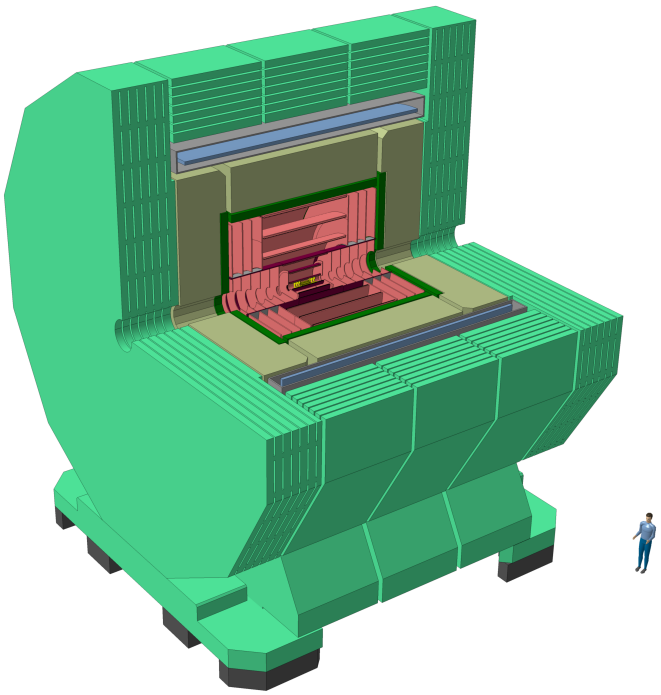

Figure 4.5: Isometric view of the CLD detector[98].

4.3.1 Baseline geometry

The inner radius of the innermost vertex barrel layer is determined by the radius and thickness of the central beam pipe, which are set by MDI constraints [130]. Consequently, this layer is positioned at R = 17.5 mm. The positions of the subsequent vertex barrel layers were derived by scaling down the layout of the CLICdet [99] vertex detector, resulting in radii of R = 37 mm for the second layer and R = 57 mm for the third. The nominal CLD geometry [98] includes a beam pipe with a radius of 15 mm, made entirely of beryllium, with a thickness of 1200 μm. Including the cooling fluid, this corresponds to approximately 0.47% of X/X_0, as published in the FCC Conceptual Design Report (CDR) [82]. Further details on the dimensions of the vertex detector barrel layers used in the simulation model are given in Table 4.3.

The vertex detector employs high-granularity silicon sensors with pixel dimensions of 25 × 25 μm^2 and a sensor thickness of 50 μm. By exploiting charge sharing between neighbouring pixels, the design aims to achieve a single-point spatial resolution of 3 μm.

The forward region of the vertex detector includes three discs on each side of the interaction point, with each disc implemented as a double-layer structure. Positioned at distances of 160, 230, and 300 mm from the IP, the discs are assembled from eight trapezoidal modules that together approximate a circular shape. Their inner radii are designed to comply with the 150 mrad cone reserved for MDI components [130]. The dimensions of the forward vertex discs are detailed in Table 4.2, and Figure 4.6a, 4.6b, 4.7 illustrate an example of the petal arrangement used in the simulation.

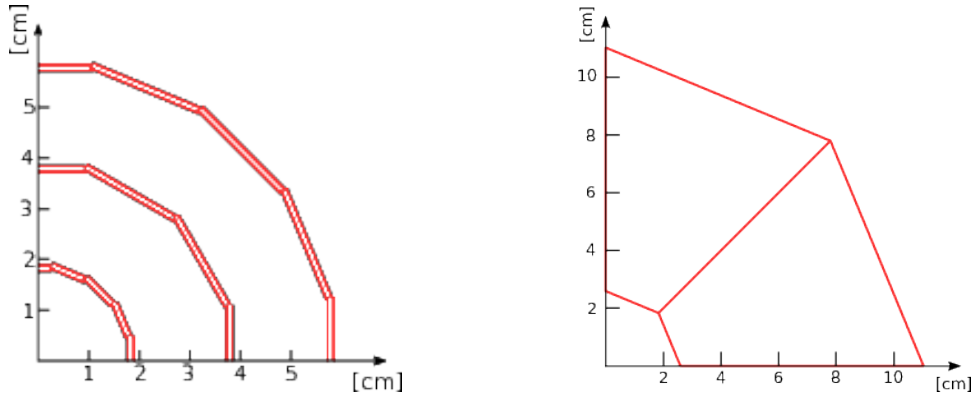

(a) Schematic view of the double layers in the vertex barrel, in the transverse (x,y) plan[98].

(b) Schematic view of the first vertex forward disc in the transverse (x,y) plan [98].

Figure 4.6

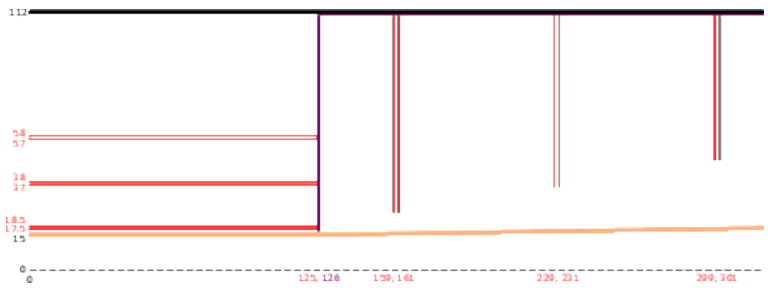

Figure 4.7: Sketch of the CLD vertex detector, representing a quarter of the detector in the longitudinal (z,r) plan. Dimensions are in mm, with the vacuum beam pipe highlighted in orange [98].

Barrel layers	Inner radius [mm]	No. of staves	Stave width [mm]
1 – 2	17.5 – 18.5	16	7.3
3 – 4	37 – 38	12	20.2
5 – 6	57 – 58	16	23.1

Table 4.1: Vertex barrel layout for **CLD baseline geometry**

Vertex disc	Inner radius [mm]	Outer radius [mm]
1	24	102
2	34.5	102
3	45	102

Table 4.2: Dimensions of the vertex discs for **CLD baseline geometry**

4.4 CLD tracking Detector

Particle tracking is the process of reconstructing the trajectories of charged particles as they traverse a particle detector. This task involves the measurement of position coordinates at various points along the particle's trajectory, typically through the use of sensitive detectors and their associated readout electronics.
Accurate particle tracking is essential for a wide range of physics analyses. Whether in the context of searches for new particles or precision measurements of known particles, tracking plays a central role in identifying and characterising the final-state particles produced in high-energy collisions.
Overall layout of the CLD tracking system illustrated in Figure 4.8.
The studies and measurements presented in this section refer to the previous baseline configuration of the CLD detector.

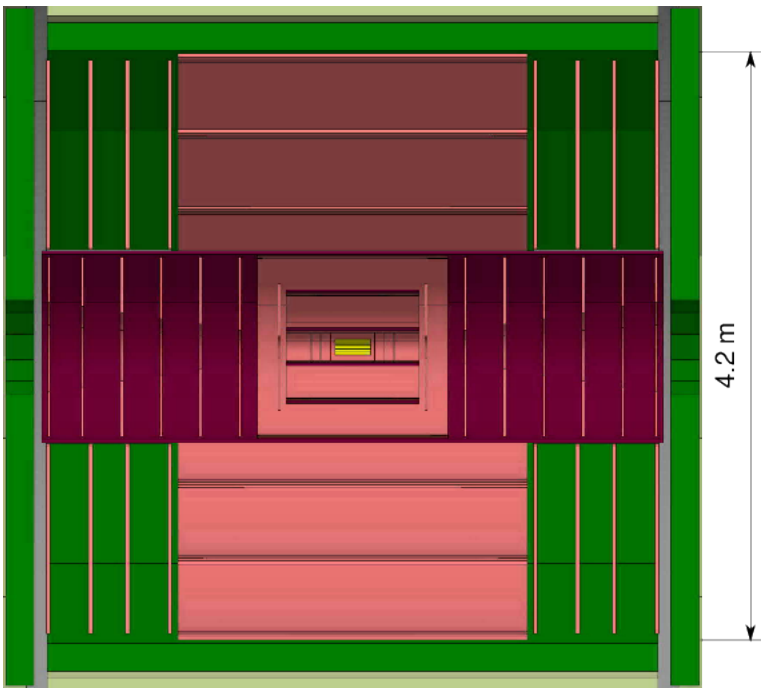

Figure 4.8: Overall layout of the CLD tracking system: the vertex barrel detector is shown in yellow, the tracking layers in lighter red. The area in darker red illustrates the main support tube for the inner tracking region and the vertex detector. The surrounding ECAL is shown in green [98].

Similar to CLICdet [99], the CLD concept[98] features an all-silicon tracker, supported by a central tube that holds the inner tracking region, including the vertex detector. The inner tracker consists of three barrel layers and seven forward discs, while the outer tracker adds another three barrel layers and four discs. The overall layout of the CLD silicon tracker is shown in Figure 4.9.

The silicon sensors used throughout the tracker vary by region to meet specific performance requirements. In both the inner and outer barrel, as well as in the outer tracker discs, all modules are equipped with 30×30 mm^2 silicon sensors. For the inner tracker discs, where higher spatial granularity is needed due to proximity to the interaction point, smaller 15×15 mm^2 sensors are used.

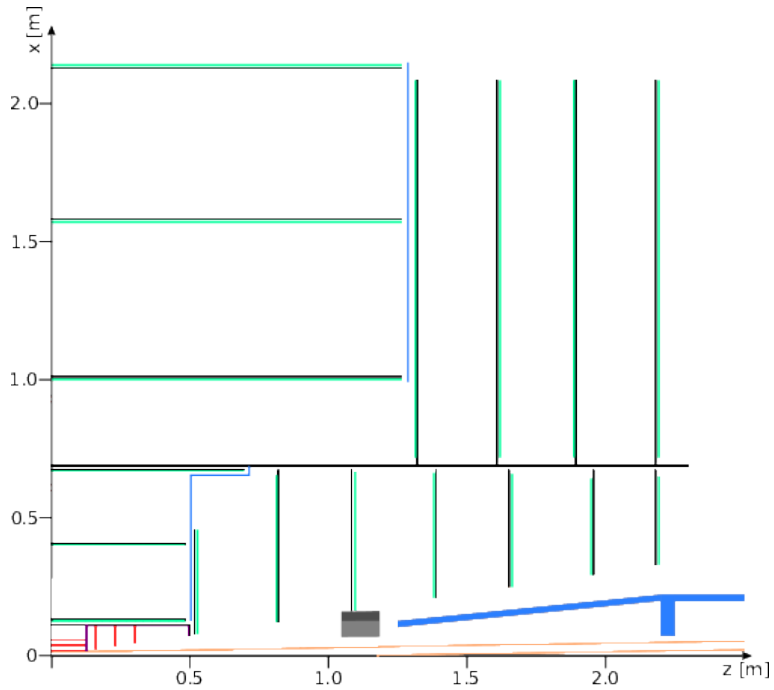

Figure 4.9: Overall layout of the CLD tracking system: the vertex barrel detector is shown in yellow, the tracking layers in lighter red. The area in darker red illustrates the main support tube for the inner tracking region and the vertex detector.

4.4.1 Baseline geometry

The tracking volume extends to a half-length of 2.2 m and reaches a maximum radius of 2.1 m. This larger radius enables the CLD tracking system, operating with a 2 T magnetic field, to achieve a momentum resolution comparable to that of the CLICdet [99] tracker, which uses a 4 T field and a 1.5 m radius. The main support tube has inner and outer radii of 0.686 m and 0.690 m, respectively, and a half-length of 2.3 m. The layout also accommodates the 150 mrad cone allocated for beamline and MDI equipment [130]. A detailed summary of the tracker geometry is provided in Table 4.3 and Table 4.4 for the barrel and disc regions, respectively.

4.5 Calorimetry

The CLD calorimeter system is designed to support high-granularity particle flow reconstruction, a global event reconstruction technique that combines information from all subdetectors. Particle Flow aims to reconstruct the four-momenta of all visible particles by using tracking and calorimetric information for charged particles (which carry about 60% of the jet energy), and calorimetric

Layer No.	Name	R [mm]	L/2 [mm]
1	ITB1	127	482
2	ITB2	400	482
3	ITB3	670	692
4	OTB1	1000	1264
5	OTB2	1568	1264
6	OTB3	2136	1264

Table 4.3: Main parameters of the tracker barrel layout, radius R and half-length L/2. ITB and OTB denote inner and outer tracker barrel, respectively, for **CLD baseline geometry** [98]

Disc No.	Name	Z [mm]	R_{in} [mm]	R_{out} [mm]
1	ITD1	542	79.5	457
2	ITD2	808	123.5	652
3	ITD3	1093	165	663
4	ITD4	1377	207.5	660.5
5	ITD5	1661	249.5	657
6	ITD6	1946	293	640
7	ITD7	2190	330	647
8	OTD1	1310	718	2080
9	OTD2	1617	718	2080
10	OTD3	1883	718	2080
11	OTD4	2190	718	2080

Table 4.4: Main parameters of the tracker discs. ITD and OTD denote inner and outer tracker discs, respectively, for **CLD baseline geometry** [98]

measurements for photons and neutral hadrons. This approach enables a jet energy resolution of 3–4%, sufficient to distinguish W and Z bosons on an event-by-event basis. The reconstruction is performed using dedicated software such as `PandoraPFA` [131]. Based on studies from CALICE [132] and CLICdet [99], which employ similar calorimeter designs, a time resolution of a few nanoseconds per hit is expected, enabling bunch-crossing identification and background suppression. Although current simulations show limited sensitivity to beam-induced backgrounds, even without timing cuts, future physics studies may further investigate the role of time-based selections.

4.5.1 Electromagnetic Calorimeter

The ECAL features high spatial granularity, with a transverse cell size of 5×5 mm^2, enabling the separation of nearby energy deposits in dense jets. Its baseline design is a silicon–tungsten (Si–W) sampling calorimeter, where alternating layers of tungsten serve as absorbers and silicon sensors detect the resulting electromagnetic showers. The total depth of the calorimeter is approximately 22–23 radiation lengths (X_0), effectively containing high-energy showers and minimising leakage.

Simulation studies for CLICdet [99] have shown that a configuration with 40 identical layers, each consisting of a 1.9 mm tungsten absorber, achieves excellent photon energy resolution across a wide energy range. This layout is adopted for the CLD simulation model [98]. The ECAL structure, shown in Figure 4.10 and detailed in Table 4.6, includes 3.15 mm spacing between absorber plates to accommodate silicon sensors and readout electronics. The layer sequence starts with a tungsten absorber and alternates with silicon sensor layers, ending with a final sensor/electronics layer.

The overall ECAL dimensions are listed in Table 4.5. In a future update of the CLD design, the forward acceptance may be extended by reducing the endcap inner radius, in line with the

most recent MDI layout [130], which reserves a 100 mrad cone for accelerator components instead of the previous 150 mrad.

ECAL barrel r_{min}	2150
ECAL barrel r_{max}	2352
ECAL barrel z_{max}	2210
ECAL endcap z_{min}	2307
ECAL endcap z_{max}	2509
ECAL endcap r_{min}	340
ECAL endcap r_{max}	2455

Table 4.5: ECAL layout as implemented in the simulation model (dimensions in mm), for **CLD baseline geometry** [98]

Function	Material	Layer thickness [mm]
Absorber	tungsten alloy	1.90
Insulator	G10	
Connectivity	mixed (86% Cu)	0.15
Sensor	silicon	0.50
Space	air	0.10
PCB	mixed (86% Cu)	1.30
Space	air	0.25
Insulator	G10	0.75
Total between W plates		3.15
Total SiW layer		5.05

Table 4.6: Parameters for the ECAL layer stack as implemented in the simulation model, with a total of 40 SiW layers, for **CLD baseline geometry** [98]

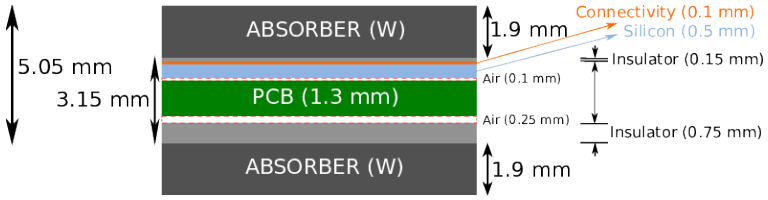

Figure 4.10: Schematic drawing of the ECAL segmentation as implemented in the simulation model [98].

4.5.2 Hadronic Calorimeter

The CLD HCAL adopts the same structure and granularity as the CLICdet [99] design, based on extensive optimisation studies performed for detectors at both ILC [124] and CLIC [125]. It uses 19 mm thick steel absorber plates interleaved with 3 mm thick polystyrene scintillator tiles, arranged in 7.5 mm gaps to accommodate the sensitive layers and their cassettes, similar to the CALICE [132] design for ILD [128]. The tiles, sized 30 × 30 mm^2, are read out via analogue SiPMs. The HCAL includes 44 layers, corresponding to a depth of about 5.5 interaction lengths (λ_i), resulting in a total depth of $\sim$ 6.5 λ_i when combined with the ECAL. This depth has been shown to be adequate for hadronic showers in previous ILC studies [124]. The HCAL geometry and dimensions are detailed in Table 4.7 and Table 4.8, with the layer structure illustrated in Figure 4.12 and a

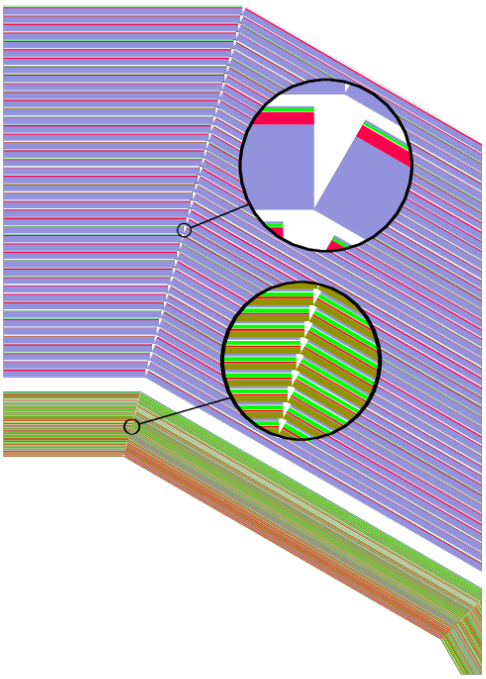

Figure 4.11: Illustration of the ECAL and HCAL implementation in the simulation model, focusing on the junction between two barrel sectors of the dodecagonal geometry. In the ECAL, tungsten absorber layers appear in olive green, silicon sensors in red, G10 insulators in purple, PCBs in green, and air gaps in white. The HCAL shows steel absorbers in blue (with thinner sheets forming the cassette), scintillator layers in red, and again, green and white representing PCB and air, respectively [98].

barrel section shown in Figure 4.11. In the simulation, the part of the HCAL endcap surrounding the ECAL is modeled separately as the "HCAL ring." As with the ECAL, future updates to the CLD design may reduce the HCAL endcap inner radius to match the updated MDI [130] layout and improve forward acceptance.

HCAL barrel r_{min}	2400
HCAL barrel r_{max}	3566
HCAL barrel z_{max}	2210
HCAL endcap z_{min}	2530
HCAL endcap z_{max}	3705
HCAL endcap r_{min}	340
HCAL endcap r_{max}	3566
HCAL ring z_{min}	2353.5
HCAL ring z_{max}	2539
HCAL ring r_{min}	2475
HCAL ring r_{max}	3566

Table 4.7: HCAL overall layout as implemented in the simulation model (dimensions in mm), for **CLD baseline geometry** [98].

Function	Material	Layer thickness [mm]
Absorber	steel	19
Space	air	2.7
Cassette	steel	0.5
PCB	mixed	0.7
Conductor	Cu	0.1
Scintillator	polystyrene	3
Cassette	steel	0.5
Total between steel plates		7.5
Total Fe-scintillator layer		26.5

Table 4.8: Parameters for the HCAL layer stack as implemented in the simulation model, with a total of 44 Fe-Scintillator layers, for **CLD baseline geometry** [98].

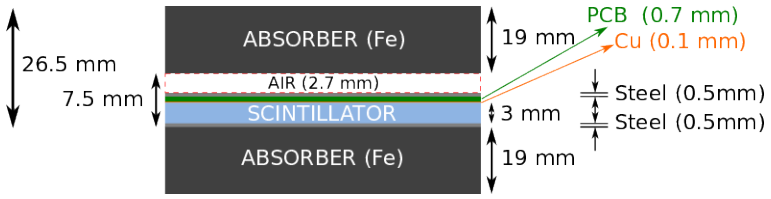

Figure 4.12: Schematic drawing of HCAL segmentation as implemented in the simulation model [98].

4.6 Magnet System

The magnet system of the CLD detector provides the magnetic field required to bend charged particle trajectories and enable precise momentum reconstruction. It consists of a superconducting solenoid generating a uniform axial field and a surrounding return yoke that contains the magnetic flux and supports the integration of muon detectors. The design is adapted from CLICdet, with modifications to accommodate the specific requirements of the FCCee environment, such as lower magnetic field strength and compatibility with the machine-detector interface (MDI) constraints.

4.6.1 Superconducting Solenoid

The CLD detector [98] operates with a 2 T solenoidal magnetic field, constrained by MDI [130] requirements, matching the design of other FCCee detectors [82]. In the simulation model, this 2 T field is uniform inside the superconducting coil, while the return field in the yoke barrel reaches 1 T in the opposite direction. No magnetic field is currently assumed in the yoke endcaps or beyond the yoke. The solenoid's implementation follows the parameters listed in Table 4.9, with a material budget of approximately 0.7 interaction lengths (λ_i).

Element	Material	z_{min} [mm]	z_{max} [mm]	r_{min} [mm]	r_{max} [mm]
Inner Barrel	Steel	0	3705	3719	3759
Coil	Aluminium	0	3467	3885	3975
Outer Barrel	Steel	0	3705	4232	4272
End plates	Steel	3665	3705	3759	4232

Table 4.9: Description of the solenoid elements (coil and cryostat) as implemented in the simulation. For all elements the material, the longitudinal extent in one half of the detector $z_{min/max}$ and the radial extent $r_{min/max}$ are given [98].

4.6.2 Yoke and Muon Detectors

The iron return yoke of the CLD detector [98] is segmented into three barrel rings and two endcaps, as illustrated in Figure 4.13. Its thickness is reduced compared to CLICdet [99], reflecting the lower 2 T solenoid field. The muon system consists of six detection layers, as in CLICdet, with an additional seventh layer placed close to the coil in the barrel region to serve as a potential tail catcher for hadronic showers. The muon detectors are designed as RPCs with 30×30 mm^2 cells. A 40 mm gap between steel layers provides sufficient space for their integration. Following the approach used in CMS [133] and CLICdet, the yoke and muon detector (represented in Figure 4.14) layers are staggered to avoid alignment gaps.

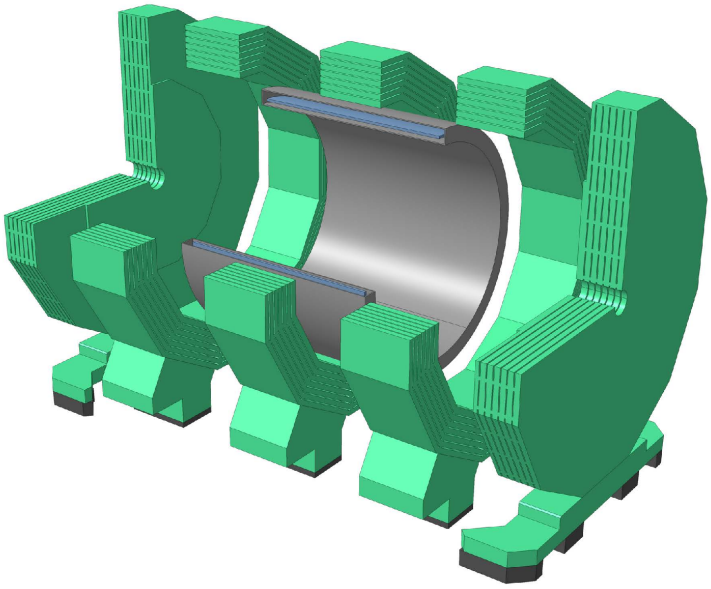

Figure 4.13: Segmentation of the iron return yoke of CLD into endcaps and three barrel rings [98].

4.7 Tracking Performances at CLD

Following the detailed description of the tracking system layout, this section presents the expected tracking performance of the CLD detector [98], as evaluated through full simulation studies. Key aspects include the efficiency and precision of track reconstruction, momentum and impact parameter resolution, and the detector's robustness in the presence of background. These performance metrics are essential for achieving the physics goals of FCCee [82], particularly in reconstructing charged particles with high accuracy across a wide momentum and angular range. The studies indicate that the CLD tracking system is well suited to meet these requirements, under the realistic conditions provided by full simulation.

4.7.1 K4DetPerformance Framework

The ability to accurately reconstruct particle tracks directly influences measurements of important quantities such as momentum, energy, and the vertex position. Given the complexity and the variety of particle interactions in the high-energy environment of FCC-ee, assessing the performance of the tracking system is a necessary step in understanding the potential of a detector.

The `k4DetPerformance` framework has been developed in the context of this PhD work, to provide a systematic and reproducible methodology for evaluating the tracking performance of

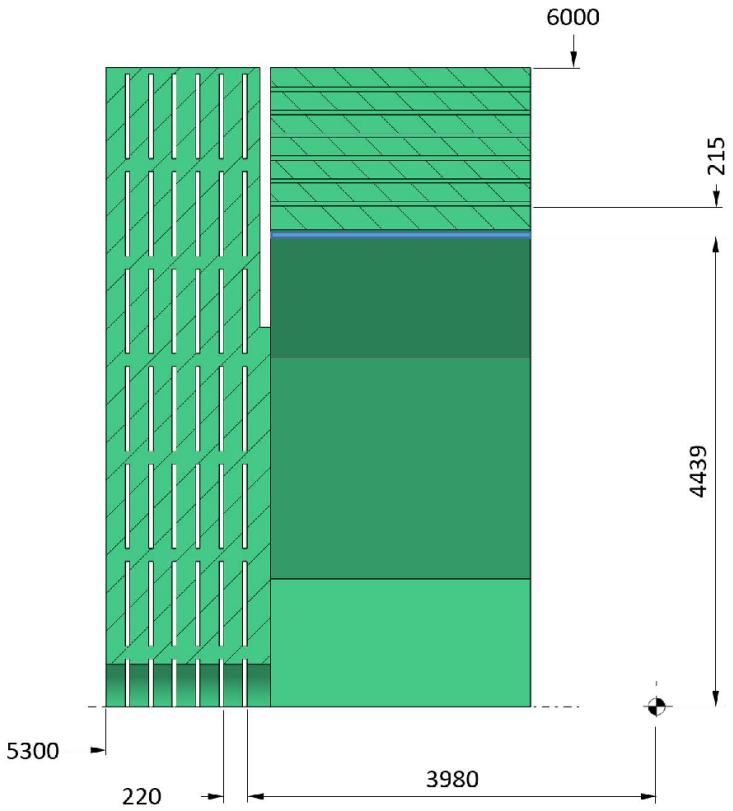

Figure 4.14: Schematic cross section of the muon system layout in the yoke of CLD. Dimensions are in mm. The staggering of the layers is not visible in this cross section [98].

detectors such as CLD. By offering a suite of performance metrics, this framework aids in the characterisation of a detector's tracking capabilities, allowing for detailed comparisons across different detector concepts. This is particularly important when exploring new designs or optimizing detector parameters.

Developing the `k4DetPerformance` framework was not a straightforward task, and the early stages of this work were marked by several technical challenges. While the full simulation for the CLD detector was functional, the reconstruction step initially failed to produce valid outputs. These issues required extensive debugging in collaboration with experts and were eventually resolved. At the same time, it became evident that no existing framework was available for evaluating tracking performance within the FCC software ecosystem. This gap motivated the development of the `k4DetPerformance` framework, which was built from the ground up and later integrated into the `Key4HEP` software [134] suite. In parallel, some CLD geometry descriptions were affected by inconsistencies and bugs, which also required significant debugging efforts to ensure a reliable setup for performance studies. These developments ultimately led to a robust framework that is now routinely used for CLD tracking evaluations.

4.7.1.1 Overview

The `k4DetPerformance` framework[2] operates on data formatted according to the `EDM4hep` [135] standard, which allows seamless integration with other software tools used in the `Key4HEP` project. `k4DetPerformance` is also built on `FCCAnalyses` [136] for data handling and analysis. This modular structure ensures that the framework can be adapted to various types of tracking systems and

[2] github.com/key4hep/k4DetPerformance

configurations, providing a flexible platform for testing new detector concepts.

The `k4DetPerformance` framework has been applied to the CLD detector to evaluate its tracking performance. In these studies, the full CLD simulation setup, including realistic beam backgrounds and detector parameters, were used to generate performance results. These results, including momentum resolution, and impact parameter resolution, provide valuable insights into the strengths and limitations of the CLD tracking system.

4.7.1.2 Full Simulation and Digitisation Setup

The tracking performance results presented in this chapter are based on a full simulation of the CLD detector using the `Key4HEP` software stack [134]. The detector simulation relies on `Geant4` [137], which accurately models particle interactions with matter, including the full detector geometry, material composition, and magnetic field configuration. All relevant subdetectors are included, providing realistic conditions.

Monte Carlo (MC) events are generated over a broad range of particle types and kinematic conditions, and are passed through the full reconstruction chain. While a complete digitisation of detector signals is not yet implemented, a simplified approach is used: instead of simulating detailed effects such as charge deposition or signal shaping, a Gaussian smearing is applied to the MC hit positions. The smearing width corresponds to the spatial resolution defined in the detector geometry. This method offers a fast and consistent approximation of position uncertainties, though it does not capture the full complexity of the actual detector response. More advanced digitisation models may be incorporated in the future for increased realism, in particular to account for cluster size broadening in tracks with large incidence angles.

4.7.1.3 Track-Truth Matching Procedure

One of the key steps in tracking performance evaluation is the track-truth matching procedure. This process involves associating reconstructed tracks with the corresponding true particles in the simulation. The `k4DetPerformance` framework defines matching criteria based on several factors, including the number of shared hits between reconstructed tracks and true particles.

This matching procedure ensures that performance metrics such as efficiency and fake rate are accurately calculated, as it allows the framework to differentiate between genuine tracks, fake tracks, and duplicate tracks. The matching is crucial for understanding the detector's ability to identify and correctly reconstruct tracks from different particle species.

4.7.1.4 Tracking resolution

Tracking resolution studies are performed using single-particle events generated with a particle gun. In each case, reconstructed tracks are matched to the corresponding simulated particles. Resolution distributions are defined as $\sigma(\Delta = \text{reco} - \text{true})$, and as $\sigma(\Delta = \text{reco} - \text{true})/\text{true}$ for the momentum p and transverse momentum p_T. Each resolution measurement is based on a sample of 10,000 events per configuration.

4.8 Tracking Performance Studies with CLD Detector

The FCC is a proposed high-energy circular collider, its first phase, FCCee, will operate as a high-luminosity e^+e^- collider, enabling precision measurements and searches for new physics.

To successfully carry out this ambitious program, the detectors will need to achieve high performance. The vertex detector in particular, likely equipped with CMOS pixel sensors [138], will need to enable impact parameter measurement resolution at the vertex on the order of 5 microns, with a material budget of less than $\sim$0.15% X_0 per layer, while being capable of handling the data

flux generated by beam-induced background noise. The vertex detector will play a crucial role in the identification of heavy flavours (b and c quarks, tau leptons), enabling jet charge measurements and the reconstruction of low-momentum tracks. However, fine optimisation remains to be done and can only be achieved through a comprehensive analysis of the physics where the vertex detector plays a predominant role, such as in analyses where the final states contain heavy-flavour quarks or displaced vertices.

The objectives of this study are to define different geometries for the vertex detector and to evaluate its physical performances in terms of tracking. This study would have to be completed for vertexing, flavour identification, and comprehensive analysis. To achieve these objectives, a full simulation is necessary, therefore the CLD [98] concepts is used for this studies.

4.8.1 Tracking Performance with the Baseline CLD Geometry

To evaluate the tracking capabilities of the CLD detector, performance studies have been conducted using the geometry defined in the FCC CDR [82].

In this section, tracking resolutions are presented for key parameters that characterize the reconstructed tracks: the transverse (d_0) and longitudinal (z_0) impact parameters, the azimuthal angle difference ($\Delta\phi_0$), the solid angle resolution ($\Delta\Omega$), the track curvature (expressed via $\tan\lambda$), and the angular variables ϕ and θ. In addition, momentum resolutions are shown for both the total momentum (p) and transverse momentum (p_T).

These quantities are studied using single-particle samples of muons, electrons, and charged pions, which provide a clean environment to isolate the intrinsic performance of the tracking system. These three particle types are used because they interact differently with the detector material: muons behave as minimum ionising particles, electrons are subject to bremsstrahlung, and pions can undergo hadronic interactions. Comparing them helps identify the specific effects of these interactions on tracking performance. However, in practice, muons alone are often sufficient to characterise the core tracking performance, while electrons and pions provide complementary insights into material effects and secondary interactions. Resolution plots are first shown as a function of particle momentum, Figure 4.15, 4.16 ,4.17, 4.18, followed by their dependence on the polar angle θ, Figure 4.19, 4.20 ,4.21, 4.22, offering a detailed view of the detector's response across different kinematic regimes.

4.8.2 Impact of a More Realistic Beam Pipe and Vertex Geometry

The nominal CLD geometry includes a cylindrical beryllium beam pipe with a radius of 15 mm and a thickness of 1.2 mm, corresponding to approximately 0.47% of a radiation length (X/X_0), as specified in the Conceptual Design Report (CDR) [82]. Here, X/X_0 denotes the thickness of a material expressed in units of its radiation length X_0, which characterizes the mean distance over which high-energy electrons lose a significant fraction of their energy by bremsstrahlung, or the mean free path for pair production by high-energy photons. A newer version of the geometry introduces a more realistic beam pipe featuring a cooling layer and a reduced radius of 10 mm [139]. This modification increases the material budget to 0.61% of X/X_0, a 33% rise compared to the baseline, but enables a more compact detector layout.

The reduced beam pipe radius allows the vertex detector to be positioned closer to the interaction point. This leads to a new vertex detector configuration with smaller radii for the first two barrel layers and a shorter overall length, while keeping the stave design unchanged. However, the choice of the inner beam pipe radius is tightly constrained by the level of beam-induced background, in particular from incoherent pair production in the strong electromagnetic fields of the colliding beams [75, 82]. Reducing the beam pipe radius to a too small values could lead to a significant increase of the hit density and occupancy in the vertex detector, which could in turn degrade the

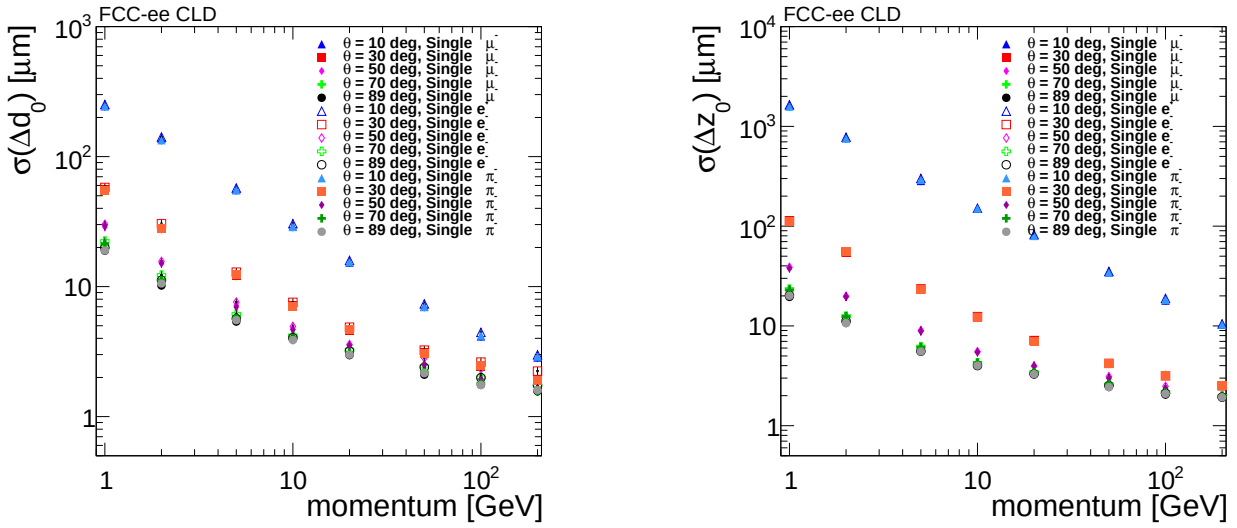

(a) Transverse impact parameter d_0 resolution

(b) Longitudinal impact parameter z_0 resolution

Figure 4.15: Transverse (d_0) and longitudinal (z_0) impact parameter resolutions as a function of momentum for single muons, electrons, and pions simulated in the CLD baseline geometry. The resolutions are derived from the standard deviation of the residual distributions between reconstructed and true parameters at the origin.

tracking performance and impact parameter resolution. Table 4.10 shows that, in the updated layout, the first two double layers are positioned closer to the interaction point. This configuration may improve the vertex resolution at small radii, while remaining, according to current studies, compatible with the anticipated background levels.

Vertex Barrel [mm]	R_1	R_2	R_3	L
CLD baseline geometry	17.5	37	57	125
CLD with new beam pipe	**13.0**	**35**	**57**	**109**

Table 4.10: Vertex detector dimension for CLD baseline geometry and CLD with new beam pipe

Figure 4.23, A.25, A.26, A.27 show the resolution of these parameters as a function of particle momentum for both the nominal and updated geometries, while Figure 4.24, A.28, A.29, A.30 shows the same resolutions as a function of the polar angle θ.

The results reveal that the improved spatial proximity of the vertex detector more than compensates for the increase in beam pipe material. For instance, as seen in the d_0 resolution (also highlighted in Figure 4.24a), the newer geometry shows an improvement of up to 20% at 10 GeV compared to the baseline. This trend is consistently reflected across most tracking parameters, particularly in the low-momentum and forward regions where vertex resolution plays a dominant role.

The choice of the beam pipe radius is constrained by beam-induced backgrounds, in particular incoherent pair production. Reducing the radius below approximately 15 mm at the Z-pole is expected to lead to hit densities that could compromise track reconstruction efficiency. While a 10 mm radius would improve the impact parameter resolution, its implementation remains contingent on the development of effective mitigation strategies for background suppression.

4.8.3 Impact of vertex detector spatial resolution

The spatial resolution of the vertex detector plays a crucial role in the overall tracking performance, particularly for the determination of impact parameters such as the transverse (d_0) and longitudinal

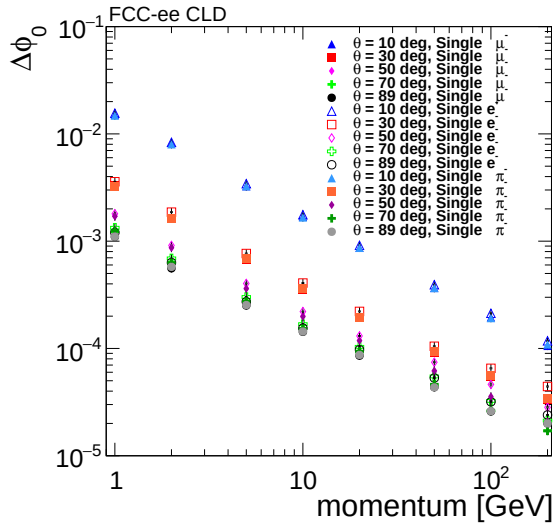

(a) Residual on the azimuthal angle at the point of closest approach ϕ_0 resolution

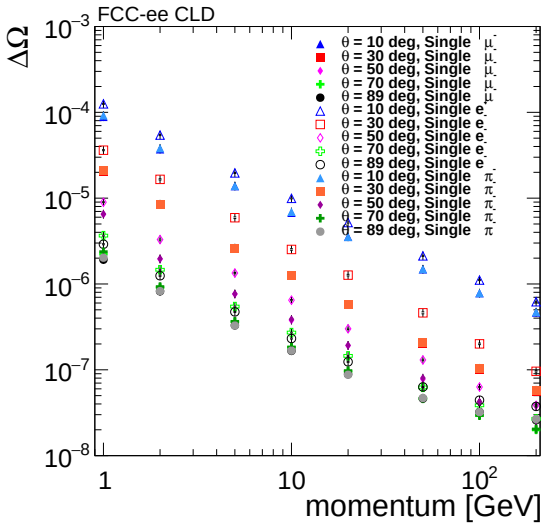

(b) Curvature Ω resolution

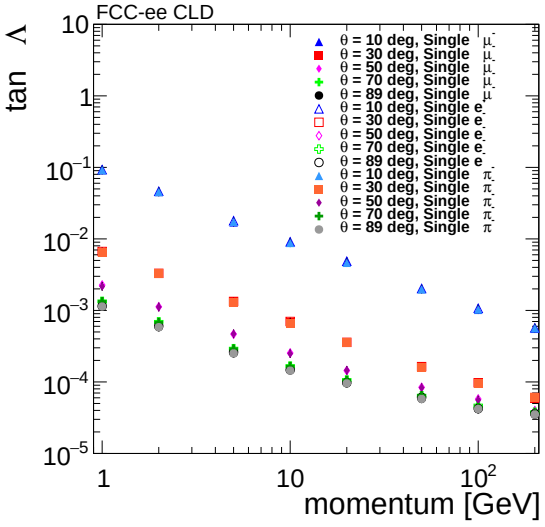

(c) track dip angle $\tan\lambda$ resolution

Figure 4.16: Resolution of the track parameters ϕ_0, Ω, and $\tan\lambda$ as a function of momentum for single muons, electrons, and pions simulated in the CLD baseline geometry. The resolutions are obtained from the standard deviation of the residual distributions between reconstructed and true track parameters at the point of closest approach.

(z_0) distances from the track to the interaction point. A better position resolution directly improves the measurement of hit positions along the track, which in turn enhances the accuracy of the reconstructed trajectory. This leads to a more precise determination of where the track originates, which is essential for reconstructing displaced vertices and for efficient flavour tagging.

To evaluate the sensitivity of the CLD tracking system to the vertex detector's intrinsic resolution, studies have been performed using simulated single-muon samples while varying the spatial resolution of the vertex detector hits. The baseline resolution of 3 μm is compared to degraded configurations with 5 μm and 7 μm resolution, as well as an idealised case with 1 μm resolution.

Figure 4.25, A.31, A.32, A.33 and Figure 4.26, A.34, A.35, A.36 present the tracking resolution for all key track parameters as a function of momentum and polar angle θ, respectively. As

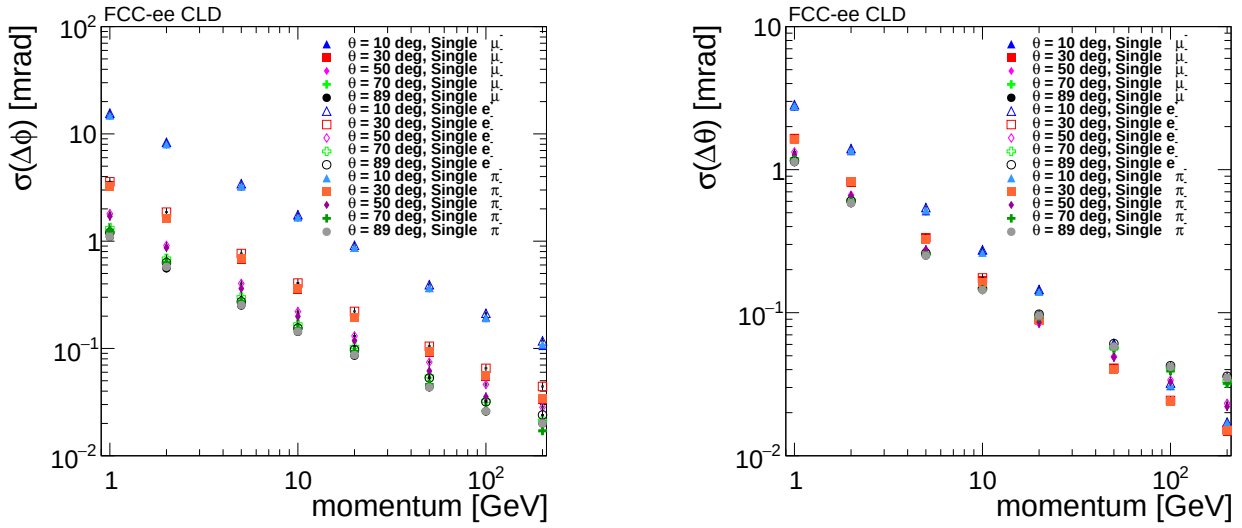

(a) Azimuthal angle ϕ resolution

(b) Polar angle θ resolution

Figure 4.17: Resolution of the reconstructed azimuthal (ϕ) and polar (θ) angles as a function of momentum for single muons, electrons, and pions simulated in the CLD baseline geometry. The resolutions are derived from the standard deviation of the residual distributions between reconstructed and true directions at the point of closest approach.

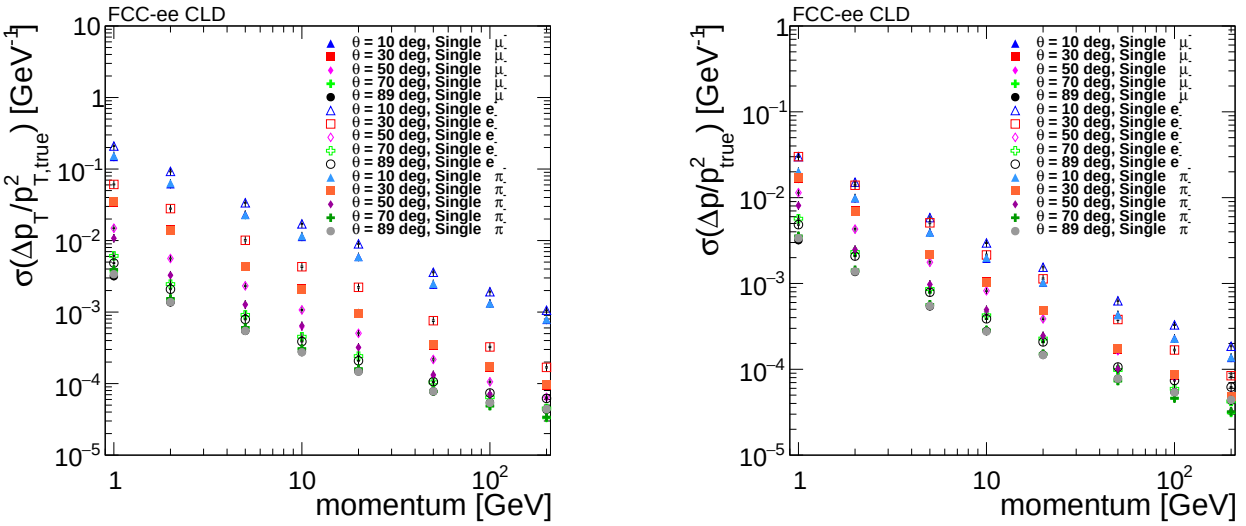

(a) Transverse momentum resolution

(b) Momentum resolution

Figure 4.18: Transverse momentum (p_T) and total momentum (p) resolutions as a function of momentum for single muons, electrons, and pions simulated in the CLD baseline geometry. The resolutions are obtained from the relative width of the $(p_{\text{reco}} - p_{\text{true}})/p_{\text{true}}$ distributions.

expected, the most pronounced effects are observed for the d_0 and z_0 resolutions, especially at high momentum and in the central detector region where vertex resolution is most critical.

These results highlight that a degradation in vertex spatial resolution leads to a noticeable deterioration in impact parameter resolution, whereas parameters such as ϕ_0, Ω, and momentum (p, p_T) are only mildly affected.

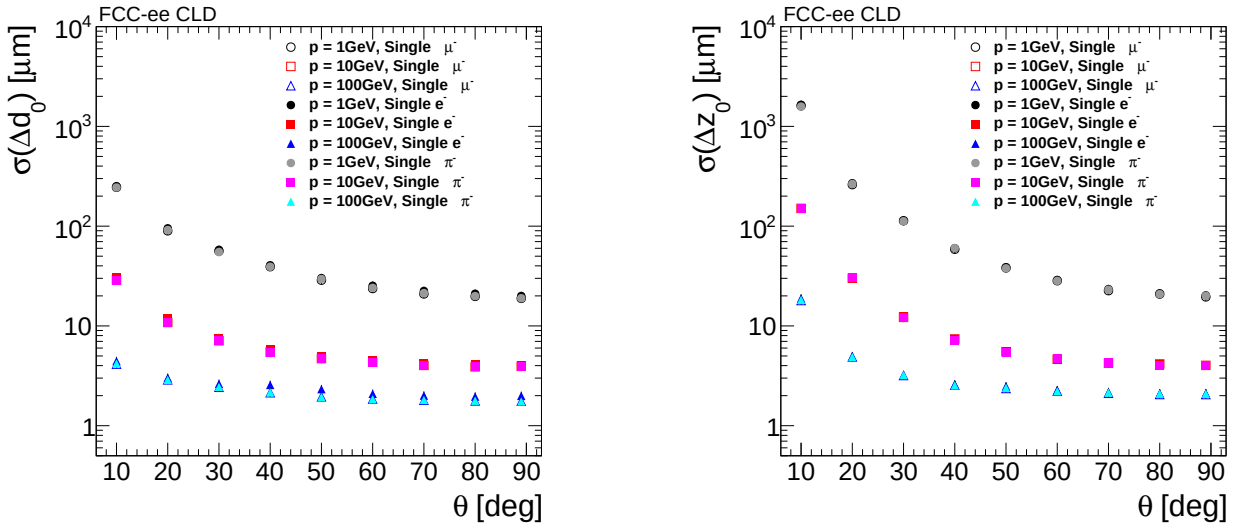

(a) Transverse impact parameter d_0 resolution

(b) Longitudinal impact parameter z_0 resolution

Figure 4.19: Transverse (d_0) and longitudinal (z_0) impact parameter resolutions as a function of the polar angle for single muons, electrons, and pions simulated in the CLD baseline geometry. The resolutions are extracted from the standard deviation of the residual distributions between reconstructed and true parameters.

From the comparison of spatial resolutions, the improvement in impact parameter resolution becomes significant (over 10% improvement) for momenta above 10 GeV, where multiple scattering effects subside, and intrinsic detector resolution dominates. At lower momenta, the resolution remains dominated by multiple scattering, rendering improvements in the intrinsic hit resolution less effective.

4.8.4 Impact of a Reduced Tracker Volume for PID Integration

In the baseline CLD design, no dedicated particle identification (PID) system is foreseen. However, ongoing studies are evaluating the potential integration of a Ring Imaging Cherenkov (RICH) detector, such as the ARC concept, within the tracking volume. RICH detectors enable efficient hadron identification by detecting Cherenkov light emitted as charged particles traverse a radiator medium. This functionality could significantly improve the detector's physics reach, particularly in analyses that rely on distinguishing between hadron species.,

The ARC (Aerogel RICH Cellular) concept [140] proposes a compact, low-mass RICH detector suitable for FCCee experiments [141], featuring a pressurized gas radiator and aerogel layers in a cellular, mirror-based layout with a material budget around 10% X_0.

To enable the inclusion of such a system, a more compact tracker layout is being considered. In particular, a modified geometry has been studied that incorporates a reduced beam pipe radius and allocates space for a RICH detector, as described in Section 4.8.3. In this configuration, the outer tracking layers are shifted inward, creating the necessary gap between the tracker and the electromagnetic calorimeter to accommodate the PID system.

This design change has a direct impact on tracking performance, especially in terms of momentum resolution. Equation 4.1 [92] illustrates how the transverse momentum resolution (p_T) depends on several parameters, including the spatial resolution in the transverse plane ($\sigma_{r\phi}$), the magnetic field strength (B_0), the number of tracking layers (N), and critically, the track lever arm (L_0), the radial span over which the particle trajectory is measured. Because L_0 appears quadratically

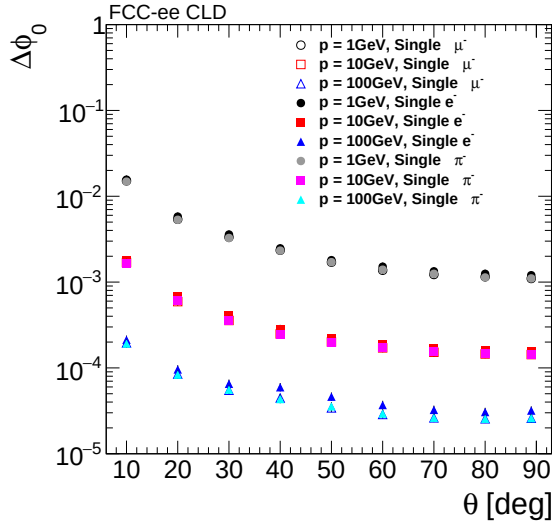

(a) Residual on the azimuthal angle at the point of closest approach ϕ_0 resolution

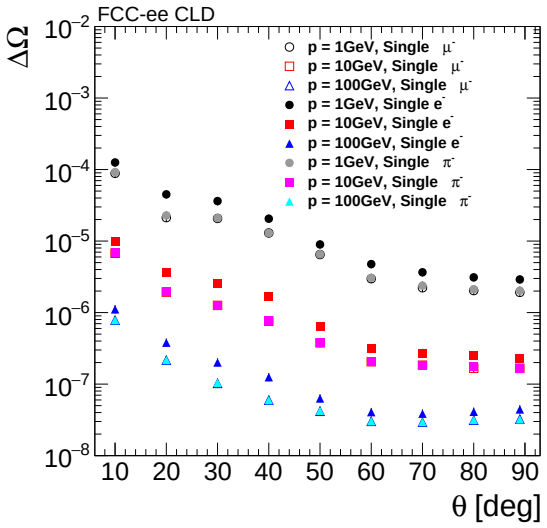

(b) Curvature Ω resolution

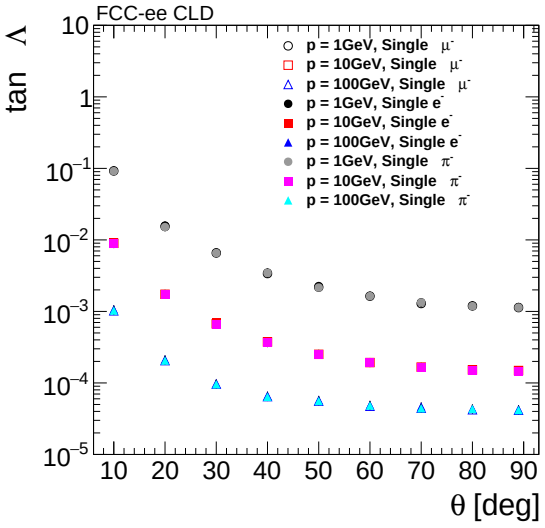

(c) track dip angle $\tan\lambda$ resolution

Figure 4.20: Resolution of the track parameters ϕ_0, Ω, and $\tan\lambda$ as a function of the polar angle for single muons, electrons, and pions simulated in the CLD baseline geometry. The resolutions are extracted from the standard deviation of the residual distributions between reconstructed and true parameters at the point of closest approach.

in the denominator, even modest reductions in this parameter can lead to notable performance degradation.

$$\frac{\Delta p_T}{p_T}|_{res} \approx \frac{12\sigma_{r\phi}p_T}{0.3B_0L_0^2}\sqrt{\frac{5}{N+5}} \tag{4.1}$$

For example, integrating a RICH detector such as ARC reduces the available radial space for tracking, thereby shortening the lever arm. Based on Equation 4.1, a 10 % decrease in L_0 translates to an expected 20 % degradation in p_T resolution. This theoretical expectation aligns well with simulation results, which show an approximate 15 % deterioration in p_T resolution when the PID system is included.

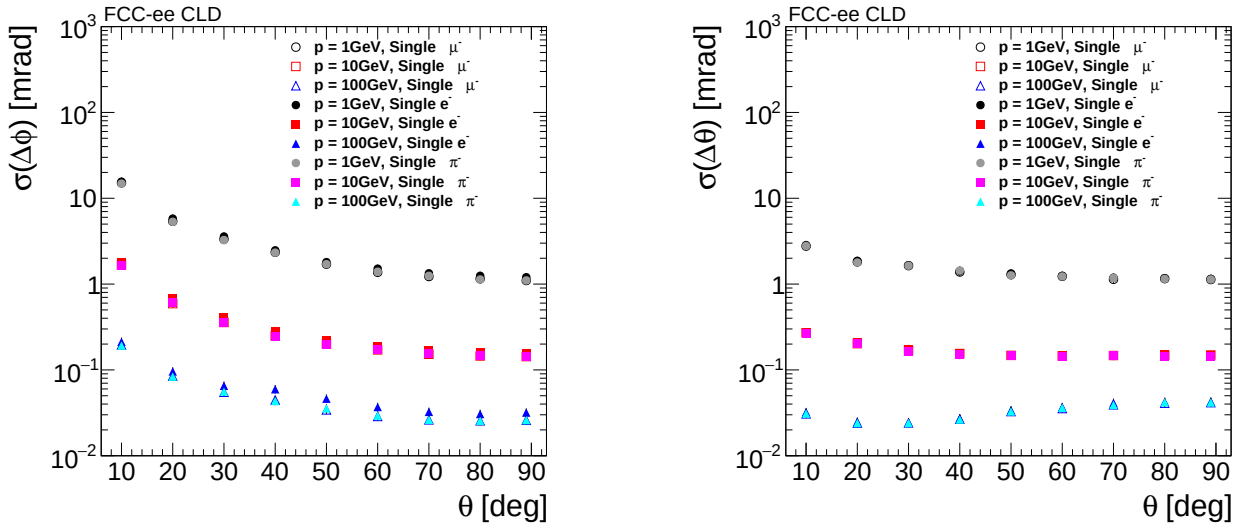

(a) Azimuthal angle ϕ resolution

(b) Polar angle θ resolution

Figure 4.21: Resolution of the reconstructed azimuthal (ϕ) and polar (θ) angles as a function of the polar angle for single muons, electrons, and pions simulated in the CLD baseline geometry. The resolutions are obtained from the width of the residual distributions between reconstructed and true directions.

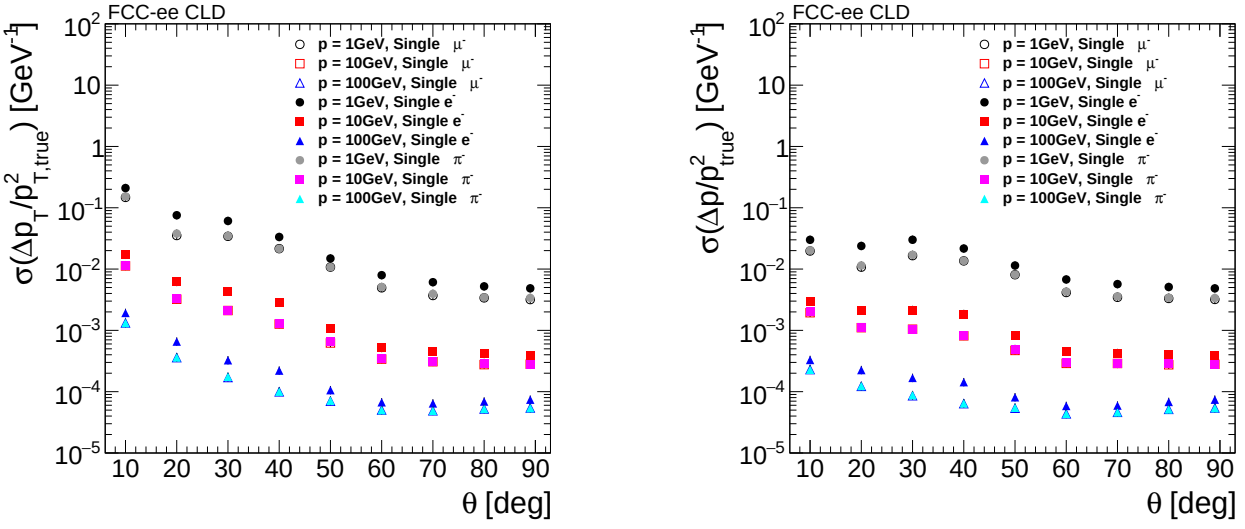

(a) Transverse momentum resolution

(b) Momentum resolution

Figure 4.22: Transverse momentum (p_T) and total momentum (p) resolutions as a function of the polar angle for single muons, electrons, and pions simulated in the CLD baseline geometry. The resolutions are computed from the relative width of the $(p_{\text{reco}} - p_{\text{true}})/p_{\text{true}}$ distributions.

All other aspects of the detector design, such as the material budget and intrinsic spatial resolution of the tracking sensors, remain unchanged. This allows for a focused evaluation of the effect of reduced tracking volume on performance. The revised dimensions of the outer tracker barrel and endcap used in this study are summarised in Table 4.11.

Figure A.37, A.38, A.39, 4.27 and Figure A.40, A.41, A.42, 4.28 show the tracking resolution for key track parameters as a function of particle momentum and polar angle, respectively, comparing

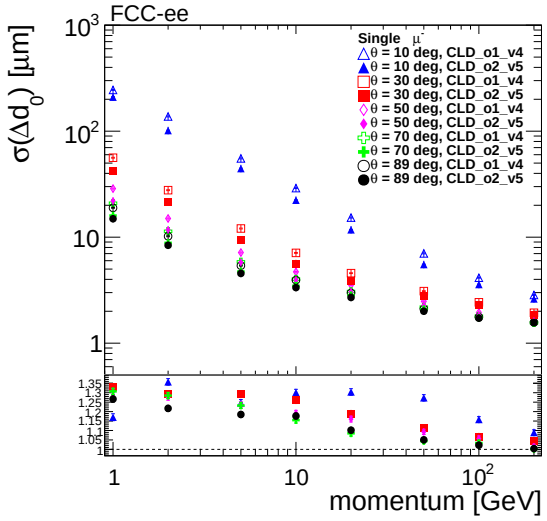

(a) Transverse impact parameter d_0 resolution

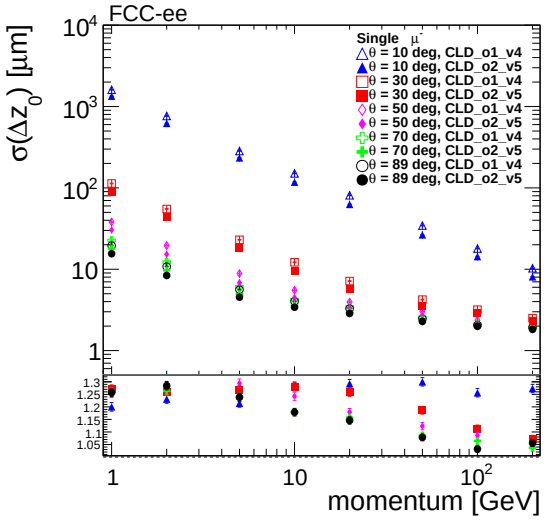

(b) Longitudinal impact parameter z_0 resolution

Figure 4.23: Comparison of the transverse (d_0) and longitudinal (z_0) impact parameter resolutions as a function of momentum for single muons simulated in 2 CLD detector configurations: the baseline geometry and a modified geometry includes a smaller beam pipe radius and an updated vertex detector layout, resulting in improved impact parameter resolutions, particularly at high momentum. The resolutions are computed from the standard deviation of the residual distributions between reconstructed and true parameters.

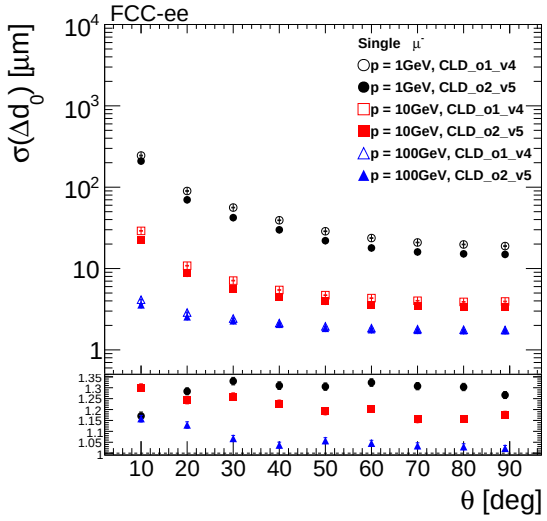

(a) Transverse impact parameter d_0 resolution

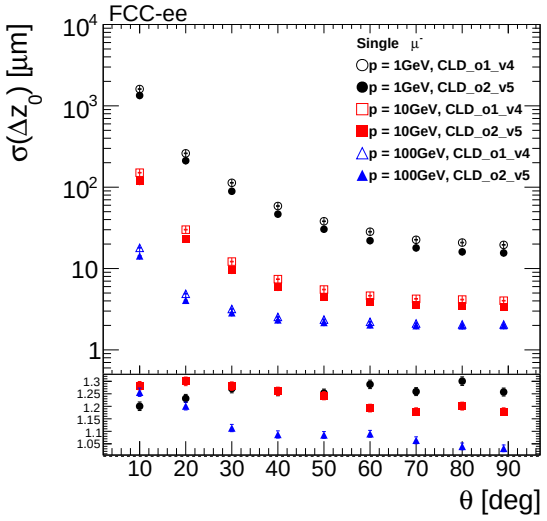

(b) Longitudinal impact parameter z_0 resolution

Figure 4.24: Comparison of the transverse (d_0) and longitudinal (z_0) impact parameter resolutions as a function of the polar angle for single muons in the CLD baseline geometry and in a modified geometry includes a smaller beam pipe radius and an updated vertex detector layout, resulting in improved impact parameter resolutions, particularly at high momentum.

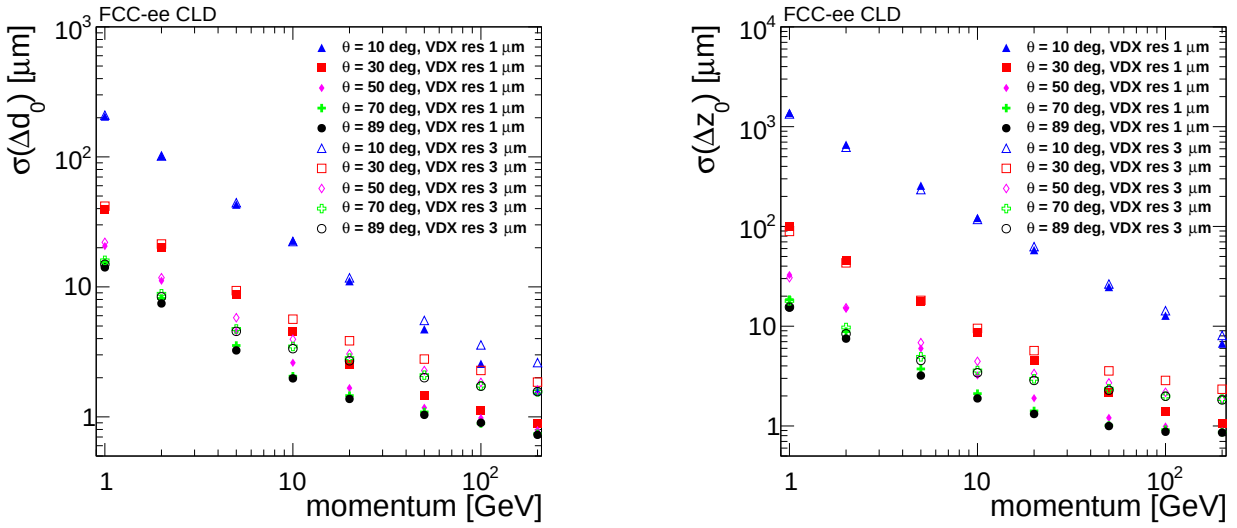

(a) Transverse impact parameter d_0 resolution

(b) Longitudinal impact parameter z_0 resolution

Figure 4.25: Effect of the vertex detector single-point spatial resolution on the transverse (d_0) and longitudinal (z_0) impact parameter resolutions as a function of momentum. Simulations are performed using the new CLD baseline configuration, assuming spatial resolutions of 1 and 3 μm in the vertex detector.

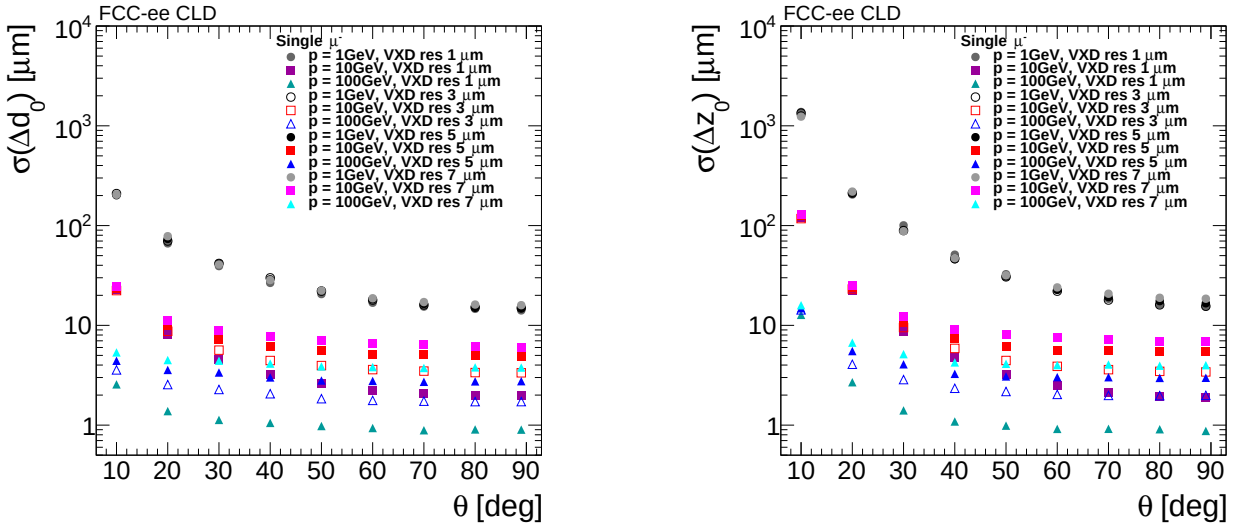

(a) Transverse impact parameter d_0 resolution

(b) Longitudinal impact parameter z_0 resolution

Figure 4.26: Effect of the vertex detector single-point spatial resolution on the transverse (d_0) and longitudinal (z_0) impact parameter resolutions as a function of the polar angle. Simulations are performed for resolutions of 1, 3, 5, and 7 μm in the vertex detector, using the new CLD baseline configuration.

Outer Tracker Barrel [mm]	R_4	R_5	R_6
CLD without PID	1000	1568	2136
CLD with PID	**1000**	**1446.8**	**1849.2**
Outer Tracker Endcap [mm]	Z_8	Z_9	Z_{10}	Z_{11}
CLD without PID	1310	1617	1883	2190
CLD with PID	**1310**	**1547**	**1752**	**1990**

Table 4.11: Tracker dimension for CLD without PID and CLD with PID

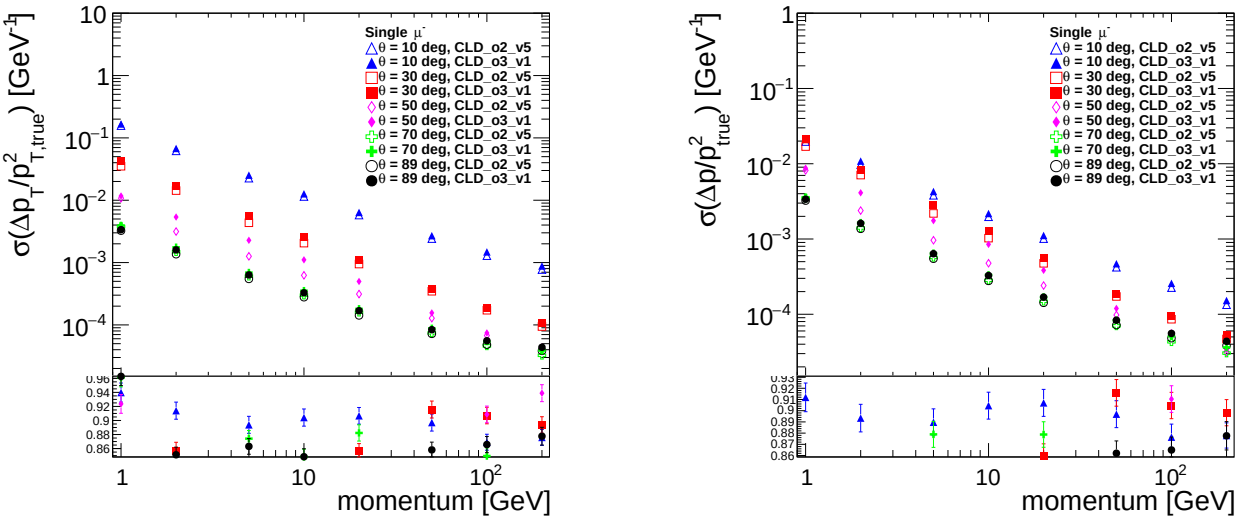

(a) Transverse momentum resolution

(b) Momentum resolution

Figure 4.27: Comparison of the transverse (p_T) and total momentum (p) resolutions for single muons simulated in the CLD new baseline geometry and in a configuration with a reduced tracker volume designed to accommodate particle identification (PID) detectors.

the nominal geometry with the reduced tracker volume configuration.

As expected, the most affected quantities are those related to momentum measurement, especially at high momentum, due to the shorter lever arm in the transverse plane. The resolutions of the total momentum p and transverse momentum p_T degrade by approximately 15% in the reduced geometry. Impact parameter resolutions are less sensitive to this change, as they primarily depend on the vertex detector and inner tracker.

4.8.5 Impact of larger magnetic field

To offset the degradation in transverse momentum (p_T) resolution introduced by a reduced tracker volume, required to accommodate a PID detector, one possible mitigation strategy is to increase the magnetic field strength. A stronger magnetic field enhances the curvature of charged particle trajectories, effectively increasing the lever arm available for momentum measurements.

While a magnetic field of 2 T is foreseen for operation at the Z pole ($\sqrt{s} = 91$ GeV), this study explores the potential tracking performance gains from increasing the field to 3 T, independent of machine-level feasibility considerations.

Figure A.43, A.44, A.45, 4.29 and Figure A.46, A.47, A.48, 4.30 show the tracking performance for the nominal CLD geometry without PID, comparing configurations with 2 T and 3 T magnetic fields. As expected, increasing the magnetic field improves the curvature measurement, resulting in

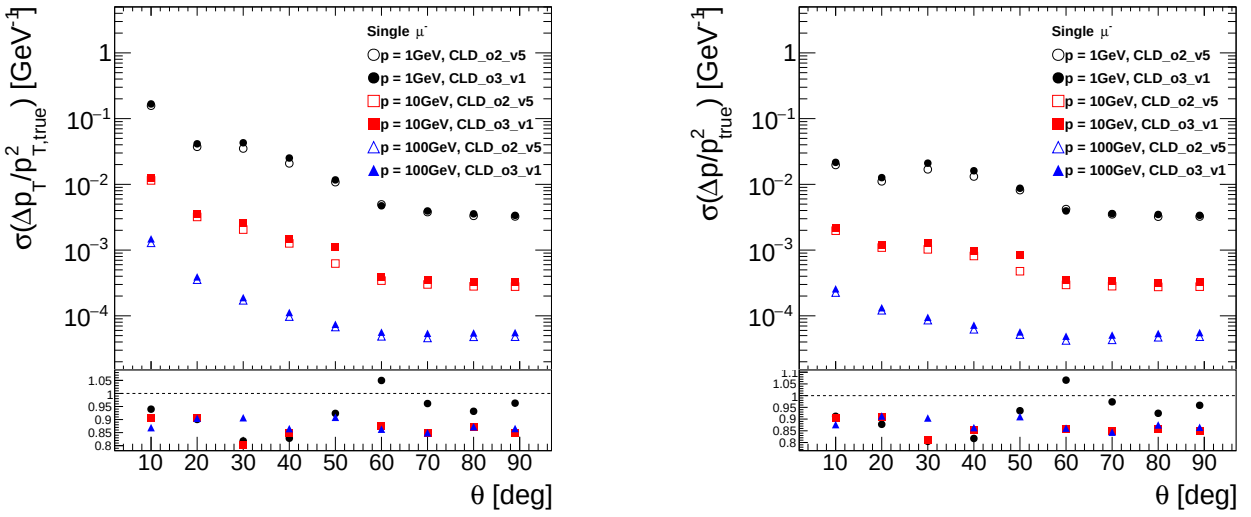

(a) Transverse momentum resolution

(b) Momentum resolution

Figure 4.28: Comparison of the transverse (p_T) and total momentum (p) resolutions as a function of the polar angle for single muons in the CLD new baseline geometry and in the reduced tracker volume configuration.

significantly better momentum and angular resolutions. In particular, the transverse momentum resolution improves by approximately 50–60 % across most momentum and angle ranges.

Figure A.49, A.50, A.51, 4.31 and Figure A.52, A.53, A.54, 4.32 extend the study by comparing the reduced tracker geometry with integrated PID at 3 T to the nominal geometry at 2 T. Despite the smaller tracker volume, the enhanced magnetic field not only compensates for the reduced lever arm but also leads to an overall performance gain of about 30–40% in key observables such as p_T, and impact parameter resolutions.

These results indicate that increasing the magnetic field could be an effective way to preserve, or even enhance, tracking performance when design constraints limit the tracking volume. However, this approach may come at the cost of reduced reconstruction efficiency for low-p_T tracks, which are more easily deflected in a stronger magnetic field.

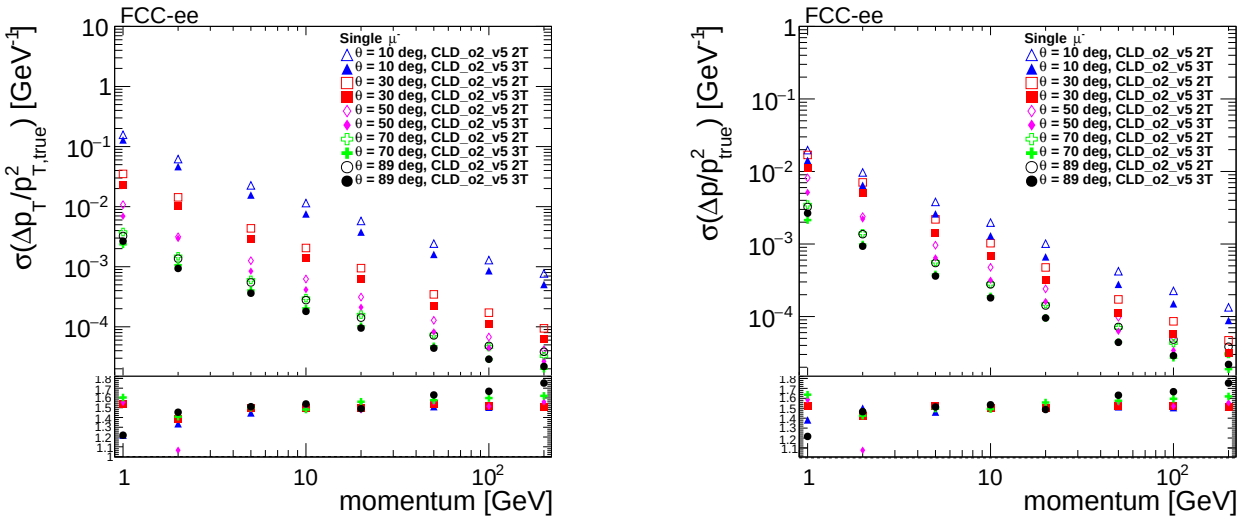

(a) Transverse momentum resolution

(b) Momentum resolution

Figure 4.29: Comparison of the transverse (p_T) and total momentum (p) resolutions as a function of momentum for single muons in the CLD new baseline geometry with magnetic field strengths of 2 T and 3 T.

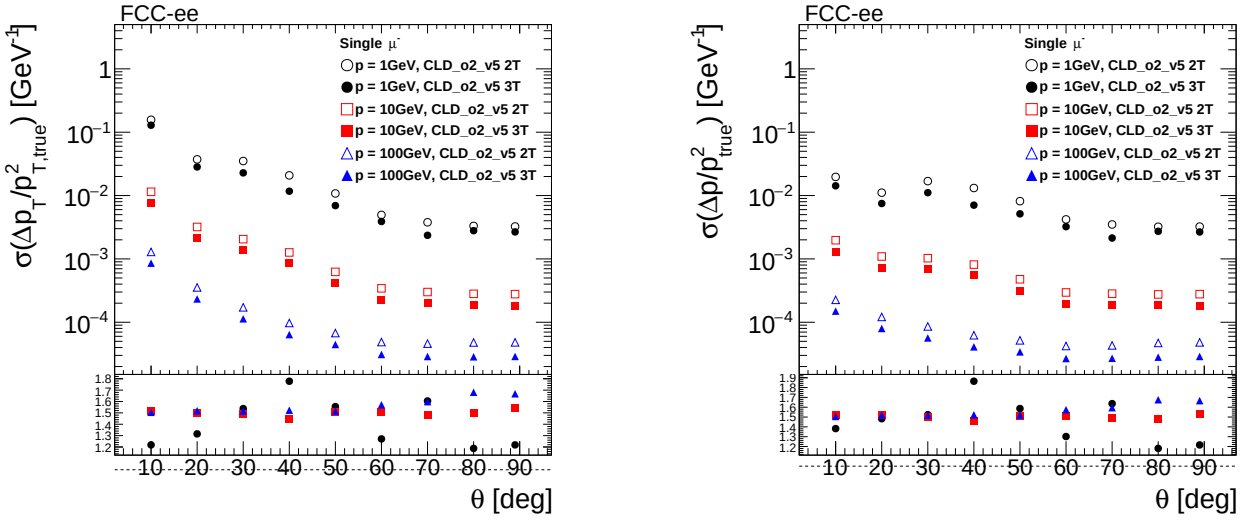

(a) Transverse momentum resolution

(b) Momentum resolution

Figure 4.30: Comparison of the transverse (p_T) and total momentum (p) resolutions as a function of the polar angle for single muons in the CLD new baseline geometry at 2 T and 3 T.

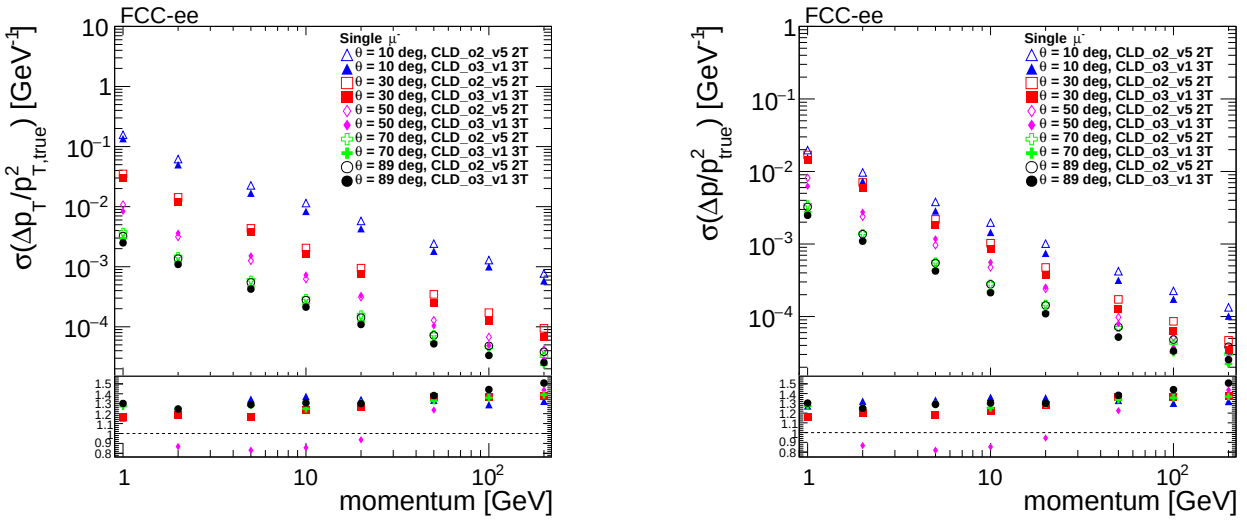

(a) Transverse momentum resolution

(b) Momentum resolution

Figure 4.31: Comparison of the transverse (p_T) and total momentum (p) resolutions as a function of momentum for the CLD new baseline geometry with a 2 T magnetic filed and a reduced tracker configuration with a 3 T magnetic field.

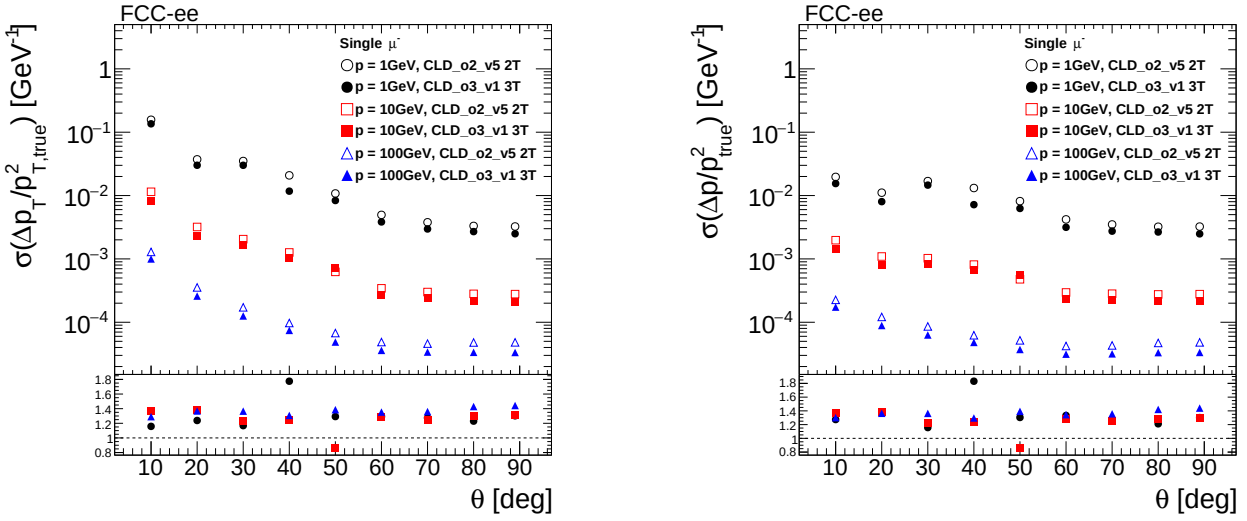

(a) Transverse momentum resolution

(b) Momentum resolution

Figure 4.32: Comparison of the transverse (p_T) and total momentum (p) resolutions as a function of the polar angle for the CLD new baseline with a 2 T magnetic field and reduced tracker volume configurations with a 3 T magnetic field.

4.9 Conclusion

An extensive study of the tracking performance of the CLD detector has been presented in this chapter, including its sensitivity to several key design parameters. The baseline CLD geometry is shown to achieve excellent tracking resolution, meeting the requirements set by the FCCee for precision measurements. Several detector configuration variations were explored to investigate possible optimisations and trade-offs:

Beam Pipe Radius & Vertex Geometry: Reducing the beam pipe radius from 15 mm to 10 mm improved the transverse impact parameter resolution by up to 20% at 10 GeV, despite a 33% increase in material budget.

Vertex Detector Spatial Resolution: Degrading the spatial resolution from 3 μm to 7 μm worsens impact parameter resolution by up to 30% at high momentum. The benefit of improving resolution below 3 μm is visible primarily for tracks with p $>$ 10 GeV, where multiple scattering is less dominant. Below this momentum, improvements are negligible, indicating that for FCCee, an optimised pixel pitch around the 3 μm resolution is sufficient for most physics cases.

Tracker Volume Reduction for PID: Shrinking the tracker volume to integrate a PID system (e.g., RICH detector) led to a 15% degradation in momentum resolution, especially at high momenta. This is expected from the reduced lever arm, as confirmed by theoretical models (Equation 1.1).

Magnetic Field Increase: Raising the magnetic field from 2 T to 3 T can compensate for the reduced tracker volume, yielding up to 60% improvements in p_T resolution, albeit potentially at the cost of reduced low-p_T track efficiency.

These results underline the interplay between geometric constraints, material budget, and magnetic field in achieving optimal tracking performance. Furthermore, any tracker upgrade must consider FCCee-specific backgrounds, particularly when approaching tighter beam pipe designs.

Recommendations for R&D:

Focus on achieving 3 μm spatial resolution for vertex detectors as a practical target, given diminishing returns below this value for FCCee kinematics.

Investigate low-material vertex detector technologies to enable inner radii closer to 10 mm, provided that beam-induced background studies confirm manageable occupancies.

Further study of high magnetic field solenoids (>2 T) is warranted if PID integration within the tracker is prioritised.

These quantitative insights should guide future detector design optimisations and technology developments for FCCee.

Chapter 5

Heavy Neutral Leptons

Contents

5.1 Introduction and Motivation

In the quest to uncover physics beyond the Standard Model (BSM), long-lived particles (LLPs)[142] have emerged as a compelling and not yet fully explored class of signatures at colliders. Unlike most particles predicted or discovered within the Standard Model, which typically decay promptly at the interaction point, LLPs are characterised by macroscopic lifetimes. This means they can travel measurable distances, ranging from micrometres to more than metres, before decaying into Standard Model (SM) particles. The resulting displaced vertices or unusual detector signatures offer powerful handles to distinguish LLPs from SM backgrounds [143].

Theoretical motivations for LLPs arise naturally in many extensions of the Standard Model, including but not limited to:

- **Supersymmetry (SUSY)**[144, 145], with small mass splittings or R-parity violation,
- **Heavy Neutral Leptons (HNLs)**[146], or sterile neutrinos, which interact weakly with SM neutrinos,
- **Axion-like particles** [147], **dark photons**, and other light exotic states.

This chapter focuses on HNLs as a benchmark LLP scenario, exploring their theoretical motivations, kinematics, and the expected experimental signatures at future lepton colliders.

5.2 Lifetime and Decay Length

The lifetime τ of a particle is fundamentally related to its total decay width Γ via:

$$\tau = \frac{\hbar}{\Gamma}, \tag{5.1}$$

where $\hbar$ is the reduced Planck constant. The decay width Γ quantifies how quickly a particle decays and is the sum over the partial widths of all possible decay channels.

Several physical mechanisms can lead to suppressed decay widths, and thus long lifetimes:

- **Suppressed couplings:** A common cause of long lifetimes is weak interaction with Standard Model (SM) particles. Since the decay width scales as $\Gamma \sim g^2$, small couplings yield

$$\tau \sim \frac{1}{\Gamma} \sim \frac{1}{g^2}. \tag{5.2}$$

- **Phase-space suppression:** If the final-state particles are nearly as massive as the parent particle, the available phase space is small, suppressing the decay rate and increasing the lifetime.
- **Heavy mediator suppression:** In many Beyond the Standard Model (BSM) scenarios, decays occur via virtual heavy mediators. The corresponding decay width scales as

$$\Gamma \sim \frac{1}{\Lambda^n}, \tag{5.3}$$

  for some $n > 0$, where Λ is the mass scale of the mediator. A large Λ therefore leads to a small decay width.

In collider environments, lifetimes are commonly expressed as decay lengths in the laboratory frame:

$$L = \beta\gamma c\tau, \tag{5.4}$$

where $\beta = v/c$ (with v the particle velocity), $\gamma = 1/\sqrt{1-\beta^2}$, and c the speed of light. For a fixed *proper* lifetime τ, the mean decay length in the lab frame is $L = \beta\gamma\, c\,\tau$, so more boosted particles travel farther before decaying. Equivalently, the mean decay time measured in the lab is $t_{\text{lab}} = \gamma\tau$.

5.2.1 Illustrative Example: Charged Pion

To illustrate the relationship between decay width and lifetime, let us consider a well-understood Standard Model example, namely the decay of the charged pion $\pi^{\pm}$ into a lepton and neutrino:

$$\Gamma(\pi^{\pm} \to \ell^{\pm}\nu_{\ell}) = \frac{G_F^2 f_\pi^2 m_\ell^2 m_\pi}{8\pi}\left(1 - \frac{m_\ell^2}{m_\pi^2}\right)^2 \tag{5.5}$$

where G_F is the Fermi constant, f_π the pion decay constant, m_π the pion mass, and m_ℓ the mass of the final-state lepton.

The corresponding lifetime is then given by:

$$\tau_{\pi^{\pm}} = \frac{\hbar}{\Gamma(\pi^{\pm} \to \ell^{\pm}\nu_{\ell})} \tag{5.6}$$

5.3 Experimental Implications of LLPs

Experimentally, LLPs present both challenges and opportunities. Their decays may result in:

- Displaced vertices,
- Disappearing or kinked tracks,
- Non-pointing photons (photons whose reconstructed flight direction does not intersect the interaction point) or delayed calorimeter energy deposits.

These unconventional signatures often escape traditional searches optimised for prompt decays. However, they can be effectively probed through dedicated analyses and with detector components that offer excellent spatial and timing resolution.

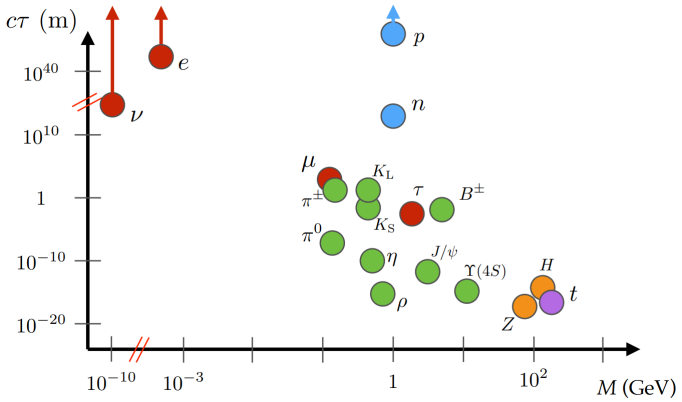

Figure 5.1: Particle lifetime $c\tau$, expressed in meters, as a function of particle mass in GeV, for various Standard Model particles. LLPs can exhibit decay lengths spanning many orders of magnitude [143].

Figure 5.1 illustrates how the decay length $c\tau$ varies as a function of particle mass. LLPs may decay anywhere within the detector, from the interaction point to well beyond the outermost layers, depending on their kinematics and intrinsic lifetime.

5.4 Heavy Neutral Leptons as LLPs

Heavy Neutral Leptons (HNLs)[146] are a well-motivated class of LLPs, especially in the context of neutrino mass generation mechanisms such as the Type-I seesaw. HNLs are hypothetical fermions that extend the SM by mixing with light neutrinos, leading to possible observable signatures at colliders.

In the remainder of this chapter, we investigate the sensitivity of future lepton colliders, such as FCCee, to HNLs through dedicated LLPs analyses. We present the production modes, decay channels, reconstruction strategies, and performance metrics relevant to HNLs searches.

Heavy Neutral Leptons (HNLs) are hypothetical fermions introduced in extensions of the Standard Model to explain the origin of neutrino masses, the baryon asymmetry of the Universe, and possibly dark matter. These particles might be for example singlets under the Standard Model gauge group, though other models predict HNLs as members of $\mathrm{SU}(2)_L$ doublets or triplets and mix with active neutrinos through Yukawa interactions, which leads to suppressed couplings and long lifetimes, making them excellent candidates for LLPs searches.

5.4.1 Type-I Seesaw Mechanism

The Type-I seesaw mechanism [148] is a minimal and theoretically well-motivated extension of the SM that explains the small but non-zero neutrino masses observed in oscillation experiments. This mechanism introduces one or more right-handed neutrinos, commonly referred to as HNLs. Because a right-handed neutrino N is a complete SM gauge singlet $(\mathbf{1}, \mathbf{1}, 0)$, the Majorana mass term

$$-\tfrac{1}{2}\, M\, \overline{N^c} N$$

is allowed: it is *gauge invariant*, since N carries no $SU(3)_C \times SU(2)_L \times U(1)_Y$ charges and the bilinear $\overline{N^c}N$ therefore transforms trivially under all SM gauge transformations. It is also *renormalisable*, because the operator has mass dimension three and thus can be consistently included in a quantum field theory without introducing non-renormalisable divergences. Importantly, this term does not rely on electroweak symmetry breaking, so the scale M can naturally be much larger than the electroweak scale. It violates global lepton number by two units but remains fully consistent with SM gauge symmetries.

After electroweak symmetry breaking and rotation to mass eigenstates, the interactions of the heavy neutrinos are [149]:

$$\mathcal{L}_{\text{int}}^{\text{Type I}} \;=\; \mathcal{L}_W \;+\; \mathcal{L}_Z \;+\; \mathcal{L}_H, \tag{5.7}$$

with

$$\mathcal{L}_W = -\frac{g_W}{\sqrt{2}} \sum_{\ell=e}^{\tau} \sum_{i=1}^{n_s} \overline{N_i}\, V_{\ell i}^{*} \gamma^{\mu} P_L\, \ell\, W_{\mu}^{+} \;+\; \text{h.c.}, \tag{5.8}$$

$$\mathcal{L}_Z = -\frac{g_W}{2\cos\theta_W} \sum_{\ell=e}^{\tau} \sum_{i=1}^{n_s} \overline{N_i}\, V_{\ell i}^{*} \gamma^{\mu} P_L\, \nu_{\ell}\, Z_{\mu} \;+\; \text{h.c.}, \tag{5.9}$$

$$\mathcal{L}_H = -\frac{g_W}{2M_W}\, h \sum_{\ell=e}^{\tau} \sum_{i=1}^{n_s} \overline{N_i}\, V_{\ell i}^{*} m_{N_i}\, P_L\, \nu_{\ell} \;+\; \text{h.c.} \tag{5.10}$$

Here g_W is the $SU(2)_L$ gauge coupling, θ_W the weak mixing angle, M_W the W mass, h the physical Higgs field, and $P_L = (1-\gamma^5)/2$. The matrices $V_{\ell i}$ encode the active–sterile mixings; n_s is the number of heavy states considered. This framework treats m_{N_i} and $V_{\ell i}$ as independent

phenomenological parameters and is sufficient to capture production and decay of Dirac or Majorana HNLs at colliders to leading order in $|V_{\ell i}|$.

After electroweak symmetry breaking (EWSB), the Higgs field acquires a vacuum expectation value (VEV) v, generating Dirac masses $m_D = Y\,v$ (choice of convention discussed below). In the basis (ν_L, N^c) the neutrino mass matrix reads

$$\mathcal{M}_\nu \;=\; \begin{pmatrix} 0 & m_D \\ m_D^T & M \end{pmatrix}. \tag{5.11}$$

In the seesaw limit, defined by small active–sterile mixing

$$\theta \;\equiv\; m_D\, M^{-1}, \qquad \|\theta\| \ll 1,$$

(equivalently, the largest singular value of m_D is much smaller than the smallest eigenvalue of M), block-diagonalisation gives

$$m_\nu \;\simeq\; -\,m_D\, M^{-1}\, m_D^T \;=\; -\,v^2\, Y\, M^{-1}\, Y^T, \tag{5.12}$$

so that in the single-flavour limit $m_\nu \simeq m_D^2/M$ and the light mass scales inversely with the heavy scale.

After electroweak symmetry breaking (EWSB), the Higgs field acquires a vacuum expectation value (VEV) $v \approx 174$ GeV, generating Dirac mass terms $m_D = Yv$. In the basis (ν_L, N^c), the neutrino mass matrix takes the form:

$$\mathcal{M}_\nu = \begin{pmatrix} 0 & m_D \\ m_D^T & M \end{pmatrix}. \tag{5.13}$$

Here m_D is the Dirac mass matrix between active and singlet states, and M is the (complex symmetric) Majorana mass matrix for the gauge-singlet (right-handed) neutrinos N.

Convention for v. In the standard SM normalisation $H = \big(0, (v+h)/\sqrt{2}\big)^T$ with $v \simeq 246$ GeV, one has $m_D = Y\,v/\sqrt{2}$ and v is fixed by G_F as $v = (\sqrt{2}\,G_F)^{-1/2}$ [14]. If instead one writes $m_D = Y\,v$ with $v \simeq 174$ GeV, the factor of $\sqrt{2}$ is absorbed into the definition of Y. We follow a single convention consistently throughout this thesis.

This relation naturally explains the smallness of light neutrino masses: the heavier the Majorana mass M, the lighter the observed neutrinos. For instance, if $M \sim 1$ GeV and the light neutrino masses are around 0.1 eV, the Dirac mass scale must be approximately 10^{-4} GeV, corresponding to very small Yukawa couplings $Y \sim 10^{-6}$. Thus, light neutrino masses can be generated without fine-tuning, provided the right-handed neutrinos are sufficiently heavy.

The diagonalization of $\mathcal{M}_\nu$ yields three mostly active, light neutrino states, matching the SM neutrinos, and additional heavy, mostly sterile states, the HNLs. The mixing between active and sterile neutrinos is characterised by the active-sterile mixing angle:

$$\theta \sim \frac{m_D}{M}. \tag{5.14}$$

Here "sterile" means SM–gauge singlet. "Mostly sterile" indicates that the heavy mass eigenstate is aligned with the singlet N up to an $\mathcal{O}(\theta)$ active admixture, e.g.

$$\nu_{\text{light}} \simeq \nu_L - \theta\, N^c, \qquad N_{\text{heavy}} \simeq N + \theta^T\, \nu_L^c,$$

so its couplings to W, Z, h are suppressed by the small mixings $V_{\ell i} \sim \theta_{\ell i}$.

This mixing allows HNLs to couple to Standard Model particles via the weak interactions: their production and decay proceed through charged-current ($W^{\pm}$) and neutral-current (Z, h) processes with amplitudes proportional to the active–sterile mixings (e.g. $V_{\ell i} \sim \theta_{\ell i}$). Consequently, rates scale as $\sum_{\ell} |V_{\ell i}|^2$, and the typically small mixings imply long proper lifetimes.

To fully account for the observed neutrino mass differences and mixing patterns, the minimal Type-I seesaw model requires at least two HNLs. Often, a third HNL is introduced to address cosmological phenomena, such as dark matter relic abundance, as in the neutrino Minimal Standard Model (νMSM)[150, 48].

In summary, the Type-I seesaw mechanism elegantly explains the tiny neutrino masses and predicts new heavy states with potentially long lifetimes. These Heavy Neutral Leptons are a key target for current and future experimental searches, particularly at high-precision colliders like the FCCee.

5.4.2 Dirac vs Majorana HNLs

HNLs introduced in seesaw models can be either Dirac or Majorana fermions [151]. The distinction affects their phenomenology:

- Majorana HNLs violate lepton number and allow same-sign dilepton signals, $\nu = \bar{\nu}$.
- Dirac HNLs conserve lepton number and exhibit only opposite-sign leptons, neutrino (ν) and antineutrino ($\bar{\nu}$) are distinct.

Disentangling these cases experimentally is non-trivial because neutrinos are not directly observed, but differences in angular distributions, polarisations, and decay lengths can provide distinguishing features.

Majorana HNLs

A Majorana fermion is its own antiparticle. In the context of HNLs, this means that a Majorana HNL N satisfies $N = N^c$, where N^c is the charge-conjugated field. The Majorana nature violates total lepton number by two units ($\Delta L = 2$), enabling lepton-number-violating (LNV) processes.

The most well-known consequences include:

- Neutrinoless double beta decay ($0\nu\beta\beta$) [152].
- Same-sign dilepton production at proton–proton colliders via an on-shell *Majorana* N, e.g.

$$pp \to W^{\pm} \to \ell^{\pm} N, \qquad N \to \ell^{\pm} W^{\mp} \to \ell^{\pm}\ell^{\pm} jj \quad (\Delta L = 2), \tag{5.15}$$

  where the two charged leptons have the same sign and little/no genuine missing energy [153, 154].

At e^+e^- colliders operating at the Z pole (e.g. FCC-ee), the typical production is single-N:

$$e^+e^- \to Z \to N\,\nu, \qquad N \to \ell^{\pm} W^{\mp} \to \begin{cases} \ell^{\pm} jj, \\ \ell^{\pm}\ell'^{\mp}\nu, \end{cases} \tag{5.16}$$

so the classic same-sign dilepton LNV handle is absent: the event always contains a light neutrino from $Z \to N\nu$ (and often another from W decay), yielding opposite-sign dileptons with MET. For a *Majorana* N both lepton-number–conserving (LNC) $N \to \ell^- W^+$ and lepton-number–violating

(LNV) $N \to \ell^+ W^-$ decays occur with comparable rates at fixed mixings, leading to charge-symmetric spectra; for a *Dirac* N only the LNC mode is present. If N is long-lived, displaced vertices provide an additional, robust handle [153].

These signatures are forbidden if the HNLs are Dirac particles. For Majorana HNLs, decay rates into final states with opposite-sign and same-sign leptons are typically comparable, and the ratio of lepton-number-conserving (LNC) to lepton-number-violating (LNV) decays can be used to probe the Majorana nature.

Importantly, for a given mixing angle, Majorana HNLs have shorter lifetimes than Dirac HNLs, since they can decay through both LNC and LNV channels, effectively doubling the decay rate:

$$\Gamma_{Majorana} \approx 2\Gamma_{Dirac} \tag{5.17}$$

Dirac HNLs

A Dirac fermion, unlike a Majorana particle, has distinct particle and antiparticle components. In this case, total lepton number is conserved, and the HNL can only mediate lepton number conserving interactions.

Dirac HNLs cannot produce same-sign dilepton signatures. Their decays always involve a net lepton number of ± 1 and are otherwise similar in final-state kinematics to those of Majorana HNLs. This makes it more challenging to distinguish Dirac HNLs from background in purely collider-based searches unless polarization or asymmetry observables are accessible.

Intermediate Cases: Pseudo-Dirac HNLs

In many models, especially those involving approximate symmetries, HNLs may form pseudo-Dirac pairs. These are pairs of nearly degenerate Majorana neutrinos with small mass splittings[155]. In this case, lepton number violation is suppressed, and the HNL phenomenology interpolates between the Dirac and Majorana limits.

This can result in:

- Suppressed LNV signatures (e.g. rare same-sign dileptons),
- Oscillations between the two states (*i.e.* the two nearly degenerate Majorana mass eigenstates N_1 and N_2 that form the pseudo-Dirac pair) on timescales comparable to their lifetimes,
- A dependence of observable rates on the size of the mass splitting Δm and the lifetime τ.

The lepton number violation (LNV) can be quantified using observables such as the LNV ratio $R_{\ell\ell}$:

$$R_{\ell\ell} = \frac{\Gamma(LNV)}{\Gamma(LNV) + \Gamma(LNC)} \tag{5.18}$$

which varies smoothly between 0 (pure Dirac) and 0.5 (pure Majorana), LNC is the Lepton Number Conserving. Here, if N is a Majorana particle, it can decay to both $\ell^+\ell^-$, violating lepton number conservation. This distinction is crucial in identifying whether neutrinos (and HNLs) are Dirac (LNC only) or Majorana (LNC + LNV). Measuring this ratio would allow a collider to probe the fundamental nature of neutrinos.

5.4.3 Collider Signatures and Lifetime

The decay width of HNLs is suppressed by the small active–sterile mixings $|\theta_{\ell N}|^2$:

$$\Gamma_N \sim |\theta_{\ell N}|^2 m_N^5 \tag{5.19}$$

leading to macroscopic decay lengths for small mixings. This makes HNLs interesting LLPs at lepton colliders like FCCee [156], where high statistics and low backgrounds enable sensitivity to lifetimes corresponding to decay lengths from millimeters to larger than meters.

This makes HNLs excellent candidates for LLP searches at current and future colliders.

The total decay width of an HNL with mass m_N and mixing angle $|\theta_{lN}|^2$ scales approximately as:

$$\Gamma_N \propto G_F^2\, m_N^5 \sum_\ell |\theta_{\ell N}|^2 \tag{5.20}$$

Here $\theta_{\ell N}$ denotes the active–sterile mixing element between lepton flavour $\ell = e, \mu, \tau$ and the heavy neutrino N. In Type-I seesaw (leading order), $\theta_{\ell N} \simeq (m_D M^{-1})_{\ell N}$, i.e. the matrix version of Eq. (1.10). For $m_N \ll m_W$, $\Gamma_N \propto G_F^2\, m_N^5 \sum_\ell |\theta_{\ell N}|^2$, while for $m_N \gtrsim m_W$, $\Gamma_N \propto G_F\, m_N^3 \sum_\ell |\theta_{\ell N}|^2$.

This leads to a lifetime of:

$$\tau_N \propto \frac{1}{G_F^2\, m_N^5 \sum_\ell |\theta_{\ell N}|^2}\,. \tag{5.21}$$

For GeV-scale masses and small mixings (e.g $|\theta^2| \sim 10^{-8}$), the resulting decay lengths can range from a few millimeters up to several meters in the detector frame, depending on the boost.

Displaced Vertex Signatures

If the HNL decays inside the detector, it can give rise to displaced vertices, which are among the most striking signatures at colliders:

- Displaced charged tracks originating away from the interaction point, .
- Vertices with missing energy (from neutrinos),

FCCee is particularly well-suited for HNL searches due to:

- High luminosity and clean environment,
- High vertex resolution,
- Large statistics of Z bosons (up to 10^{12} in the Z-pole run).

With these capabilities, FCCee provides an good environment to probe extremely small active–sterile mixings via displaced decays. In the Z-pole run, single-N production proceeds through $Z \to N\nu$, so the kinematic reach in mass is limited to $m_N < m_Z$. Access to heavier N is possible only at higher $\sqrt{s}$ runs (e.g. 240–250 and 365 GeV) through off-shell W/Z production.

5.4.4 Leptogenesis and Cosmological Connections

Beyond explaining the origin of neutrino masses, HNLs may also play a central role in the evolution of the early Universe. In particular, HNLs can contribute to generating the observed matter–antimatter asymmetry through a mechanism known as leptogenesis [157, 158].

In leptogenesis, CP-violating interactions of HNLs in the early Universe generate a net lepton asymmetry while the HNLs are out of thermal equilibrium. Electroweak processes active above the electroweak phase transition then partially convert this lepton asymmetry into the observed baryon asymmetry. Two archetypal realizations are often discussed: (i) *thermal* leptogenesis, where heavy

N decays at very high scales create the asymmetry, and (ii) *low-scale* leptogenesis, where GeV-scale, nearly degenerate HNLs produce the asymmetry via coherent oscillations in the plasma. The viability and size of the asymmetry depend on the HNL masses, mixings, and CP phases, and are subject to cosmological constraints (e.g. from Big Bang Nucleosynthesis) in addition to neutrino data.

In low-scale leptogenesis scenarios, the presence of two or more HNLs with CP-violating interactions allows for the generation of a positive lepton number in the early Universe. This asymmetry can develop through HNL oscillations, decays, and interactions with the thermal bath. The generated lepton asymmetry can then influence the abundances of particles in the primordial plasma and ultimately lead to a Universe dominated by matter, as we observe today.

A minimal and well-studied framework that realises this idea is the Neutrino Minimal Standard Model (νMSM). It extends the Standard Model by three right-handed neutrinos: two responsible for neutrino masses and leptogenesis, and a third, lighter HNL that could serve as a dark matter candidate [159]. In this model, the mass and mixing patterns of the HNLs are tightly connected to both low-energy neutrino data and cosmological observations, making it highly predictive and testable.

Additionally, depending on their mass and lifetime, HNLs can impact Big Bang Nucleosynthesis (BBN)[160], the cosmic microwave background (CMB), and the formation of large-scale structure. These cosmological considerations place stringent constraints on the allowed parameter space of HNLs and further motivate searches.

5.4.5 Model Parameters

Realistic models generally require at least two or three HNLs to explain the observed neutrino oscillation data and enable successful leptogenesis. In this thesis we adopt the same phenomenological Type-I seesaw benchmark used in Ref. [156], where production and decay are controlled by the active–sterile mixings $V_{\ell i}$ (see Figure 5.2).

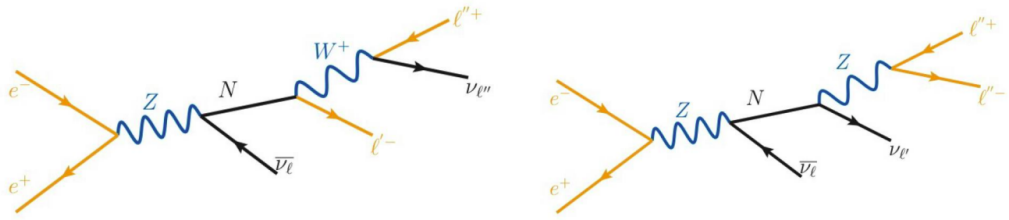

Figure 5.2: Single-N production and decay at the Z pole [156].

The key parameters of interest include:

- **HNL Mass (m_N)**: The mass of the heavy neutrino is a central quantity. It determines kinematically which production and decay channels are accessible. Depending on whether m_N is below or above the electroweak scale, different search strategies become relevant. Concretely, for $m_N \lesssim m_W, m_Z$ only off–shell three-body decays are available, making N long-lived and favouring displaced-vertex searches; for $m_N \gtrsim m_W, m_Z$ the two-body modes $N \to \ell W, \nu Z, \nu h$ open, the lifetime shrinks, and prompt-signature searches dominate (with same-sign dileptons if N is Majorana).

- **Active-Sterile Mixing Angles ($|\theta_{\ell N}|^2$)**: These govern the strength of the interaction between the HNL and the Standard Model via mixing with each lepton flavour $\ell = e, \mu, \tau$.

They control both the production rate and the decay width (and hence the lifetime) of the HNL. The mixing pattern across flavours also determines the decay branching ratios.

- **CP-Violating Phases**: If more than one HNL is introduced, complex phases in the Yukawa couplings can lead to CP violation in the HNL sector. These phases are critical in scenarios aiming to explain the baryon asymmetry of the Universe through low-scale leptogenesis.

Together, these parameters form the basis for experimental searches and sensitivity projections. Constraints or measurements of any of them can provide valuable insights into the origin of neutrino masses and the possible extension of the Standard Model with sterile neutrinos.

5.4.6 Signal Generation and Benchmark Points

Branching ratio assumption. The HNL branching ratio was set to the analysed topology to **100**% ($N \to e\,e\,\nu$ in the leptonic charged–current channel). This isolates the detector/selection performance from model-dependent decay fractions; rates for other final states can be obtained by rescaling with the appropriate BR.

Event generation. Signal samples are generated at leading order with MadGraph5_aMC@NLO (`v3.6`, latest stable at the time of production)using the `HeavyN` (Majorana) UFO model. Parton showering and hadronisation are performed with Pythia 8. Unless noted, we consider single-N production at the Z pole, $e^+e^- \to Z \to N\nu$, with a single non-zero mixing $V_{eN} = 1.41 \times 10^{-6}$ and $V_{\mu N} = V_{\tau N} = 0$.

Table 5.1: Benchmark points at the Z pole with $V_{eN} = 1.41 \times 10^{-6}$. Cross sections $\sigma(e^+e^- \to Z \to N\nu)$ are shown both as in the paper (σ_{paper}) and as used here after a global rescaling by 10^5 ($\sigma_{\text{used}} = 10^5 \times \sigma_{\text{paper}}$) to ensure non-negligible expected yields. The quoted $c\tau$ are indicative rest-frame values computed with the off-shell scaling $\Gamma_N \simeq \frac{G_F^2 m_N^5}{96\pi^3} \sum_\ell |U_{\ell N}|^2$ (Majorana, $m_N \ll m_W$); for $m_N \simeq 90$ GeV the opening of on-shell W further *shortens* the lifetime.

m_N [GeV]	$\lvert V_{eN}\rvert^2$	σ_{paper} [pb]	σ_{used} [pb]	$c\tau$ at rest [m]
30	1.99×10^{-12}	6.637×10^{-10}	6.637×10^{-5}	8.9×10^{1}
50	1.99×10^{-12}	4.535×10^{-10}	4.535×10^{-5}	6.9×10^{0}
70	1.99×10^{-12}	1.968×10^{-10}	1.968×10^{-5}	1.3×10^{0}
90	1.99×10^{-12}	1.749×10^{-12}	1.749×10^{-7}	$\lesssim 3.7 \times 10^{-1}$ ()

For $m_N \approx 90$ GeV, $N \to \ell W$ is kinematically open (W on-shell) while $N \to \nu Z$ is near threshold; the true lifetime is *shorter* than the off-shell m_N^5 scaling quoted here.

Note on the rescaling. The cross sections used in our samples were multiplied by 10^5 relative to the paper values to avoid $\mathcal{O}(< 1)$ expected events in our limited-statistics studies; event yields shown in this thesis are rescaled back by the same global factor when compared to the reference predictions.

5.5 Detector Simulation and Reconstruction Framework

In the context of the HNLs analysis, understanding the impact of detector modelling and reconstruction is essential, especially given the sensitivity of the study to tracking performance and displaced vertex reconstruction. This section reviews and contrasts the two main simulation paradigms, fast simulation (Delphes) and full simulation (Geant4 and full event reconstruction), highlighting their respective strengths and limitations. The motivation for re-implementing the HNL study in full simulation is presented, followed by a detailed comparison of tracking-related performance metrics.

Subsequent subsections address key technical observations uncovered during this transition, including:

- the importance of tuning reconstruction parameters to recover displaced vertices,
- the behaviour of tracking efficiency and fake rate for electrons using as a SM benchmark $Z \to \tau\tau$ events,
- and the identification of a specific inefficiency in electron reconstruction due to track-cluster matching failures, which significantly affects displaced electron reconstruction.

Together, these studies provide both a validation of the full simulation approach and insight into current software limitations, guiding the development of a more robust and accurate HNL analysis framework.

5.5.1 IDEA Fast Simulation vs. CLD Full Simulation: Motivations and Limitations

In high-energy physics, two main simulation approaches are commonly used to model detector response: fast simulation and full simulation. Each approach is suited to different stages of analysis, depending on the balance between computational efficiency and the level of detail required.

Fast simulation, exemplified by frameworks such as Delphes, plays a crucial role in phenomenological studies and early-stage analyses. It uses parametrised models of detector response, typically applying smearing functions directly to Monte Carlo (MC) truth particles to emulate the effects of finite resolution and acceptance. This enables rapid event generation and the production of large datasets with modest computational resources, making it ideal for scanning large parameter spaces, optimising analysis strategies, or developing selection criteria.

Delphes includes many configurable modules that mimic aspects of tracking, calorimetry, and particle identification, providing a streamlined yet versatile tool for a wide range of studies. While fast simulation provide an overall correct and robust estimation of detector effects, a detailed and complete full simulations remains the ultimate tool to have the most precise descriptions of detector effects.

Full simulation, typically based on Geant4, offers a much more granular description of how particles interact with the detector environment. This is followed by a realistic reconstruction stage, in which raw detector signals are processed to reconstruct physical objects such as tracks and vertices, closely mimicking real experimental data processing. While this approach is considerably more computationally demanding, it provides a high-fidelity model of detector behaviour, incorporating effects like misreconstruction, hit inefficiencies, fake tracks, and material interactions, essential for analyses that rely heavily on reconstruction performance.

5.5.2 Motivation for Reproducing the HNL Analysis in Full Simulation

The HNL analysis was initially conducted using Delphes. To ensure that the conclusions of the HNL analysis remain valid under more realistic detector conditions, the study was reproduced using full simulation and reconstruction within the Key4HEP software. The emphasis here is on comparing tracking performance, which is a critical component of the analysis, especially for identifying displaced muons originating from secondary vertices.

5.5.3 Tracking Performance Comparison: Fast vs. Full Simulation

To benchmark the realism of the full simulation, a dedicated study of tracking performance using prompt muons was performed. Although the analysis targets displaced muons, prompt tracks offer a clean reference sample to evaluate baseline tracking efficiency and resolution.

The comparison reveals that the tracking performance in full simulation is comparable to that in fast simulation for prompt muons, in terms of reconstruction efficiency and momentum resolution. This suggests that the simplified smearing approach used in Delphes captures the core tracking features reasonably well in the prompt regime.

This performance validation supports the continued use of full simulation in HNL studies involving displaced muons, especially in the context of high-precision detectors like those proposed for the FCCee.

Due to the different frameworks and output formats used by fast and full simulation, the tracking performance results are presented side by side rather than as superimposed plots. This allows for a clear and fair comparison of the overall trends and resolutions, without conflating the distinct methodologies employed by each simulation approach.

Although prompt tracks are not the primary focus of this study, they provide a clean baseline to validate the core tracking performance. We therefore first compare the momentum resolution, expressed as $\sigma(p)/p$, as a function of the track momentum and polar angle (see Figure 5.3 and Figure 5.4). The results from fast and full simulations are comparable, showing similar trends and resolution magnitudes across the kinematic range.

The second observable is the transverse impact parameter resolution, σ_{d_0}. Again, the results from both simulation frameworks show comparable performance, with resolutions of the same order of magnitude Figure 5.5, 5.6.

When comparing the angular resolutions, it is essential to take into account the units used in the different plots. In particular, Figure 5.7 presents the θ resolution in degrees, while 5.8 shows it in milliradians. Likewise, Figure 5.9 is expressed in radians, whereas 5.10 is given in milliradians. Once the unit conversions are properly considered, however, it becomes clear that the performance of the two approaches is comparable.

We do not overlay the fast- and full-simulation curves for both technical and definition-related reasons. On the *fast-simulation* side (Delphes), we relied on the standard Delphes output, which provides histograms that are already binned during the simulation, based on parametrised detector responses. On the *full-simulation* side, the distributions are obtained with our dedicated analysis code presented in the chapter on track-resolution, based on full reconstruction (Geant4 + tracking), track-fit parameters, and slightly different object selections. These distinct processing chains, object definitions, binning, event weights, and the estimator used for $\sigma(p)/p$, make a strict curve-on-curve overlay not meaningful without fully harmonising both workflows (same definitions, same binning, same analysis code). We therefore show the results *side by side*, which is sufficient for a robust qualitative comparison of trends and magnitudes between fast and full simulation.

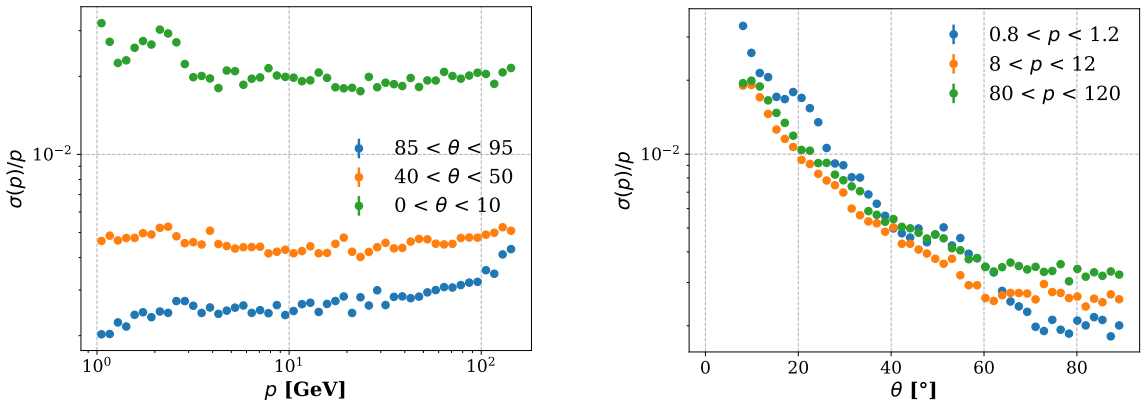

Figure 5.3: Momentum resolution ($\sigma(p)/p$) as a function of the momentum (left) and polar angle θ (right) for prompt muons, obtained with fast simulation (Delphes).

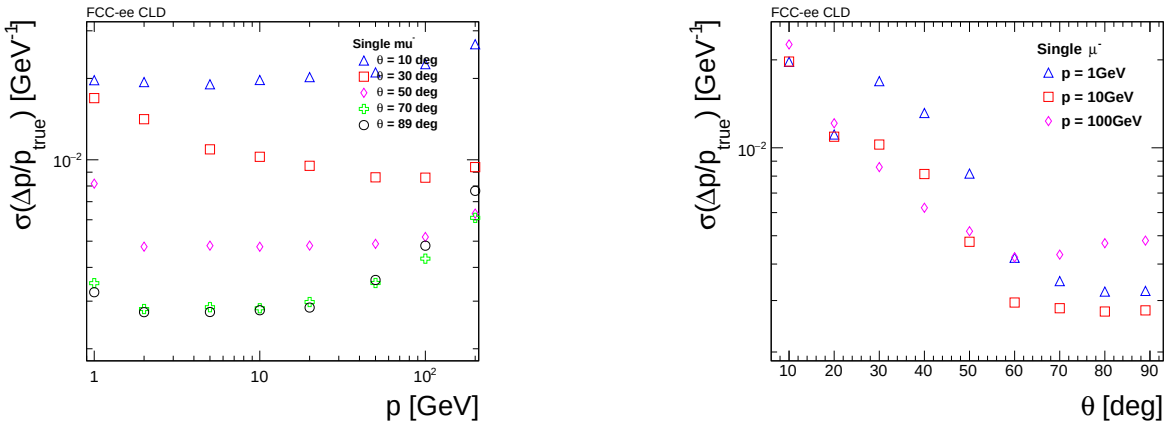

Figure 5.4: Momentum resolution (σ_p/p) as a function of the momentum (left) and polar angle θ (right) for prompt muons, obtained with full simulation (Geant4 + reconstruction).

5.5.4 Tracking Efficiency and Fake Rate in $Z \to \tau^+\tau^-$ Events

Tracking performance was further evaluated using electrons from $Z \to \tau^+\tau^-$ events, focusing on electrons from tau decays. A good reconstructed track is defined as one that matches a single MC particle with at least 99% of its hits, while tracks with less than 99% matching are classified as fake.

The results show very good tracking efficiency for electrons with transverse momentum above 2 GeV and polar angle θ between 0.2 and 2.8 radians, corresponding to the central region of the detector. As expected, the performance is mainly limited by the tracker acceptance, with reduced efficiency observed at low momentum and near the detector edges, Figure 5.11.

5.5.4.1 Displaced Vertex Reconstruction Issue in ConformalTracking

While the conformal tracking algorithm is designed to enable efficient reconstruction of displaced vertices, with published results showing some successful vertex reconstruction up to 600 mm of displacement [88], initial results in this HNL study revealed a stark discrepancy: no displaced

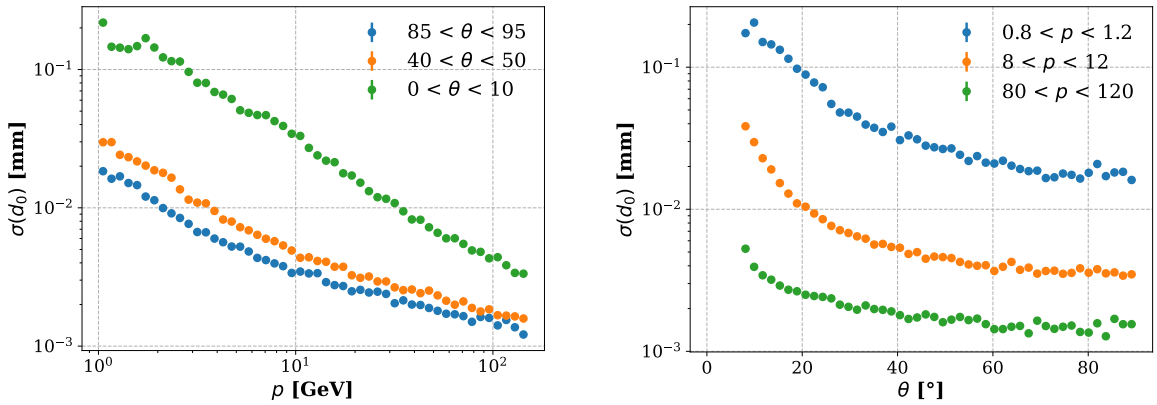

Figure 5.5: Transverse impact parameter resolution (d_0) as a function of the momentum (left) and polar angle θ (right) for prompt muons, obtained with fast simulation (Delphes).

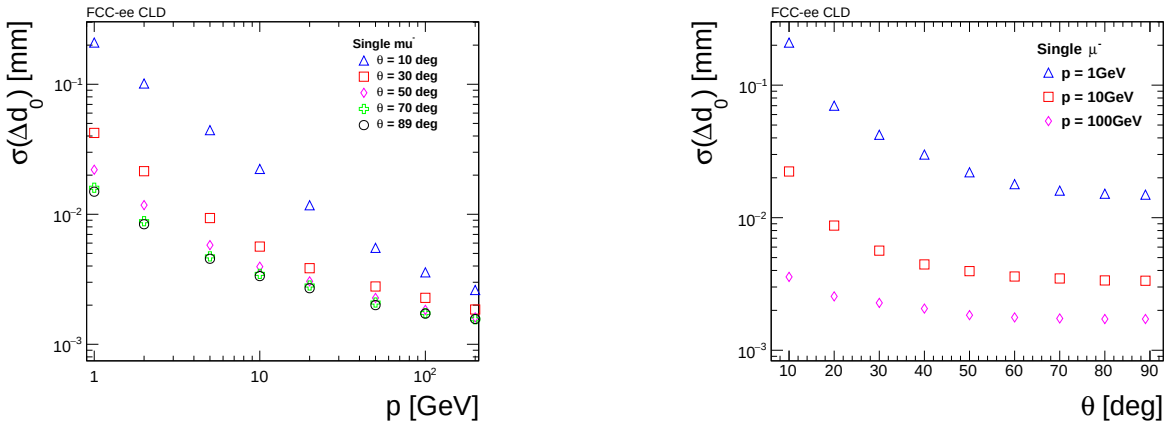

Figure 5.6: Transverse impact parameter resolution (d_0) as a function of the momentum (left) and polar angle θ (right) for prompt muons, obtained with full simulation (Geant4 + reconstruction).

vertices were reconstructed beyond 100 mm, Figure 5.12.

This unexpected limitation was traced to the absence of the final "displaced" tracking step in the standard reconstruction sequence. This step is specifically designed to enhance the reconstruction of non-prompt tracks and vertices. However, tests performed with and without this step showed no difference in vertex reconstruction efficiency for displaced HNL decays, Figure 5.12, suggesting the issue lay deeper in the tracking configuration.

A detailed investigation revealed that the problem originated from the `MaxCellAngle` and `MaxCellAngleRZ` parameters, which define the angular window used by the conformal seeding algorithm to search for the next hit. These parameters were inherited from the CLICdet geometry and had not been re-optimised for the CLD detector geometry. The default value of 0.1 was found to be too restrictive for reconstructing highly displaced tracks.

A dedicated study was conducted to evaluate the impact of increasing these parameters. Setting both `MaxCellAngle` and `MaxCellAngleRZ` to 0.5 resulted in significant improvement, allowing efficient reconstruction of displaced vertices up to 600 mm, in line with conformal tracking's

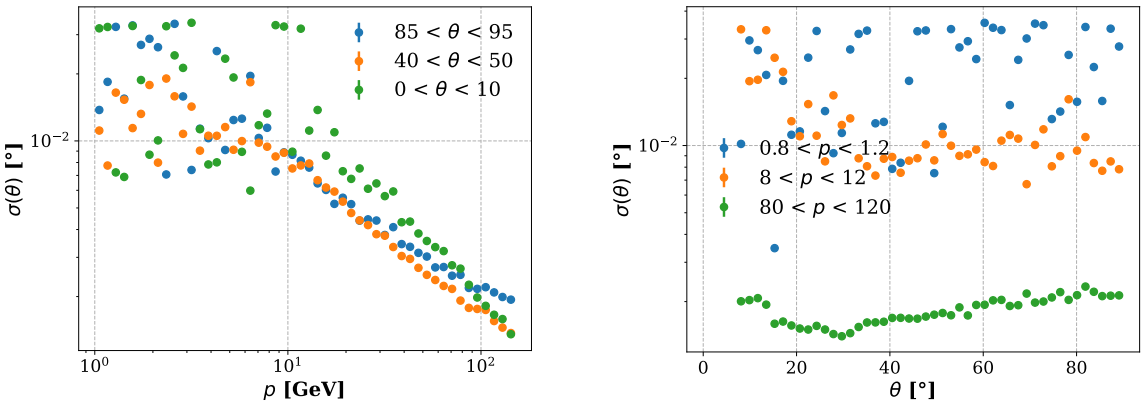

Figure 5.7: Polar angle resolution (θ) as a function of the momentum (left) and polar angle θ (right) for prompt muons, obtained with fast simulation (Delphes). The scattered "clouds" of points are an artifact of the parametrised, binned Delphes response: the resolution is evaluated per (p, θ) bin and plotted as discrete points, not a continuous surface; this is not a physical effect.

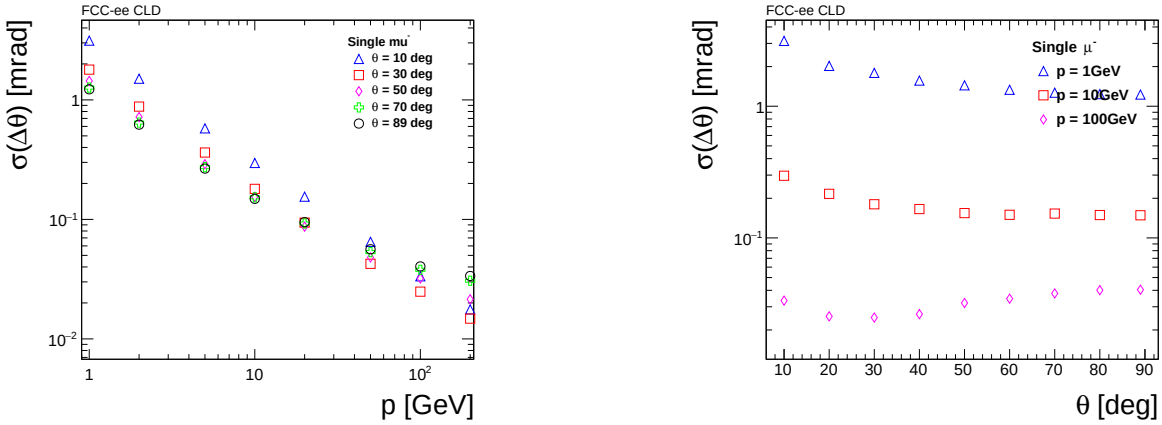

Figure 5.8: Polar angle resolution (θ) as a function of the momentum (left) and polar angle θ (right) for prompt muons, obtained with full simulation (Geant4 + reconstruction).

published performance. This was validated using HNL events.

To assess potential side effects, the fake rate was determined using $Z \to b\bar{b}$ events. The results showed an increase in fake tracks by about 5–10% for very displaced tracks Figure 5.13, 5.14, 5.15, a trade-off that may be acceptable in analyses focusing on long-lived particles. This study was performed without including Beam-Induced Background. Nonetheless, the fake rate remains higher than expected, and further optimisation or filtering strategies may be required.

5.5.5 Electron Reconstruction Inefficiency due to Track-Cluster Matching

During the analysis of displaced HNL decays, an issue was identified in the reconstruction of electrons, potentially stemming from inefficiencies in the track-cluster matching procedure. This was investigated by comparing the reconstructed vertex displacement distributions using two different definitions of electron candidates.

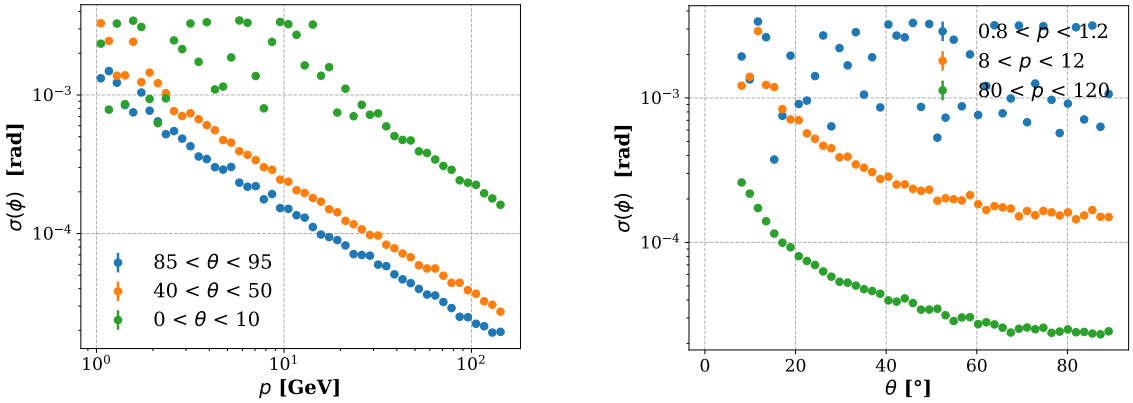

Figure 5.9: Azimuthal angle resolution (ϕ) as a function of the momentum (left) and polar angle θ (right) for prompt muons, obtained with fast simulation (Delphes).

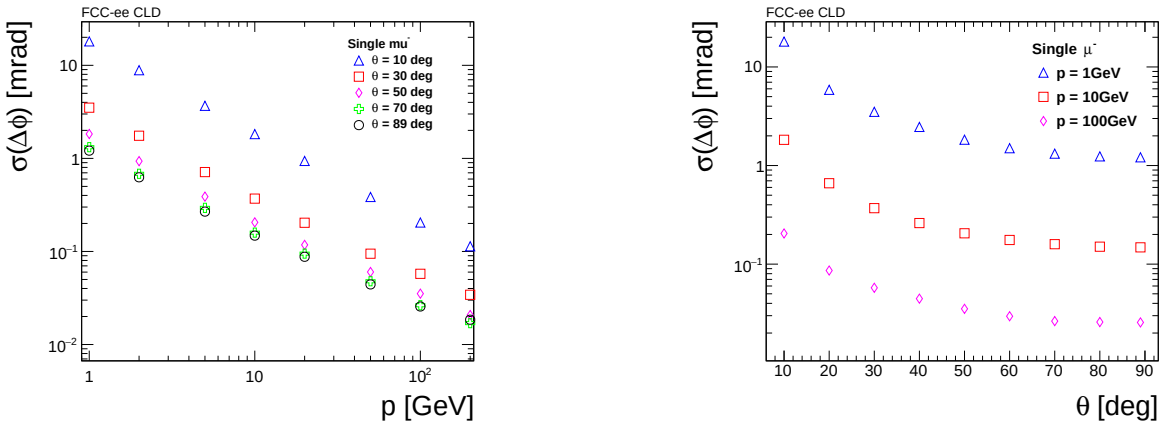

Figure 5.10: Azimuthal angle resolution (ϕ) as a function of the momentum (left) and polar angle θ (right) for prompt muons, obtained with full simulation (Geant4 + reconstruction).

In the first case, only tracks associated with reconstructed electrons were considered. In the second, a broader selection was used: reconstructed particles matching MC electrons within a $\Delta R < 0.2$ (in η–ϕ space), regardless of whether they were classified as electrons. The resulting plots show a striking difference: the number of reconstructed vertices doubles in the second case, Figure 5.16.

This indicates that the relevant tracks are present and correctly reconstructed, but not identified as electrons, likely due to a failure in associating tracks with electromagnetic clusters in the calorimeter. Such mismatches are especially problematic for displaced electrons, where the reconstruction is more challenging due to the unusual track–cluster geometry.

To ensure a more inclusive and realistic estimate of electron reconstruction efficiency in displaced topologies, the broader matching definition (reconstructed particles matching MC electrons within $\Delta R < 0.2$) will be adopted as the effective "reconstructed electrons" for the remainder of this study.

Scope note. A dedicated debugging and re-optimisation of the electron–reconstruction chain (in particular the track–cluster matching) was beyond the scope and timeline of this thesis. Where relevant, we therefore treat the effect as a reconstruction limitation and use the broader matching

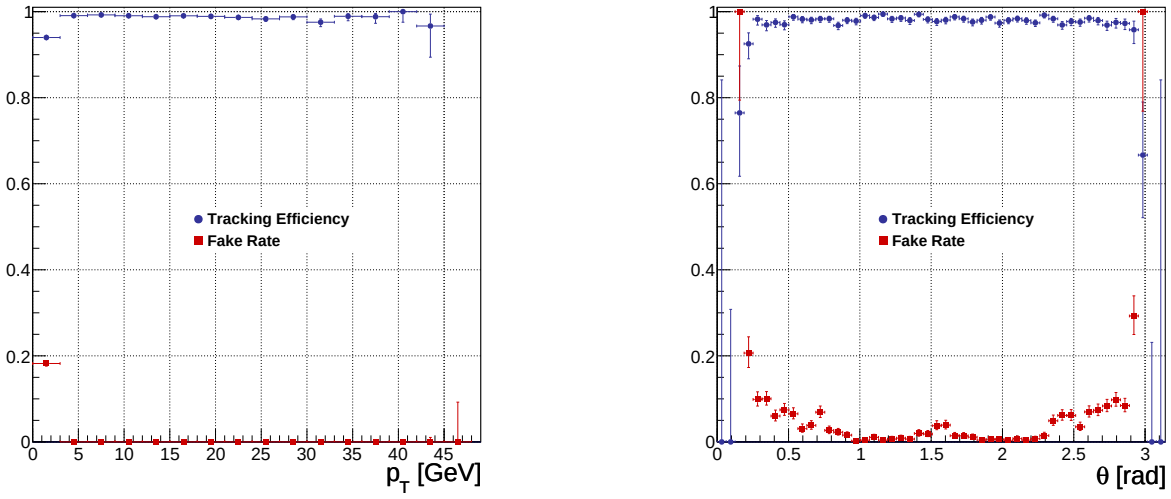

Figure 5.11: Tracking efficiency and fake rate as a function of transverse momentum p_T (left) and polar angle θ (right) for electrons in $Z \to \tau\tau$ events. Very good performance is observed for $p_T > 2$ GeV and θ in the range $0.2 < \theta < 2.9$ rad, consistent with the tracking detector acceptance.

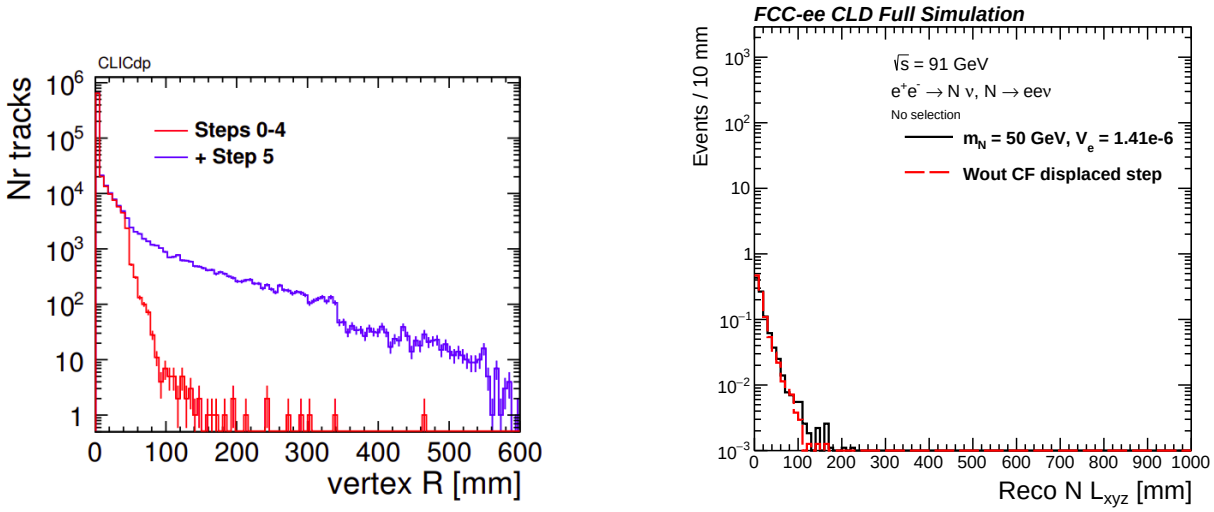

Figure 5.12: Impact of the displaced step in the conformal tracking algorithm. Left: Vertex reconstruction efficiency as a function of performance for $t\bar{t}$ events, results from the CLIC tracking performance paper [88], showing improved reconstruction with the displaced tracking step for large displacements. Right: Vertex reconstruction performance for 50 GeV HNL events, comparing configurations with and without the displaced tracking step. In contrast to the CLIC study, no significant gain in vertex reconstruction is observed for HNL at CLD.

definition described above to assess its impact on the analysis.

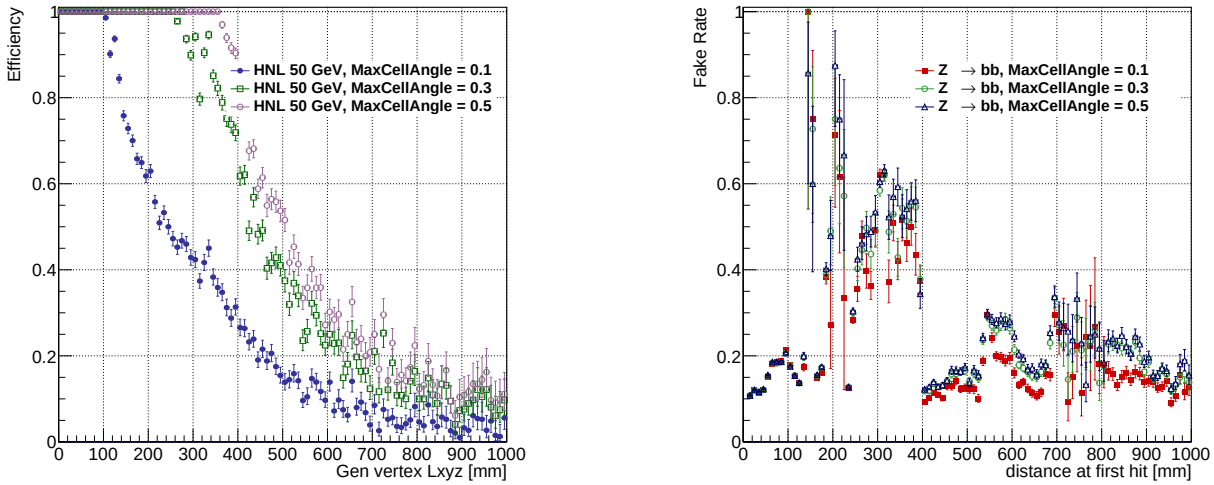

Figure 5.13: Effect of the `MaxCellAngle` and `MaxCellAngleRZ` parameters on tracking performance. Left: Tracking efficiency as a function of vertex displacement for HNL events, showing improved reconstruction of highly displaced vertices when increasing the angle parameters. Right: Fake rate as a function of vertex displacement for $Z \to b\bar{b}$ background events. While the fake rate increases slightly for highly displaced tracks, the impact remains moderate (less than 10%). These results confirm the benefit of retuning conformal tracking parameters for displaced vertex reconstruction.

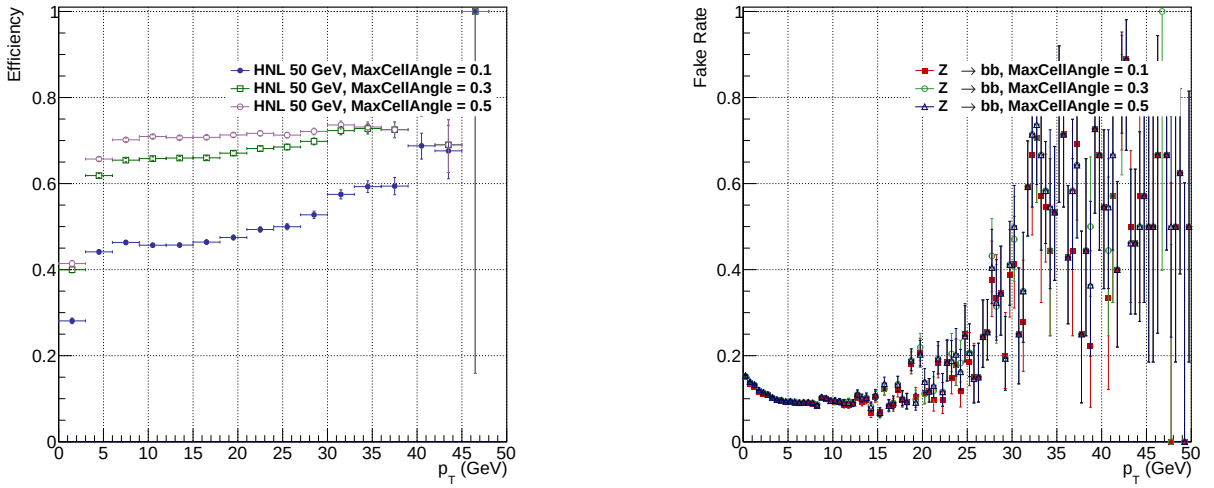

Figure 5.14: Impact of `MaxCellAngle` and `MaxCellAngleRZ` parameters on tracking performance as a function of transverse momentum (p_T). Left: Tracking efficiency for HNL events, showing noticeable improvement across the p_T spectrum when the angle parameters are increased. Right: Fake rate for $Z \to b\bar{b}$ background events, showing minimal variation with p_T, indicating that the parameter change does not significantly deteriorate background rejection.

5.6 Analysis

With the detector performance now validated in full simulation, we proceed to the physics analysis stage of the HNL study. The goal of this section is to evaluate how the transition from fast to

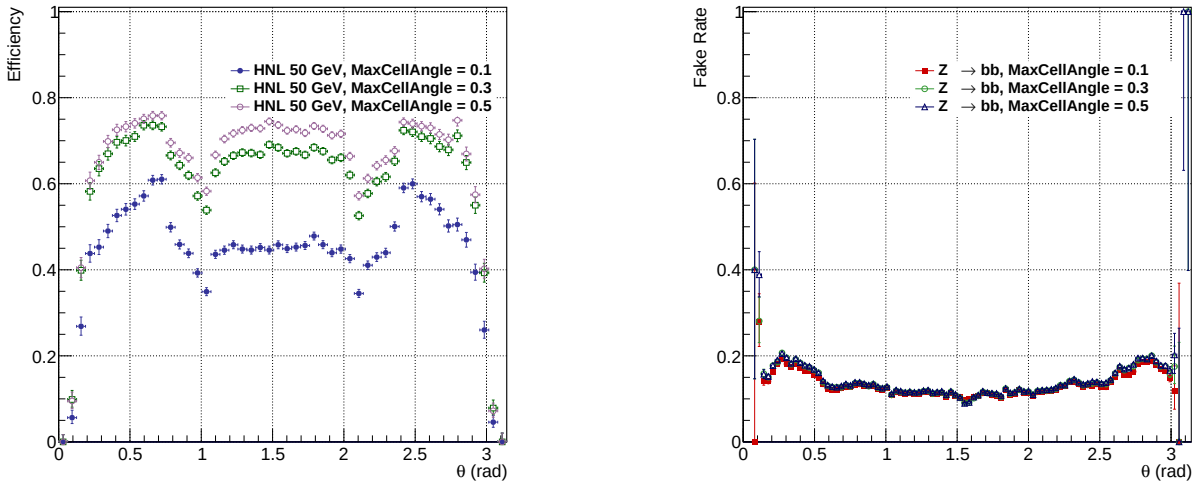

Figure 5.15: Impact of `MaxCellAngle` and `MaxCellAngleRZ` parameters on tracking performance as a function of polar angle (θ). Left: Tracking efficiency for HNL events, which improves across a wide range of θ values when increasing the angle parameters. Right: Fake rate for $Z \to b\bar{b}$ background events, which remains mostly stable across θ, indicating limited degradation of performance in terms of background rejection.

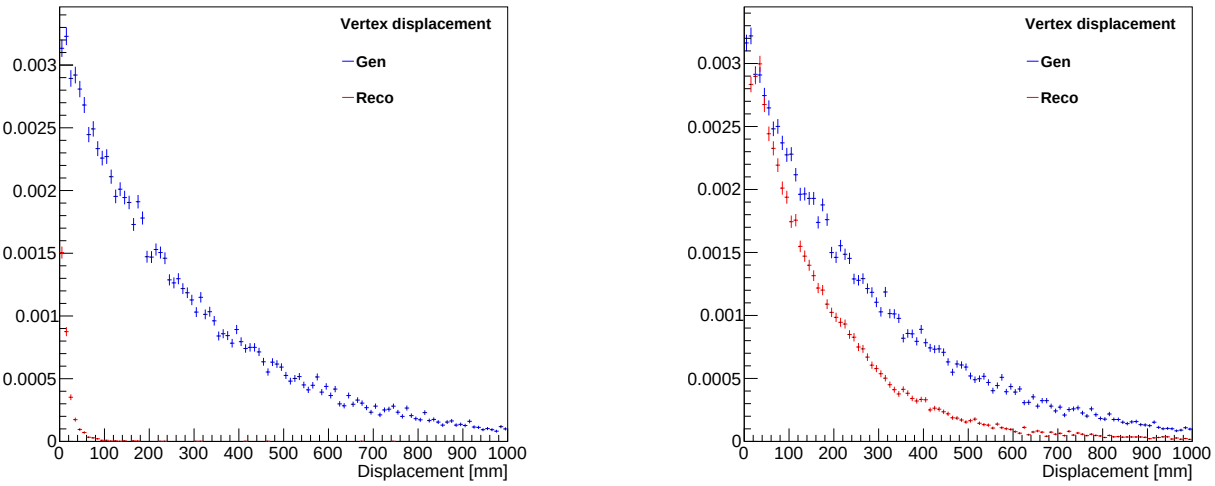

(a) HNL vertices with reconstructed electron tracks

(b) HNL vertices with all reconstructed tracks matching with MC electron within $\Delta R < 0.2$

Figure 5.16: Comparison of reconstructed HNL vertex displacement. Left: Using only tracks from reconstructed electron candidates, a clear discrepancy is observed between generated and reconstructed vertices, with many vertices missing. Right: Including all reconstructed tracks matched to MC electrons within $\Delta R < 0.2$, the number of reconstructed vertices significantly increases and the difference with the generated distribution primarily appears at large displacements, as expected from tracking inefficiencies.

full simulation impacts the key observables used in displaced vertex analyses. Given that HNL decays often produce long-lived particles with displaced vertices, accurate modeling of tracking

and reconstruction is essential to correctly estimate signal efficiencies and background suppression.

We begin with a preliminary comparison of key analysis variables between fast and full simulation.

5.6.1 Preliminary Comparison of Analysis Variables: Fast (IDEA) vs. Full (CLD) Simulation

This subsection presents a first look at how core analysis observables differ when reconstructed using fast simulation (Delphes) versus full simulation (Geant4 + reconstruction).

In fast simulation, reconstructed vertex displacement closely matches the truth-level displacement, as Delphes does not simulate detector inefficiencies or failures in vertex reconstruction. Importantly, Delphes does not account for tracking efficiency, which leads to an over-optimistic estimate of displaced vertex reconstruction performance.

This subsection presents a first look at how core analysis observables differ when reconstructed using fast simulation (Delphes) versus full simulation (Geant4 + reconstruction).

Detector note: the fast simulation uses the IDEA Delphes card, whereas the full simulation uses the CLD geometry with full reconstruction; accordingly, the comparison is indicative rather than strictly quantitative. In fast simulation, reconstructed vertex displacement closely matches the truth-level displacement, as Delphes does not simulate detector inefficiencies or failures in vertex reconstruction. For the Delphes setup and validation plots used in this work, see Section 5.5.1.

Interestingly, Figure 5.17 shows that the reconstructed di-electron invariant mass (m_{ee}) is very similar in both fast and full simulation. Likewise, the distribution of missing transverse momentum in the full simulation (Figure 5.18a) remains consistent with expectations, suggesting that key kinematic observables are robust against the choice of simulation.

In contrast, when examining displaced vertex reconstruction, full simulation provides a more realistic picture. Thanks to the correction of the `MaxCellAngle` and `MaxCellAngleRZ` parameters in the conformal tracking algorithm, the expected reconstruction range extends up to 600 mm, as originally reported in performance studies. However, the number of reconstructed vertices drops significantly at large displacements, reflecting the impact of tracking inefficiencies, particularly for low-momentum or non-prompt tracks that are more challenging to reconstruct.

This contrast is clearly illustrated in Figure 5.19, which compares the vertex–displacement distributions for fast and full simulation. While the full simulation successfully covers the expected displacement range, a reduced reconstruction efficiency at large displacements becomes evident. *Part of the difference may also intrinsic to the detector concepts:* the fast simulation uses the IDEA card, whose gaseous central tracker is generally more efficient for large-d_0 / LLP topologies, whereas the full simulation uses the all-silicon CLD tracker, where pattern-recognition and acceptance effects can reduce efficiency at large radii. Hence the discrepancy should not be attributed solely to reconstruction algorithms; it also reflects different detector responses. A quantitative assessment would require a harmonised setup (common geometry and reconstruction). For reference, the distribution of generated HNL vertex displacements is shown in Figure 5.18b, which we use as the baseline for evaluating reconstruction performance.

5.6.1.1 Event Selection

The analysis presented here is based on the following selection criteria:

- **"Reco electron"**: A reconstructed track matched within $\Delta R < 0.2$ to a generator-level (truth) electron that is a *final-state* particle (`status`=1 in the MC record)[1], using MC information only for identification.

[1] "Status" refers to the MC truth record (e.g. HepMC/EDM4hep). Particles with `status`=1 are stable at generator level and form the final state; other codes label intermediate or decayed states.

- The final electron candidate is selected from Pandora Particles (regardless of their particle identification) that match both the MC electron and the reconstructed track within $\Delta R < 0.2$.

- **Object selection:**
  - Reco electron momentum > 1 GeV

- **Event selection:**
  - Exactly two reco electrons with sum electric charge equal to zero
  - Invariant mass incompatible with a Z boson: 2 GeV $< m_{ee} <$ 50 GeV
  - Missing transverse energy $\not{p}_T > 10$ GeV

- **Vertex reconstruction**: Performed using the two electron tracks

These differences underline the importance of using full simulation when studying observables that are sensitive to detailed reconstruction effects, demonstrating that while key kinematic observables remain stable, displaced vertex reconstruction is significantly impacted by realistic tracking performance.

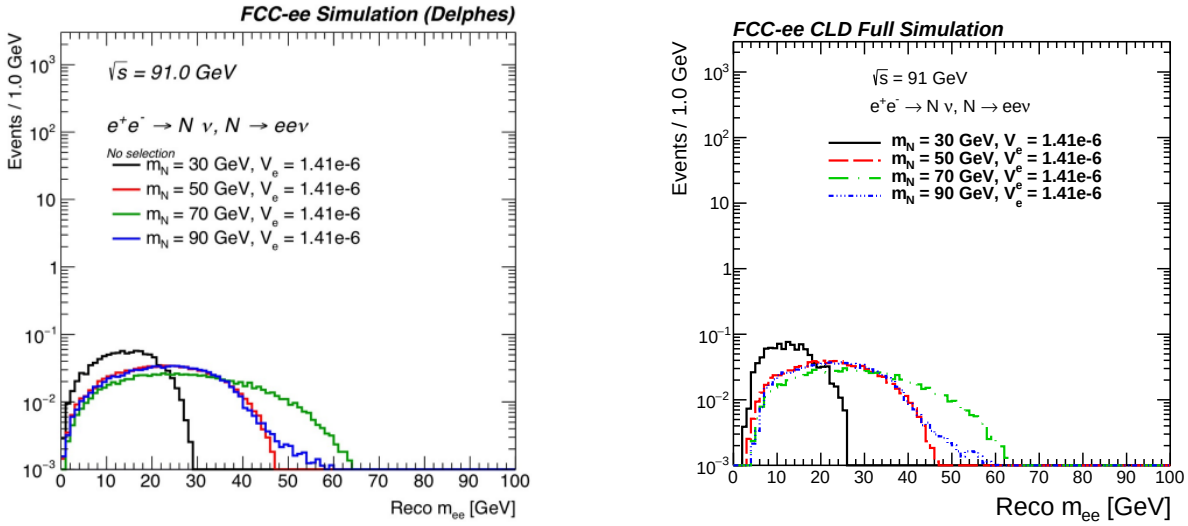

(a) (b)

Figure 5.17: Comparison of reconstructed di-electron invariant mass (m_{ee}) distributions between fast simulation with IDEA (a) and full simulation with CLD (b) for different HNL mass hypotheses. The shapes of the distributions are very similar across simulation methods, indicating stable reconstruction of this observable.

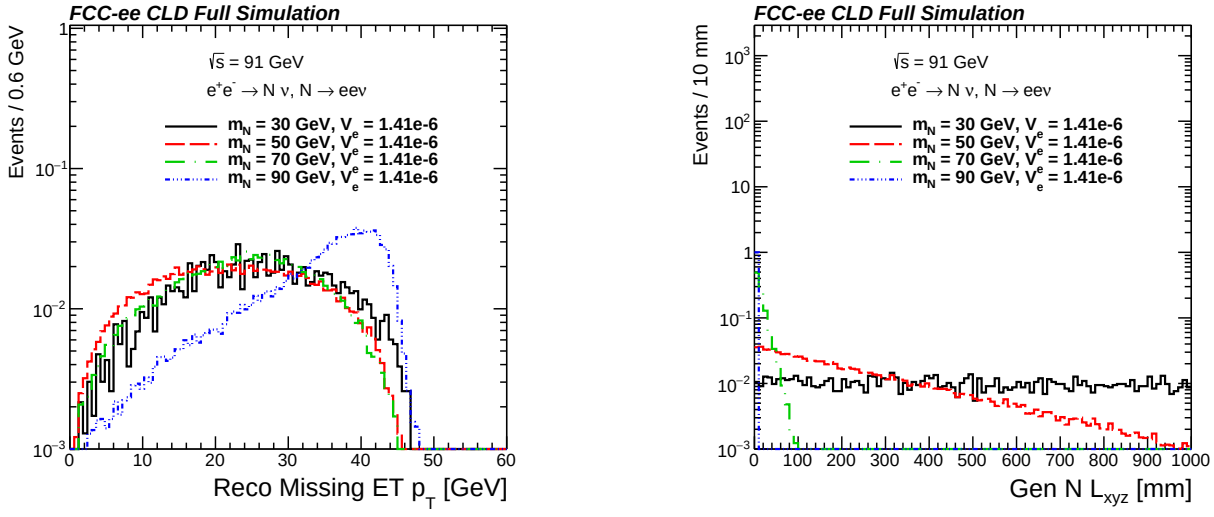

(a) (b)

Figure 5.18: Distributions from full simulation for various HNL masses: reconstructed missing transverse energy (a) and generated HNL vertex displacement (b). The missing transverse energy distributions are consistent with expectations from invisible decays, while the vertex displacement reflects the proper lifetime of the HNL for each mass point.

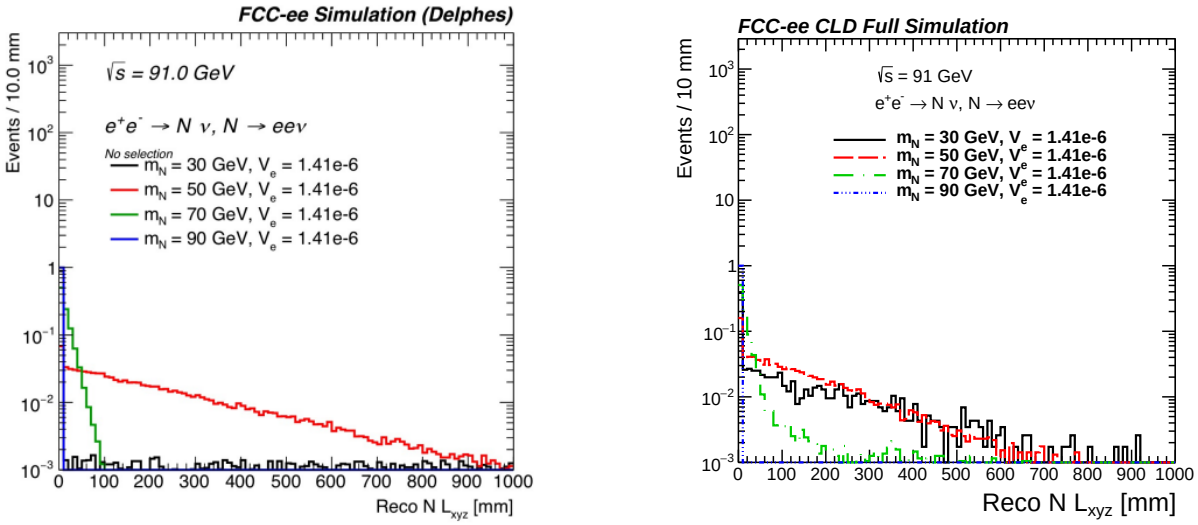

(a) (b)

Figure 5.19: Comparison of reconstructed HNL vertex displacement between fast simulation and full simulation. In fast simulation with IDEA (a), the reconstructed displacement closely follows the generated distribution, as tracking inefficiencies are not modelled. In full simulation with CLD (b), the distribution shows a significant drop in reconstruction efficiency at large displacements, probably reflecting the impacts of having a smaller number of hit in the outermost layers in CLD.

5.6.2 Backgrounds and Simulation Choices

We consider the following Standard Model backgrounds and their physical origins:

- $Z \to b\bar{b}$**:** electrons arise from heavy-flavour semileptonic decays and photon conversions; genuine $\not{p}_T$ comes from neutrinos in b decays (fake-electron component).

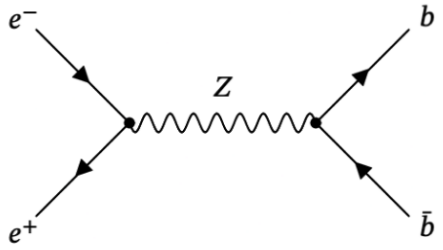

- $Z \to \tau^+\tau^-$ **(inclusive):** electrons originate from leptonic $\tau \to e\nu\bar{\nu}$ decays; events with two electrons and missing energy naturally mimic the signal topology ($ee\nu\nu$).

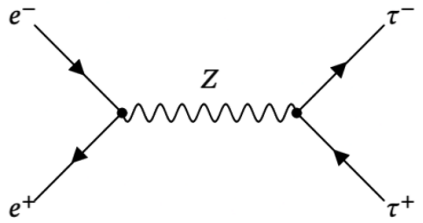

- $Z \to e^+e^-$**:** an irreducible dielectron final state; apparent $\not{p}_T$ can arise from resolution or acceptance effects.

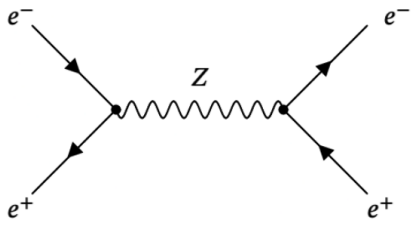

- $Z \to e^+e^-\nu\bar{\nu}$**:** four-fermion final state via off-shell electroweak diagrams; at the Z pole this contribution is strongly suppressed.

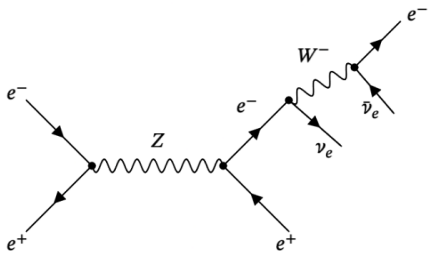

Practical constraint. It was not feasible to generate all background channels with the required statistics within the available computing quota. We therefore focused on what is expected to be the *dominant* background for the $ee+\not{p}_T$ topology at the Z pole, namely

$$Z \to \tau^+\tau^- \quad \text{with} \quad \tau^\pm \to e^\pm\nu\bar{\nu},$$

and used this sample in the analysis. The other channels are listed for completeness and context.

To align with the signal setup, backgrounds were generated at the Z pole with the same toolchain: MadGraph5_aMC@NLO (LO, `v3.6`, latest stable at production time) and Pythia 8 for decays, parton shower and hadronisation.

Table 5.2: Background summary at the Z pole. "Nominal" cross sections refer to the Z-pole (lineshape) values and serve as indicative scales; absolute rates depend on the beam energy spread and ISR treatment. For $Z \to \tau^+\tau^-$ we also quote the effective branching and cross section to the $ee\nu\nu$ final state using $\mathrm{BR}(\tau \to e\nu\bar{\nu}) \simeq 0.178$.

Background	Nominal σ at pole	Effective BR to $ee\nu\nu$	$\sigma(ee\nu\nu)$	Events (generated)
$Z \to b\bar{b}$	~ 9 nb	–	–	5×10^4
$Z \to \tau^+\tau^-$ (inclusive)	~ 2.0 nb	$(0.178)^2 \simeq 3.2 \times 10^{-2}$	~ 63 pb	1×10^7
$Z \to e^+e^-$	~ 2.0 nb	–	–	5×10^4
$Z \to e^+e^-\nu\bar{\nu}$	$\ll 1$ pb at m_Z	–	–	5×10^4

Notes: Cross sections were computed at leading order using MadGraph.

Reference to validation. The Delphes (fast-simulation) setup and validation plots used to benchmark these backgrounds are presented in Section 5.5.1.

5.6.3 Discriminating Variable Between $Z \to \tau\tau$ Background and HNL Signal

To effectively distinguish the heavy neutral lepton (HNL) signal from the dominant background process $Z \to \tau\tau$, several kinematic and topological variables were investigated.

To further optimise signal selection, a set of discriminant variables was tested:

- Total momentum (p)
- Transverse momentum (p_T)
- Polar angle (θ)
- Vertex displacement
- Angular separation between electrons ($\Delta R_{e1,e2}$)
- Di-electron invariant mass (m_{ee})
- Missing transverse energy (MET)
- Angular separation between MET and each electron ($\Delta R_{\mathrm{MET},e1}$ and $\Delta R_{\mathrm{MET},e2}$)
- Track multiplicity

Preliminary studies show that applying a lower cut on the transverse displacement of the vertex (e.g., $d_0 > 5$ mm) substantially reduces the contribution from $Z \to \tau\tau$ while retaining a large fraction of HNL signal events. When combined, potentially using multivariate analysis techniques, these variables can provide a robust framework for enhancing sensitivity to the HNL signal.

This study was conducted using 50,000 simulated events for each tested HNL mass, and 1 million events for the $Z \to \tau\tau$ background. The goal was to evaluate the discriminating power of several variables to separate the HNL signal from the dominant background.

The results show that variables such as momentum (p), transverse momentum (p_T) (Figure 5.20), polar angle (θ), vertex displacement (for 70 and 90 GeV HNL masses)(Figure 5.21), invariant mass of the electron pair (m_{ee}) (Figure 5.22), and track multiplicity do not provide strong separation

between the HNL signal and the $Z \to \tau\tau$ background. Their distributions are relatively similar for signal and background, making them less effective as standalone discriminants.

In contrast, the angular separation between the two electrons ($\Delta R_{e1,e2}$), Figure 5.22 and the angular separation between the MET and each electron ($\Delta R_{\not{p}_T,e1}$ and $\Delta R_{\not{p}_T,e2}$), Figure 5.23 are highly discriminating variables. These observables show clear differences between signal and background, allowing for a much better distinction. In particular, they highlight unique topological features of the HNL decays compared to the standard model background, making them extremely valuable for improving signal selection.

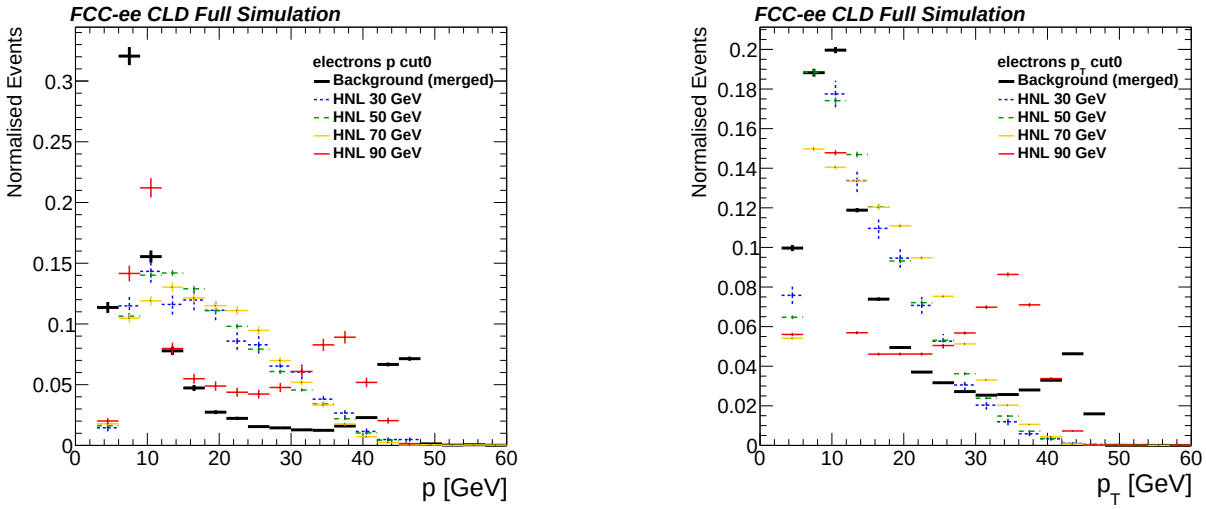

Figure 5.20: Comparison of the momentum (p, left) and transverse momentum (p_T, right) distributions for several HNL mass signals and the $Z \to \tau\tau$ background. No significant differences are observed between signal and background in these kinematic variables.

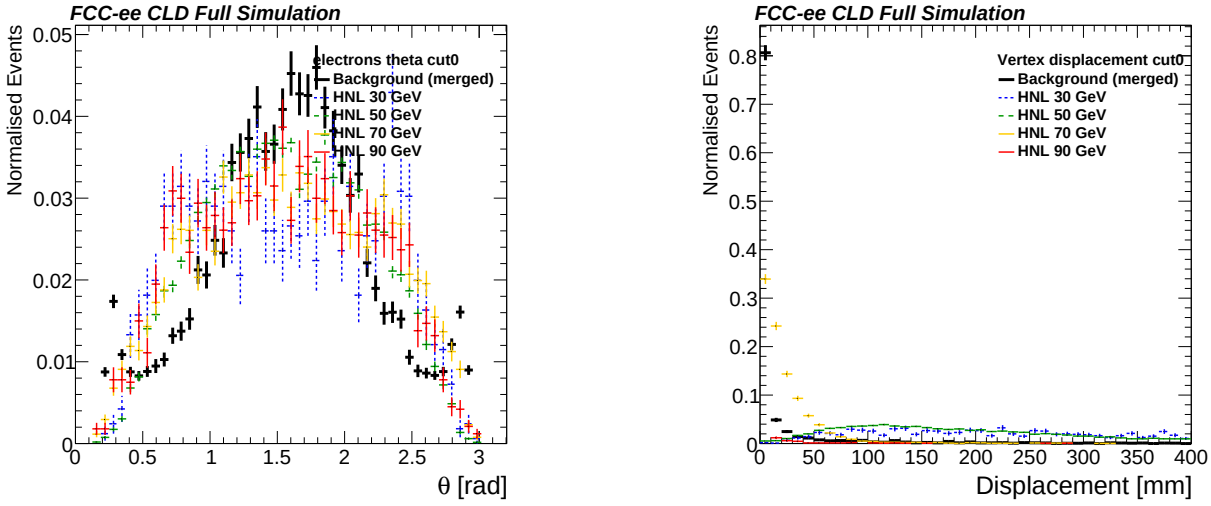

Figure 5.21: Comparison of the polar angle (θ, left) and vertex displacement (right) distributions for several HNL mass signals and the $Z \to \tau\tau$ background. No significant differences are observed in the θ distributions. For vertex displacement, the 90 and 70 GeV HNL signals are mostly prompt, resulting in distributions similar to the background.

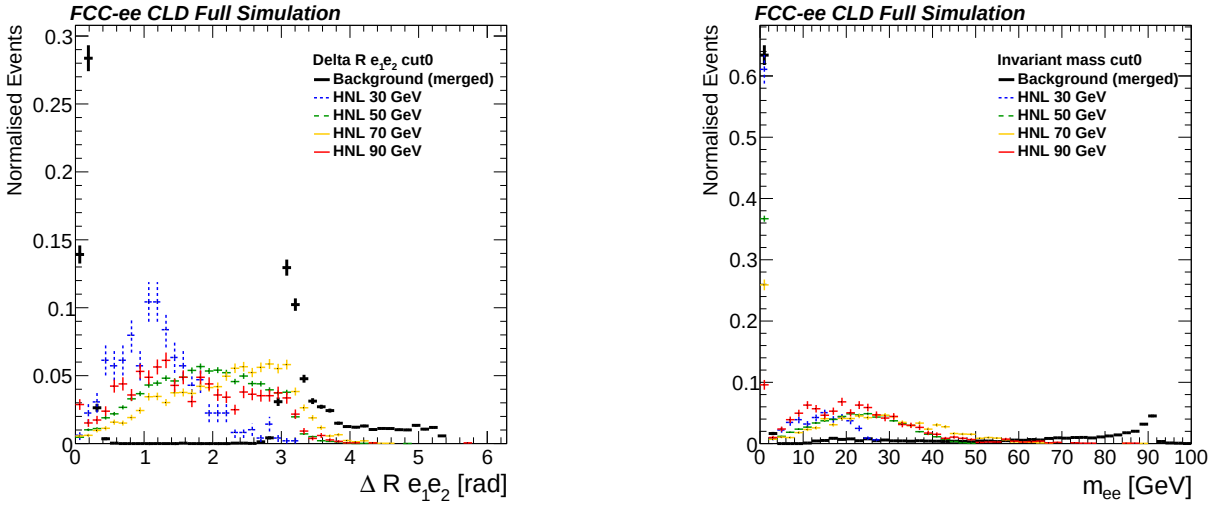

Figure 5.22: Distributions of $\Delta R(e_1, e_2)$ (left) and di-electron invariant mass m_{ee} (right) for various HNL mass signals and the $Z \to \tau\tau$ background. A clear separation between signal and background is visible in the $\Delta R(e_1, e_2)$ distribution, making it a highly discriminant variable. In contrast, the m_{ee} distribution shows less distinction between signal and background.

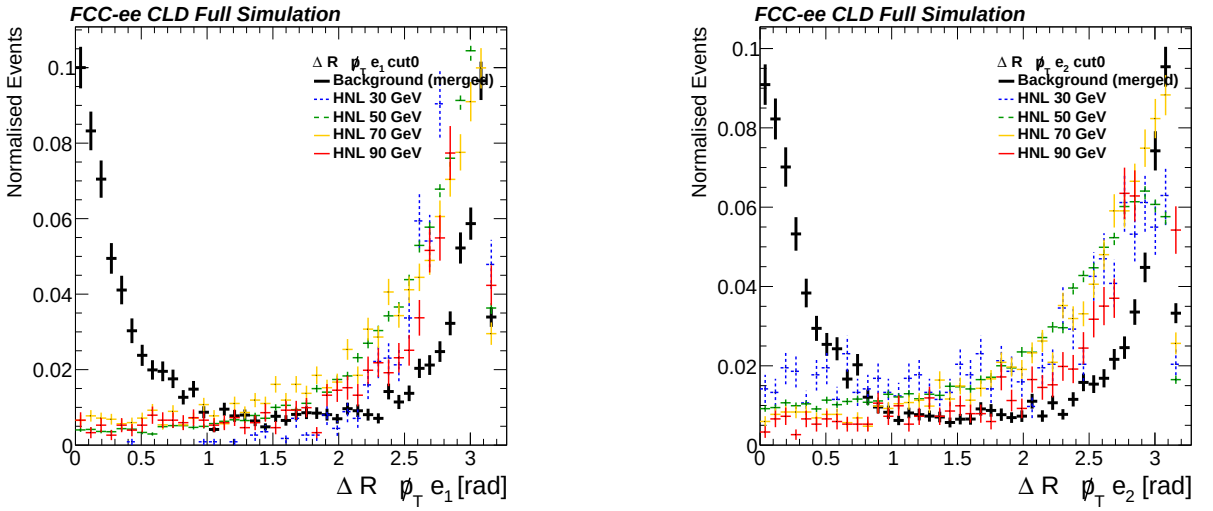

Figure 5.23: Distributions of $\Delta R(\not{p}_T, e_1)$ (left) and $\Delta R(\not{p}_T, e_2)$ (right) for various HNL mass signals and the $Z \to \tau\tau$ background. The background shows distinct features at $\Delta R < 0.5$ and around $\Delta R > 3$, while the signal distributions overlap these regions but maintain differentiable shapes, making these variables useful for signal-background discrimination.

To further enhance the separation between the HNL signal and the dominant $Z \to \tau\tau$ background, a multivariate approach based on a Boosted Decision Tree (BDT) classifier was employed. The BDT combines several kinematic and topological variables into a single discriminant, allowing for improved sensitivity compared to individual cut-based selections. The input features to the training include the reconstructed di-electron invariant mass, missing transverse energy, vertex displacement, angular separations $\Delta R_{e_1,e_2}$, $\Delta R_{\mathrm{MET},e_1}$, $\Delta R_{\mathrm{MET},e_2}$. Figure 5.25 displays the

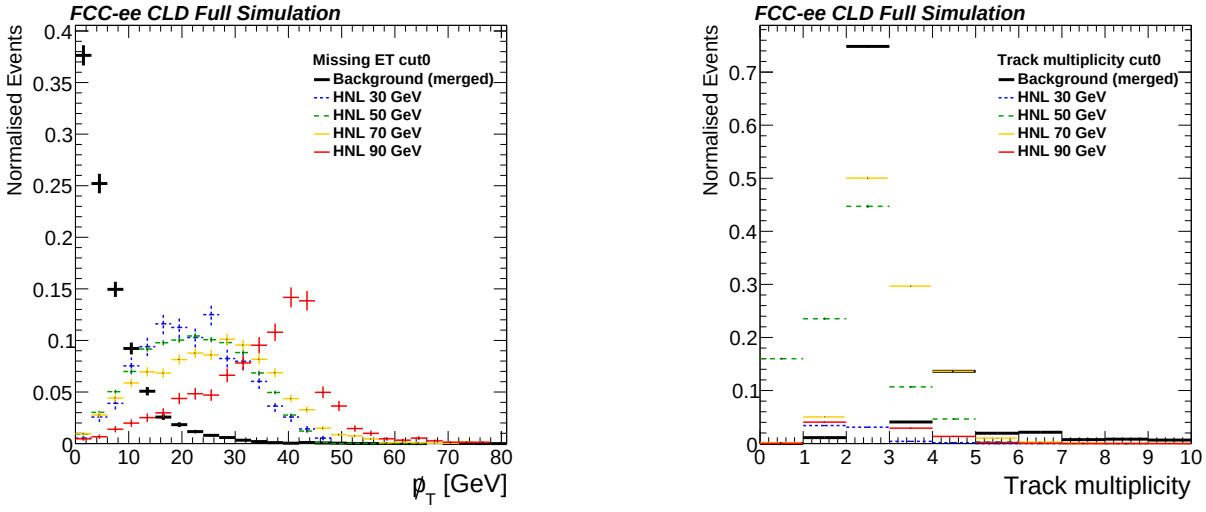

Figure 5.24: Distribution of missing transverse energy ($\not{E}_T$, left) and track multiplicity (right) for HNL signals with various masses and the $Z \to \tau\tau$ background. The background peaks sharply near zero $\not{E}_T$, while the signal distributions spread over higher values. Track multiplicity distributions show similar behaviour for both signal and background.

distributions of these variables for signal (green) and background (red) in the case of a benchmark HNL mass of 50 GeV. The figure illustrates that, while some observables provide limited discriminating power individually, their combination through the BDT maximises the overall separation between signal and background.

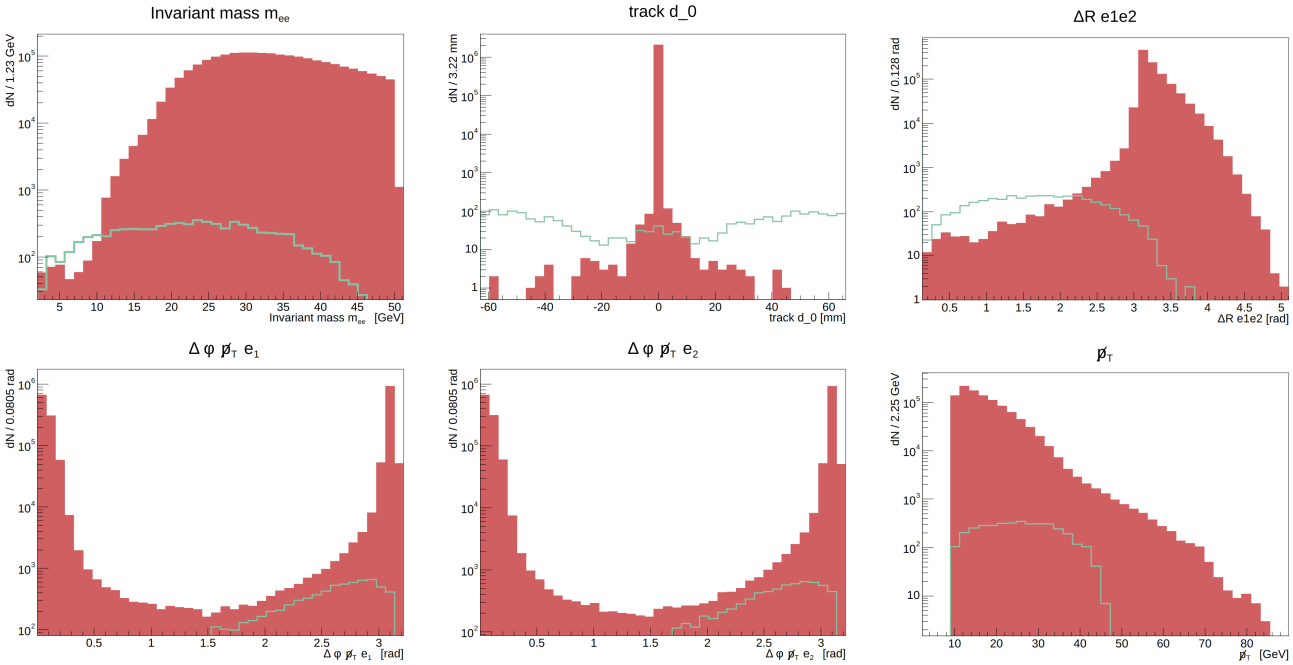

Figure 5.25: Signal (green) and background (red) variable distributions used as input features for the BDT training for N = 50 GeV.

Cutflow and Expected Yields

The cutflows below report *expected event yields* after each selection step. All templates are normalised to the integrated luminosity $\mathcal{L} = 150$ ab^{-1}. Signal cross sections are the *rescaled* values used in our production (factor 10^5 larger than in the reference paper, see Sec. 5.6.2); only **statistical** uncertainties are shown.

Table 5.3: Signal cutflow at the Z pole for benchmark HNL masses. Yields are normalised to $\mathcal{L} = 150$ ab^{-1}. The quoted cross sections are those *used* in our samples (rescaled by 10^5 relative to the paper values). Uncertainties are statistical only.

Process	HNL 30 [GeV]	HNL 50 [GeV]	HNL 70 [GeV]	HNL 90 [GeV]
Cross Section [pb] ($\times 10^5$)	$(6.64 \pm 0.01) \times 10^{-5}$	$(4.54 \pm 0.01) \times 10^{-5}$	$(6.64 \pm 0.01) \times 10^{-5}$	$(1.75 \pm 0.03) \times 10^{-7}$
Before selection	$9.96 \pm 0.05 \times 10^2$	$6.80 \pm 0.03 \times 10^2$	$2.95 \pm 0.01 \times 10^2$	2.62 ± 0.01
Exactly 2 reco e	2.09 ± 0.21	40.7 ± 0.7	148 ± 0.9	2.03 ± 0.01
Invariant mass $\neq Z$ boson	2.09 ± 0.21	40.7 ± 0.7	148 ± 0.9	2.02 ± 0.01
$\not{p}_T > 10$ GeV	1.83 ± 0.20	34.5 ± 0.7	135 ± 0.9	1.97 ± 0.01
Reconstructed vertex	1.74 ± 0.19	33.2 ± 0.7	129 ± 0.9	1.94 ± 0.01
$\lvert d_0 \rvert > 5$ mm	1.29 ± 0.16	25.9 ± 0.6	91.7 ± 0.7	0

Table 5.4: Background cutflow at the Z pole (yields normalised to $\mathcal{L} = 150$ ab^{-1}). "Cross Section" lists nominal values at the pole; only statistical uncertainties are quoted.

Process	$Z \to e^+e^-$	$Z \to b\bar{b}$	$Z \to \tau^+\tau^-$	$Z \to e^+e^-\nu\bar{\nu}$
Cross Section [pb]	1.46×10^3	6.65×10^3	1.48×10^3	$(3.05 \pm 0.01) \times 10^{-4}$
Before selection	$(2.19 \pm 0.01) \times 10^{11}$	$(9.97 \pm 0.05) \times 10^{11}$	$(2.21 \pm 0.01) \times 10^{11}$	$(4.57 \pm 0.02) \times 10^4$
Exactly 2 reco e	$(1.98 \pm 0.01) \times 10^{11}$	$(9.05 \pm 0.13) \times 10^{10}$	$(8.80 \pm 0.02) \times 10^9$	$(3.77 \pm 0.02) \times 10^4$
Invariant mass $\neq Z$ boson	$(3.92 \pm 0.04) \times 10^{10}$	$(9.05 \pm 0.13) \times 10^{10}$	$(8.87 \pm 0.02) \times 10^9$	$(3.76 \pm 0.02) \times 10^4$
$\not{p}_T > 10$ GeV	$(6.71 \pm 0.05) \times 10^8$	$(1.22 \pm 0.05) \times 10^{10}$	$(3.30 \pm 0.01) \times 10^9$	$(2.98 \pm 0.02) \times 10^4$
Reconstructed vertex	$(6.10 \pm 0.05) \times 10^8$	$(1.21 \pm 0.05) \times 10^{10}$	$(3.24 \pm 0.01) \times 10^9$	$(2.91 \pm 0.02) \times 10^4$
$\lvert d_0 \rvert > 5$ mm	0	0	0	0

The output of the BDT is shown in Figure 5.26 for different benchmark HNL masses. The distributions demonstrate that the multivariate classifier achieves a clear separation between signal (green) and background (red). For all tested HNL mass points, the signal events are clustered towards high BDT response values, while the background events populate the lower part of the distribution. This confirms that the BDT successfully exploits the combined information of the input variables to enhance discrimination power beyond what can be achieved with individual cuts.

For the 30 GeV and 50 GeV benchmarks, an additional requirement of $|d_0| > 0.5$ mm was applied to the signal in order to exploit the characteristic displaced topology. For the background, however, this cut removes nearly all MC events, while some physical events are still expected, leaving too few statistics to train the BDT. To address this, the background histograms shown after the BDT response have been renormalised to the expected number of events after the d_0 cut. The BDT has been trained with a sample of background without the d0 cut, and the output has been renormalised to the expected number of events after the d0. It has been verified that there are weak correlations between the d0 variable and the other variables of the BDT. In the 30 GeV case, where the HNL has the longest flight distance, the BDT achieves an almost perfect separation between signal and background, although only a small number of signal events survive due to the large displacement and associated inefficiencies in electron reconstruction. The 50 GeV benchmark achieves a similarly good separation, representing a balanced case between signal yield and background rejection.

For the 70 GeV and 90 GeV benchmarks, no explicit cut on d_0 is applied; instead, d_0 itself is included as an input variable to the BDT. At 70 GeV, the performance appears visually less striking, since the smaller displacements resemble more closely the topology of $Z \to \tau\tau$ events. Nevertheless, the BDT still provides good discrimination power. At 90 GeV, the decays are almost prompt, and the separation quality improves again compared to 70 GeV, reaching a level similar to the 50 GeV case.

A closer inspection of the individual benchmark masses reveals distinct behaviours. In the 30 GeV case, where the HNL has the longest time of flight, the BDT achieves an almost perfect separation of signal and background. However, only a small number of signal events survive due to the large displacements and the associated inefficiencies in electron reconstruction. For the 50 GeV benchmark, the separation remains very good, with a balanced compromise between signal yield and background rejection. The 70 GeV case appears visually to be the least favourable, as the displacement is smaller and thus closer to the topology expected from $Z \to \tau\tau$ background events; nevertheless, the BDT still provides good separation. Finally, for the 90 GeV benchmark, the situation improves slightly compared to 70 GeV: the decays are mostly prompt, leading to distributions similar to those at 50 GeV, and the separation remains robust.

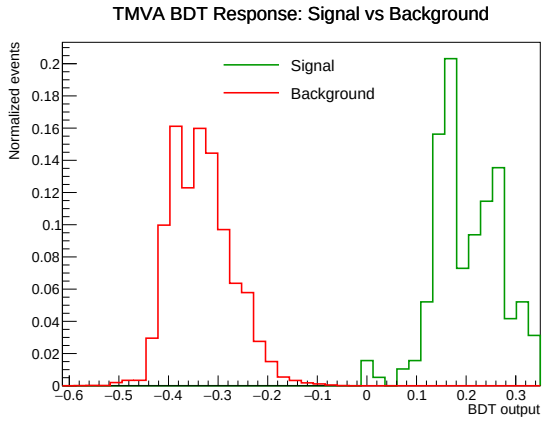

(a) $N = 30$ GeV

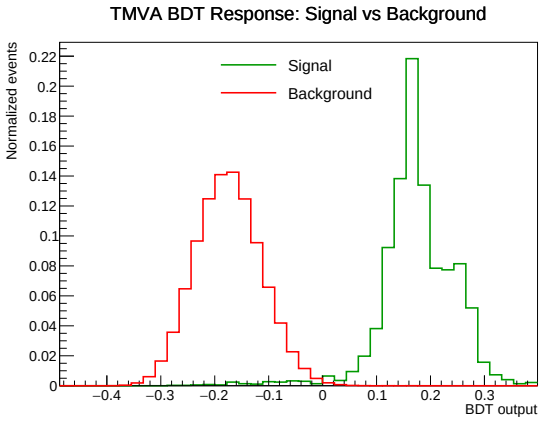

(b) $N = 50$ GeV

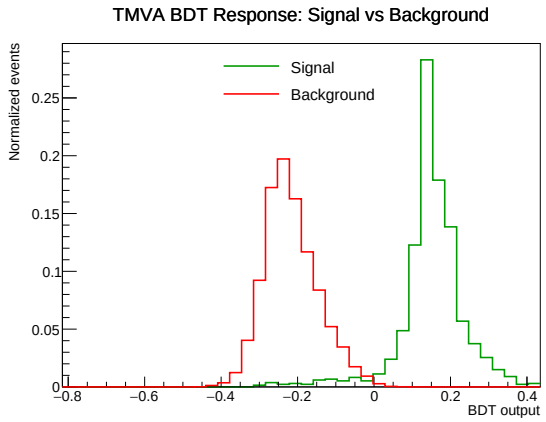

(c) $N = 70$ GeV

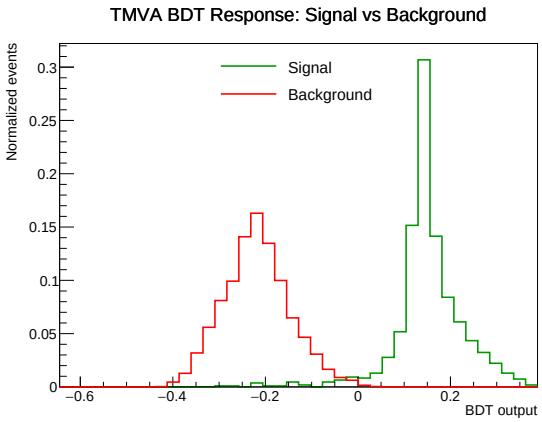

(d) $N = 90$ GeV

Figure 5.26: BDT response distributions for the different HNL benchmark masses. Signal is shown in green and background in red.

In summary, the study of discriminating observables has shown that while variables such as

momentum, polar angle, and invariant mass alone provide limited separation, angular correlations and displaced vertex observables offer stronger sensitivity. By combining all features in a BDT, a powerful discriminant is obtained, enabling efficient separation of HNL signal from the $Z \to \tau\tau$ background. These results form the basis for the statistical interpretation presented in the following section, where expected exclusion limits on the HNL production cross section and the active–sterile mixing parameters are derived.

5.6.4 Expected Sensitivity

Exclusion limits are derived from a binned fit to the BDT output distribution. Signal and background templates are normalised to their expected event yields,

$$N_k \;=\; \sigma_k \times \mathcal{L} \times \varepsilon_k\,, \qquad \text{with} \quad \mathcal{L} = 150 \text{ ab}^{-1},$$

where σ_k is the process cross section, ε_k the total selection efficiency, and $\mathcal{L}$ the integrated luminosity. The fit is performed on the BDT score histogram, with the total expectation per bin given by the sum of the normalised signal and background templates. The reported limits (e.g. on $\sigma \times \text{BR}$ or on the mixing parameter) are obtained from this template fit.

Uncertainties. Only **statistical** uncertainties are considered in this baseline result; systematic effects (detector modelling, background cross sections, luminosity calibration, and template-shape systematics) are not included and will make the limits conservative/optimistic depending on their size and treatment.

Based on the BDT discriminant introduced in the previous section, the expected exclusion limits on the HNL production cross section are derived. The statistical interpretation is performed with the `Combine` framework [161], employing the CL_s method with the BDT output distributions serving as the final discriminant. The expected 95% confidence level (CL) upper limits are obtained for each of the tested benchmark masses.

The results are shown in Figure 5.27, where the expected limits on the production cross section are presented for $N = 30$, 50, 70 and 90 GeV. For all benchmark points, the expected sensitivity extends well below the theoretical cross sections, highlighting a good potential of FCCee to probe HNL production across a wide mass range.

These results can be further interpreted in terms of the active–sterile mixing angle $|U_\ell|^2$. The corresponding exclusion limits are displayed in Figure 5.28. The obtained sensitivities reach values of $|U_\ell|^2$ down to $\mathcal{O}(10^{-6})$, depending on the HNL mass. This demonstrates that FCCee, with its clean environment and large statistics at the Z pole, offers discovery potential for HNLs covering both long-lived and nearly prompt regimes.

Limits in the mixing plane. The cross-section limits can be recast into constraints on the active–sterile mixing by exploiting the proportionality $\sigma(e^+e^- \to Z \to \nu N) \propto |U_{\ell N}|^2$, assuming single-flavour mixing and the same signal model as used in the simulation. The resulting expected 95% CL upper limits on $|U_{\ell N}|^2$ are shown in Figure 5.29 for the four benchmark masses. The sensitivity reaches the $\mathcal{O}(10^{-6})$ level, with mild mass dependence driven by the interplay of displacement, reconstruction efficiency, and the BDT discriminating power established in the previous section. As anticipated, the 70 GeV benchmark performs slightly worse than the other mass points, due to its smaller displacement being closer to the $Z \to \tau\tau$ background topology. Nevertheless, the sensitivity remains competitive, and the overall results highlight that FCCee would probe HNL scenarios across both long-lived and nearly prompt regimes.

Summary and outlook. In this chapter we validated the transition from fast to full simulation, identified and mitigated displaced-tracking limitations through a dedicated retuning, and addressed

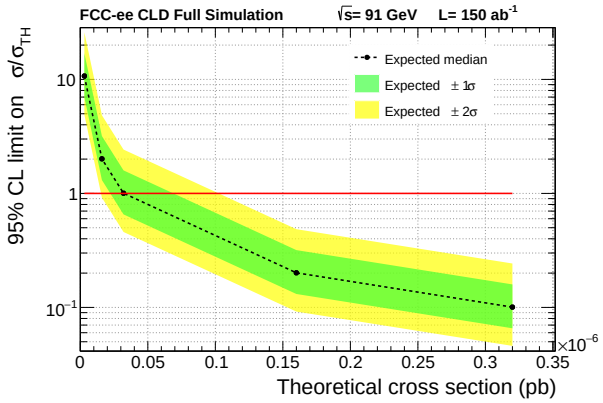

(a) $N = 30$ GeV

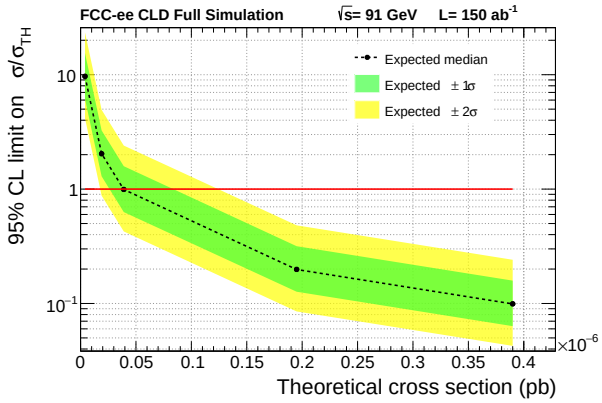

(b) $N = 50$ GeV

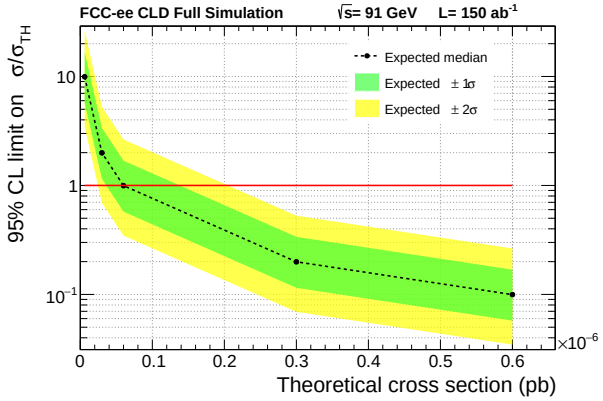

(c) $N = 70$ GeV

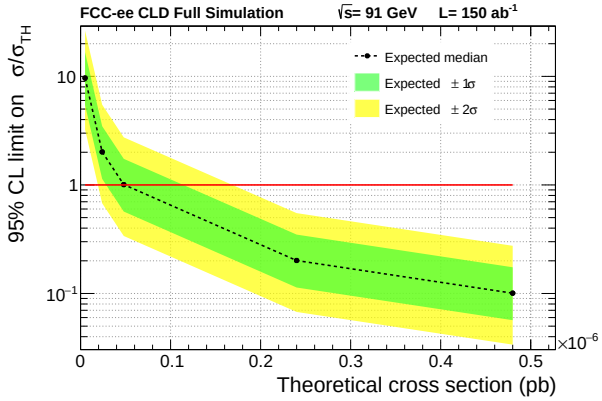

(d) $N = 90$ GeV

Figure 5.27: Expected exclusion limits on the HNL production cross section for different benchmark masses.

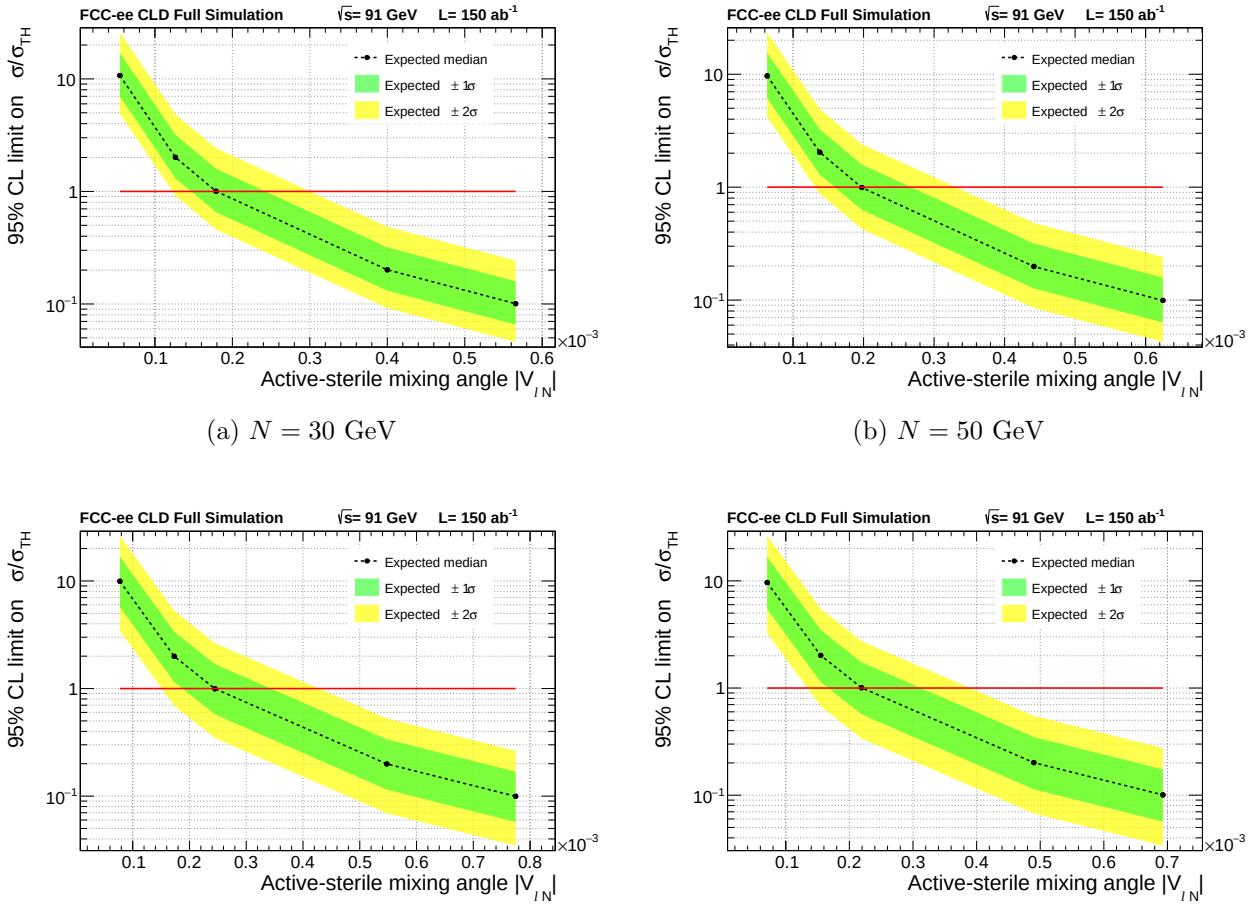

(a) $N = 30$ GeV

(b) $N = 50$ GeV

(c) $N = 70$ GeV

(d) $N = 90$ GeV

Figure 5.28: Expected exclusion limits on the mixing angle for different benchmark masses.

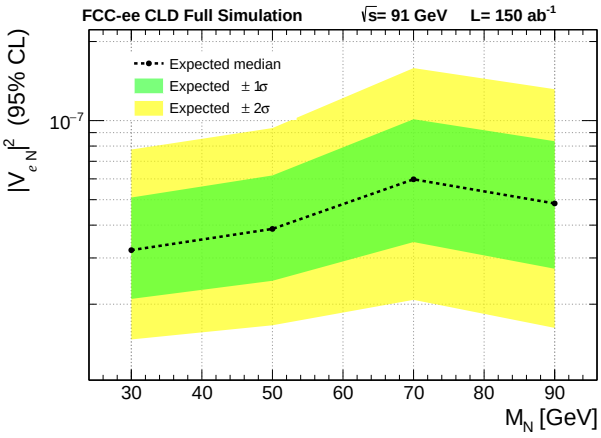

Figure 5.29: Expected and observed exclusion limits on the squared mixing angle $|V_{eN}|^2$ as a function of the HNL mass, combining all benchmark points.

an electron reconstruction inefficiency relevant for displaced topologies. Building on these improvements, we constructed a BDT that combines kinematic and topological observables, and used its output as the final discriminant in a CL_s framework with `Combine`. The analysis delivers robust expected limits on the production cross section (Figure 5.27) and on the active–sterile mixing (Figure 5.28). Future work will focus on refining the displaced-electron reconstruction, extending the training to additional backgrounds, and exploring systematic uncertainties to convert these expected reaches into full sensitivity projections.

Conclusion

The work presented in this thesis has explored the interplay between detector technology, tracking performance, and new physics searches in the context of the Future Circular Collider in its electron–positron phase (FCC-ee).

Both the theoretical and practical aspects of charged-particle tracking have been reviewed, with particular emphasis on reconstruction methods such as conformal mapping, Kalman filtering, and vertexing. Based on these techniques, dedicated tools have been developed to perform systematic studies of tracking performance across different detector geometries, providing a robust framework for guiding design optimisation and evaluating the impact of various layout choices.

On the technological side, the performance of advanced Monolithic Active Pixel Sensors (MAPS) has been investigated through beam tests of the CE-65 prototypes. A detailed study of digitisation strategies has shown that two-bit digitisation achieves a spatial resolution close to that of the analogue case, and significantly better than one-bit encoding. This approach could allow a resolution of around 5 μm even with larger pixel pitches, thus enabling reduced power consumption, a critical factor for the innermost vertex detectors at FCC-ee. These results highlight the potential of MAPS technologies to meet the demanding requirements of future collider experiments.

At the detector level, the tracking performance of the CLD concept has been evaluated through detailed simulation studies. The tracking efficiency, momentum resolution, and vertexing capabilities have been characterised under different assumptions on geometry, magnetic field, and material budget. These results confirm the suitability of the CLD design for the FCC-ee physics programme, while identifying key parameters that drive performance and that must be carefully optimised.

The physics reach of FCC-ee has then been illustrated with a benchmark study of Heavy Neutral Leptons (HNLs). Sensitivity estimates obtained with full detector simulation have been found to be broadly consistent with those derived from fast simulation, but the full simulation provides a much more reliable description of detector effects, especially those affecting displaced-vertex signatures. This underlines the importance of full-simulation studies for robust physics projections. At the same time, it should be emphasised that a systematic treatment of uncertainties is still lacking and will be necessary to provide definitive sensitivity estimates for HNL searches.

Looking ahead, several outlooks emerge from this work:

- Detector R&D: Continued development of MAPS technologies is essential, with a focus on radiation hardness, timing capabilities, and power consumption. The CE-65 studies show that innovative digitisation strategies can deliver excellent spatial resolution while addressing power constraints, an encouraging direction for future sensor generations.

- Reconstruction techniques: Improvements in tracking algorithms, possibly including machine learning approaches for pattern recognition and vertex finding, could enhance performance in complex environments and extend sensitivity to challenging long-lived particle signatures.

- Physics prospects: While HNLs provide a representative benchmark, the methods developed here, from tracking studies to full-simulation analyses, are applicable to a broader class of long-lived particles, reinforcing the role of FCC-ee as a discovery machine at the precision frontier.

In conclusion, this thesis has demonstrated how advances in sensor technology, reconstruction tools, and detector performance studies directly enable progress in the search for new physics. By linking sensor R&D, systematic detector performance evaluation, and full-simulation analyses of long-lived particle signatures, it contributes to preparing the experimental tools and methodologies necessary to maximise the discovery potential of FCC-ee.

Appendix A

Tracking performances Appendix

A.0.1 Electrons and muons tracking performances

To further understand the detector's response to different particle species, the tracking performance for electrons is compared to that of muons by examining the ratio of their respective resolutions. This comparison is performed for the same set of variables as in the previous section, impact parameters (d_0, z_0), curvature-related quantities (ϕ_0, Ω, $\tan\lambda$), as well as polar and azimuthal angles (ϕ, θ), momentum p, and transverse momentum p_T. Ratio plots are shown first as a function of momentum, Figure A.1, A.2 ,A.3, A.4, and subsequently as a function of the polar angle θ, Figure A.5, A.6 ,A.7, A.8. These ratios highlight the specific challenges in reconstructing electrons due to their greater tendency for bremsstrahlung, especially at low momentum or small polar angles.

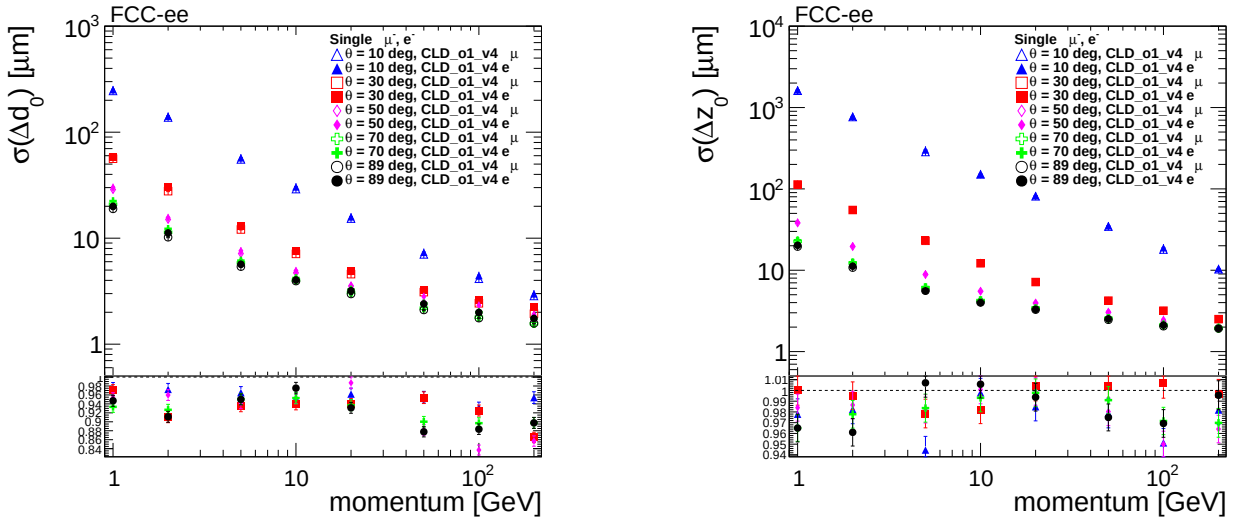

(a) Transverse impact parameter d_0 resolution

(b) Longitudinal impact parameter z_0 resolution

Figure A.1: Transverse (d_0) and longitudinal (z_0) impact parameter resolutions as a function of momentum for single muons and electrons in the CLD baseline geometry. The resolutions are extracted from the width of the residual distributions, $(x_{\text{reco}} - x_{\text{true}})$, for each track parameter.

A.0.2 Pions and muons tracking performances

In addition to electrons, tracking performance is also compared between muons and charged pions. As in the previous case, the ratio of resolution values is used to highlight differences in detector

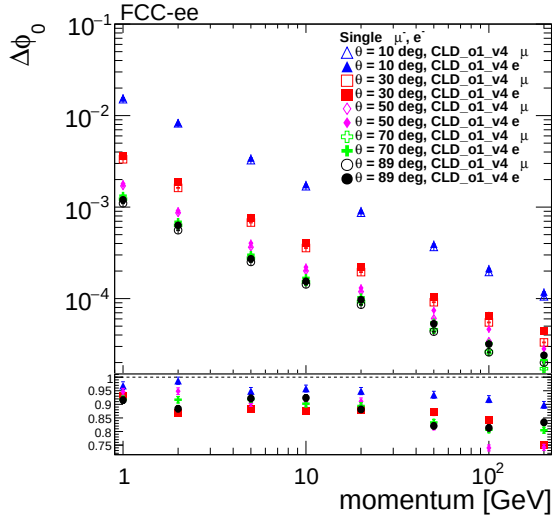

(a) Residual on the azimuthal angle at the point of closest approach ϕ_0 resolution

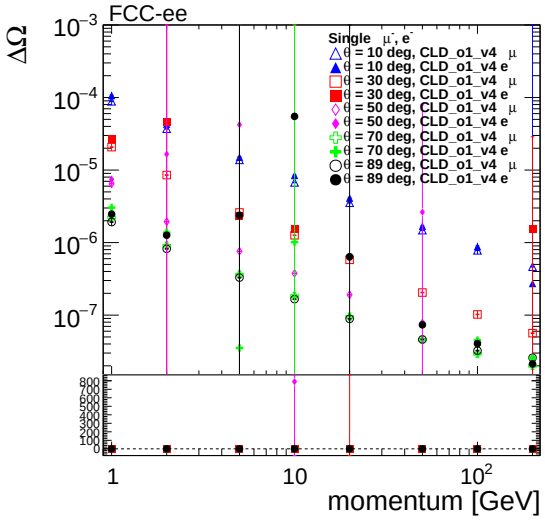

(b) Curvature Ω resolution

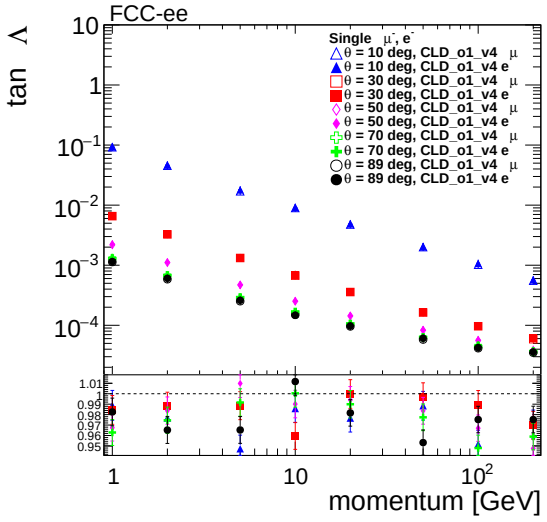

(c) track dip angle $\tan\lambda$ resolution

Figure A.2: Resolutions of the azimuthal angle at the point of closest approach (ϕ_0), curvature (Ω), and track dip angle ($\tan\lambda$) for single muons and electrons in the CLD baseline geometry. These parameters are derived from the helix model used in the track fit.

response. These comparisons are carried out for the same set of track parameters, d_0, z_0, ϕ_0, Ω, $\tan\lambda$, ϕ, θ, p, and p_T. The ratio plots are presented as a function of momentum, Figure A.9, A.10 ,A.11, A.12, and polar angle θ, Figure A.13, A.14 ,A.15, A.16,. This comparison helps identify the effects of hadronic interactions and energy loss mechanisms specific to pions. The tracking performance remains very similar, with only minor differences observed.

A.0.3 Impact of LumiCal Geometry Variations

The CLD_o2_v07 model is an updated version of CLD_o2_v05 Section 4.8.3, incorporating several improvements and refinements to the detector geometry. One key modification concerns the LumiCal (Luminosity Calorimeter), located in the very forward region of the detector and responsible for precise luminosity measurements via Bhabha scattering. In this version, the outer radius of the

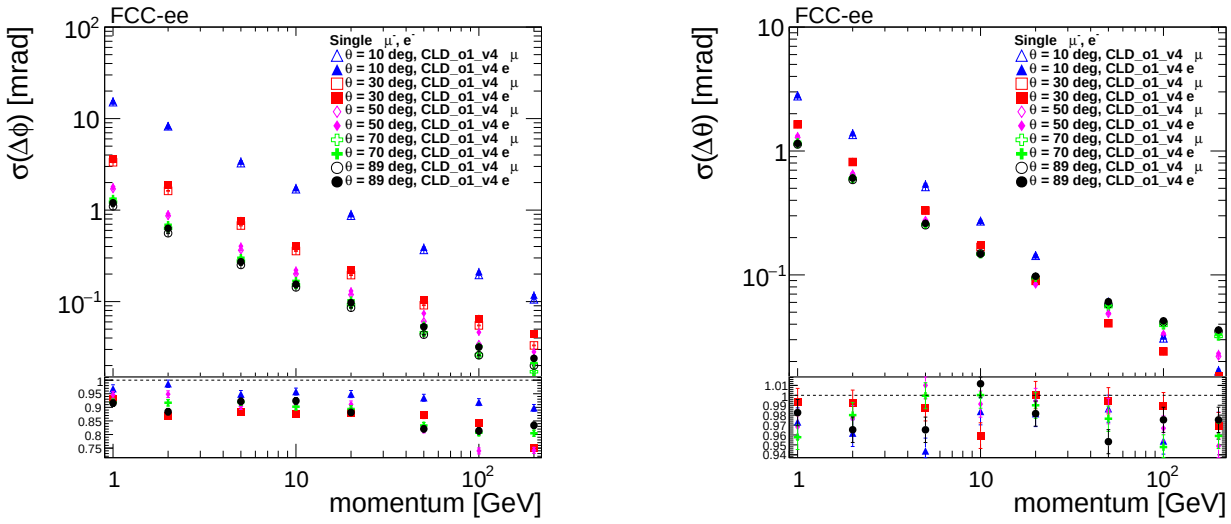

(a) Azimuthal angle ϕ resolution

(b) Polar angle θ resolution

Figure A.3: Azimuthal (ϕ) and polar (θ) angular resolutions for single muons and electrons in the CLD baseline geometry. The resolutions are obtained from the residuals between reconstructed and true track directions at the point of closest approach.

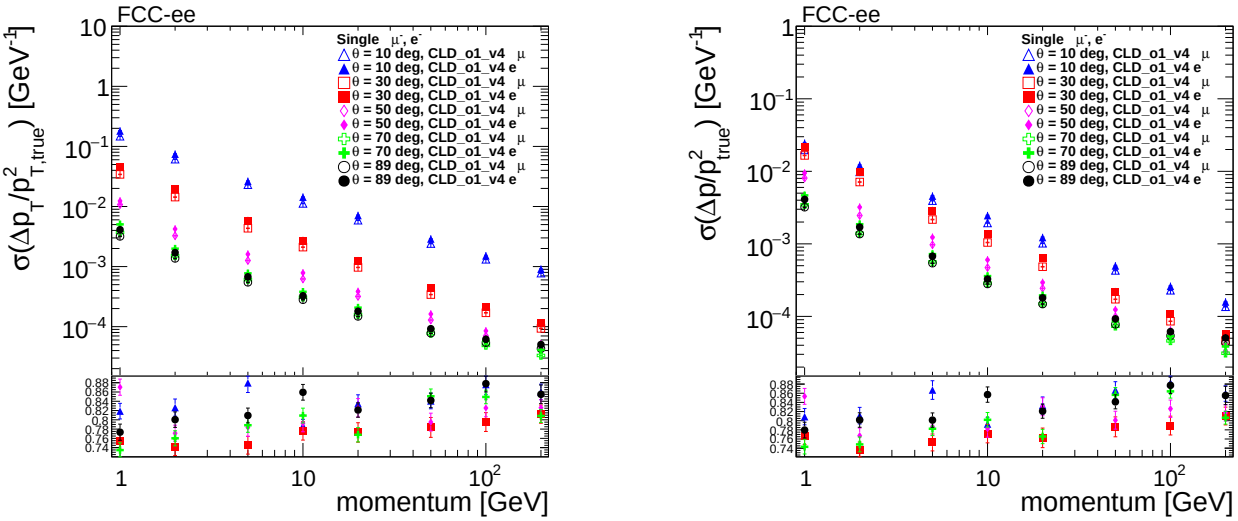

(a) Transverse momentum resolution

(b) Momentum resolution

Figure A.4: Transverse (p_T) and total momentum (p) resolutions as a function of momentum for single muons and electrons in the CLD baseline geometry. The resolutions are computed from the relative width of the $(p_{\text{reco}} - p_{\text{true}})/p_{\text{true}}$ distributions.

LumiCal has been slightly increased from 112 mm to 115 mm, and its position along the beam axis has been shifted to 1074 mm, with a fine alignment adjustment of 100 μm. Additionally, unused nose shield parameters were removed to streamline the geometry.

Although the LumiCal's primary function is calorimetric, such geometric modifications could, in principle, impact tracking performance in the forward region, either through changes in material distribution or spatial constraints close to the beamline. However, no significant changes in tracking resolution were observed. To improve loading performance in simulation and reconstruction workflows, stave assemblies were also introduced in the tracker barrel.

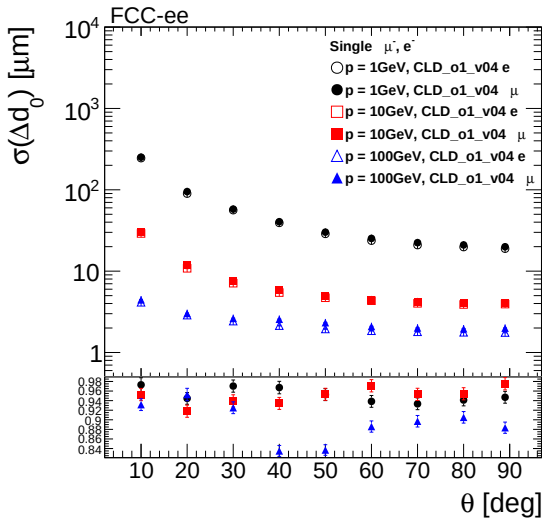

(a) Transverse impact parameter d_0 resolution

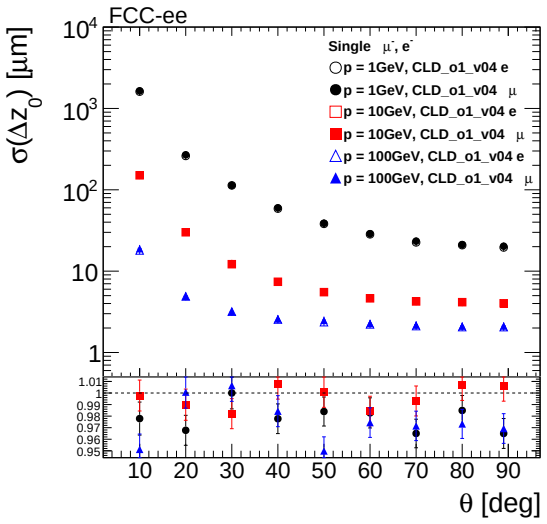

(b) Longitudinal impact parameter z_0 resolution

Figure A.5: Transverse (d_0) and longitudinal (z_0) impact parameter resolutions as a function of momentum for single muons and electrons in the CLD baseline geometry.

The results, shown in Figure A.17, A.18, A.19, A.20 and Figure A.21, A.22, A.23, A.24 , demonstrate that tracking performance remains essentially unchanged across all LumiCal configurations considered. This indicates that, under the tested scenarios, the LumiCal design has negligible influence on the intrinsic performance of the tracking system, even in the forward regions where its presence is most prominent.

These findings provide flexibility in LumiCal optimisation, allowing its design to be tuned for calorimetric performance without compromising track reconstruction quality.

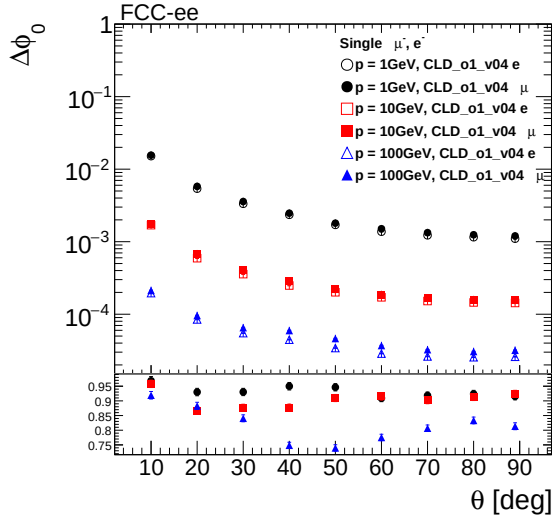

(a) Residual on the azimuthal angle at the point of closest approach ϕ_0 resolution

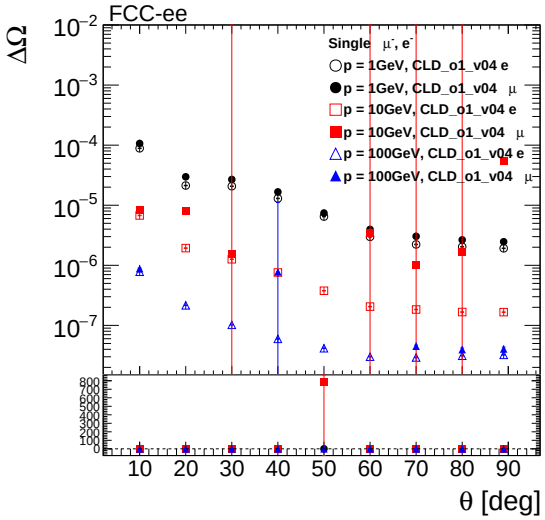

(b) Curvature Ω resolution

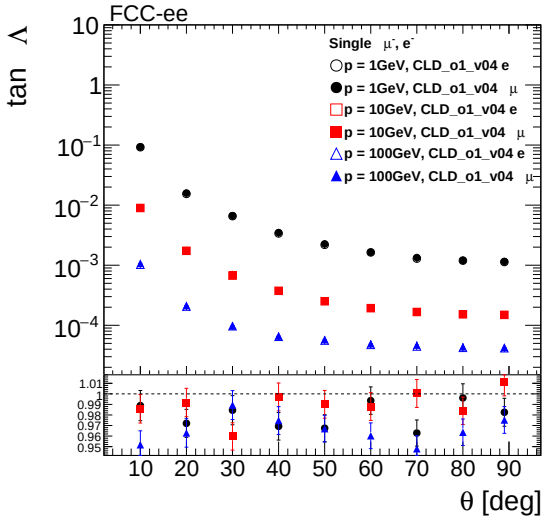

(c) track dip angle $\tan\lambda$ resolution

Figure A.6: Resolutions of the azimuthal angle at the point of closest approach (ϕ_0), curvature (Ω), and dip angle ($\tan\lambda$) as a function of momentum for single muons and electrons.

A.0.4 Impact of a More Realistic Beam Pipe and Vertex Geometry

A.0.5 Impact of vertex detector spatial resolution

A.0.6 Impact of a Reduced Tracker Volume for PID Integration

A.0.7 Impact of larger magnetic field

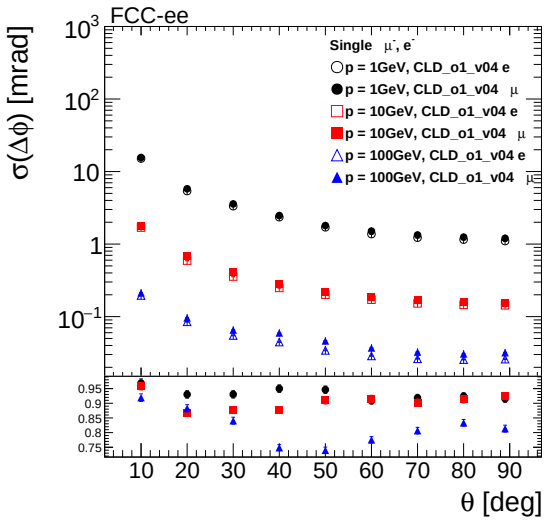

(a) Azimuthal angle ϕ resolution

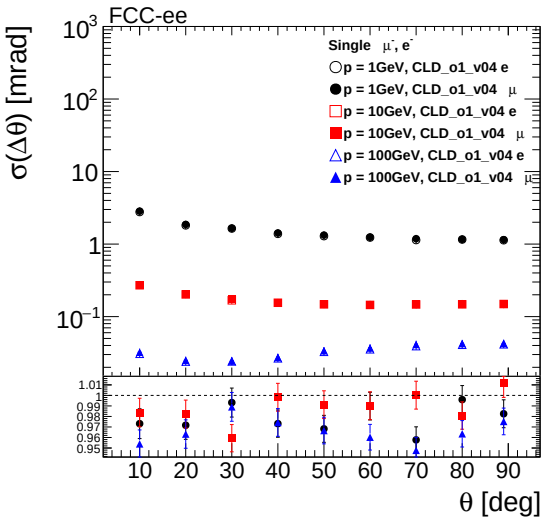

(b) Polar angle θ resolution

Figure A.7: Azimuthal (ϕ) and polar (θ) angle resolutions as a function of momentum for single muons and electrons.

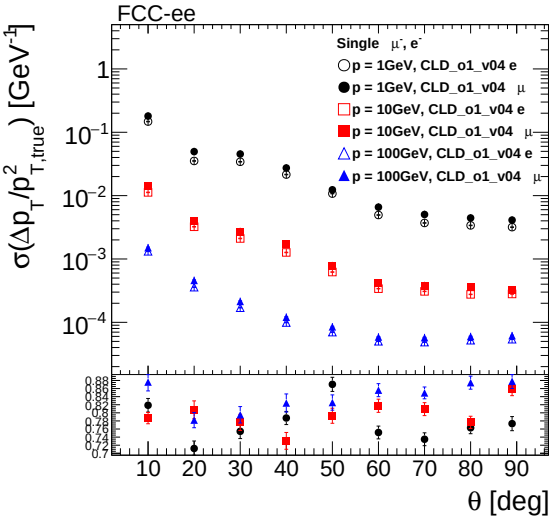

(a) Transverse momentum resolution

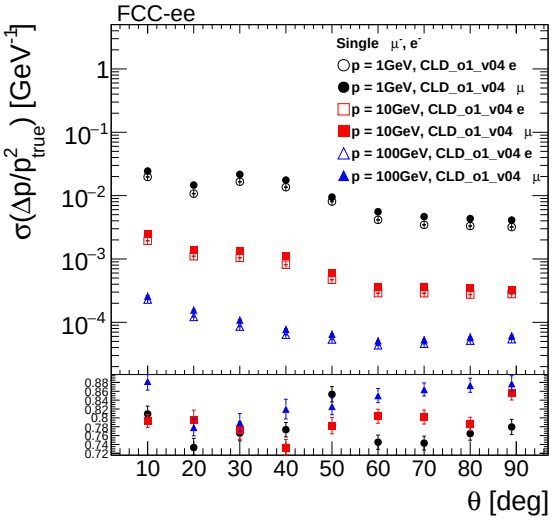

(b) Momentum resolution

Figure A.8: Transverse (p_T) and total momentum (p) resolutions as a function of momentum for single muons and electrons.

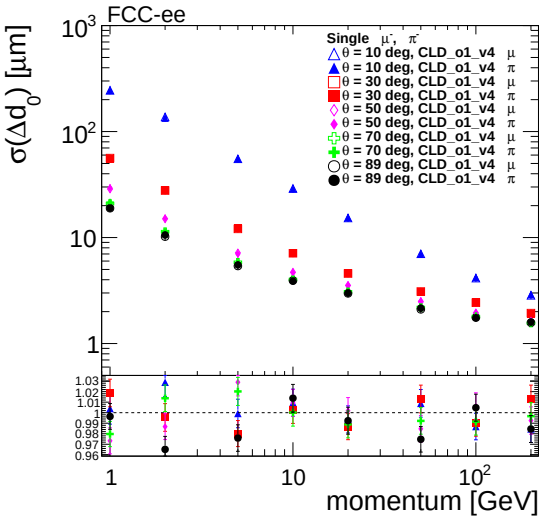

(a) Transverse impact parameter d_0 resolution

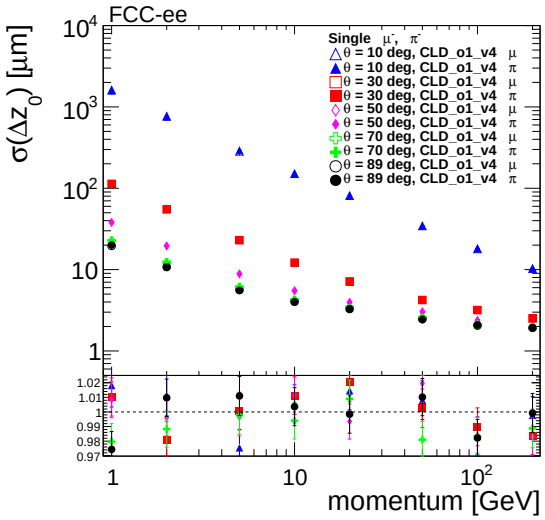

(b) Longitudinal impact parameter z_0 resolution

Figure A.9: Resolution of the transverse (d_0) and longitudinal (z_0) impact parameters as a function of momentum for muons and pions in the CLD baseline geometry.

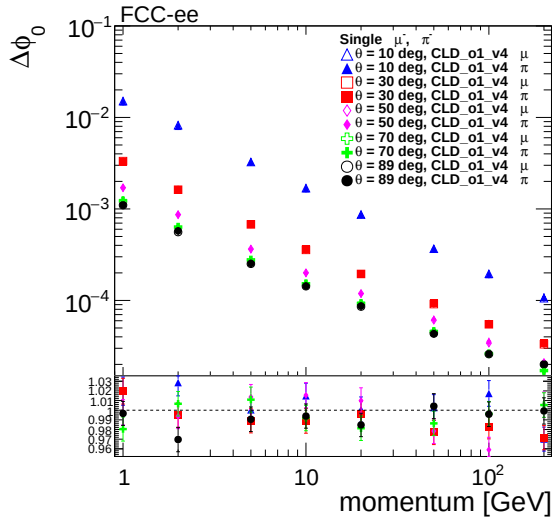

(a) Residual on the azimuthal angle at the point of closest approach ϕ_0 resolution

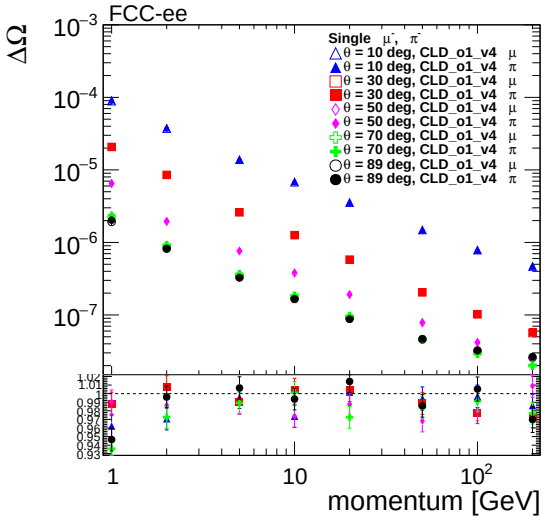

(b) Curvature Ω resolution

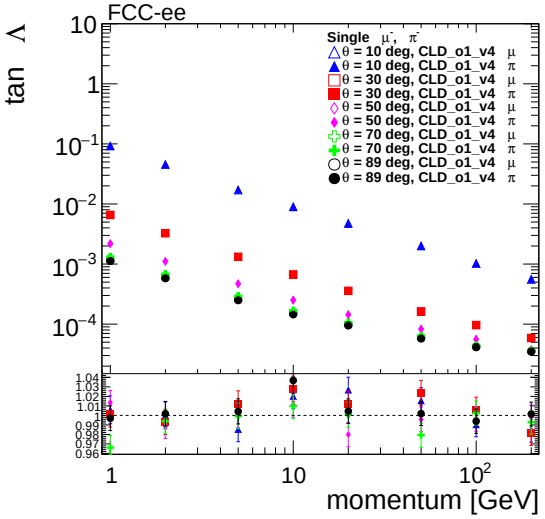

(c) track dip angle $\tan\lambda$ resolution

Figure A.10: Resolution of the azimuthal angle at the point of closest approach (ϕ_0), curvature (Ω), and track dip angle ($\tan\lambda$) as a function of momentum for muons and pions in the CLD baseline geometry.

s

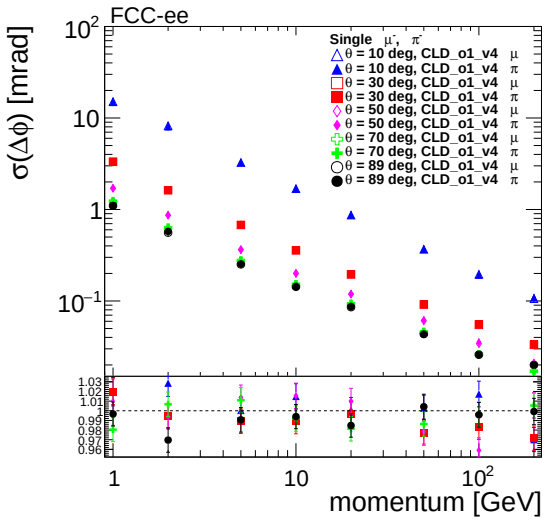

(a) Azimuthal angle ϕ resolution

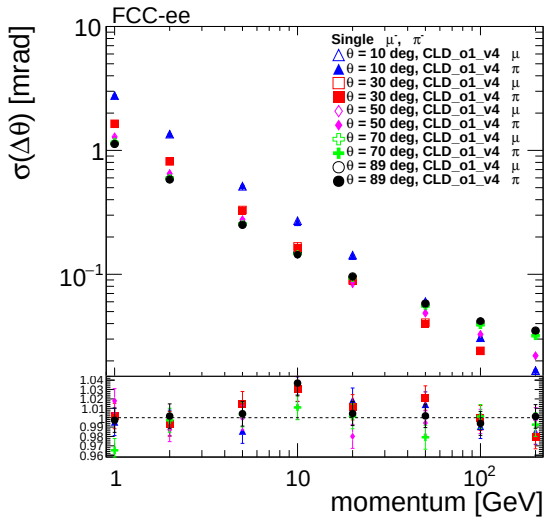

(b) Polar angle θ resolution

Figure A.11: Resolution of the azimuthal (ϕ) and polar (θ) angles as a function of momentum for muons and pions in the CLD baseline geometry.

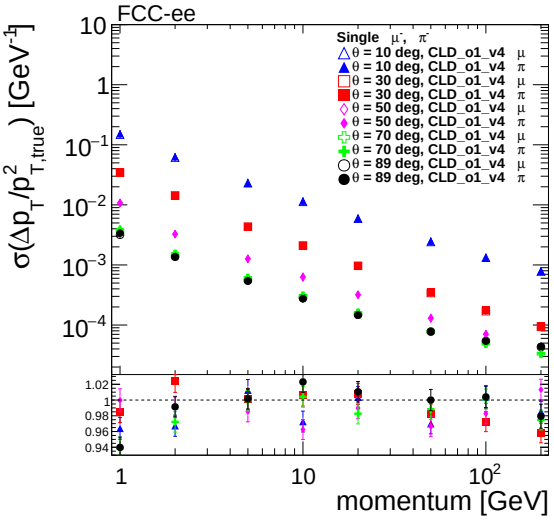

(a) Transverse momentum resolution

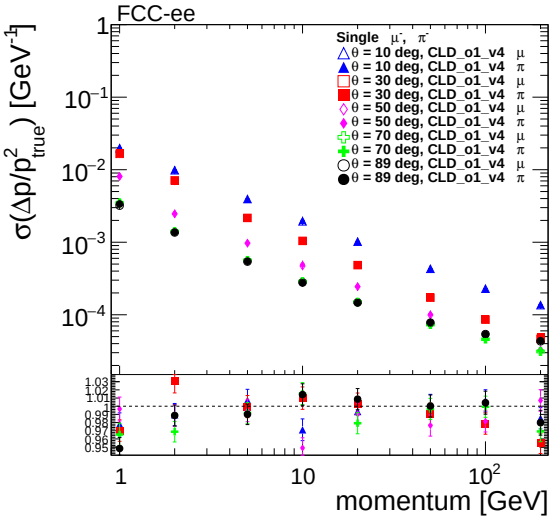

(b) Momentum resolution

Figure A.12: Transverse momentum and total momentum resolution as a function of momentum for muons and pions in the CLD baseline geometry.

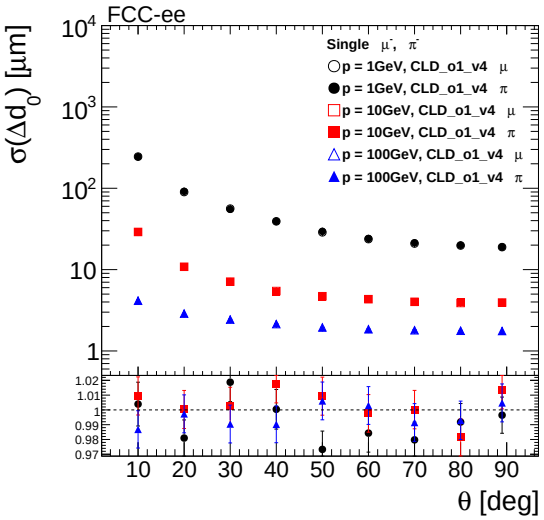

(a) Transverse impact parameter d_0 resolution

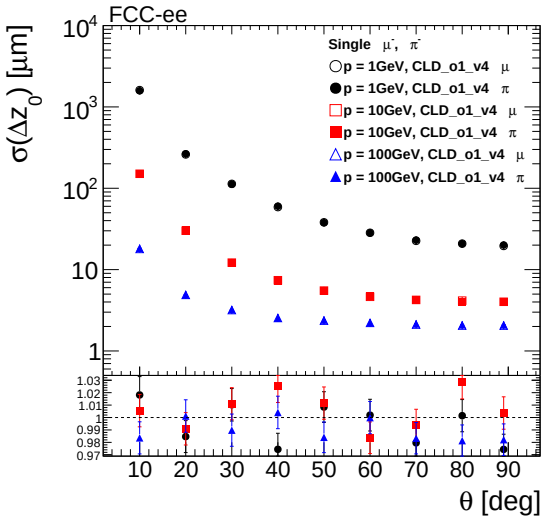

(b) Longitudinal impact parameter z_0 resolution

Figure A.13: Resolution of the transverse (d_0) and longitudinal (z_0) impact parameters as a function of polar angle for muons and pions in the CLD baseline geometry.

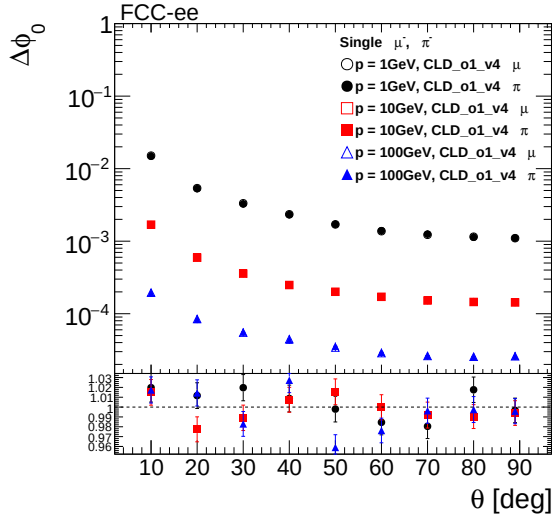

(a) Residual on the azimuthal angle at the point of closest approach ϕ_0 resolution

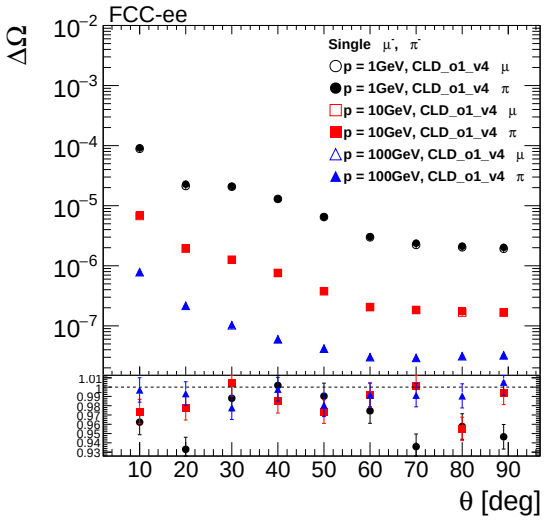

(b) Curvature Ω resolution

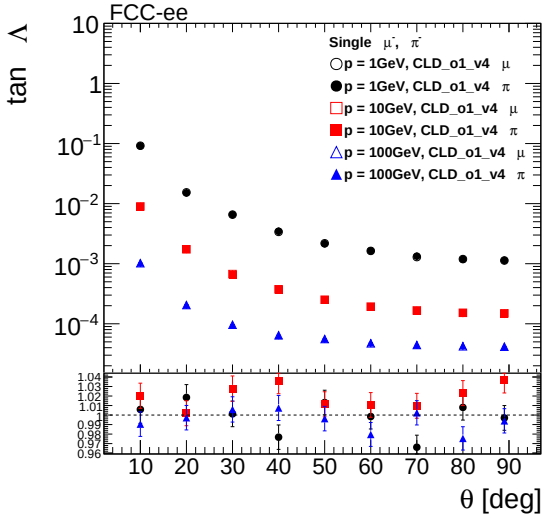

(c) track dip angle $\tan\lambda$ resolution

Figure A.14: Resolution of the azimuthal angle at the point of closest approach (ϕ_0), curvature (Ω), and track dip angle ($\tan\lambda$) as a function of polar angle for muons and pions in the CLD baseline geometry.

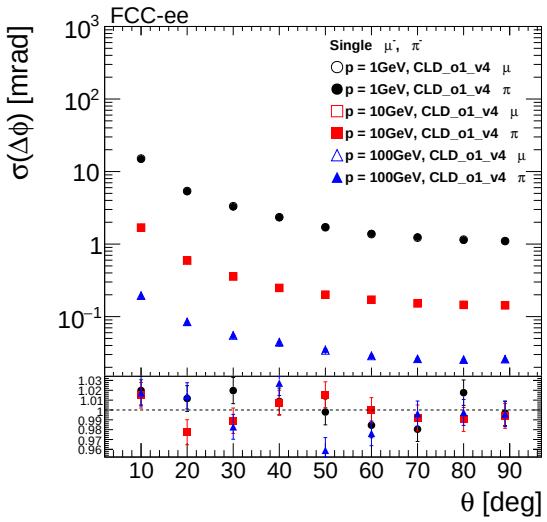

(a) Azimuthal angle ϕ resolution

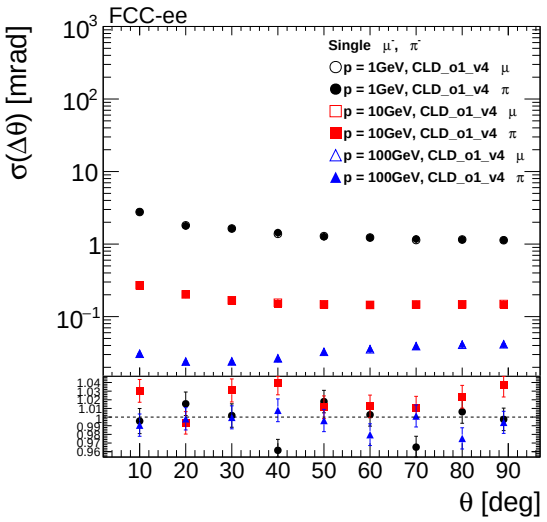

(b) Polar angle θ resolution

Figure A.15: Resolution of the azimuthal (ϕ) and polar (θ) angles as a function of polar angle for muons and pions in the CLD baseline geometry.

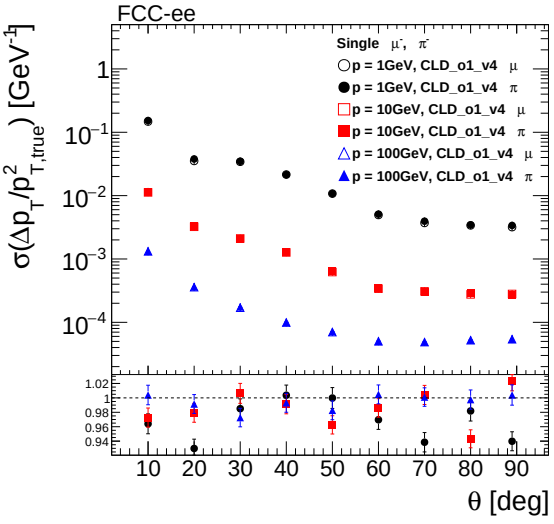

(a) Transverse momentum resolution

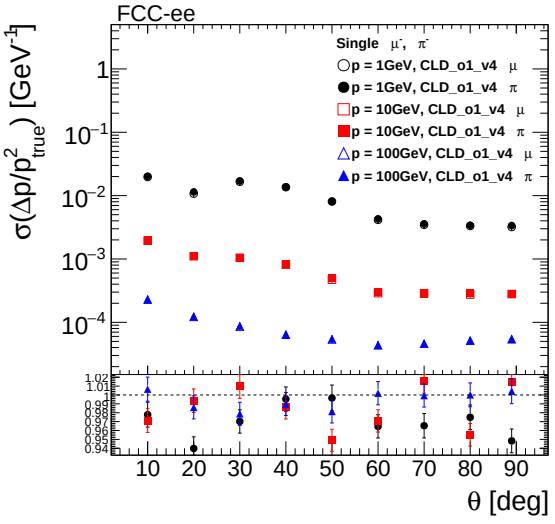

(b) Momentum resolution

Figure A.16: Transverse momentum and total momentum resolution as a function of polar angle for muons and pions in the CLD baseline geometry.

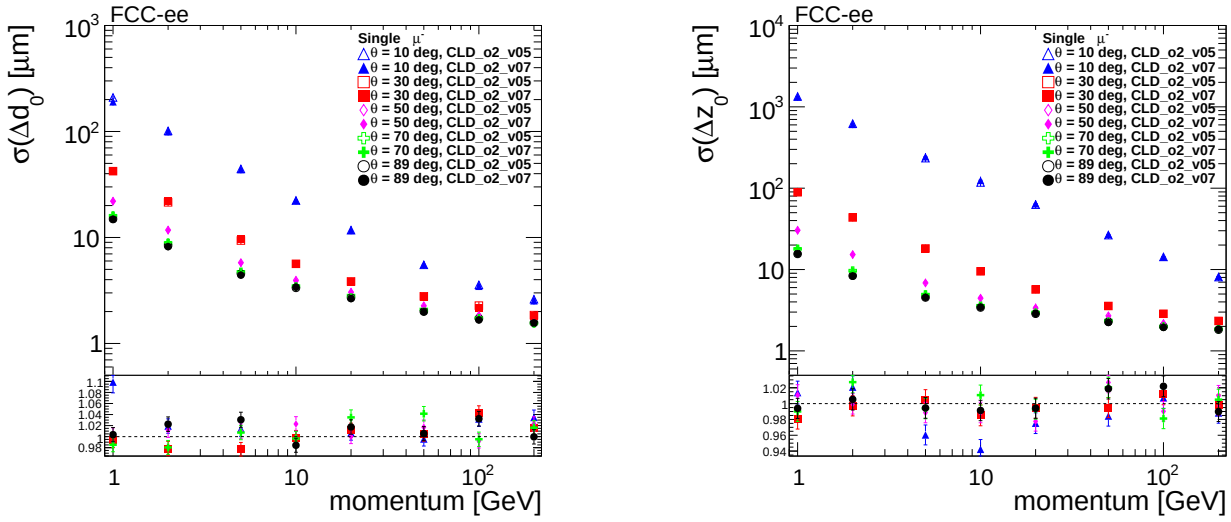

(a) Transverse impact parameter d_0 resolution

(b) Longitudinal impact parameter z_0 resolution

Figure A.17: Resolution of the transverse (d_0) and longitudinal (z_0) impact parameters as a function of momentum for muons, comparing the CLD new baseline and the CLD geometry with improved LumiCal.

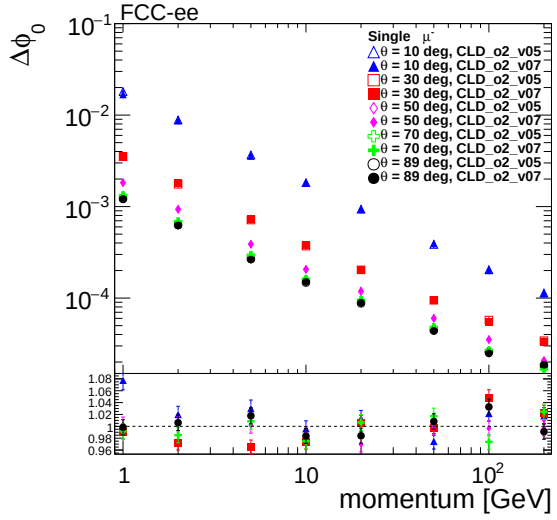

(a) Residual on the azimuthal angle at the point of closest approach ϕ_0 resolution

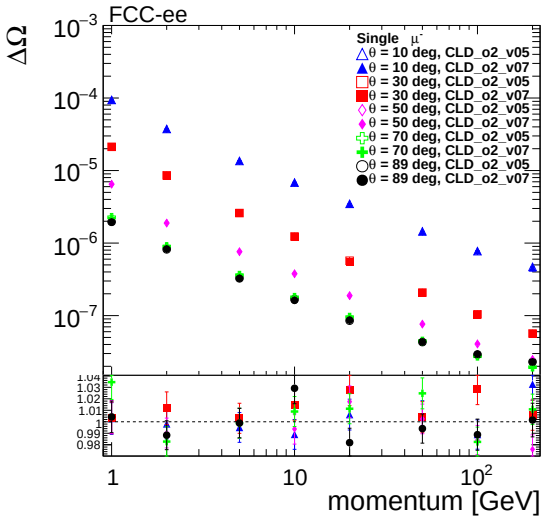

(b) Curvature Ω resolution

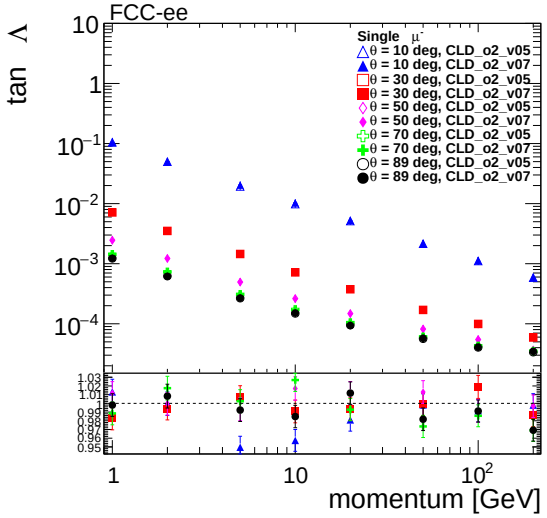

(c) track dip angle $\tan\lambda$ resolution

Figure A.18: Resolution of the azimuthal angle at the point of closest approach (ϕ_0), curvature (Ω), and track dip angle ($\tan\lambda$) as a function of momentum for muons, comparing the CLD new baseline and the CLD geometry with improved LumiCal.

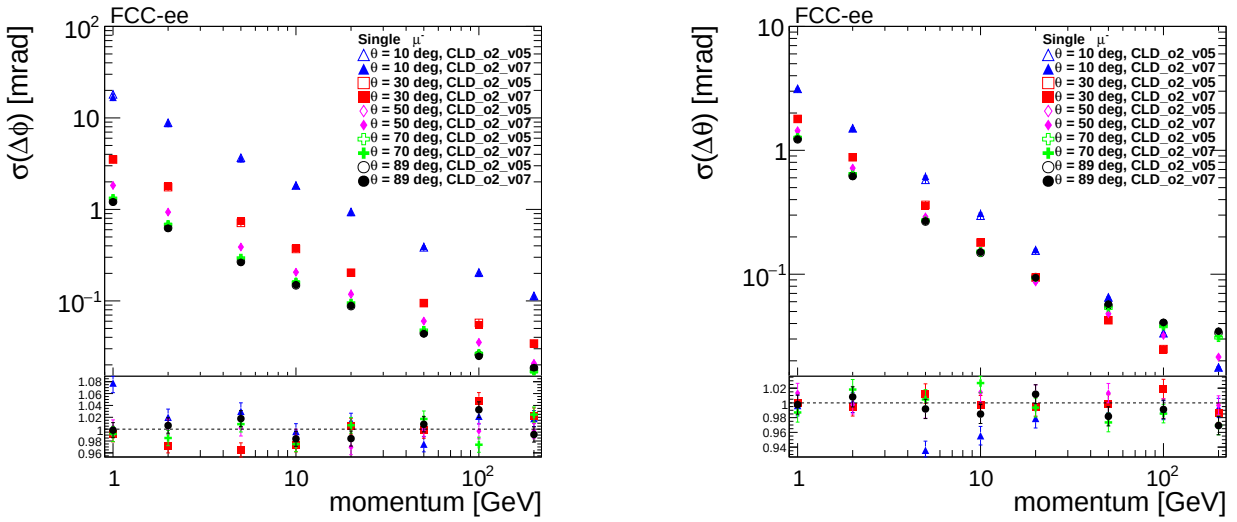

(a) Azimuthal angle ϕ resolution

(b) Polar angle θ resolution

Figure A.19: Resolution of the azimuthal (ϕ) and polar (θ) angles as a function of momentum for muons, comparing the CLD new baseline and the CLD geometry with improved LumiCal.

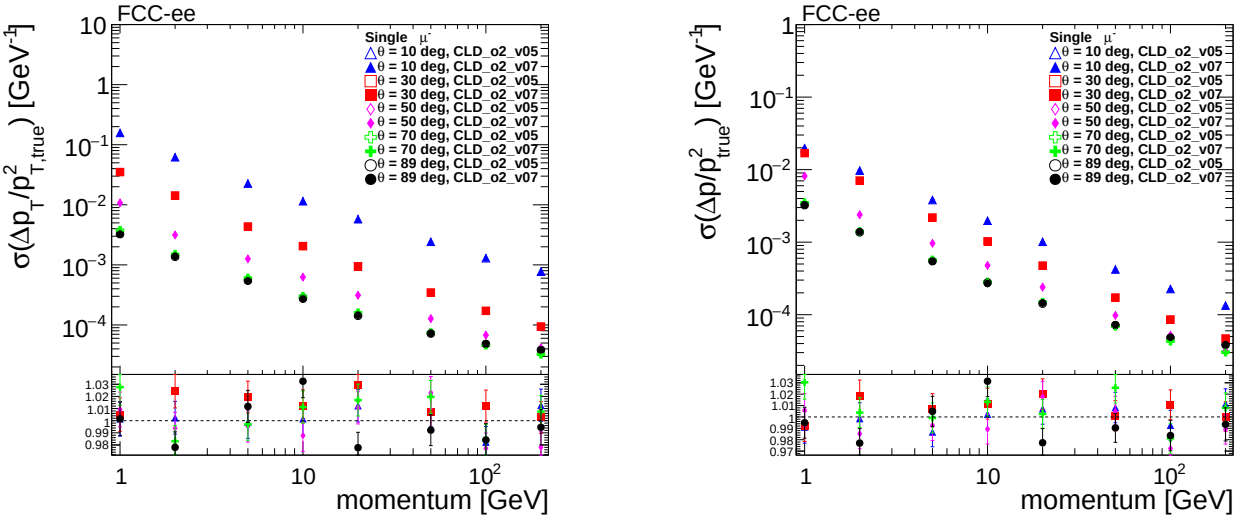

(a) Transverse momentum resolution

(b) Momentum resolution

Figure A.20: Transverse momentum and total momentum resolution as a function of momentum for muons, comparing the CLD new baseline and the CLD geometry with improved LumiCal.

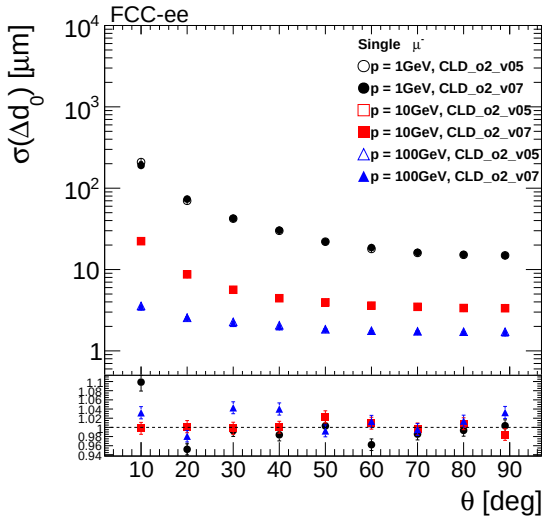

(a) Transverse impact parameter d_0 resolution

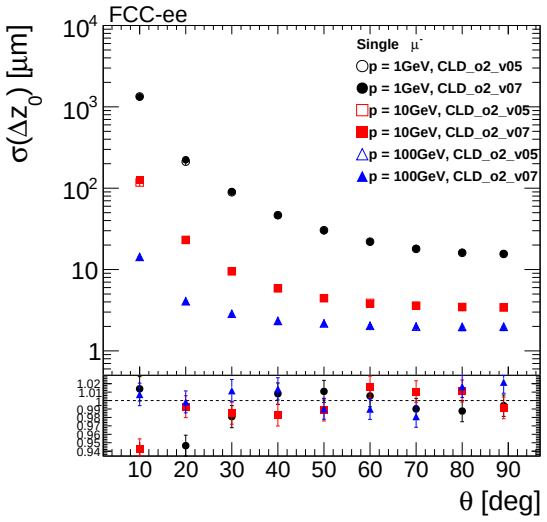

(b) Longitudinal impact parameter z_0 resolution

Figure A.21: Resolution of the transverse (d_0) and longitudinal (z_0) impact parameters as a function of polar angle for muons, comparing the CLD new baseline and the CLD geometry with improved LumiCal.

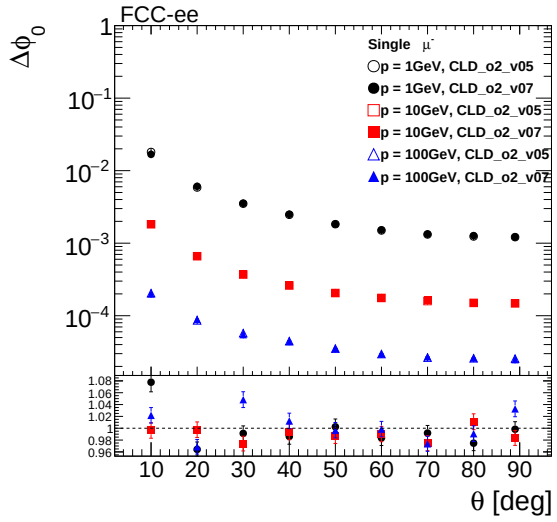

(a) Residual on the azimuthal angle at the point of closest approach ϕ_0 resolution

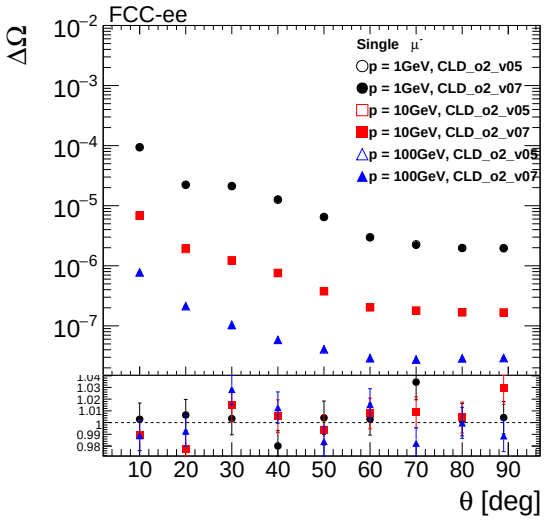

(b) Curvature Ω resolution

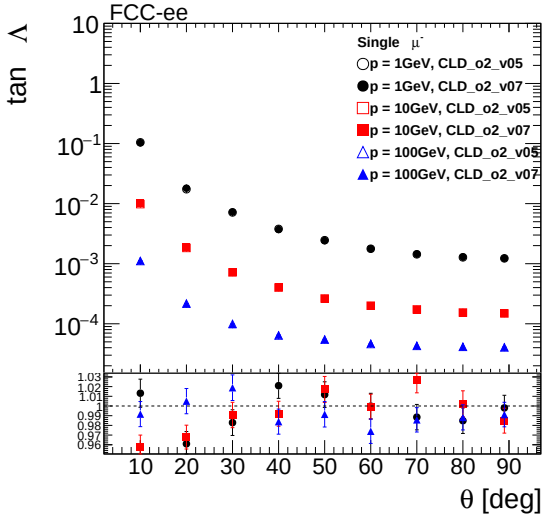

(c) track dip angle $\tan\lambda$ resolution

Figure A.22: Resolution of the azimuthal angle at the point of closest approach (ϕ_0), curvature (Ω), and track dip angle ($\tan\lambda$) as a function of polar angle for muons, comparing the CLD new baseline and the CLD geometry with improved LumiCal.

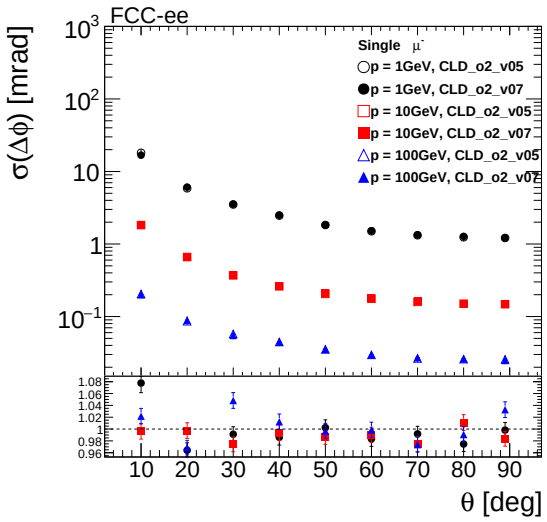

(a) Azimuthal angle ϕ resolution

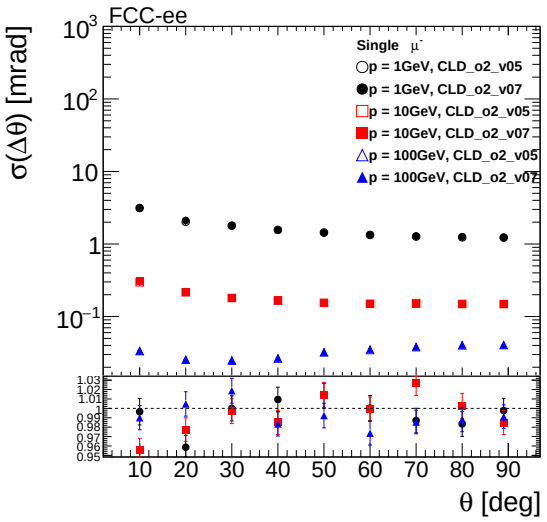

(b) Polar angle θ resolution

Figure A.23: Resolution of the azimuthal (ϕ) and polar (θ) angles as a function of polar angle for muons, comparing the CLD new baseline and the CLD geometry with improved LumiCal.

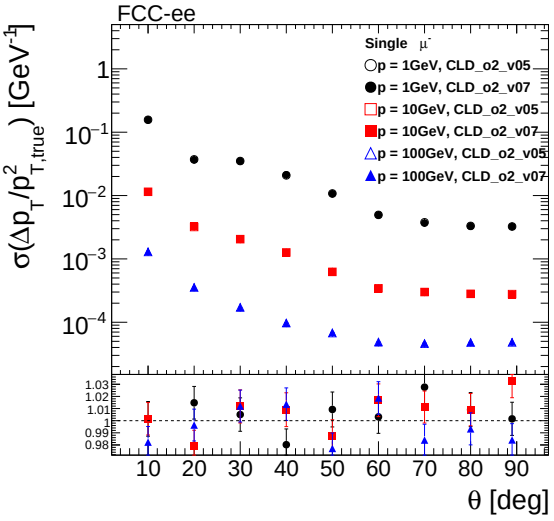

(a) Transverse momentum resolution

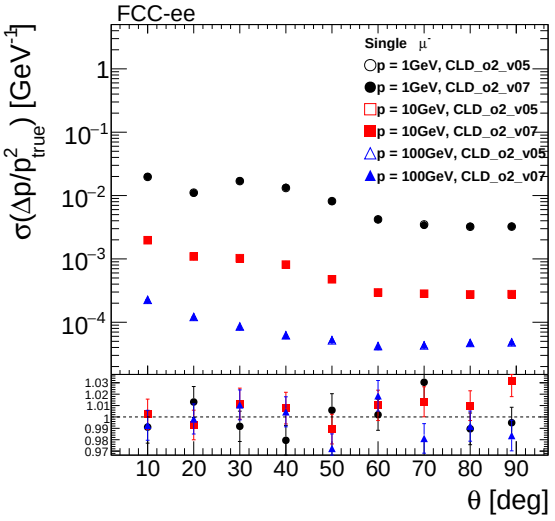

(b) Momentum resolution

Figure A.24: Transverse momentum and total momentum resolution as a function of polar angle for muons, comparing the CLD new baseline and the CLD geometry with improved LumiCal.

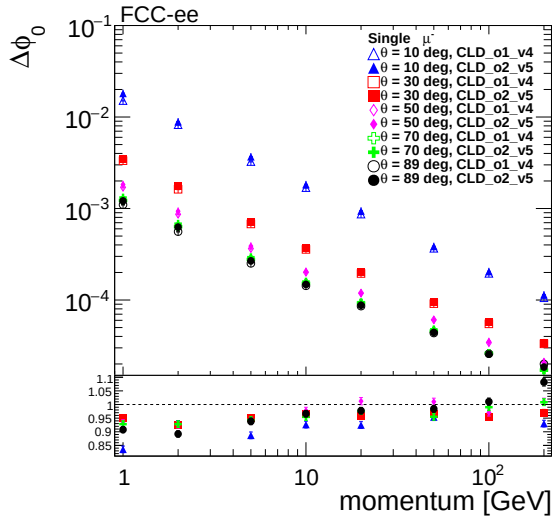

(a) Residual on the azimuthal angle at the point of closest approach ϕ_0 resolution

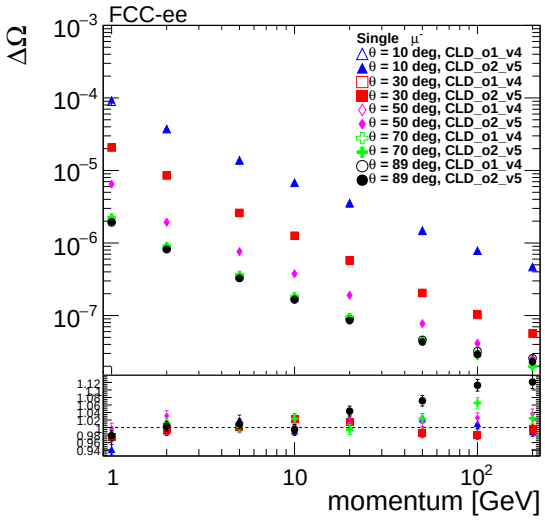

(b) Curvature Ω resolution

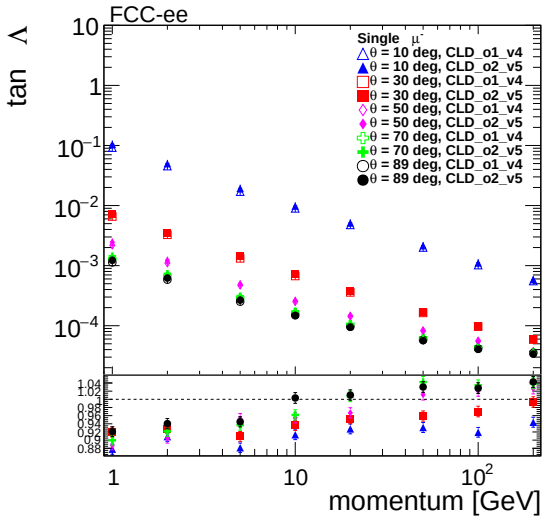

(c) track dip angle $\tan\lambda$ resolution

Figure A.25: Resolution of the azimuthal angle at the point of closest approach (ϕ_0), curvature (Ω), and track dip angle ($\tan\lambda$) as a function of momentum for muons, comparing the CLD baseline geometry and the geometry with a more realistic beam pipe, closer to interaction point, and adapted vertex detector (new CLD baseline).

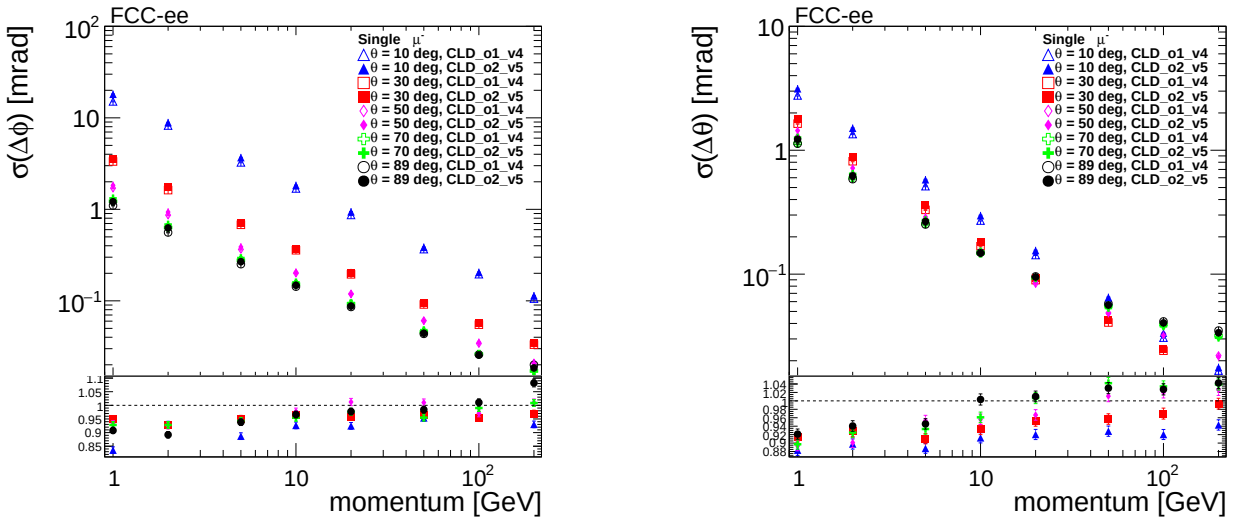

(a) Azimuthal angle ϕ resolution

(b) Polar angle θ resolution

Figure A.26: Resolution of the azimuthal (ϕ) and polar (θ) angles as a function of momentum for muons, comparing the CLD baseline geometry and the geometry with a more realistic beam pipe, closer to interaction point, and adapted vertex detector (new CLD baseline).

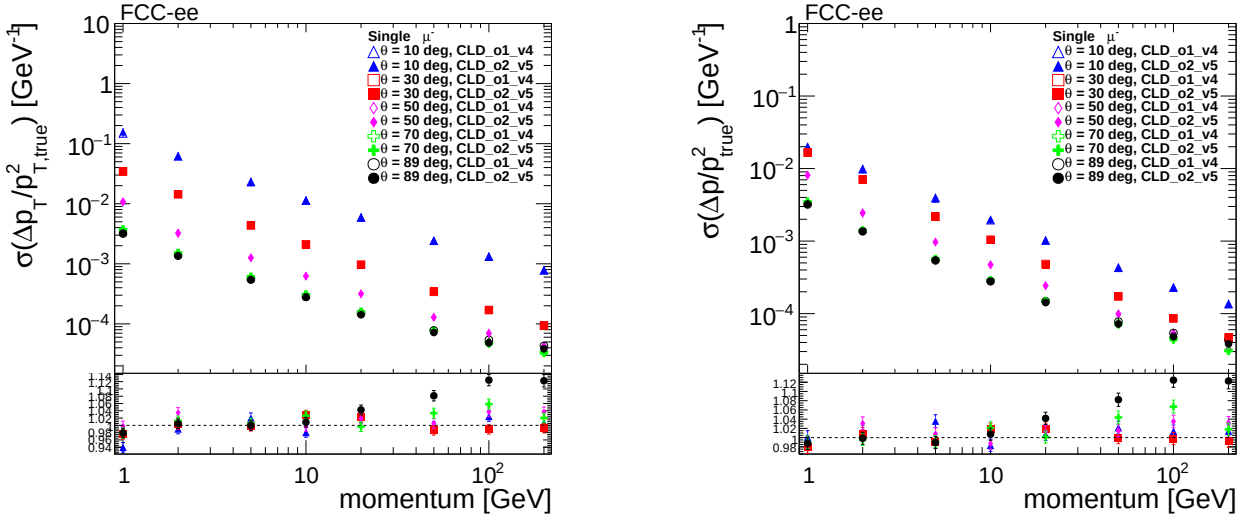

(a) Transverse momentum resolution

(b) Momentum resolution

Figure A.27: Transverse momentum and total momentum resolution as a function of momentum for muons, comparing the CLD baseline geometry and the geometry with a more realistic beam pipe, closer to interaction point, and adapted vertex detector (new CLD baseline).

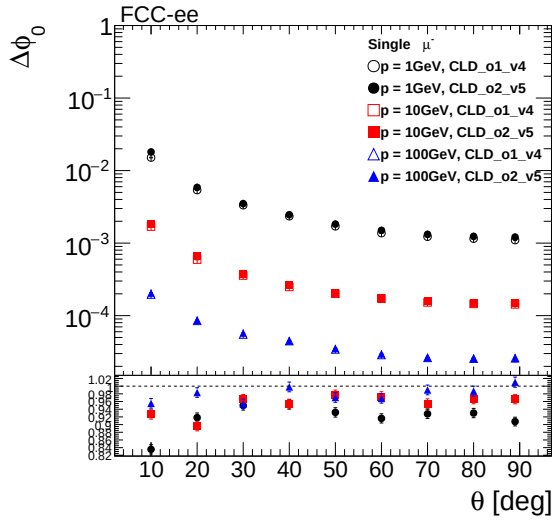

(a) Residual on the azimuthal angle at the point of closest approach ϕ_0 resolution

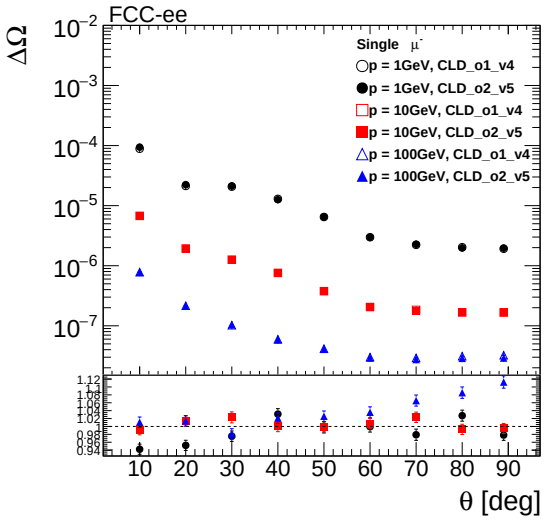

(b) Curvature Ω resolution

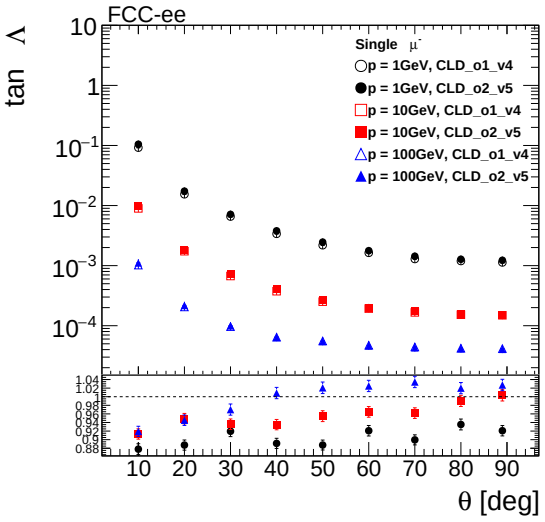

(c) track dip angle $\tan\lambda$ resolution

Figure A.28: Resolution of the azimuthal angle at the point of closest approach (ϕ_0), curvature (Ω), and track dip angle ($\tan\lambda$) as a function of polar angle for muons, comparing the CLD baseline geometry and the geometry with a more realistic beam pipe, closer to interaction point, and adapted vertex detector (new CLD baseline).

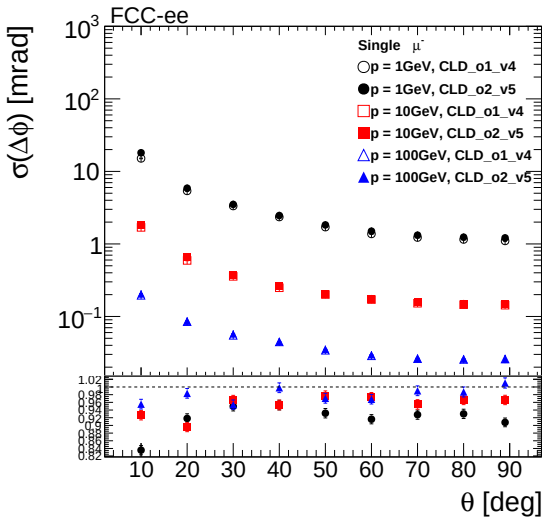

(a) Azimuthal angle ϕ resolution

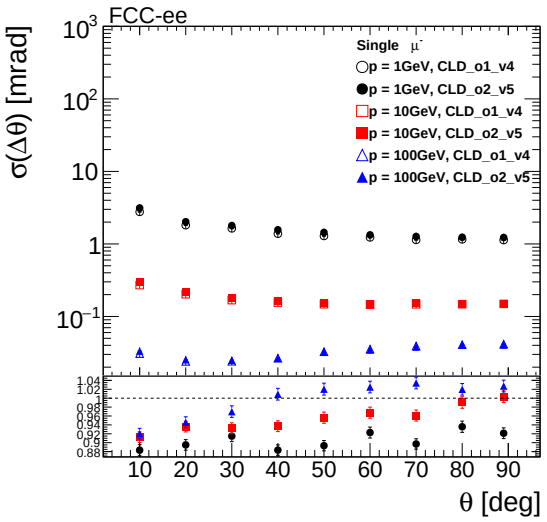

(b) Polar angle θ resolution

Figure A.29: Resolution of the azimuthal (ϕ) and polar (θ) angles as a function of polar angle for muons, comparing the CLD baseline geometry and the geometry with a more realistic beam pipe, closer to interaction point, and adapted vertex detector (new CLD baseline).

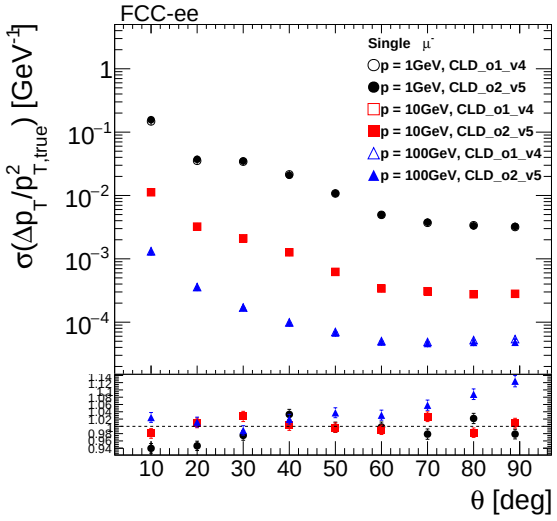

(a) Transverse momentum resolution

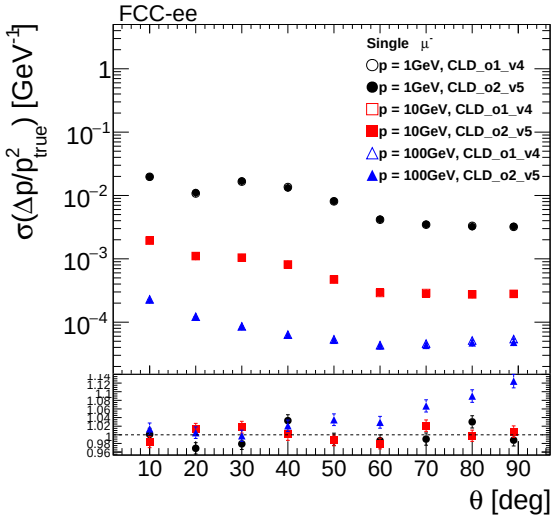

(b) Momentum resolution

Figure A.30: Transverse momentum and total momentum resolution as a function of polar angle for muons, comparing the CLD baseline geometry and the geometry with a more realistic beam pipe, closer to interaction point, and adapted vertex detector (new CLD baseline).

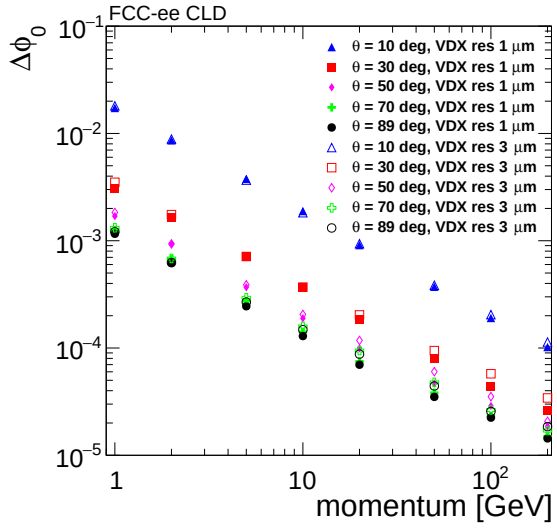

(a) Residual on the azimuthal angle at the point of closest approach ϕ_0 resolution

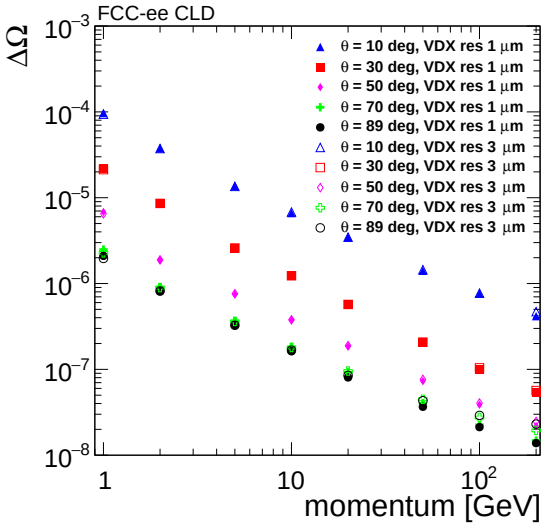

(b) Curvature Ω resolution

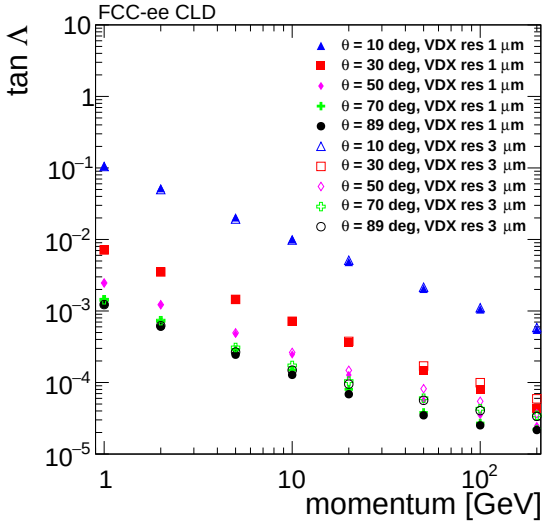

(c) track dip angle $\tan\lambda$ resolution

Figure A.31: Resolution of the azimuthal angle at the point of closest approach (ϕ_0), curvature (Ω), and track dip angle ($\tan\lambda$) as a function of momentum for muons, showing the impact of the vertex detector spatial resolution.

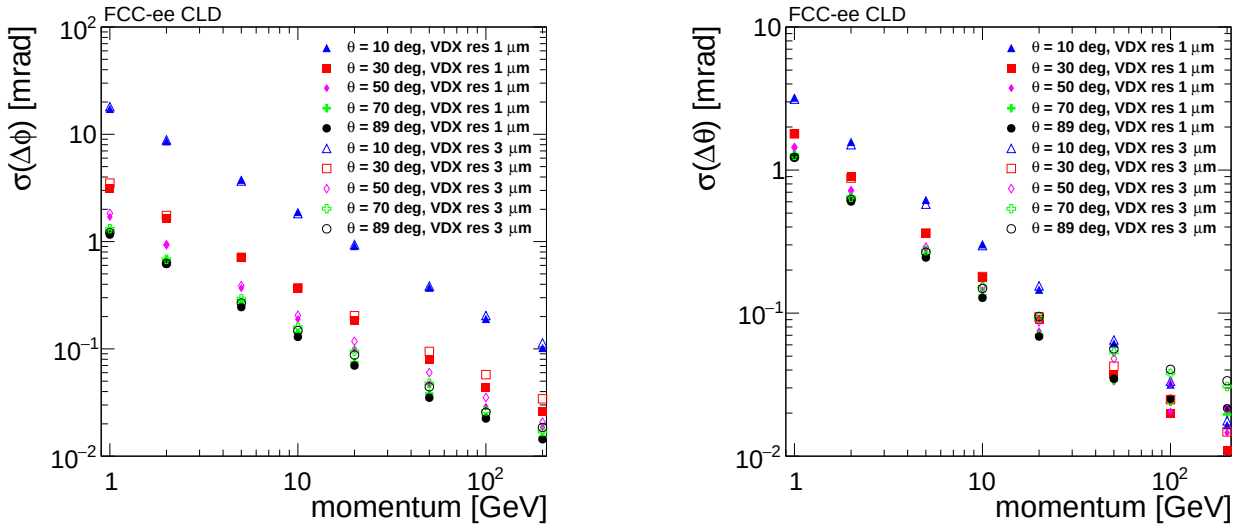

(a) Azimuthal angle ϕ resolution

(b) Polar angle θ resolution

Figure A.32: Resolution of the azimuthal (ϕ) and polar (θ) angles as a function of momentum for muons, showing the impact of the vertex detector spatial resolution.

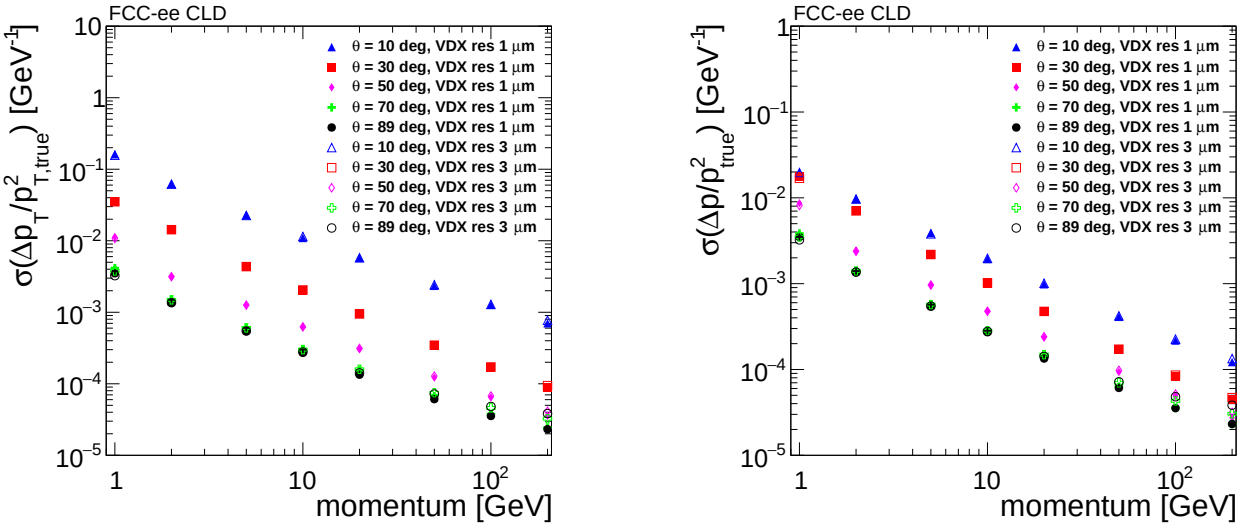

(a) Transverse momentum resolution

(b) Momentum resolution

Figure A.33: Transverse momentum and total momentum resolution as a function of momentum for muons, showing the impact of the vertex detector spatial resolution.

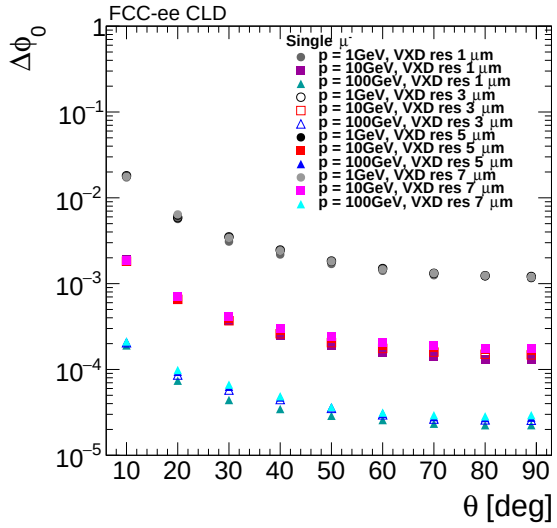

(a) Residual on the azimuthal angle at the point of closest approach ϕ_0 resolution

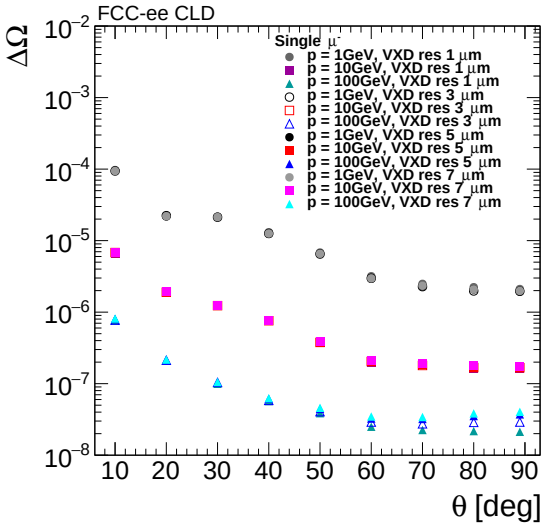

(b) Curvature Ω resolution

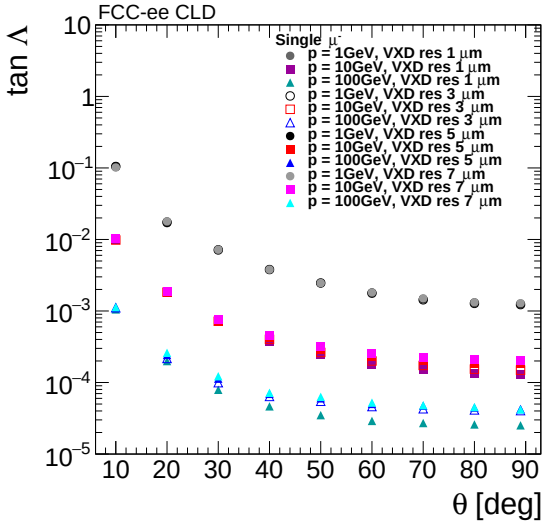

(c) track dip angle $\tan\lambda$ resolution

Figure A.34: Resolution of the azimuthal angle at the point of closest approach (ϕ_0), curvature (Ω), and track dip angle ($\tan\lambda$) as a function of the polar angle θ for muons, showing the impact of the vertex detector spatial resolution.

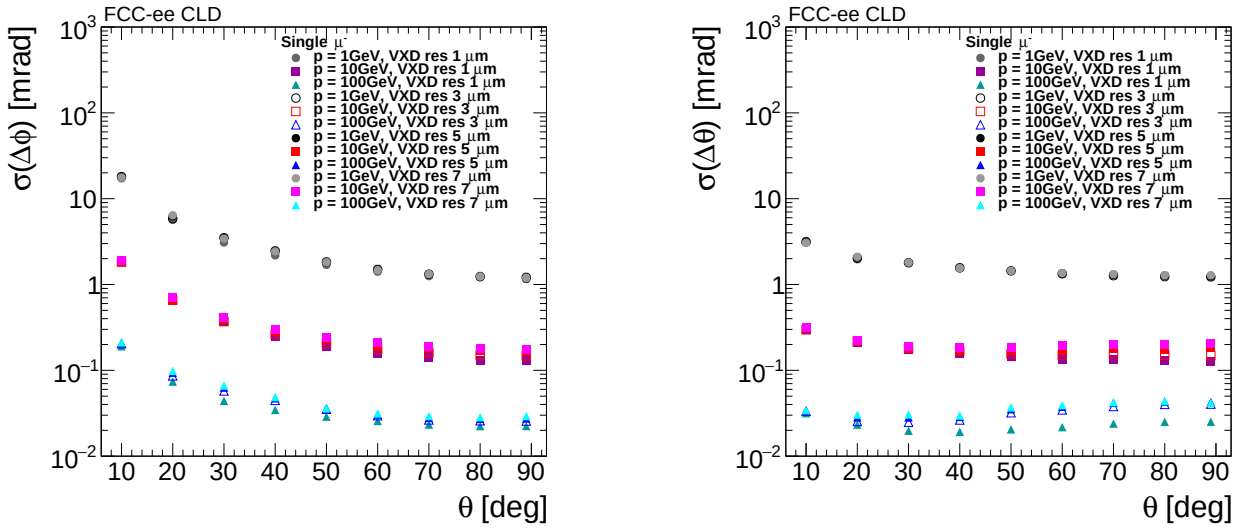

(a) Azimuthal angle ϕ resolution

(b) Polar angle θ resolution

Figure A.35: Resolution of the azimuthal (ϕ) and polar (θ) angles as a function of the polar angle θ for muons, showing the impact of the vertex detector spatial resolution.

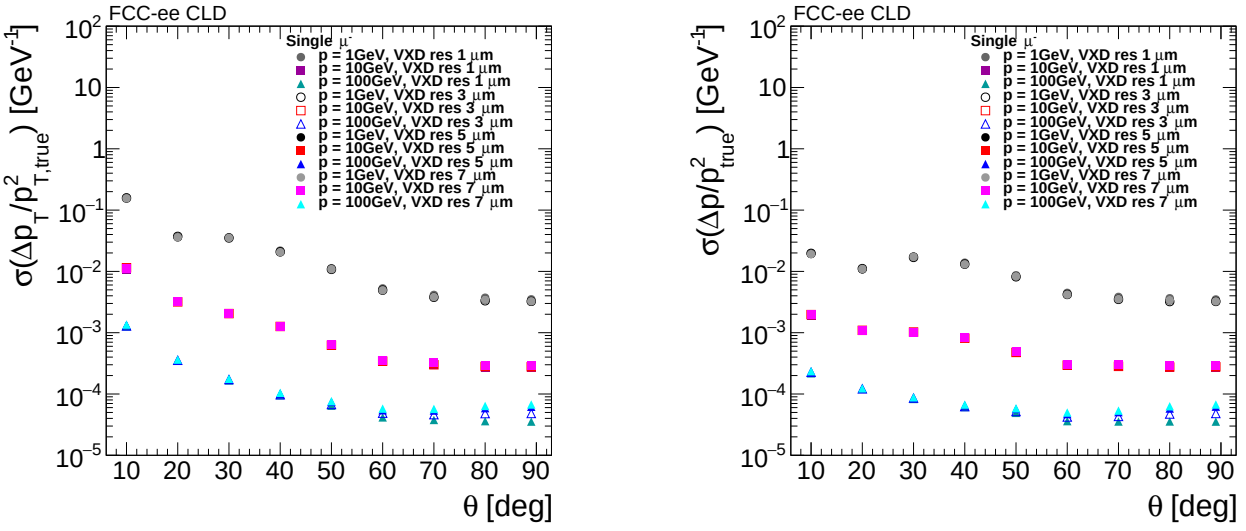

(a) Transverse momentum resolution

(b) Momentum resolution

Figure A.36: Transverse momentum and total momentum resolution as a function of the polar angle θ for muons, showing the impact of the vertex detector spatial resolution.

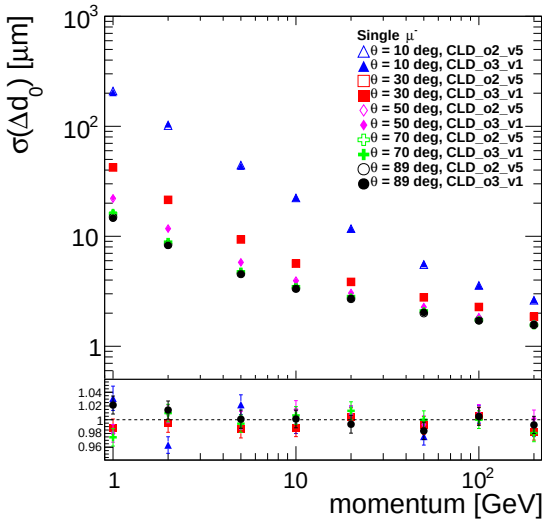

(a) Transverse impact parameter d_0 resolution

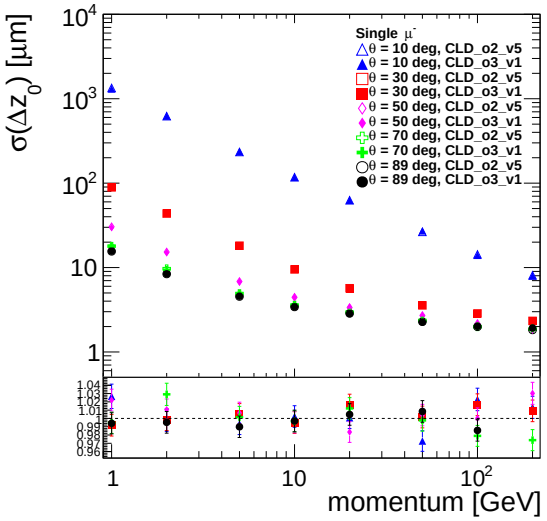

(b) Longitudinal impact parameter z_0 resolution

Figure A.37: Comparison between the CLD new baseline geometry and a configuration with a reduced tracker volume for PID integration: transverse and longitudinal impact parameter (d_0, z_0) resolutions as a function of momentum for muons.

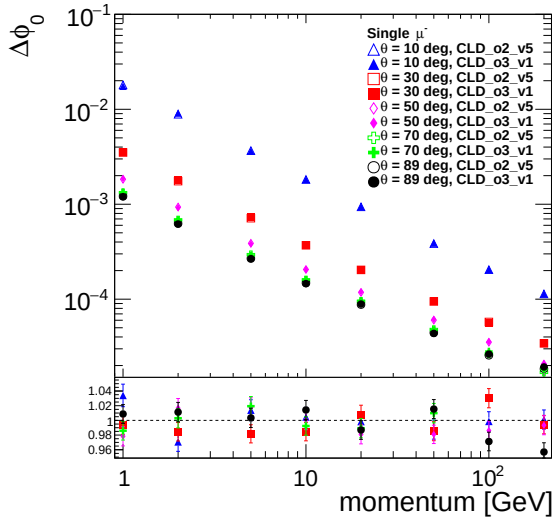

(a) Residual on the azimuthal angle at the point of closest approach ϕ_0 resolution

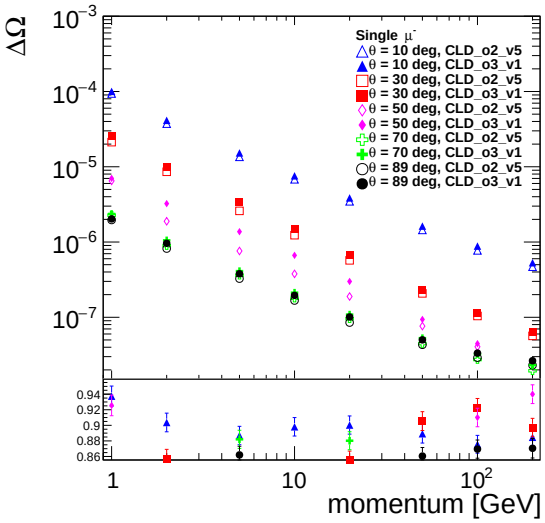

(b) Curvature Ω resolution

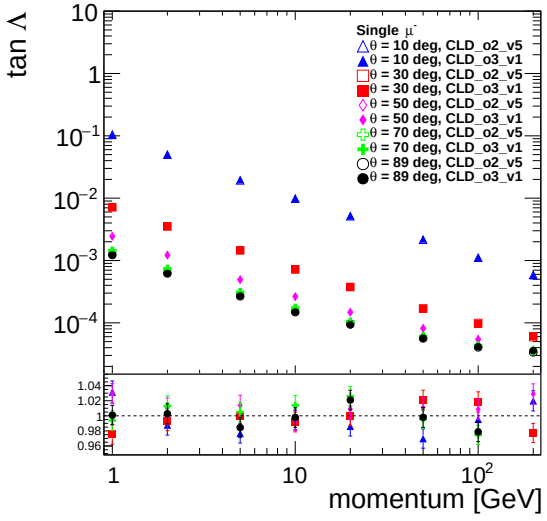

(c) track dip angle $\tan\lambda$ resolution

Figure A.38: Comparison between the CLD new baseline geometry and a configuration with a reduced tracker volume for PID integration: resolutions of the azimuthal angle at the point of closest approach (ϕ_0), curvature (Ω), and track dip angle ($\tan\lambda$) as a function of momentum for muons.

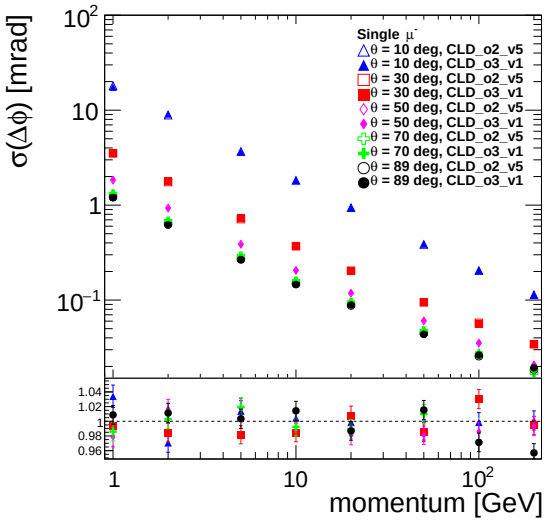

(a) Azimuthal angle ϕ resolution

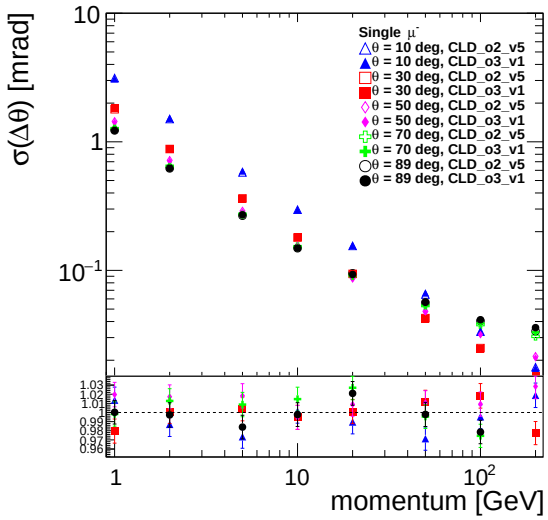

(b) Polar angle θ resolution

Figure A.39: Comparison between the CLD new baseline geometry and a configuration with a reduced tracker volume for PID integration: azimuthal (ϕ) and polar (θ) angle resolutions as a function of momentum for muons.

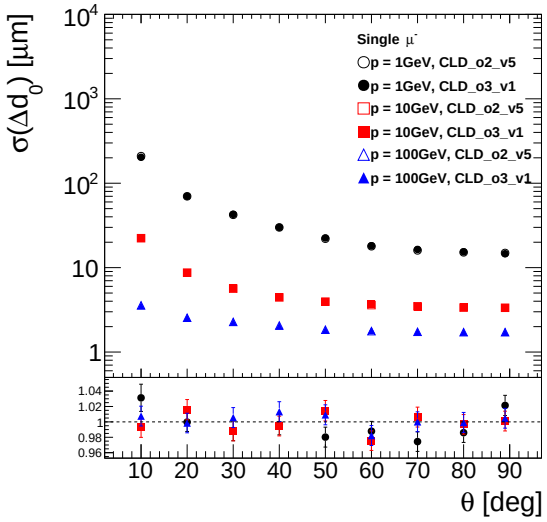

(a) Transverse impact parameter d_0 resolution

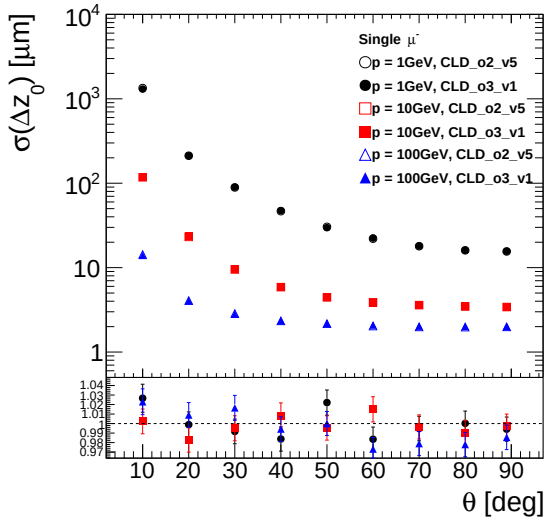

(b) Longitudinal impact parameter z_0 resolution

Figure A.40: Comparison between the CLD new baseline geometry and a configuration with a reduced tracker volume for PID integration: transverse and longitudinal impact parameter (d_0, z_0) resolutions as a function of polar angle for muons.

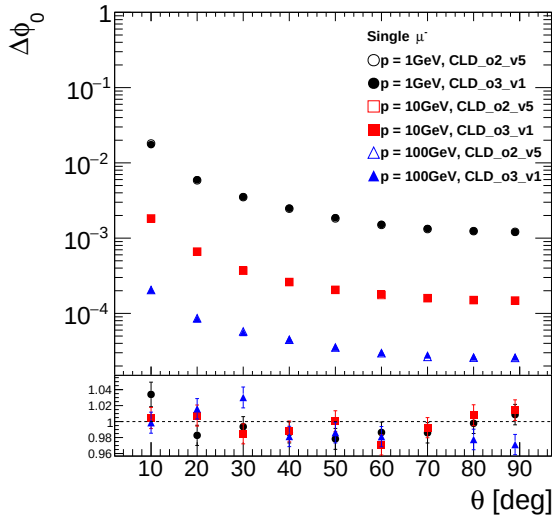

(a) Residual on the azimuthal angle at the point of closest approach ϕ_0 resolution

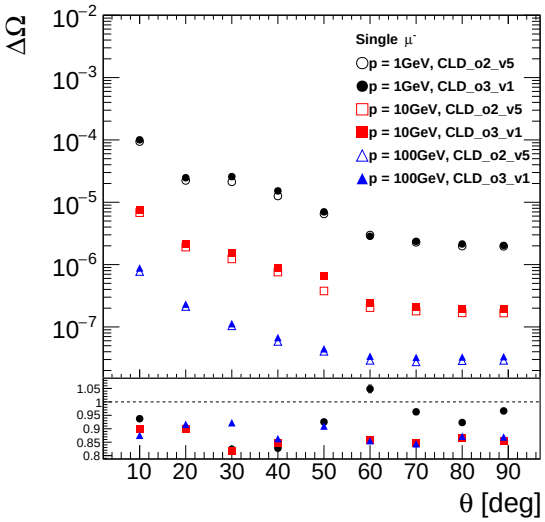

(b) Curvature Ω resolution

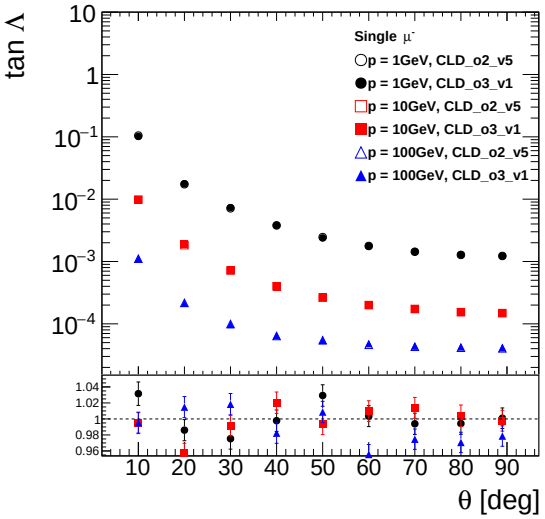

(c) track dip angle $\tan\lambda$ resolution

Figure A.41: Comparison between the CLD new baseline geometry and a configuration with a reduced tracker volume for PID integration: resolutions of the azimuthal angle at the point of closest approach (ϕ_0), curvature (Ω), and track dip angle ($\tan\lambda$) as a function of polar angle for muons.

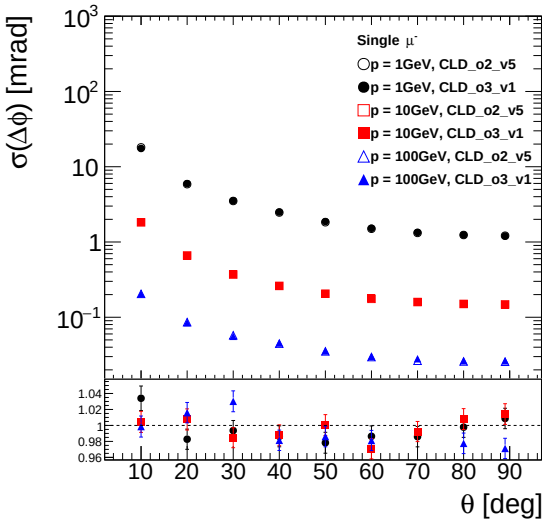

(a) Azimuthal angle ϕ resolution

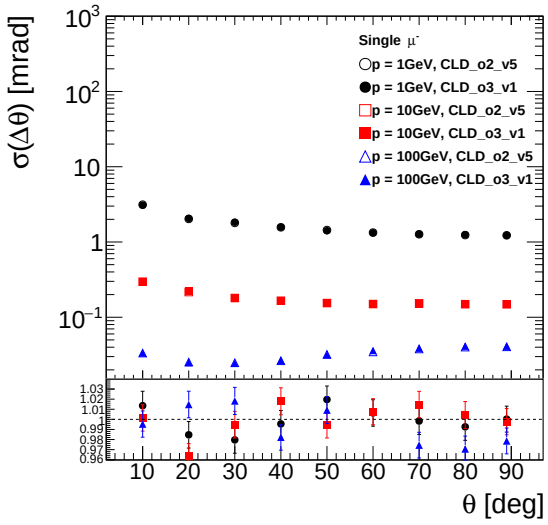

(b) Polar angle θ resolution

Figure A.42: Comparison between the CLD new baseline geometry and a configuration with a reduced tracker volume for PID integration: azimuthal (ϕ) and polar (θ) angle resolutions as a function of polar angle for muons.

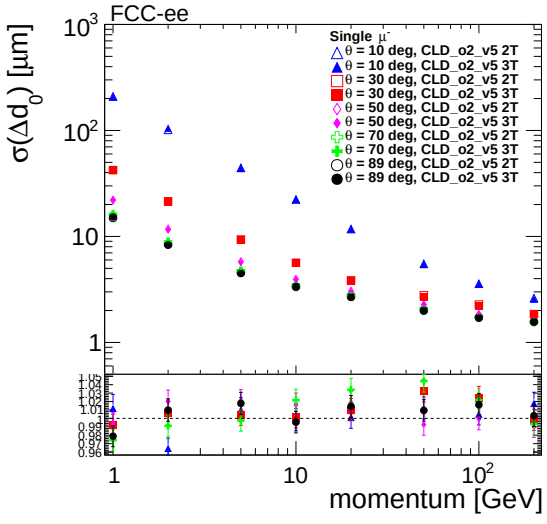

(a) Transverse impact parameter d_0 resolution

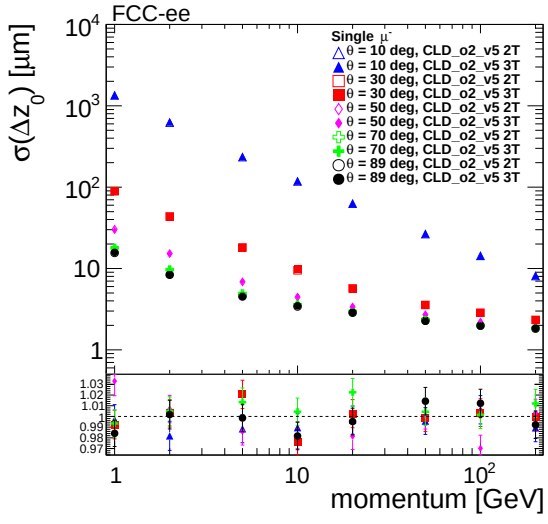

(b) Longitudinal impact parameter z_0 resolution

Figure A.43: Impact of a larger magnetic field: comparison between the CLD new baseline geometry with a 2 T solenoid and a configuration with a 3 T field. Transverse and longitudinal impact parameter (d_0, z_0) resolutions as a function of momentum for muons.

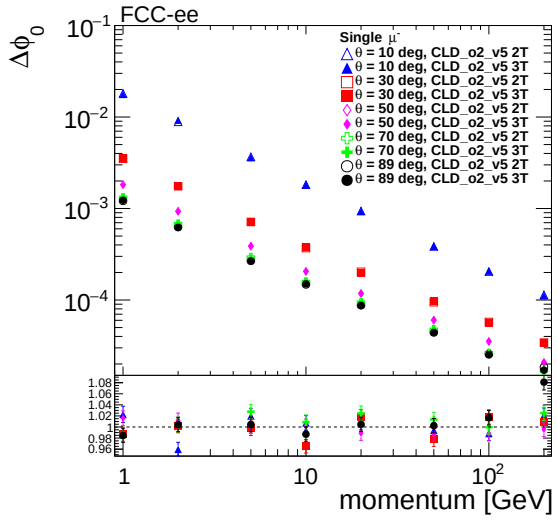

(a) Residual on the azimuthal angle at the point of closest approach ϕ_0 resolution

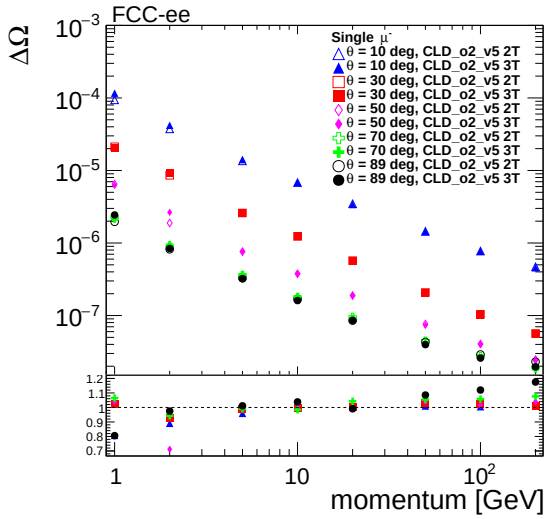

(b) Curvature Ω resolution

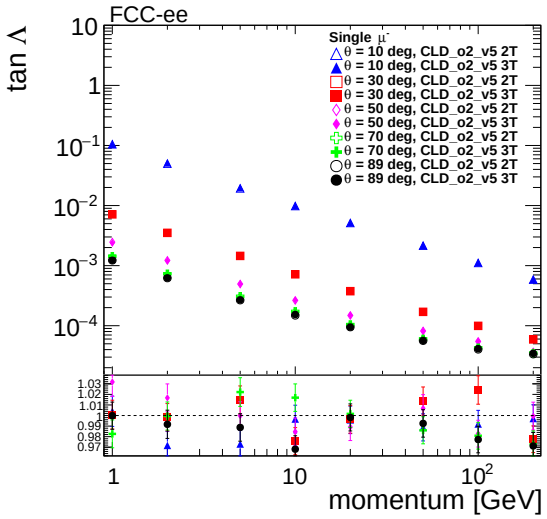

(c) track dip angle $\tan\lambda$ resolution

Figure A.44: Impact of a larger magnetic field: comparison between the CLD new baseline geometry with a 2 T solenoid and a configuration with a 3 T field. Resolutions of the azimuthal angle at the point of closest approach (ϕ_0), curvature (Ω), and track dip angle ($\tan\lambda$) as a function of momentum for muons.

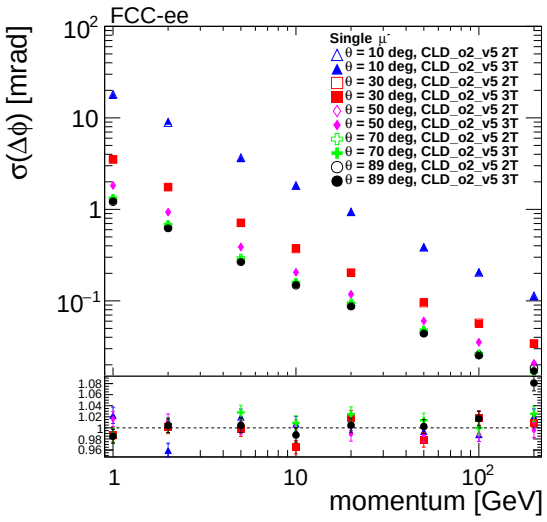

(a) Azimuthal angle ϕ resolution

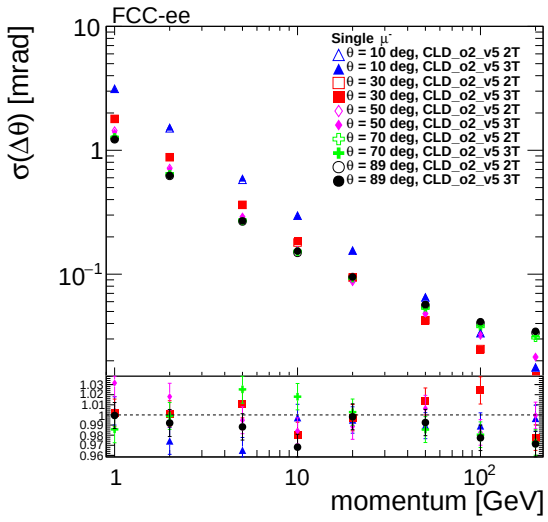

(b) Polar angle θ resolution

Figure A.45: Impact of a larger magnetic field: comparison between the CLD new baseline geometry with a 2 T solenoid and a configuration with a 3 T field. Azimuthal (ϕ) and polar (θ) angle resolutions as a function of momentum for muons.

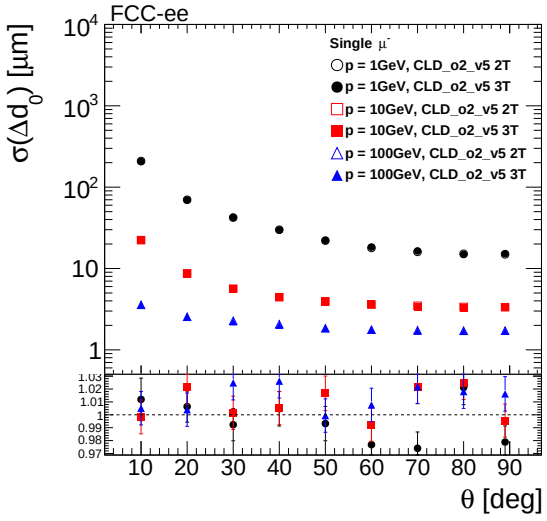

(a) Transverse impact parameter d_0 resolution

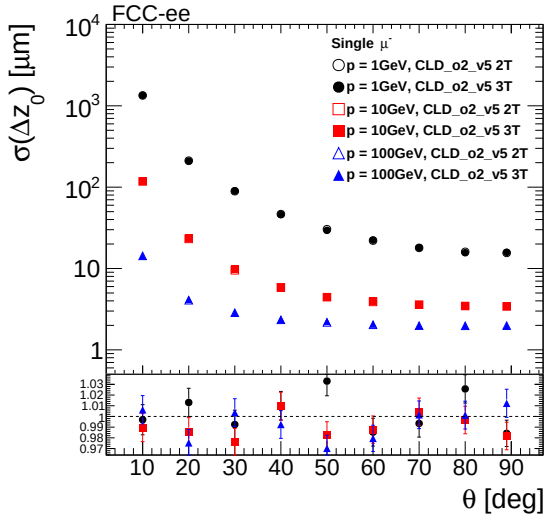

(b) Longitudinal impact parameter z_0 resolution

Figure A.46: Impact of a larger magnetic field: comparison between the CLD new baseline geometry with a 2 T solenoid and a configuration with a 3 T field. Transverse and longitudinal impact parameter (d_0, z_0) resolutions as a function of polar angle for muons.

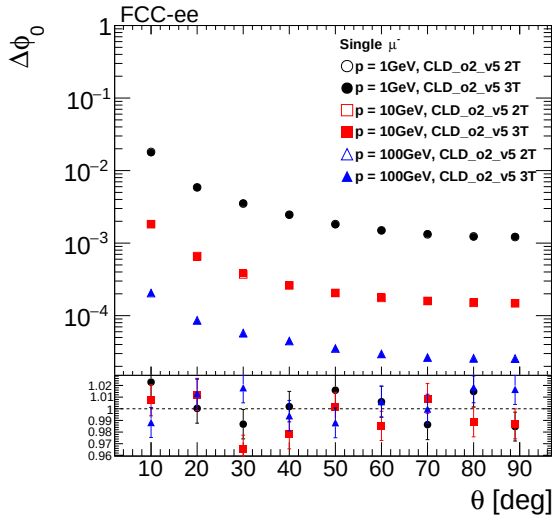

(a) Residual on the azimuthal angle at the point of closest approach ϕ_0 resolution

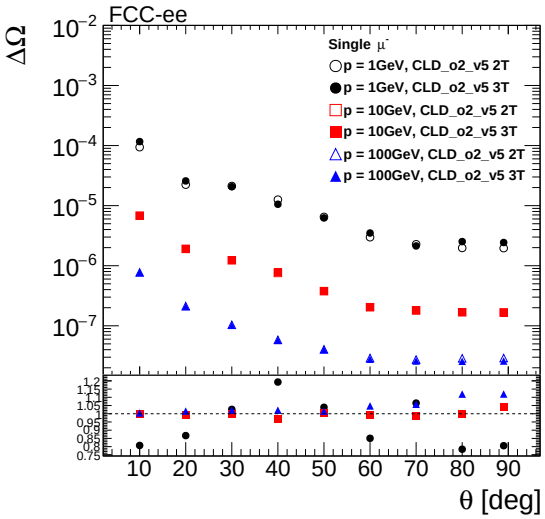

(b) Curvature Ω resolution

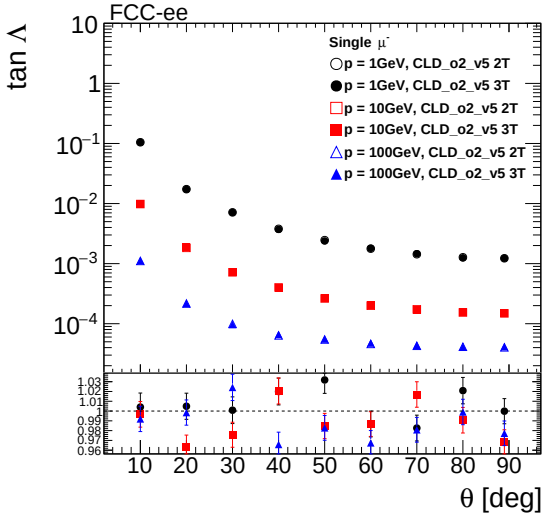

(c) track dip angle $\tan\lambda$ resolution

Figure A.47: Impact of a larger magnetic field: comparison between the CLD new baseline geometry with a 2 T solenoid and a configuration with a 3 T field. Resolutions of the azimuthal angle at the point of closest approach (ϕ_0), curvature (Ω), and track dip angle ($\tan\lambda$) as a function of polar angle for muons.

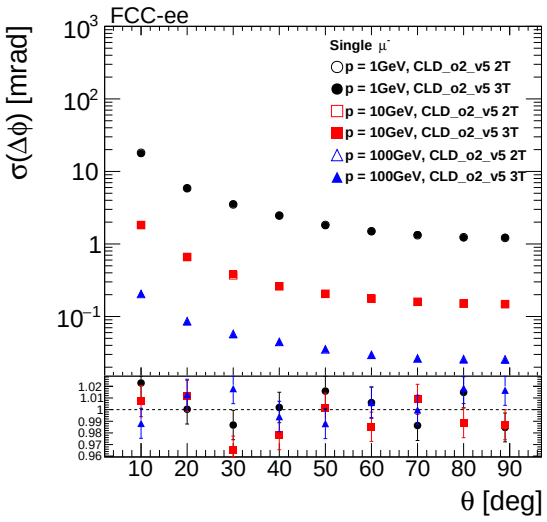

(a) Azimuthal angle ϕ resolution

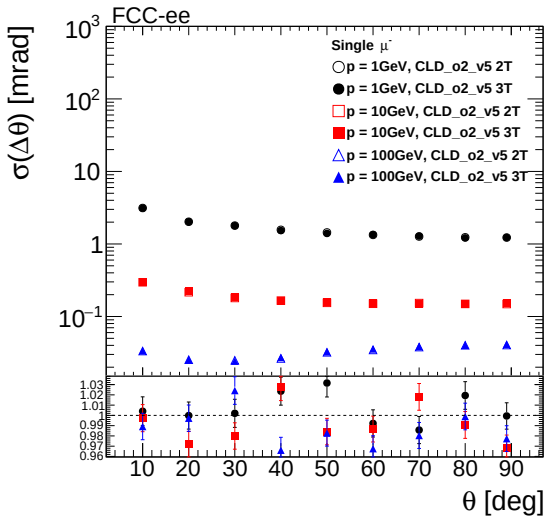

(b) Polar angle θ resolution

Figure A.48: Impact of a larger magnetic field: comparison between the CLD new baseline geometry with a 2 T solenoid and a configuration with a 3 T field. Azimuthal (ϕ) and polar (θ) angle resolutions as a function of polar angle for muons.

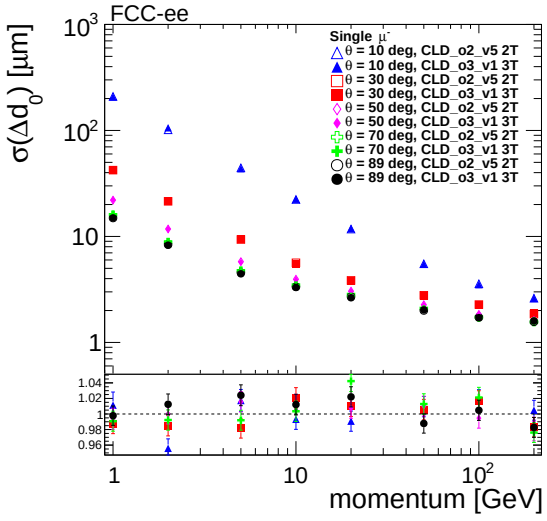

(a) Transverse impact parameter d_0 resolution

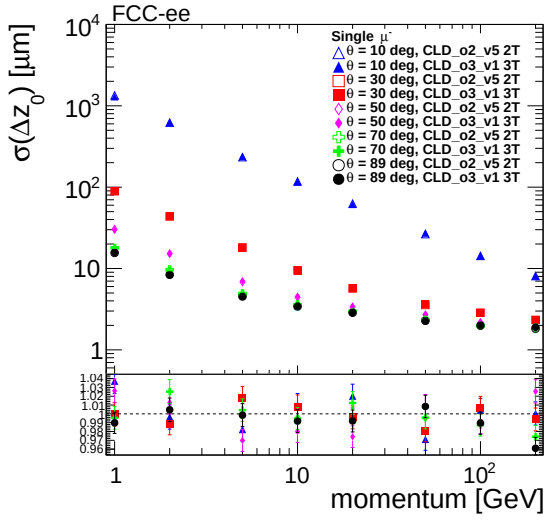

(b) Longitudinal impact parameter z_0 resolution

Figure A.49: Impact of a reduced tracker volume: comparison between the CLD new baseline geometry at 2 T and a configuration with a shrunk tracker at 3 T. Transverse and longitudinal impact parameter (d_0, z_0) resolutions as a function of momentum for muons.

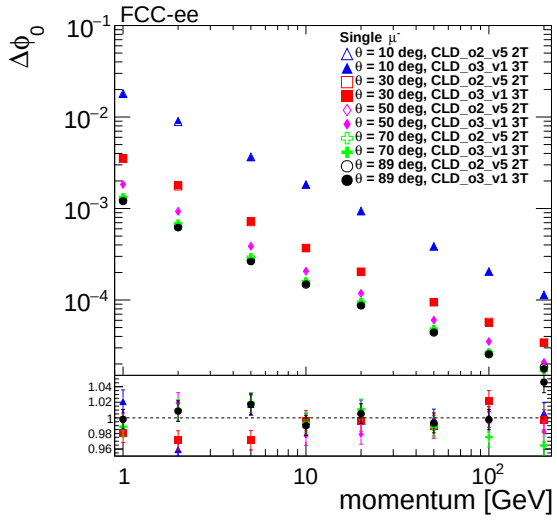

(a) Residual on the azimuthal angle at the point of closest approach ϕ_0 resolution

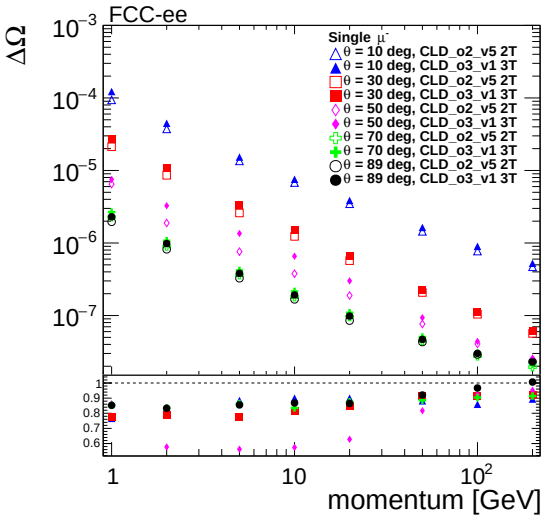

(b) Curvature Ω resolution

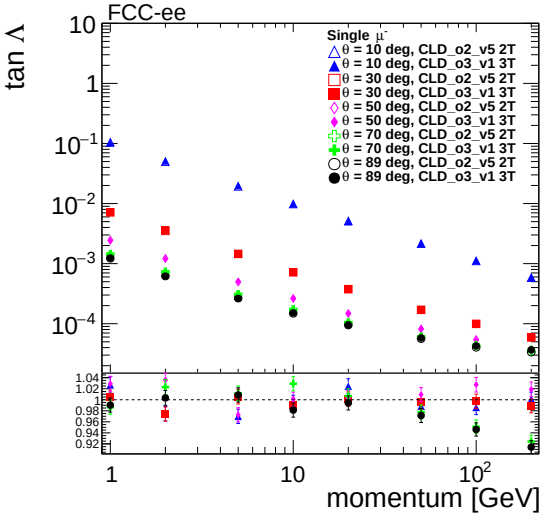

(c) track dip angle $\tan\lambda$ resolution

Figure A.50: Impact of a reduced tracker volume: comparison between the CLD new baseline geometry at 2 T and a configuration with a shrunk tracker at 3 T. Resolutions of the azimuthal angle at the point of closest approach (ϕ_0), curvature (Ω), and track dip angle ($\tan\lambda$) as a function of momentum for muons.

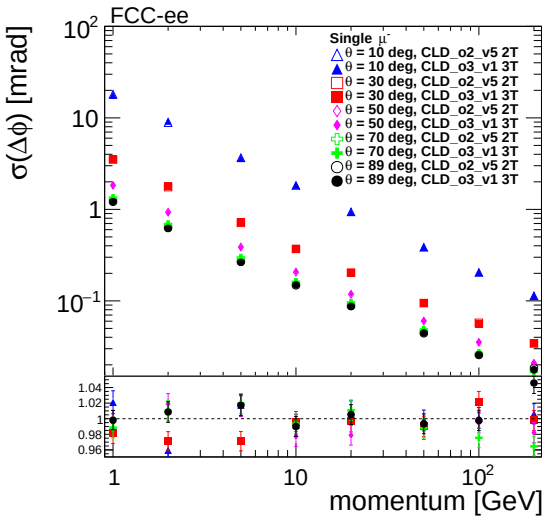

(a) Azimuthal angle ϕ resolution

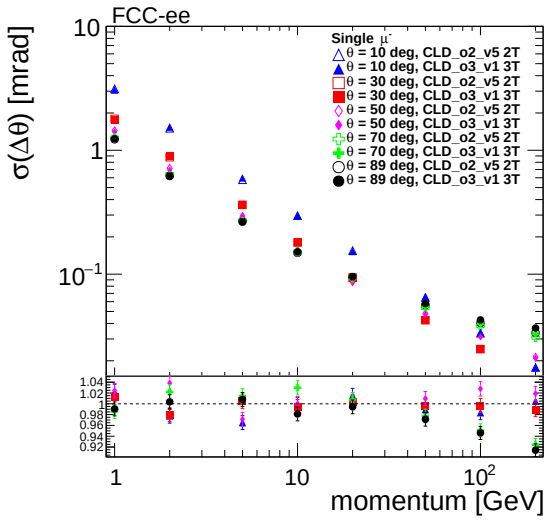

(b) Polar angle θ resolution

Figure A.51: Impact of a reduced tracker volume: comparison between the CLD new baseline geometry at 2 T and a configuration with a shrunk tracker at 3 T. Azimuthal (ϕ) and polar (θ) angle resolutions as a function of momentum for muons.

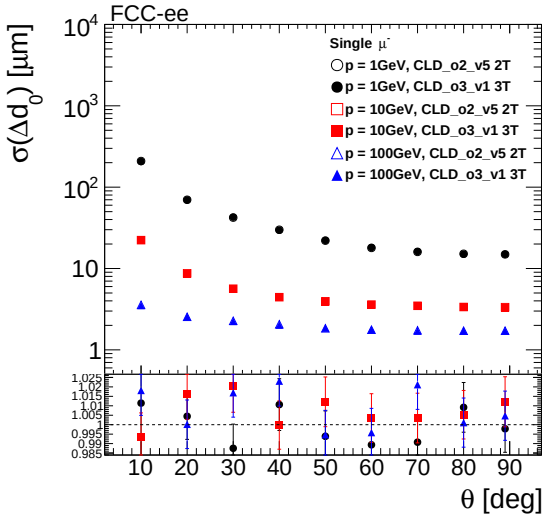

(a) Transverse impact parameter d_0 resolution

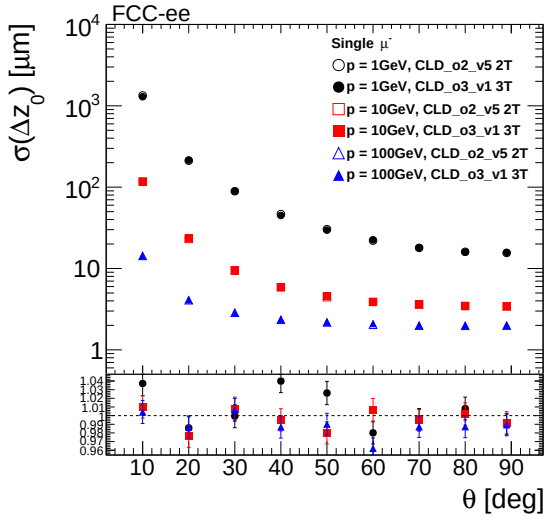

(b) Longitudinal impact parameter z_0 resolution

Figure A.52: Impact of a reduced tracker volume: comparison between the CLD new baseline geometry at 2 T and a configuration with a shrunk tracker at 3 T. Transverse and longitudinal impact parameter (d_0, z_0) resolutions as a function of polar angle for muons.

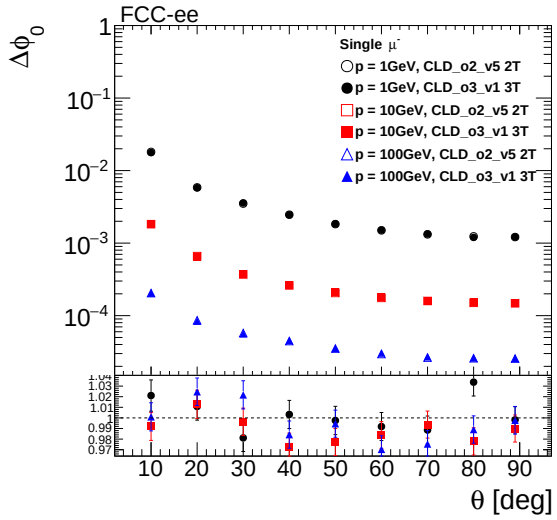

(a) Residual on the azimuthal angle at the point of closest approach ϕ_0 resolution

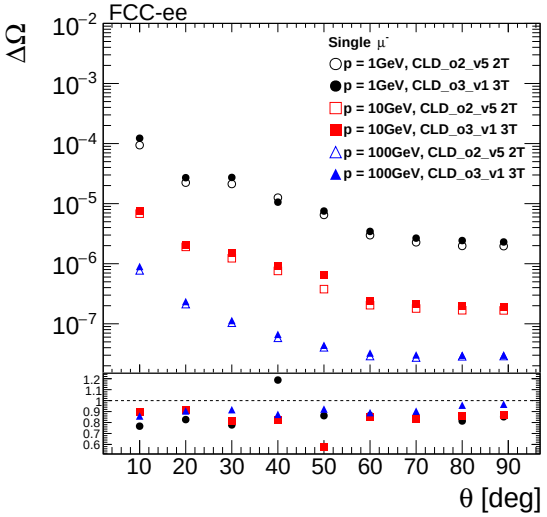

(b) Curvature Ω resolution

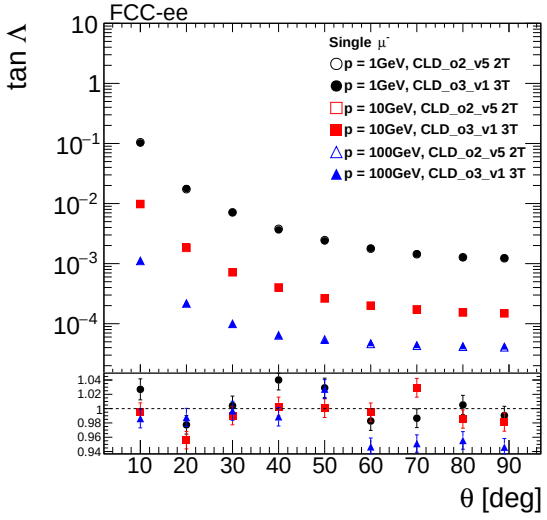

(c) track dip angle $\tan\lambda$ resolution

Figure A.53: Impact of a reduced tracker volume: comparison between the CLD new baseline geometry at 2 T and a configuration with a shrunk tracker at 3 T. Resolutions of the azimuthal angle at the point of closest approach (ϕ_0), curvature (Ω), and track dip angle ($\tan\lambda$) as a function of polar angle for muons.

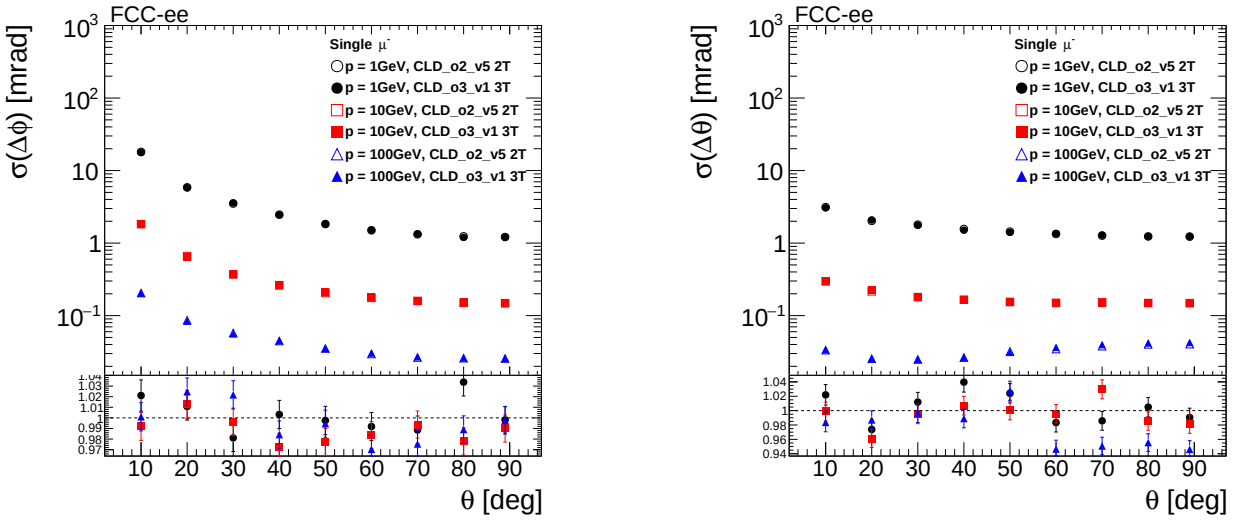

(a) Azimuthal angle ϕ resolution

(b) Polar angle θ resolution

Figure A.54: Impact of a reduced tracker volume: comparison between the CLD new baseline geometry at 2 T and a configuration with a shrunk tracker at 3 T. Azimuthal (ϕ) and polar (θ) angle resolutions as a function of polar angle for muons.

Acronyms

ALLEGRO A Lepton-Lepton collider Experiment with Granular Read-Out. 89

BSM Beyond the Standard Model. 24

CA cellular automaton. 49, 50, 55, 56

CLD CLIC-Like Detector. 39, 53–57, 59, 85, 87, 90–101, 103, 105, 129

CLIC Compact LInear Collider. 41, 48, 53–57, 85, 87, 95

CLICdet Compact LInear Collider Detector. 94, 129

ECAL Electromagnetic Calorimeter. 86, 94–96

FCC Future Circular Collider. 86, 99–101

FCCee Future circular collider e^+e^-. 41, 53, 64, 67, 69, 74, 75, 81, 82, 85–87, 89, 90, 97, 98, 100, 105, 119, 121, 123, 145

FCChh Future circular collider hadron-hadron. 85, 86

HCAL Hadronic Calorimeter. 86, 95, 96

HNLs Heavy Neutral Leptons. 119, 121–124, 126

IDEA Innovative Detector for E+e- Accelerator. 88

ILC Iternational Linear Collider. 89, 90, 95

ILD Iternational Linear Detector. 89, 90, 95

IP Interaction Point. 58, 91

KF Kalman Filter. 51–54, 57

LCIO LCIO is a framework that defines a data model for linear collider detector studies. It is intended to be used in both simulation studies and analysis frameworks. Its light weight and portability makes it also suitable for use in detector R&D applications. It provides a C++ and a Java implementation with a common interface (API). 43

LDC Large Detector Concept. 43

LHC Large Hadron Collider. 24, 85, 86

LLPs Long lives particles. 119, 123

LumiCal Luminosity Calorimeter. 154–156

MDI Machine Detector Interface. 87, 90, 91, 93, 95–97

pca point of closest approach. 44–46

PID particle identification. 90, 105, 110, 111

PV Primary Vertex. 58

SM Standard Model. 24, 120

TPC Time Projection Chamber. 90

VTX Vertex detector. 86

Bibliography

[1] J. J. Thomson. Cathode Rays. 1897.
DOI: 10.1080/14786449708621070.

[2] E. Rutherford. The Scattering of α and β Particles by Matter and the Structure of the Atom. 1911.
DOI: 10.1080/14786440508637080.

[3] J. Chadwick. The Existence of a Neutron. 1932.
DOI: 10.1098/rspa.1932.0112.

[4] S. L. Glashow. Partial-symmetries of weak interactions. 1961.
DOI: 10.1016/0029-5582(61)90469-2.

[5] Steven Weinberg. A Model of Leptons. 1967.
DOI: 10.1103/PhysRevLett.19.1264.

[6] Abdus Salam. Weak and Electromagnetic Interactions. 1968.

[7] Peter W.higg. Broken Symmetries and the Masses of Gauge Bosons. 1964.
DOI: 10.1103/PhysRevLett.13.508.

[8] The ATLAS Collaboration. Observation of a new particle in the search for the Standard Model Higgs boson with the ATLAS detector at the LHC. 2012.
arXiv:1207.7214v2.

[9] The CMS Collaboration. Observation of a new boson at a mass of 125 GeV with the CMS experiment at the LHC. 2012.
arXiv:1207.7235v2.

[10] Lyndon R Evans and Philip Bryant. LHC Machine. 2008.
DOI: 10.1088/1748-0221/3/08/S08001.

[11] Chris Quigg. Unanswered Questions in the Electroweak Theory. 2009.
DOI: 10.48550/arXiv.0905.3187.

[12] François Englert and Robert Brout. Broken Symmetry and the Mass of Gauge Vector Mesons. 1964.
DOI: 10.1103/PhysRevLett.13.321.

[13] Standard model of elementary particles. https://en.wikipedia.org/wiki/File:Standard_Model_of_Elementary_Particles.svg, 2006. Accessed: 2025-07-21.

[14] Particle Data Group. Review of Particle Physics. *Prog. Theor. Exp. Phys.*, 2022.
DOI: 10.1093/ptep/ptac097.

[15] Steven Weinberg. *The Quantum Theory of Fields, Vol. 1: Foundations*. 1995. DOI: 10.1017/CBO9781139644167.

[16] R. P. Feynman. Space-time approach to quantum electrodynamics. 1949. DOI: 10.1103/PhysRev.76.769.

[17] Julian S. Schwinger. On Quantum electrodynamics and the magnetic moment of the electron. 1948. DOI: 10.1103/PhysRev.73.416.

[18] David J. Gross and Frank Wilczek. Ultraviolet Behavior of Non-Abelian Gauge Theories. 1973. DOI: 10.1103/PhysRevLett.30.1343.

[19] H. David Politzer. Reliable Perturbative Results for Strong Interactions? 1973. DOI: 10.1103/PhysRevLett.30.1346.

[20] S. Fogwell D. Hanneke and G. Gabrielse. New Measurement of the Electron Magnetic Moment and the Fine Structure Constant. 2008. DOI: 10.1103/PhysRevLett.100.120801.

[21] Willis E. Lamb and Robert C. Retherford. Fine Structure of the Hydrogen Atom by a Microwave Method. 1947. DOI: 10.1103/PhysRev.72.241.

[22] C. S. Wu et al. Experimental Test of Parity Conservation in Beta Decay. 1957. DOI: 10.1103/PhysRev.105.1413.

[23] J. H. Christenson et al. Evidence for the 2π Decay of the K_2^0 Meson. 1964. DOI: 10.1103/PhysRevLett.13.138.

[24] Steven Weinberg. Conceptual Foundations of the Unified Theory of Weak and Electromagnetic Interactions. 1980. DOI: 10.1103/RevModPhys.52.515.

[25] Kenneth G. Wilson. Confinement of quarks. 1974. DOI: 10.1103/PhysRevD.10.2445.

[26] Jeff Greensite. *An Introduction to the Confinement Problem*. 2011. DOI: 10.1007/978-3-642-14382-3.

[27] Michael E. Peskin and Daniel V. Schroeder. *An Introduction to Quantum Field Theory*. Westview Press, Boulder, Colorado, 1995.

[28] Paul Langacker. *The Standard Model and Beyond*. Series in High Energy Physics, Cosmology and Gravitation. CRC Press, 2010.

[29] G. Arnison et al. Experimental Observation of Isolated Large Transverse Energy Electrons with Associated Missing Energy at s = 540 GeV. 1983. DOI: 10.1016/0370-2693(83)91177-2.

[30] M. Banner et al. Observation of Single Isolated Electrons of High Transverse Momentum in Events with Missing Transverse Energy at the CERN p anti-p Collider. 1983. DOI: 10.1016/0370-2693(83)91605-2.

[31] ALEPH DELPHI L3 OPAL and SLD Collaborations. Precision electroweak measurements on the Z resonance. 2006.
DOI: 10.1016/j.physrep.2005.12.006.

[32] Kazuhiko Nishijima. Charge Independence Theory of V Particles. 1955.
DOI: 10.1143/PTP.13.285.

[33] F. J. Hasert et al. Observation of neutrino-like interactions without muon or electron in the Gargamelle neutrino experiment. 1973.
DOI: 10.1016/0370-2693(73)90499-1.

[34] Sheldon L. Glashow, John Iliopoulos, and Luciano Maiani. Weak Interactions with Lepton-Hadron Symmetry. 1970.
DOI: 10.1103/PhysRevD.2.1285.

[35] Gerald S. Guralnik C. R. Hagen and T. W. B. Kibble. Global Conservation Laws and Massless Particles. 1964.
DOI: 10.1103/PhysRevLett.13.585.

[36] Tevatron Electroweak Working Group. Combination of CDF and D0 results on the mass of the top quark. *Phys. Rev. D*, 2014.
DOI: 10.1103/PhysRevD.89.072001.

[37] Y. Fukuda et al. Evidence for oscillation of atmospheric neutrinos. 1998.
DOI: 10.1103/PhysRevLett.81.1562.

[38] Q. R. Ahmad et al. Direct evidence for neutrino flavor transformation from neutral current interactions in the Sudbury Neutrino Observatory. 2002.
DOI: 10.1103/PhysRevLett.89.011301.

[39] Planck Collaboration. Planck 2018 results. VI. Cosmological parameters. 2020.
DOI: 10.1051/0004-6361/201833910.

[40] Mikhail Shaposhnikov Laurent Canetti, Marco Drewes. Matter and Antimatter in the Universe. 2012.
DOI: 10.1088/1367-2630/14/9/095012.

[41] Carlo Rovelli. Loop quantum gravity. 1998.
DOI: 10.12942/lrr-1998-1.

[42] Stephen P. Martin. A Supersymmetry primer. 2016.
arxiv.org/abs/hep-ph/9709356.

[43] Paul Langacker. Grand Unified Theories and Proton Decay. 1981.
DOI: 10.1016/0370-1573(81)90059-4.

[44] Gia Dvali Nima Arkani-Hamed, Savas Dimopoulos. The Hierarchy problem and new dimensions at a millimeter. 1998.
DOI: 10.1016/S0370-2693(98)00466-3.

[45] Lisa Randall and Raman Sundrum. A Large mass hierarchy from a small extra dimension. 1999.
DOI: 10.1103/PhysRevLett.83.3370.

[46] P. Minkowski. mu $\rightarrow$ eγ at a Rate of One Out of 10^9 Muon Decays? 1977.
DOI: 10.1016/0370-2693(77)90435-X.

[47] R. N. Mohapatra and G. Senjanovic. Neutrino Mass and Spontaneous Parity Violation. 1980. DOI: 10.1103/PhysRevLett.44.912.

[48] Takehiko Asaka and Mikhail Shaposhnikov. The nuMSM, dark matter and baryon asymmetry of the universe. 2005. DOI: 10.1016/j.physletb.2005.06.020.

[49] Lyn Evans and Philip Bryant. LHC Machine. 2008. DOI: 10.1088/1748-0221/3/08/S08001.

[50] ATLAS Collaboration. The ATLAS Experiment at the CERN Large Hadron Collider. 2008. DOI: 10.1088/1748-0221/3/08/S08003.

[51] CMS Collaboration. The CMS Experiment at the CERN LHC. 2008. DOI: 10.1088/1748-0221/3/08/S08004.

[52] ATLAS Collaboration. Search for supersymmetry in final states with missing transverse momentum and multiple b-jets in proton–proton collisions at 13 TeV with the ATLAS detector. 2020. DOI: 10.1140/epjc/s10052-023-11543-6.

[53] CMS Collaboration. Search for dark matter produced in association with a leptonically decaying Z boson in proton-proton collisions at $\sqrt(s) = 13$ TeV. 2021. DOI: 10.1140/epjc/s10052-020-08739-5.

[54] ATLAS Collaboration. Measurements of the Higgs boson production and decay rates and constraints on its couplings from a combined ATLAS analysis of the LHC pp collision data at $\sqrt(s) = 7$ and 8 TeV. 2015. DOI: 10.1103/PhysRevD.91.012006.

[55] CMS Collaboration. Precise determination of the mass of the Higgs boson and studies of the compatibility of its couplings with the standard model. 2015. DOI: 10.1140/epjc/s10052-015-3351-7.

[56] O. Brüning G. Apollinari, I. Bejar Alonso, M. Lamont, and L. Rossi. High-Luminosity Large Hadron Collider (HL-LHC): Technical Design Report V. 0.1. *CERN Yellow Report*, 2017. DOI: 10.23731/CYRM-2017-004.

[57] T2K Collaboration. Constraint on the Matter-Antimatter Symmetry-Violating Phase in Neutrino Oscillations. 2020. DOI: 10.1038/s41586-020-2177-0.

[58] NOvA Collaboration. First Measurement of Neutrino Oscillation Parameters using Neutrinos and Antineutrinos by NOvA. 2019. DOI: 10.1103/PhysRevLett.123.151803.

[59] Fengpeng An and others [JUNO Collaboration]. Neutrino Physics with JUNO. 2016. DOI: 10.1088/0954-3899/43/3/030401.

[60] B. Abi and others [DUNE Collaboration]. Deep Underground Neutrino Experiment (DUNE), Far Detector Technical Design Report, Volume II: DUNE Physics. 2020. DOI: 10.48550/arXiv.2002.03005.

[61] K. Abe and others [Hyper-Kamiokande Proto-Collaboration]. Hyper-Kamiokande Design Report. 2018. DOI: 10.48550/arXiv.1805.04163.

[62] KATRIN Collaboration. Improved Upper Limit on the Neutrino Mass from a Direct Kinematic Method by KATRIN. 2019.
DOI: 10.1103/PhysRevLett.123.221802.

[63] GERDA Collaboration. Final Results of GERDA on the Search for Neutrinoless Double-β Decay. 2020.
DOI: 10.1103/PhysRevLett.125.252502.

[64] CUORE Collaboration. Improved Limit on Neutrinoless Double-Beta Decay in ^{130}Te with CUORE. 2020.
DOI: 10.1103/PhysRevLett.124.122501.

[65] Kevork N. Abazajian et al. Light Sterile Neutrinos: A White Paper. 2012.
https://arxiv.org/abs/1204.5379.

[66] XENON Collaboration. First Dark Matter Search with Nuclear Recoils from the XENONnT Experiment. 2023.
DOI: 10.48550/arXiv.2303.14729.

[67] LZ Collaboration. First Dark Matter Search Results from the LUX-ZEPLIN (LZ) Experiment. 2022.
DOI: 10.1103/PhysRevLett.131.041002.

[68] PandaX-4T Collaboration. Dark Matter Search Results from the PandaX-4T Experiment. 2021.
DOI: 10.1103/PhysRevLett.127.261802.

[69] IceCube Collaboration. Neutrino emission from the direction of the blazar TXS 0506+056 prior to the IceCube-170922A alert. 2018.
DOI: 10.1126/science.aat2890.

[70] ANTARES Collaboration. First search for point sources of high energy cosmic neutrinos with the ANTARES neutrino telescope. 2011.
DOI: 10.1088/2041-8205/743/1/L14.

[71] S. Adrian-Martinez and others [KM3NeT Collaboration]. Letter of intent for KM3NeT 2.0. 2016.
DOI: 10.1088/0954-3899/43/8/084001.

[72] Pierre Auger Collaboration. Depth of Maximum of Air-Shower Profiles at the Pierre Auger Observatory: Measurements at Energies above $10^{17.8}$ eV. 2014.
DOI: 10.1103/PhysRevD.90.122005.

[73] LIGO Scientific and Virgo Collaborations. Observation of Gravitational Waves from a Binary Black Hole Merger. 2016.
DOI: 10.1103/PhysRevLett.116.061102.

[74] Chiara Caprini and Daniel G. Figueroa. Cosmological Backgrounds of Gravitational Waves. 2018.
DOI: 10.1088/1361-6382/aac608.

[75] A.Blondel et al. Theory Requirements and Possibilities for the FCC-ee and other Future High Energy and Precision Frontier Lepton Colliders. 2019.
DOI: 10.48550/arXiv.1901.02648.

[76] CEPC Study Group. CEPC Conceptual Design Report: Volume 2 - Physics & Detector. 2018.
https://arxiv.org/abs/1811.10545.

[77] European Strategy Group. 2020 Update of the European Strategy for Particle Physics. *CERN-ESU-015*, 2020.
https://cds.cern.ch/record/2721370.

[78] P. Bambade et al. The International Linear Collider: A Global Project. 2019.
https://arxiv.org/abs/1903.01629.

[79] CLICdp and CLIC Collaborations. The Compact Linear Collider (CLIC) - 2018 Summary Report. 2018.
DOI: 10.23731/CYRM-2018-002.

[80] FCC Collaboration. FCC Physics Opportunities: Future Circular Collider Conceptual Design Report Volume 1. 2019.
DOI: 10.1140/epjc/s10052-019-6904-3.

[81] Michael Benedikt et al. FCC-hh: The Hadron Collider: Future Circular Collider Conceptual Design Report Volume 3. 2018.
DOI: 10.1140/epjst/e2019-900087-0.

[82] Michael Benedikt et al. FCC-ee: The Lepton Collider - Future Circular Collider Conceptual Design Report Volume 2. 2019.
10.1140/epjst/e2019-900045-4.

[83] I. Agapov et al. Future Circular Lepton Collider FCC-ee: Overview and Status. 2022.
DOI: 10.48550/arXiv.2203.08310.

[84] J. de Blas et al. Higgs Boson Studies at Future Particle Colliders. 2020.
DOI: 10.1007/JHEP01(2020)139.

[85] Z. Drasal and W. Riegler. An extension of the Gluckstern formulas for multiple scattering: analytic expressions for track parameter resolution using optimum weights. *physics.ins-det*, (2018).

[86] V.L. Highland. Some practical remarks on multiple scattering. 1975.
DOI: 10.1016/0029-554X(75)90743-0.

[87] R. Frühwirth and M. Regler. Data analysis techniques for high-energy physics. *Cambridge Monographs on Particle Physics, Nuclear Physics and Cosmology, Cambridge University Press*, (2000).

[88] E. Brondolin, E. Leogrande, et al. Conformal Tracking for all-silicon trackers at future electron–positron colliders. *physics.ins-det*, (2019).

[89] J. D. Jackson. *Classical Electrodynamics*. Wiley, 1998.

[90] E.Brondolin. *Track reconstruction in the CMS experiment for the High Luminosity LHC*. PhD thesis, (2017).

[91] A.Vogel. The Coordinate System for LDC Detector Studies. *LC-DET-2005-009*, (2005).

[92] T.Krämer. Track Parameters in LCIO. *LC-DET-2006-004*, (2006).

[93] M. Hansroul, H. Jeremie, and D. Savard. Fast circle fit with the conformal mapping method. *Nucl. Instrum. Meth. A270.2*, page 498–501, (1998). DOI: 10.1016/0168-9002(88)90722-X.

[94] A. Glazov et al. Filtering tracks in discrete detectors using a cellular automaton. *Nucl. Instrum. Meth. A329.1*, page 262–268, (1993). DOI: 10.1016/0168-9002(93)90945-E.

[95] R. Frühwirth. Application of Kalman filtering to track and vertex fitting. 1987. DOI: 10.1016/0168-9002(87)90887-4.

[96] S. Qian P. Billoir. Track fitting with multiple scattering: A new method. 1984. DOI: 10.1016/0168-9002(90)91835-Y.

[97] B.Jones and B.Tompkins. A Physicist's Guide to Kalman Filters.

[98] N. Bacchetta, J.-J. Blaising, et al. Cld - a detector concept for the fcc-ee. *physics.ins-det*, 2019. arXiv: 1911.12230v3.

[99] D.Arominski et al. A detector for CLIC: main parameters and performance. 2018. arXiv: 1812.07337v1.

[100] R. Frühwirth and M. Regler. *Data Analysis Techniques for High-Energy Physics*. Cambridge Monographs on Particle Physics, Nuclear Physics and Cosmology, 2000. URL: https://books.google.at/books?id=2mq94rdFd3gC.

[101] A. Strandlie and R. Frühwirth. Track and vertex reconstruction: From classical to adaptive methods. *Rev. Mod. Phys. 82*, page 1419–1458, (2010). DOI: 10.1103/RevModPhys.82.1419.

[102] R. Frühwirth. Application of kalman filtering to track and vertex fitting. *Nucl. Instrum. Meth. A262*, page 444, (1987). DOI: 10.1016/0168-9002(87)90887-4.

[103] K. Fujii. Extended kalman filter. *The ACDA-Sim-J Group*. URL: http://www-jlc.kek.jp/subg/offl/kaltest/doc/ReferenceManual.pdf.

[104] Franco Bedeschi. A vertex fitting package. (2024). DOI: 10.48550/arXiv.2409.19326.

[105] John S. Marshall, Mark A. Thomson, and Brian Muon. The Pandora Software Development Kit for Pattern Recognition. DOI: 10.1140/epjc/s10052-015-3659-3.

[106] Mark A. Thomson. Particle Flow Calorimetry and the PandoraPFA Algorithm. 2009. DOI: 10.1016/j.nima.2009.09.009.

[107] E. Ploerer et al. Characterisation of analogue maps produced in the 65 nm tpsco process. 2025. DOI: 10.1088/1748-0221/20/01/C01019.

[108] Eric R. Fossum. Active pixel sensors: are ccds dinosaurs? 1993. DOI: 10.1117/12.148585.

[109] R Turchetta et al. A monolithic active pixel sensor for charged particle tracking and imaging using standard vlsi cmos technology. 2001.
DOI: 10.1016/S0168-9002(00)00893-7.

[110] W. Snoeys. Monolithic cmos sensors for high energy physics — challenges and perspectives. 2023.
DOI: 10.1016/j.nima.2023.168678.

[111] C.-A. Reidel et al. Response of the mimosa-28 pixel sensor to a wide range of ion species and energies. 2021.
DOI: 10.1016/j.nima.2021.165807.

[112] Julie Constanzo et al. Characterization of a cmos sensor array for small field fluence measurement of a low energy proton beam. 2018.
DOI: 10.1016/j.nima.2018.09.018.

[113] J. Heymes et al. Implantable cmos pixel sensor for positron imaging in rat brain. 2018.
DOI: 10.1016/j.nima.2018.09.117.

[114] on behalf of the ALICE collaboration F. Reidt. Upgrade of the alice its detector. 2022.
DOI: 10.1016/j.nima.2022.166632.

[115] M. Mager. Alpide, the monolithic active pixel sensor for the alice its upgrade. 2016.
DOI: 10.1016/j.nima.2015.09.057.

[116] Gianluca Aglieri Rinella on behalf of the ALICE collaboration. The alpide pixel sensor chip for the upgrade of the alice inner tracking system. 2017.
DOI: 10.1016/j.nima.2016.05.016.

[117] G. Aglieri Rinella et al. Characterization of analogue monolithic active pixel sensor test structures implemented in a 65 nm cmos imaging process. 2024.
DOI: 10.1016/j.nima.2024.169896.

[118] D. Dannheim et al. Corryvreckan: a modular 4d track reconstruction and analysis software for test beam data. 2021.
DOI: 10.1088/1748-0221/16/03/P03008.

[119] V. Blobel. A new fast track-fit algorithm based on broken lines. 2006.
DOI: 10.1016/j.nima.2006.05.156.

[120] M. Mager. The telescope optimiser. https://mmager.web.cern.ch/telescope/tracking.html.

[121] S. Bugiel et al. Charge sensing properties of monolithic cmos pixel sensors fabricated in a 65 nm technology. 2022.
DOI: 10.1016/j.nima.2022.167213.

[122] S. Bugiel et al. Characterization of analogue monolithic active pixel sensor test structures implemented in a 65 nm cmos imaging process. 2024.
DOI: 10.1088/1748-0221/19/01/C01019.

[123] M. Benedikt et al. Future Circular Hadron Collider FCC-hh: Overview and Status. 2022.
DOI: 10.48550/arXiv.2203.07804.

[124] ILD Concept Group. The International Linear Collider: A Global Project. 2010.
DOI: 10.48550/arXiv.1903.01629.

[125] O. Brunner et al. The CLIC project. 2022.
DOI: 10.48550/arXiv.2203.09186.

[126] IDEA Study Group. The IDEA detector concept for FCC-ee. 2025.
DOI: 10.48550/arXiv.2502.212239.

[127] Juska Pekkanen. ALLEGRO FCC-ee detector concept & Noble liquid calorimetry. 2024.
DOI: 10.1016/j.nima.2024.169921.

[128] Philip Bambade et al. The International Large Detector: Letter of Intent. 2019.
DOI: 10.48550/arXiv.1006.3396.

[129] A. Lorenzetti et al. Performance studies of the CE-65v2 MAPS prototype structure. 2025.
DOI: 10.48550/arXiv.2502.04070.

[130] Manuela Boscolo et al. Mechanical model for the FCC-ee interaction region. 2023.
DOI: 10.1140/epjti/s40485-023-00103-7.

[131] M. A. Thomson. Particle Flow Calorimetry and the PandoraPFA Algorithm. 2009.
DOI: 10.48550/arXiv.0907.3577.

[132] CALICE Collaboration. Calorimetry for Lepton Collider Experiments - CALICE results and activities. 2013.
DOI: 10.48550/arXiv.1212.5127.

[133] D Contardo et al. Technical Proposal for the Phase-II Upgrade of the CMS Detector. 2015.
DOI: 10.17181/CERN.VU8I.D59J.

[134] P. Fernandez Declara et al. The Key4hep turnkey software stack for future colliders. 2022.
DOI:10.22323/1.398.0844.

[135] Frank Gaede et al. EDM4hep - a common event data model for HEP experiments. 2022.
DOI: 10.22323/1.414.1237.

[136] C. Helsens et al. HEP-FCC/FCCAnalyses: v0.10.0, 2024.
10.5281/zenodo.13871482.

[137] S. Agostinelli et al. Geant4 – a simulation toolkit. 2003.
DOI: 10.1016/S0168-9002(03)01368-8.

[138] Ivan Perić. A novel monolithic pixelated particle detector implemented in high-voltage CMOS technology. 2007.
DOI: 10.1016/j.nima.2007.07.115.

[139] A. Ciarma et al. MACHINE INDUCED BACKGROUNDS IN THE FCC-ee MDI REGION AND BEAMSTRAHLUNG RADIATION. 2022.
DOI: 10.18429/JACoW-eeFACT2022-TUZAT0203.

[140] R. Forty et al. The ARC project: a compact RICH for FCC-ee. 2021.
FCC Physics Week 2021: ARC-presentation.pdf.

[141] A.Tolosa-Delgado. Performance of the ARC RICH detector in the FCC-ee context. 2025.
FCC Physics Week 2025: ARC-presentation.pdf.

[142] Lawrence Lee et al. Collider Searches for Long-Lived Particles Beyond the Standard Model. 2019.
DOI: 10.1016/j.ppnp.2019.02.006.

[143] Steven Lowette Simon Knapen. A guide to hunting long-lived particles at the LHC. 2022. arXiv:2212.03883.

[144] Stephen P. Martin. A Supersymmetry Primer. 2016. DOI: 10.1142/9789812839657_0001.

[145] Laurel Stephenson Haskins Howard E. Haber. Supersymmetric Theory and Models. 2022. DOI: 10.1142/9789813233348_0006.

[146] Asli M. Abdullahi et al. The Present and Future Status of Heavy Neutral Leptons. 2022. DOI: 10.1088/1361-6471/ac98f9.

[147] Nicole Righi Kiwoon Choi. Axion Theory and Model Building. 2024. DOI: 10.48550/arXiv.2401.17354.

[148] Vedran Brdar et al. Type-I Seesaw as the Common Origin of Neutrino Mass, Baryon Asymmetry, and the Electroweak Scale. 2019. DOI: 10.1103/PhysRevD.100.075029.

[149] Marco Drewes. Distinguishing Dirac and Majorana Heavy Neutrinos at Lepton Colliders. 2022. DOI: 10.22323/1.414.0608.

[150] T. Asaka, S. Blanchet, and M. Shaposhnikov. The νmsm, dark matter and neutrino masses. 2005. DOI: 10.1016/j.physletb.2005.09.070.

[151] S. Bilenky. Neutrinos: Majorana or Dirac? 2020. DOI: 10.48550/arXiv.2008.02110.

[152] Frank T. Avignone et al. Double beta decay, majorana neutrinos, and neutrino mass. 2008. DOI: 10.1103/RevModPhys.80.481.

[153] Anupama Atre et al. The search for heavy majorana neutrinos. 2009. DOI: 10.1088/1126-6708/2009/05/030.

[154] Frank F. Deppisch et al. Neutrinos and collider physics. page 075019, 2015. DOI: 10.1088/1367-2630/17/7/075019.

[155] Kyrylo Bondarenko et al. An allowed window for heavy neutral leptons below the kaon mass. 2021. DOI: 10.1007/JHEP07(2021)193 .

[156] J. Alimena et al. Searches for Long-Lived Particles at the Future FCC-ee. 2022. DOI: 10.3389/fphy.2022.967881.

[157] Zhong-Zhi Xianyu Yanou Cui. Probing Leptogenesis with the Cosmological Collider. 2022. DOI: 10.1103/PhysRevLett.129.111301.

[158] Pilar Hernandez et al. Bounds on right-handed neutrino parameters from observable leptogenesis. 2022. DOI: 10.1007/JHEP12%282022%29012.

[159] Maíra Dutra et al. A model for mixed warm and hot right-handed neutrino dark matter. 2021. DOI: 10.1007/JHEP10(2021)005 .

[160] Daniela Kirilova et al. BBN Constraints and Indications for Beyond Standard Model Neutrino Physics. 2023.
DOI: 10.20944/preprints202312.0224.v1 .

[161] Aram Hayrapetyan et al. The CMS statistical analysis and combination tool: Combine. *Comput. Softw. Big Sci.*, 8:19, 2024.

Université de Strasbourg

cnrs

Anita Sadowski

CLD full simulation and the study of displaced vertices for the FCC-ee

Résumé

Cette thèse explore l'articulation entre la technologie des détecteurs, les performances du suivi des particules et la recherche de nouvelle physique au FCC-ee. Dans un premier temps, les fondements théoriques et les méthodes de reconstruction du suivi sont présentés, incluant la transformation conforme, le filtrage de Kalman et l'ajustement de vertex, qui sont essentiels pour la mesure précise de l'impulsion et la reconstruction de sommets déplacés.
Le développement de technologies avancées pour les détecteurs de vertex a été étudié à travers des tests faisceaux des capteurs monolithiques à pixels actifs (MAPS) CE-65. Un résultat clé est que la digitalisation du signal sur deux bits permet d'atteindre des résolutions spatiales proches du cas analogique, avec une précision de l'ordre de ~ 5 μm pour des pas de pixels plus larges. Cette approche offre la possibilité de réduire significativement la consommation de puissance, une contrainte critique pour les détecteurs du FCC-ee.
Au niveau du détecteur global, les performances du concept **CLIC-Like Detector (CLD)** ont été évaluées. Pour ce faire, un cadre logiciel dédié, `k4DetPerformance`, a été développé afin de permettre des études systématiques des performances de suivi pour différentes géométries et configurations. Les études de simulation montrent que le CLD atteint les résolutions et efficacités requises pour le programme de physique du FCC-ee, tout en mettant en évidence les compromis associés aux conceptions alternatives.
Enfin, le potentiel de physique du FCC-ee a été étudié à travers le cas de référence des **Neutrinos Lourds Neutres (HNLs)**. Les études en simulation complète confirment les niveaux de sensibilité estimés en simulation rapide, tout en fournissant une description plus réaliste des effets du détecteur, en particulier pour la reconstruction des sommets déplacés. Toutefois, une prise en compte systématique des incertitudes reste à mener pour obtenir des projections robustes de sensibilité.
En résumé, ce travail montre comment les avancées en technologie de capteurs, en méthodes de reconstruction et en études de performances de détecteurs permettent directement de renforcer la recherche de nouvelle physique au FCC-ee. En reliant la R&D instrumentale, le développement logiciel et les études phénoménologiques, cette thèse contribue à préparer les outils expérimentaux nécessaires pour exploiter pleinement le potentiel de découverte de la prochaine génération de collisionneurs électron–positon.

Mots-clés : physique des particules, FCC, CERN, trajectographe en silicium, performance des détecteurs, particules à vie longue, HNL

Abstract

This thesis explores the interplay between detector technology, tracking performance, and searches for new physics at FCC-ee. First, the theoretical foundations and reconstruction methods of tracking are reviewed, including conformal mapping, Kalman filtering, and vertex fitting, which are central to precise momentum measurement and the reconstruction of displaced vertices.

The development of advanced vertex detector technologies has been studied through beam tests of CE-65 Monolithic Active Pixel Sensors (MAPS). A key result is that two-bit signal digitisation achieves spatial resolutions close to the analogue case, enabling ~ 5 μm resolution with larger pixel pitches. This approach offers the possibility of significantly reducing power consumption, a critical constraint for FCC-ee detectors.

At the detector level, the performance of the CLIC-Like Detector (CLD) concept has been evaluated. To this end, a dedicated software framework, `k4DetPerformance`, was developed to enable systematic studies of tracking performance across different detector geometries and configurations. Simulation studies show that CLD achieves the required resolutions and efficiencies for the FCC-ee physics programme, while highlighting the trade-offs involved in alternative designs.

Finally, the physics potential of FCC-ee has been investigated through the benchmark case of Heavy Neutral Leptons (HNLs). Full simulation studies confirm the sensitivity levels estimated with fast simulation, while providing a more realistic description of detector effects, especially for displaced vertex reconstruction. However, a systematic treatment of uncertainties remains to be completed to obtain robust sensitivity projections.

In summary, this work demonstrates how advances in sensor technology, reconstruction methods, and detector performance studies directly enable searches for new physics at FCC-ee. By bridging hardware R&D, software development, and phenomenological studies, this thesis contributes to preparing the experimental tools required to fully exploit the discovery potential of the next generation of electron–positron colliders.

Keywords: particle physics, FCC, CERN, silicon tracker, Detector performance, long-lived particles, HNL